



HAL
open science

Experimental and numerical analysis of single grain plasticity in an aluminium polycrystal deformed in uniaxial tension

Loïc Renversade

► **To cite this version:**

Loïc Renversade. Experimental and numerical analysis of single grain plasticity in an aluminium polycrystal deformed in uniaxial tension. Other. Université de Lyon, 2016. English. NNT : 2016LY-SEM019 . tel-01665161

HAL Id: tel-01665161

<https://theses.hal.science/tel-01665161>

Submitted on 15 Dec 2017

HAL is a multi-disciplinary open access archive for the deposit and dissemination of scientific research documents, whether they are published or not. The documents may come from teaching and research institutions in France or abroad, or from public or private research centers.

L'archive ouverte pluridisciplinaire **HAL**, est destinée au dépôt et à la diffusion de documents scientifiques de niveau recherche, publiés ou non, émanant des établissements d'enseignement et de recherche français ou étrangers, des laboratoires publics ou privés.



N° d'ordre NNT : 2016LYSEM019

THÈSE DE DOCTORAT DE L'UNIVERSITÉ DE LYON
opérée au sein de
l'École des Mines de Saint-Étienne

École doctorale N°488
Sciences, Ingénierie, Santé

Spécialité de doctorat : Science et Génie des Matériaux

Soutenue publiquement le 17/10/2016, par :

Loïc RENVERSADE

**Experimental and numerical analysis of single grain plasticity
in an aluminium polycrystal deformed in uniaxial tension**

–

**Analyse expérimentale et numérique de la plasticité à l'échelle
des grains individuels dans un polycrystal d'aluminium
déformé en traction uniaxiale**

Devant le jury composé de :

Président :	Roland	FORTUNIER	Professeur, Directeur de l'ENISE
Rapporteurs :	Olivier	CASTELNAU	Directeur de recherche CNRS, ENSAM Paris
	Veijo	HONKIMÄKI	Docteur, Group Leader à ESRF
Examineurs :	Félix	LATOURTE	Docteur, ingénieur chercheur, EDF R&D
	Wolfgang	LUDWIG	Directeur de recherche CNRS, INSA Lyon
Directeur de thèse :	András	BORBÉLY	Directeur de recherche, ENSM-SE
Encadrant de thèse :	Romain	QUEY	Chargé de recherche CNRS, ENSM-SE

Spécialités doctorales
 SCIENCES ET GENIE DES MATERIAUX
 MECANIQUE ET INGENIERIE
 GENIE DES PROCEDES
 SCIENCES DE LA TERRE
 SCIENCES ET GENIE DE L'ENVIRONNEMENT

Responsables :
 K. Wolski Directeur de recherche
 S. Drapier, professeur
 F. Gruy, Maître de recherche
 B. Guy, Directeur de recherche
 D. Graillot, Directeur de recherche

Spécialités doctorales
 MATHEMATIQUES APPLIQUEES
 INFORMATIQUE
 IMAGE, VISION, SIGNAL
 GENIE INDUSTRIEL
 MICROELECTRONIQUE

Responsables
 O. Roustant, Maître-assistant
 O. Boissier, Professeur
 JC. Pinoli, Professeur
 X. Delorme, Maître assistant
 Ph. Lalevée, Professeur

EMSE : Enseignants-chercheurs et chercheurs autorisés à diriger des thèses de doctorat (titulaires d'un doctorat d'Etat ou d'une HDR)

Nom	Responsable	Grade	Spécialité	Responsable
ABSI	Nabil	CR	Génie industriel	CMP
AUGUSTO	Vincent	CR	Image, Vision, Signal	CIS
AVRIL	Stéphane	PR2	Mécanique et ingénierie	CIS
BADEL	Pierre	MA(MDC)	Mécanique et ingénierie	CIS
BALBO	Flavien	PR2	Informatique	FAYOL
BASSEREAU	Jean-François	PR	Sciences et génie des matériaux	SMS
BATTON-HUBERT	Mireille	PR2	Sciences et génie de l'environnement	FAYOL
BEIGBEDER	Michel	MA(MDC)	Informatique	FAYOL
BLAYAC	Sylvain	MA(MDC)	Microélectronique	CMP
BOISSIER	Olivier	PR1	Informatique	FAYOL
BONNEFOY	Olivier	MA(MDC)	Génie des Procédés	SPIN
BORBELY	Andras	MR(DR2)	Sciences et génie des matériaux	SMS
BOUCHER	Xavier	PR2	Génie Industriel	FAYOL
BRODHAG	Christian	DR	Sciences et génie de l'environnement	FAYOL
BRUCHON	Julien	MA(MDC)	Mécanique et ingénierie	SMS
BURLAT	Patrick	PR1	Génie Industriel	FAYOL
CHRISTIEN	Frédéric	PR	Science et génie des matériaux	SMS
DAUZERE-PERES	Stéphane	PR1	Génie Industriel	CMP
DEBAYLE	Johan	CR	Image Vision Signal	CIS
DELAFOSSÉ	David	PR0	Sciences et génie des matériaux	SMS
DELORME	Xavier	MA(MDC)	Génie industriel	FAYOL
DESRAYAUD	Christophe	PR1	Mécanique et ingénierie	SMS
DJENIZIAN	Thierry	PR	Science et génie des matériaux	CMP
DOUCE	Sandrine	PR2	Sciences de gestion	FAYOL
DRAPIER	Sylvain	PR1	Mécanique et ingénierie	SMS
FAVERGEON	Loïc	CR	Génie des Procédés	SPIN
FEILLET	Dominique	PR1	Génie Industriel	CMP
FOREST	Valérie	MA(MDC)	Génie des Procédés	CIS
FOURNIER	Jacques	Ingénieur chercheur CEA	Microélectronique	CMP
FRACZKIEWICZ	Anna	DR	Sciences et génie des matériaux	SMS
GARCIA	Daniel	MR(DR2)	Génie des Procédés	SPIN
GAVET	Yann	MA(MDC)	Image Vision Signal	CIS
GERINGER	Jean	MA(MDC)	Sciences et génie des matériaux	CIS
GOEURIOT	Dominique	DR	Sciences et génie des matériaux	SMS
GONDRAN	Natacha	MA(MDC)	Sciences et génie de l'environnement	FAYOL
GRAILLOT	Didier	DR	Sciences et génie de l'environnement	SPIN
GROSSEAU	Philippe	DR	Génie des Procédés	SPIN
GRUY	Frédéric	PR1	Génie des Procédés	SPIN
GUY	Bernard	DR	Sciences de la Terre	SPIN
HAN	Woo-Suck	MR	Mécanique et ingénierie	SMS
HERRI	Jean Michel	PR1	Génie des Procédés	SPIN
KERMOUCHE	Guillaume	PR2	Mécanique et Ingénierie	SMS
KLOCKER	Helmut	DR	Sciences et génie des matériaux	SMS
LAFOREST	Valérie	MR(DR2)	Sciences et génie de l'environnement	FAYOL
LERICHE	Rodolphe	CR	Mécanique et ingénierie	FAYOL
MALLIARAS	Georges	PR1	Microélectronique	CMP
MOLIMARD	Jérôme	PR2	Mécanique et ingénierie	CIS
MOUTTE	Jacques	CR	Génie des Procédés	SPIN
NIKOLOVSKI	Jean-Pierre	Ingénieur de recherche	Mécanique et ingénierie	CMP
NORTIER	Patrice	PR1		SPIN
OWENS	Rosin	MA(MDC)	Microélectronique	CMP
PERES	Véronique	MR	Génie des Procédés	SPIN
PICARD	Gauthier	MA(MDC)	Informatique	FAYOL
PIJOLAT	Christophe	PR0	Génie des Procédés	SPIN
PIJOLAT	Michèle	PR1	Génie des Procédés	SPIN
PINOLI	Jean Charles	PR0	Image Vision Signal	CIS
POURCHEZ	Jérémy	MR	Génie des Procédés	CIS
ROBISSON	Bruno	Ingénieur de recherche	Microélectronique	CMP
ROUSSY	Agnès	MA(MDC)	Génie industriel	CMP
ROUSTANT	Olivier	MA(MDC)	Mathématiques appliquées	FAYOL
STOLARZ	Jacques	CR	Sciences et génie des matériaux	SMS
TRIA	Assia	Ingénieur de recherche	Microélectronique	CMP
VALDIVIESO	François	PR2	Sciences et génie des matériaux	SMS
VIRICELLE	Jean Paul	DR	Génie des Procédés	SPIN
WOLSKI	Krzysztof	DR	Sciences et génie des matériaux	SMS
XIE	Xiaolan	PR1	Génie industriel	CIS
YUGMA	Gallian	CR	Génie industriel	CMP

Remerciements

Ce travail a été mené au sein du centre Sciences des Matériaux et des Structures (SMS) de l'École Nationale Supérieure des Mines de Saint-Étienne, dans le laboratoire Georges Friedel (LGE, UMR CNRS 5307).

Je remercie tout d'abord mon directeur de thèse, András Borbély, pour la confiance qu'il m'a accordée en me confiant la responsabilité de ce projet et pour m'avoir fait profiter de toute son expérience des techniques de synchrotron. J'ai particulièrement apprécié son optimisme permanent et sa persévérance face aux problèmes rencontrés, qui ont souvent été déterminants dans l'avancement et la réussite de mes travaux. Je remercie également mon encadrant de thèse, Romain Quey, dont la rigueur et l'efficacité dans le travail ont été pour moi de réels exemples tout au long de ces quatre années. Je le remercie pour toute l'aide qu'il m'a apportée, en particulier durant la phase de rédaction de ce manuscrit.

Je tiens à remercier tous les membres du jury : Olivier Castelnau et Veijo Honkimäki pour avoir accepté d'être rapporteurs et pour leurs nombreux commentaires et conseils, Roland Fortunier pour m'avoir fait l'honneur de présider le jury et Félix Latourte pour ses questions et remarques très instructives. Je remercie tout particulièrement Wolfgang Ludwig, qui était présent lors des expériences à ESRF et qui m'a initié aux techniques de reconstruction DCT.

Je remercie tous les chercheurs ayant contribué à ce travail : Jonathan Wright (ESRF) pour sa participation aux expériences de 3DXRD et à l'étape de calibration du détecteur, Robert M. Suter (CMU) pour m'avoir donné l'opportunité de travailler au sein de son équipe durant quatre mois à Pittsburgh et enfin Claire Maurice (ENSM-SE) pour ses conseils et l'aide qu'elle m'a apportée sur la partie EBSD. Mes remerciements également aux ingénieurs et techniciens de l'École des Mines pour leur assistance : Gilles Blanc pour la métallographie, Claire Roume pour les essais mécaniques, Marilyne Mondon et Sergio São João pour le MEB.

Ces années de thèse passées à Saint-Étienne auraient paru bien longues sans les nombreux collègues thésards qui ont fait partie ou font encore partie de la vie du laboratoire. Je pense tout d'abord à mes cobureaux, Amélie et Aly, avec qui j'ai passé des moments formidables. Merci également à tous mes amis du K4 : Étienne, Adhish, My Thu, Flavien, Alix, Lisa, Grégoire, Mélanie, Robin, sans oublier mon italien préféré, Ernesto.

Mes pensées vont également à ma famille, plus particulièrement à mes parents qui m'ont toujours soutenu et encouragé tout au long de mon parcours et sans qui je n'aurais pu aller aussi loin.

Je ne peux terminer sans remercier Agathe, qui a su à la fois me soutenir, me supporter et m'encourager durant ces dernières années et notamment durant la phase difficile de rédaction. Les mots me manquent pour t'exprimer ma gratitude, mais je tenais simplement à te remercier d'être présente chaque jour à mes côtés.

Abstract

This work aims to improve our understanding of the local deformation of polycrystalline materials. To this end, in situ synchrotron experiments and finite element simulations are coupled to study the individual grain responses in an aluminium polycrystal during plastic deformation.

In the experiment, the initial microstructure is mapped by Diffraction Contrast Tomography (DCT). The specimen is deformed in uniaxial tension and 466 grains are followed by 3D X-Ray Diffraction (3DXRD) up to 4.5% plastic strain. New original analysis methods provide the grain average orientations, elastic strains and stresses, and allow determining the intra-grain orientation distributions from the 3DXRD measurements.

In the simulation, the real microstructure (DCT) is modeled by a Laguerre tessellation, finely meshed and submitted to the experimental loading. The resulting mechanical and orientation fields can be compared to the experimental data.

The comparison reveals a first-order agreement between experiment and simulation. The experimental rotations exhibit a high variability, associated to grain interaction and well reproduced in the simulation. The orientation distributions exhibit preferential spread directions perpendicular to the tensile direction, which can be related to the deformation mechanisms. Lastly, the stresses are found to be in agreement within the measurement accuracies. Such a rich dataset provides routes to improve crystal plasticity models.

Résumé

Ce travail vise à améliorer la compréhension de la déformation locale des matériaux polycristallins. Pour cela, les comportements des grains individuels d'un polycristal d'aluminium déformé plastiquement sont étudiés par une approche couplant expériences in situ en synchrotron et simulation par élément finis.

Dans l'expérience, la microstructure initiale est cartographiée par tomographie en contraste de diffraction (DCT). L'éprouvette est déformée en traction uniaxiale et 466 grains sont suivis par microscopie 3D par diffraction des rayons X (3DXRD) jusqu'à une déformation de 4.5%. De nouvelles méthodes d'analyse originales donnent accès aux orientations, déformations élastiques et contraintes, en moyenne par grain, et permettent de déterminer les distributions d'orientations intragranulaires à partir des données 3DXRD.

Dans la simulation, la microstructure réelle (DCT) est modélisée par une partition de Laguerre, maillée finement et soumise au chargement expérimental. Les champs mécaniques et les champs d'orientations résultants peuvent être comparés aux données expérimentales.

La comparaison entre expérience et simulation révèle un accord au premier ordre. Les rotations expérimentales montrent une forte variabilité associée à l'interaction intergranulaire et bien reproduite dans la simulation. Les distributions d'orientations ont des directions d'étalement privilégiées perpendiculaires à la direction de traction, ce qui est relié aux mécanismes de déformation du matériau. Les contraintes montrent un bon accord, dans la limite de la précision de mesure. Ces données, très riches, fournissent des pistes d'amélioration pour les modèles de plasticité cristalline.

Table of contents

Introduction	1
I Literature review	3
I.1 Crystal mechanics	4
I.1.1 Elasticity	4
I.1.2 Plasticity	5
I.2 Polycrystal mechanics	8
I.2.1 Taylor model	8
I.2.2 Finite element method	8
I.3 Grain-scale analysis of polycrystal deformation	11
I.3.1 2D microstructures	11
I.3.2 Split samples	11
I.3.3 3D microstructures	13
I.3.4 Discussion	17
I.4 Objectives of the thesis	18
II Experimental techniques	21
II.1 High-energy X-ray diffraction methods	22
II.1.1 3D X-ray diffraction microscopy	22
II.1.2 Diffraction contrast tomography	25
II.1.3 High energy diffraction microscopy	26
II.1.4 Experimental limits	28
II.2 Material and samples	29
II.2.1 Microstructure	29
II.2.2 Macroscopic behaviour	29
II.2.3 Sample preparation	31
II.3 Experiments at ID11/ESRF	32
II.3.1 DCT-HEDM comparison	32
II.3.2 In situ tensile test	33
II.4 Conclusion	35
III Accurate measurement of grain average quantities	37
III.1 Geometry description	38
III.1.1 Diffraction images and spots	38
III.1.2 Coordinate systems	39
III.1.3 Parametrization	41
III.1.4 Projection equations	43
III.2 Geometry calibration	45
III.2.1 Detector tilt and distortions	45
III.2.2 Rotation axis	51
III.2.3 Complete geometry	54

III.2.4	Results	55
III.3	Calibration validation	58
III.3.1	Grain average quantities	58
III.3.2	Influence of the experimental uncertainties	59
III.3.3	Experimental results and validation	63
III.4	Conclusion	67
IV	Cross-validation of the initial grain structure	69
IV.1	Comparison between DCT and HEDM	70
IV.1.1	Data sets	70
IV.1.2	Comparative methodology	71
IV.1.3	Results of the comparisons	74
IV.1.4	Discussion	78
IV.2	Comparison between DCT and 3DXRD	79
IV.2.1	Data sets	79
IV.2.2	Rigid body transform	83
IV.2.3	Results of the comparison	84
IV.2.4	Discussion	86
IV.3	Conclusion	87
V	In-situ 3DXRD analyses of individual grain responses	89
V.1	In-situ grain monitoring throughout straining	90
V.1.1	Tracking of individual grains	90
V.1.2	Monitoring of grain average quantities	92
V.2	Assessment of intra-grain orientation distributions	94
V.2.1	Experimental data: azimuthal projection of diffraction spots	94
V.2.2	Simulated data: generation of spots from the grain ODF	96
V.2.3	Optimization problem	99
V.2.4	Application example	100
V.3	Experimental results	102
V.3.1	Representativeness	102
V.3.2	Grain rotations	102
V.3.3	Intra-grain orientation spreads	110
V.3.4	Grain elastic strains and stresses	115
V.4	Summary and discussion	120
VI	Comparison between experiment and crystal plasticity modelling	123
VI.1	Finite element model	124
VI.1.1	Polycrystal representation and meshing	124
VI.1.2	Constitutive equations	130
VI.1.3	Determination of material parameters	131
VI.1.4	Data analysis	132
VI.2	Grain average rotations	135
VI.2.1	Distributions	135
VI.2.2	Variability at constant orientation	138
VI.2.3	Grain-by-grain comparisons	139
VI.3	Intra-grain orientation spreads	141
VI.3.1	Distributions	141
VI.3.2	Relation to deformation mechanisms	145
VI.3.3	Grain-by-grain comparisons	146

VI.4	Grain average elastic strains and stresses	149
VI.4.1	Distributions	149
VI.4.2	Macroscopic response	152
VI.4.3	Relation to the grain orientations	153
VI.4.4	Grain-by-grain comparisons	154
VI.5	Summary and discussion	158
Conclusion		161
	Summary	161
	Outlook	163
A Description of the Isotropic Stress Model		165
A.1	Principles	165
A.2	Results for uniaxial tension	166
B Synthèse en français		169
	Introduction	170
B.1	Chapitre I : revue bibliographique	172
B.1.1	Mécanique du cristal	172
B.1.2	Mécanique du polycristal	173
B.1.3	Approches expérimentales	174
B.1.4	Objectifs de la thèse	174
B.2	Chapitre II : moyens expérimentaux	176
B.2.1	Techniques de synchrotron	176
B.2.2	Matériau	178
B.2.3	Expériences à ESRF sur la ligne ID11	179
B.3	Chapitre III : mesure précise des propriétés moyennes par grain	181
B.3.1	Description de la géométrie	181
B.3.2	Calibration de la géométrie	182
B.3.3	Validation de la calibration	184
B.4	Chapitre IV : validation croisée de la microstructure initiale	186
B.4.1	Comparaison entre DCT, HEDM et EBSD	186
B.4.2	Comparaison entre DCT et 3DXRD	188
B.5	Chapitre V : suivi in-situ par 3DXRD du comportement des grains	190
B.5.1	Rotations moyennes	190
B.5.2	Dispersion d'orientations intra-granulaires	192
B.5.3	Déformations élastiques et contraintes	193
B.6	Chapitre VI : comparaison à la simulation par éléments finis	195
B.6.1	Modèle éléments finis	195
B.6.2	Rotations moyennes	196
B.6.3	Dispersion d'orientations intra-granulaires	198
B.6.4	Déformations élastiques et contraintes	200
	Conclusion	202
References		205
List of figures		219
List of tables		220

Introduction

Most of structural engineering materials consist of metals and alloys, which respond to mechanical loading by the development of complex and heterogeneous mechanical fields at the microscopic scale. These are the result of the polycrystalline nature of the material, as the constitutive crystals exhibit an anisotropic behaviour and tend to evolve differently from each other within the aggregate. These phenomena are of evident interest for industrial applications: metallic components are generally plastically deformed during the preparation and forming stages, which influences their final mechanical properties and may lead during service to damage initiation and rupture.

Since the beginning of the last century, many researchers have tried to explain how polycrystals and their constitutive grains behave when they are plastically deformed. The first studies of Schmid and Boas, in 1935, brought to light crystallographic slip on specific systems as the fundamental deformation mechanism of crystals [1]. This initiated the development of the so-called crystal plasticity theory and was followed by a significant amount of efforts to predict the response of grains of a polycrystalline material subjected to an arbitrary deformation. Since the pioneering works of Taylor, for which deformation was assumed to be uniform throughout the polycrystal, several models have been proposed to incorporate grain interaction with increasing levels of accuracy [2, 3]. Today, finite element simulations of the large deformation of complex polycrystalline structures involving several millions of degrees of freedom can be run on a medium-size computer cluster, providing a tremendous amount of data [4]. Such simulations accurately account for grain interactions by directly solving for the mechanical equilibrium, which results in detailed strain and stress heterogeneities across the microstructure [5]. As refined these information are, there still are relatively few reference experimental data available for detailed comparison (and validation), especially at grain scale. That is why, historically, experiment-simulation comparisons have been carried out on macroscopic properties, *e.g.* deformation textures [6].

In the last 15 years, efforts have been led to measure experimentally the response of individual grains, but only a few of the results have been compared to advanced crystal plasticity simulations. Among the developed experimental techniques, 3D X-ray diffraction microscopy (3DXRD) has proved relatively efficient [7] and has led to the development of other techniques (DCT, HEDM, etc.). 3DXRD is a technique that uses highly-penetrating high-energy X-rays from synchrotron sources and allows for a fast and non-destructive characterization of the individual grains embedded in millimetre-sized specimens. The positions, orientations and elastic strain states of hundreds grains can thus be obtained and their dynamics can be monitored throughout deformation [8, 9].

In this thesis, we propose to study by 3DXRD the individual responses of grains in a polycrystal of aluminium during uniaxial tensile deformation. This document is developed step by step in six chapters. Chapter I explores the mechanisms and theories related to the deformation of single crystals and polycrystals, before discussing previous literature studies in that field. Chapter II presents the experimental techniques and details the experiments that were carried out at the European Synchrotron Radiation Facility (ESRF) on the beamline ID11. Chapters III and IV provide preliminary results, describing the methodologies for obtaining and validating the experimental data from diffraction measurements. The experimental results are presented in Chapter V and analysed in terms of grain rotations, intra-grain orientation distributions, elastic strains and stresses. The numerical results, obtained from a finite element simulation and the Taylor model, are presented and compared to the experimental results in Chapter VI.

This work is part of a strong thematic at the École des Mines de Saint-Étienne and follows various theses dealing with experiment-simulation comparisons of polycrystal plasticity in aluminium alloys [10–13] and recent contributions coupling finite element simulations and numerical descriptions of polycrystals [4, 14, 15].

CHAPTER -I-

Literature review

Contents

I.1	Crystal mechanics	4
I.1.1	Elasticity	4
I.1.2	Plasticity	5
I.2	Polycrystal mechanics	8
I.2.1	Taylor model	8
I.2.2	Finite element method	8
I.3	Grain-scale analysis of polycrystal deformation	11
I.3.1	2D microstructures	11
I.3.2	Split samples	11
I.3.3	3D microstructures	13
I.3.4	Discussion	17
I.4	Objectives of the thesis	18

This chapter first tackles the mechanisms and theories related to the deformation of single and poly-crystals (Sections I.1 and I.2). Then, we discuss literature studies and results related to this work (Section I.3). In what follows, \mathbf{a} , $\underline{\mathbf{A}}$ and $\underline{\underline{\mathbf{A}}}$ refer to a vector, a second-order tensor and a fourth-order tensor, respectively. Tensor contractions and dyadic products are denoted by $:$ and \otimes , respectively.

I.1 Crystal mechanics

An ideal single crystal consists of a periodic arrangement of atoms. As it is loaded, it first behaves in an elastic manner: atoms are reversibly displaced from their equilibrium positions, yielding lattice strains and reaction forces related to the chemical bonds. As the load further increases and reaches the yield stress of the material, the material deforms plastically. This occurs mainly by “crystallographic slip”, which involves movement of dislocations through the lattice, on given crystallographic systems. It results in shear displacements on crystallographic planes, in crystallographic directions and by integral numbers of inter-atomic distances [1].

I.1.1 Elasticity

As the yield stress is, for metals, several orders of magnitude lower than the elastic stiffness, the elastic strain generally remains small and significantly smaller than the plastic strain. As a consequence, second-order effects (*e.g.*, the strain at the core of dislocations) can be neglected and the elastic behaviour of single crystals can be described by the Hookean linear elasticity. In the general anisotropic case, the stress tensor, $\underline{\underline{\boldsymbol{\sigma}}}$, of components σ_{ij} , is linearly related to the elastic strain, $\underline{\underline{\boldsymbol{\epsilon}}}$, of components ϵ_{kl} :

$$\sigma_{ij} = C_{ijkl} \epsilon_{kl} \quad (\text{I.1})$$

where C_{ijkl} are the coefficients of the fourth-order elastic stiffness tensor, $\underline{\underline{\mathbf{C}}}$. Among the 81 coefficients, it can be shown by thermodynamic and symmetry considerations that only 21 are independent [16]. This number can be further reduced depending on crystal symmetry. Hence, for cubic crystals and using Mandel-Voigt’s contracted notation, the Equation I.1 can be written in the crystal coordinate system as:

$$\begin{bmatrix} \sigma_{11} \\ \sigma_{22} \\ \sigma_{33} \\ \sqrt{2}\sigma_{23} \\ \sqrt{2}\sigma_{13} \\ \sqrt{2}\sigma_{12} \end{bmatrix} = \begin{bmatrix} C_{11} & C_{12} & C_{12} & 0 & 0 & 0 \\ C_{12} & C_{11} & C_{12} & 0 & 0 & 0 \\ C_{12} & C_{12} & C_{11} & 0 & 0 & 0 \\ 0 & 0 & 0 & 2C_{44} & 0 & 0 \\ 0 & 0 & 0 & 0 & 2C_{44} & 0 \\ 0 & 0 & 0 & 0 & 0 & 2C_{44} \end{bmatrix} \begin{bmatrix} \epsilon_{11} \\ \epsilon_{22} \\ \epsilon_{33} \\ \sqrt{2}\epsilon_{23} \\ \sqrt{2}\epsilon_{13} \\ \sqrt{2}\epsilon_{12} \end{bmatrix} \quad (\text{I.2})$$

where the 1, 2 and 3 subscripts on the stress and strain refers to the [100], [010] and [001] crystal axes, respectively. The elastic behaviour of a cubic crystal can therefore be described by three independent elastic constants. Values for pure aluminium (Al) are provided in Table I.1.

The elastic response of a crystal varies with the loading direction. For cubic crystals, the elastic anisotropy can be quantified from the effective elastic stiffnesses $E_{[100]}$ and $E_{[111]}$ along the [100] and [111] directions, respectively. The ratio $E_{[111]} / E_{[100]}$ gives the

greatest anisotropy and is larger than 1 for most materials, i.e. [1 1 1] is the stiffest direction and [1 0 0] is the most compliant. For Al, the elastic anisotropy is about 1.20 and is low compared to other materials (e.g., Cu reaches 2.91).

Table I.1 – Elastic constants for Al crystals

	C_{11} (GPa)	C_{12} (GPa)	C_{44} (GPa)
Ref. [17]	107.3	60.9	28.3
Ref. [18]	108.2	61.3	28.5

I.1.2 Plasticity

Although crystallographic slip is inhomogeneous at the atomic scale, it can be treated as homogeneous shearing on the crystal scale: this is the essence of the “continuous modelling” of crystal plasticity, which describes slip on average for each system.

Slip systems generally consist of crystallographic close-packed planes and directions. They correspond for Al (face-centred cubic structure) to the 12 octahedral $\{111\} \langle 110 \rangle$ systems.

a) Kinematics

The deformation kinematics of a crystal can be analysed from its response to an imposed velocity gradient. Let $\underline{\dot{\mathbf{L}}}$ be the velocity gradient. It can be decomposed as:

$$\underline{\dot{\mathbf{L}}} = \underline{\dot{\mathbf{L}}}^p + \underline{\dot{\mathbf{R}}} \quad (\text{I.3})$$

where $\underline{\dot{\mathbf{L}}}^p$ is the plastic component due to slip and $\underline{\dot{\mathbf{R}}}$ is the rotation rate of the crystal lattice.

The plastic part, $\underline{\dot{\mathbf{L}}}^p$, can be decomposed over the individual crystallographic slip systems, s , using the Schmid tensor, $\underline{\mathbf{T}}^s = \mathbf{b}^s \otimes \mathbf{n}^s$, where \mathbf{b}^s is the slip direction and \mathbf{n}^s is the slip plane normal (both unit vectors). Denoting by $\dot{\gamma}^s$ the slip rate, we thus have:

$$\underline{\dot{\mathbf{L}}}^p = \sum_{s=1}^N \underline{\mathbf{T}}^s \dot{\gamma}^s \quad (\text{I.4})$$

Equation I.3 can be decomposed into two, symmetric and skew-symmetric, tensor equations, as follows:

$$\underline{\dot{\mathbf{E}}} = \sum_{s=1}^N \frac{1}{2} (\underline{\mathbf{T}}^s + \underline{\mathbf{T}}^{sT}) \dot{\gamma}^s = \sum_{s=1}^N \underline{\mathbf{M}}^s \dot{\gamma}^s \quad (\text{I.5})$$

$$\underline{\dot{\mathbf{W}}} = \sum_{s=1}^N \frac{1}{2} (\underline{\mathbf{T}}^s - \underline{\mathbf{T}}^{sT}) \dot{\gamma}^s + \underline{\dot{\mathbf{R}}} = \sum_{s=1}^N \underline{\mathbf{Q}}^s \dot{\gamma}^s + \underline{\dot{\mathbf{R}}} \quad (\text{I.6})$$

$$(\text{I.7})$$

where $\underline{\dot{\mathbf{E}}}$ and $\underline{\dot{\mathbf{W}}}$ refer to the symmetric and skew-symmetric parts of $\underline{\dot{\mathbf{L}}}$, respectively. $\underline{\mathbf{M}}^s$ and $\underline{\mathbf{Q}}^s$ denotes the symmetric and skew-symmetric parts of the Schmid tensor. Equation I.5 defines a system of six equations (the components of $\underline{\dot{\mathbf{E}}}$) and N unknowns (the

slip rates, $\dot{\gamma}^s$). The resolution of Equation I.5 then allows to determine the corresponding crystal rotation with Equation I.6.

In Equation I.5, only five equations are independent since there is no volume change. Therefore, an arbitrary shape change requires the activation of at least five independent slip systems. For Al crystals, the twelve octahedral systems can be activated independently, so that Equation I.5 cannot be directly solved. It requires an additional criterion, which is based on the material behaviour law and the plastic work.

b) Rigid-plastic behaviour

The Schmid law

According to the Schmid law, a slip system, s , is activated if the shear stress, τ^s , resolved on the corresponding slip plane and slip direction, reaches a critical value, τ_c^s . The resolved shear stress on system s is related to the crystal stress, $\underline{\Sigma}$, by:

$$\tau^s = \underline{\mathbf{T}}^s : \underline{\Sigma} \quad (\text{I.8})$$

Then, the yield criterion can be expressed for each system as:

$$\begin{cases} \tau^s - \tau_c^s & \leq 0 \\ \dot{\gamma}^s & \geq 0 \\ (\tau^s - \tau_c^s) \dot{\gamma}^s & = 0 \end{cases} \quad (\text{I.9})$$

Equation I.9 holds for every slip system, active ($\tau^s = \tau_c^s$ and $\dot{\gamma}^s > 0$) or inactive ($\dot{\gamma}^s = 0$).

The theory of Taylor–Bishop–Hill

As we already mentioned, Equation I.5 consists of five independent equations with N unknowns and cannot generally be solved directly. Taylor was the first in 1938 to propose an approach to solve this problem, by assuming that among all the possible combinations of slip rates $\dot{\gamma}^s$ producing the imposed shape change, those that minimize the internal work should be chosen. This can be expressed as:

$$\text{minimize} \quad P_{\text{int}} = \sum_s \tau_c^s |\dot{\gamma}^s| \quad (\text{I.10})$$

Taylor's analysis consists in finding the slip systems that produce a given shape change, without verifying whether there actually is a stress state that can activate these systems simultaneously. Thus, in 1951, Bishop and Hill developed a different approach based on the Schmid law. For a given shape change, they proposed to identify the possible stress states, which can simultaneously activate five slip systems or more. Then, they applied the maximum work principle to select the stress state that maximizes the external work. This can be expressed as:

$$\text{maximize} \quad P_{\text{ext}} = \underline{\Sigma}' : \underline{\dot{\mathbf{E}}} \quad (\text{I.11})$$

where $\underline{\Sigma}'$ is the deviatoric stress tensor. Considering that the work of the external forces contributes only to slip, we have $P_{\text{ext}} = P_{\text{int}}$. In fact, Bishop and Hill have shown that the two approaches are equivalent, that is why they are commonly referred to as the Taylor–Bishop–Hill theory.

When all values of τ_c^s are equal, for a given stress state, more than five slip systems can be activated (six or eight in fcc crystals), so that the slip rates cannot be determined unambiguously: there are different possible combinations of slip, resulting in different rotations of the crystal lattice. Several approaches have been proposed to circumvent this

problem [19], such as averaging over all possible solutions, randomly choosing among them, or minimizing not only P_{int} , but also the rate of change of P_{int} with respect to the macroscopic strain state [20]. Other authors propose to use a viscoplastic behaviour [21].

c) Viscoplastic behaviour

In the viscoplastic approach, the slip rate of each slip system is related to the resolved shear stress via a power law, as proposed first by Hutchinson [22]:

$$\dot{\gamma}^s = \dot{\gamma}_0 \left| \frac{\tau^s}{\tau_0} \right|^{\frac{1}{m}} \text{sign}(\tau^s) \quad (\text{I.12})$$

where $\dot{\gamma}_0$ is a reference slip rate, τ_0 is a reference shear stress and m is the strain rate exponent. Then, using Equation I.8 and replacing $\dot{\gamma}^s$ by the latter expression in Equation I.5, we obtain:

$$\underline{\dot{\mathbf{E}}} = \sum_{s=1}^N \underline{\mathbf{M}}^s \dot{\gamma}_0 \left(\frac{\underline{\mathbf{M}}^s : \underline{\boldsymbol{\Sigma}}'}{\tau_0} \right)^{\frac{1}{m}} \quad (\text{I.13})$$

This relation defines a non-linear system of five equations (independent components of $\underline{\dot{\mathbf{E}}}$) and five unknowns (independent components of $\underline{\boldsymbol{\Sigma}}'$).

The viscoplastic behaviour is particularly adapted for the modelling of plasticity at high temperature. As pointed out before, it is also frequently used for room-temperature deformation, as it conveniently eliminates the ambiguities of the Taylor–Bishop–Hill approach. In this case, a relatively low value of m must be used (≤ 0.05 for Al). The results are similar to those obtained with the rigid-plastic approach, that is why we employ this method.

I.2 Polycrystal mechanics

A polycrystal is made of several crystals, called “grains”, of various crystallographic orientations, shapes and sizes. As the aggregate deforms, the individual grains tends to behave differently from each others due to their anisotropy, while respecting at all time the mechanical equilibrium and compatibility conditions (i.e., continuity of stress vectors and displacements). Therefore, the deformation of a grain depends not only on its own response to the imposed load, but also on those of its surrounding grains. The latter influence is commonly referred to as “grain interaction”.

Different approaches have been proposed to model this interaction, or more generally, the transition from single to polycrystalline scales, among which the Taylor and static models, the self-consistent model [23] and the finite element model. In this work, we will focus on the Taylor model, which uses a simple yet efficient localization rule, and the finite element model, which provides an exact solution to the localization problem.

I.2.1 Taylor model

The *Taylor model*, proposed in 1938, is based on the assumption that the velocity gradient $\dot{\underline{\mathbf{L}}}$ is uniform in the polycrystal. This implies that all grains are subjected to the same plastic strain (the macroscopic plastic strain), while the elastic strains are neglected. This approach ensures the strain compatibility, but the mechanical equilibrium is generally violated, as the stresses can vary from one grain to another. The grain responses only depend on their orientations, so that they can be treated independently.

The assumption of uniform plastic strain provides an “upper-bound” for the yield stress. The “lower-bound” counterpart is obtained for a statically admissible stress field (e.g., the static model assumes that all the grains are subjected to the same stress state). Evidently, none of these two approaches are exact, as they imply neglecting either the mechanical equilibrium or the compatibility conditions. However, for fcc materials, it is generally observed that the Taylor model gives results closer to experimental observations [24].

I.2.2 Finite element method

The *finite element method* is increasingly employed to simulate and investigate the elastoplastic behaviour of polycrystalline materials. A finite element formulation, coupled with crystal plasticity, allows to model the deformation of 3D microstructures by directly solving the mechanical equilibrium. This results in realistic stress and strain heterogeneities, both among and within grains, that cannot be obtained with the Taylor model.

The first finite element simulations were based on the use of one element or integration point per grain [25–28]. Marin and Dawson, for example, simulated the plane strain compression to large strain of an Al polycrystal [26]. The deformed model, provided in Figure I.1, clearly shows strain inhomogeneities developing throughout the volume. Such simulations proved relatively efficient to predict the overall response of a polycrystal, such as texture. They usually suffer, though, from sharp variations from grain to grain, which limits the information on the local response and rather suggests discretizing each grain more finely to allow intra-grain heterogeneities.

This evidently raises the question of the representation of polycrystal morphologies. As it has long been difficult to experimentally obtain the complete structure of real aggregates, several approaches have been developed in computational methods for mod-

elling and generating realistic random polycrystals, among which *Voronoi tessellations* and *Laguerre tessellations* have become very popular. Such methods are for example implemented in the free software package Neper [4], which was employed in this work. The Voronoi tessellation divides the space into convex cells, which are defined as zones of influence of a given set of generating points. The Laguerre tessellation generalizes the Voronoi tessellation by assigning a weight to each point. In both cases, grains are convex and the geometry can be described in a vectorial way (points, lines, surfaces and volumes) which then allows meshing with standard tools. Voronoi tessellations were first used by Barbe *et al.* to investigate the plastic behaviour of random polycrystals [5, 29] and, more recently, strain localization bands in a finely-meshed random polycrystal [30]. This is illustrated on Figure I.2. Their results clearly show that grain interactions lead to significant deformation heterogeneities at both inter- and intra-granular scales.

When the structure of a real polycrystal is available, the finite element method allows in principle to take it as input. This requires however complex data treatment, since the microstructures are generally available in the form of 3D voxelated maps and cannot be readily meshed. Proudhon *et al.* [31, 32] proposed to first mesh all the grain boundaries into triangle elements and input then the resulting model in a general 3D mesher, as shown in Figure I.3. They applied this method to study the crack propagation in a β -titanium polycrystal. This meshing scheme, albeit ideal, appears likely to provide inhomogeneous elements throughout the mesh, due to strong dependencies upon grain boundary roughness and imaging artefacts. This necessitates visual inspection and manual cleaning of the boundary mesh and impedes, *de facto*, a reliable automation of the method.

Alternative methods were developed to approximate experimental polycrystals by Laguerre tessellations. Lyckegaard *et al.* [33] employed a simple heuristic scheme, using the measured grain centroids and volumes as generating points and weights in the tessellation. Spetl *et al.* [34] fitted Laguerre tessellations to tomographic data, by minimizing the distance between the experimental grain boundaries and the tessellation boundaries. However, to date, no such structures were used for modelling polycrystal deformation.

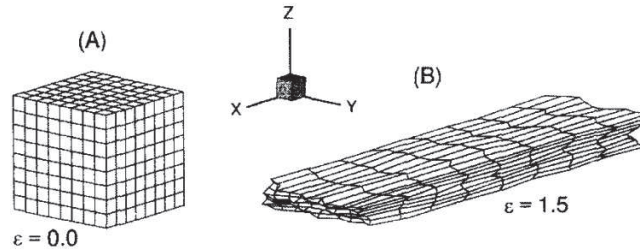


Figure I.1 – Finite element model of an Al polycrystal containing 512 elements (or crystals), from Marin & Dawson [26]: (A) initial microstructure and (B) deformed microstructure after a plain strain compression of 1.5.

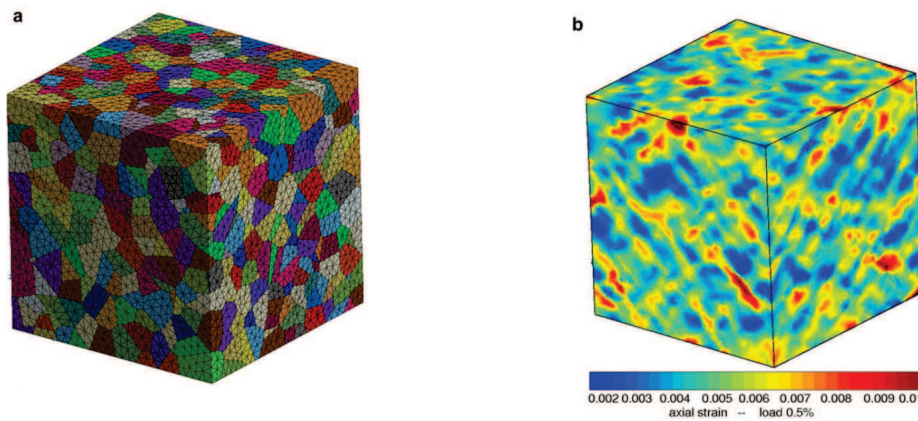


Figure I.2 – Strain field in a high-resolution polycrystal deformed to 0.5% uniaxial tension, from Barbe *et al.* [30]: (a) meshed polycrystal and (b) axial strain.

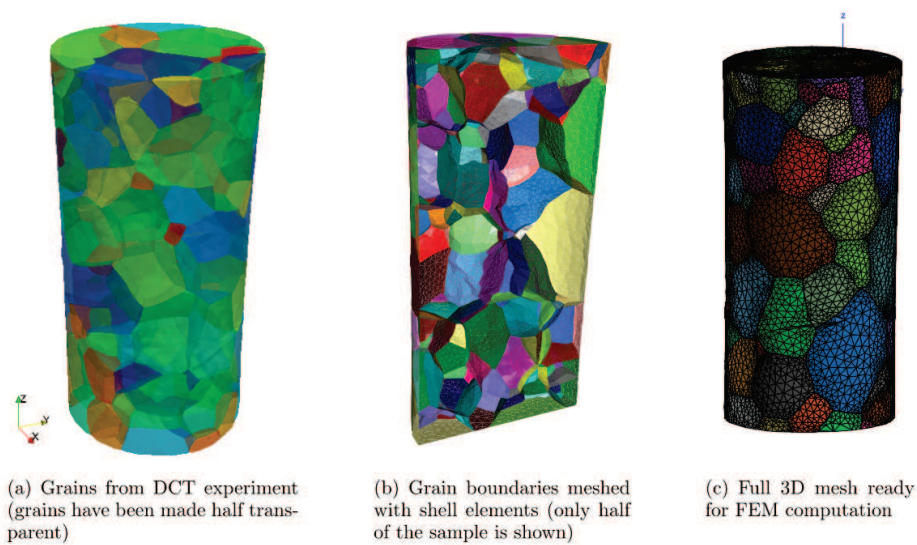


Figure I.3 – Generation of a 3D mesh based on an experimental polycrystal, after Proudhon *et al.* [31].

I.3 Grain-scale analysis of polycrystal deformation

The predictions of crystal plasticity models have often been tested against experimentally observed macro-textures, especially in the context of metal forming. The comparisons were concentrated on the orientation distributions developed over large number of grains. However, at such a global scale, it becomes difficult to analyse the differences observed between experiment and simulation and therefore to improve models. Hence, several authors have rather proposed to monitor the evolutions of individual grains, which would provide more accurate information. The following section discusses of previous experiments and studies, for which the responses of individual grains of plastically deformed specimens were followed and compared to the results of crystal plasticity models.

I.3.1 2D microstructures

From a general point of view, surface analyses of the deformation of a polycrystal are limited by the fact that the deformation depends on the 3D structure of the material. 2D microstructures have been used to circumvent this problem. Skalli *et al.* [35], in 1985, followed the rotations of 19 grains in coarse-through-grained Al sheets. The orientation were measured by X-ray diffraction at four successive strains up to 80% thickness reduction. The experimental results revealed in particular that grains of close orientations but different neighbours were very likely to behave in the same way, thus indicating a dominant influence of the initial grain orientations. The experimental rotations were compared to the results of the Taylor model in plane strain compression (PSC). Overall, the final orientations appeared to be close to the experimental rolling textures components. However, the grain scale comparisons revealed that the predictions of the model were not fully satisfactory.

Similarly, Kalidindi *et al.* [36] employed a directionally-solidified Al sample having a quasi-columnar grain structure, with a strong $\langle 100 \rangle$ fibre texture. The sample was deformed in PSC and the orientations of 19 grains from one sample face were mapped by electron backscatter diffraction (EBSD) before and after a plastic strain of 0.5. The experimental results were compared to the results of the Taylor model and a finite element model. Although both models were found, again, quite successful in predicting the deformation texture components, the Taylor model totally failed to predict the individual grain rotations. A better agreement was found with the finite element simulation, which was besides capable of reproducing the intra-grain heterogeneities. The conclusions of this study are, however, strongly limited by the initial $\langle 100 \rangle$ fibre texture and the fact that the sample was deformed along the columnar direction, for which grain rotations are unstable [14].

I.3.2 Split samples

The first study of the rotations of individual bulk grains based on surface analyses was done by Barrett and Levenson [37] in 1940. They used an Al “split sample” deformed in uni-axial compression. The sample was made of two parts assembled along the compression direction. At three successive plastic strain levels up to 0.92, the orientations of 25 grains were measured by X-ray diffraction on the internal assembly face. The authors notably observed that grains of close orientations could rotate differently. They compared the experimental results to the predictions of the Taylor model and concluded a 50-70% agreement.

The same procedure was later applied in 1996 by Panchanadeswaran, Becker and Doherty [38–40] to hot PSC of Al. The split sample was made of two identical parts assembled along the transverse direction. The orientations of 58 grains were measured by manual EBSD before and after a plastic strain of 0.5. The results were compared to the predictions of the Taylor model, and the authors concluded that the latter failed to predict most of the experimental rotations. A comparison with a 2D finite element models was also drawn, showing little improvement compared to the Taylor model. The disagreement was attributed to the kinematic restrictions due to the use of a 2D model to simulate a 3D microstructure, and the authors concluded on the necessity of either using 2D microstructures or conducting truly 3D studies.

More recently, Quey *et al.* [13, 41, 42] questioned the conclusions of Panchanadeswaran and co-workers, concerning in particular the apparent failure of the Taylor model. Similarly to them, Quey *et al.* deformed an Al split sample in hot PSC by series of four compressions to a final plastic strain of 1.2. This is illustrated on Figure I.4. On the internal sample surface, a $4 \times 4 \text{ mm}^2$ region was finely mapped by EBSD at six successive strain levels. This provided about 3000 orientations per grain, which were then used to characterize both average rotations and orientation spreads of the individual grains. The experimental results were quantitatively analysed and highlighted in particular a significant influence of grain interactions on the grain average rotations. Indeed, it was found that on average at the beginning of the deformation, two grains of the same orientation (but different neighbours), rotate by angles and axes that differ by 25% and 37° , respectively.

The experimental results were compared to the predictions of the Taylor model. Contrary to the conclusions of Panchanadeswaran and co-workers, some agreement was found between the two: although the model provided a poor agreement for the rotation angles, a strong correlation of the rotation axes was found. The average error in the first strain increment was 39° , which the authors described as a “first-order agreement”, with the mismatch attributed to the experimental rotation variabilities caused by grain interactions (37°). The experimental results were also compared to the simulation results of a finite element model [14, 15] reproducing exactly the experimental orientation distribution, but not the unknown, underlying grain arrangement. Hence, the comparisons could be done over the orientation space, but not on a grain-by-grain basis.

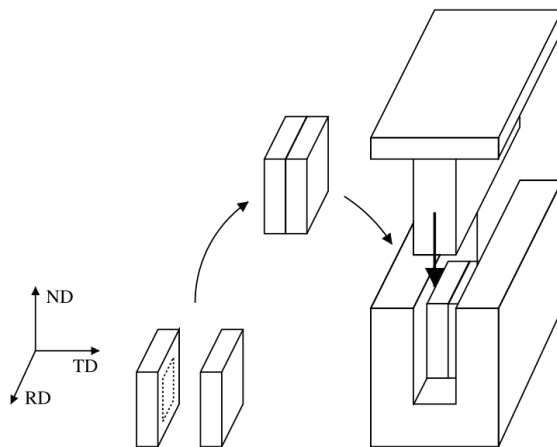


Figure I.4 – Split sample deformed by plane strain compression in a channel die, from Quey *et al.* [41].

I.3.3 3D microstructures

The advent of “three dimensional X-ray diffraction” (3DXRD) [7] during the last two decades has opened the way to *in situ* 3D studies of polycrystal plasticity. The technique uses high-energy X-rays (50–100 keV) from a third-generation synchrotron source, which provide sufficient penetration power and flux to carry out non-destructive 3D characterizations of bulk materials. In 3DXRD experiment, a polycrystalline sample is placed on a rotation stage and illuminated by a quasi-parallel monochromatic beam. Following a tomography-like approach, the sample is rotated, while the diffracted intensity is measured by a 2D detector, which results in a collection of diffraction spots corresponding to the different illuminated grains. Indexing and fitting algorithms are then employed to operate a systematic search through the measured spots, discriminate between the individual constitutive grains and assess their respective properties.

In fact, the 3DXRD method, as originally introduced by Poulsen *et al.* [7], defined a highly-versatile and general experimental framework which led, during the last decade, to the development of more specialized techniques, such as Diffraction Contrast Tomography (DCT) [43] and High Energy Diffraction Microscopy (HEDM) [44]. While the original 3DXRD is limited to the measurement of grain resolved quantities, the two others aim at 3D orientation mapping of undeformed polycrystals (DCT) and deformed polycrystals (HEDM). The three techniques will be presented in more detail in Section II.1. Here, we present and discuss several results obtained by 3DXRD and its variants.

a) Rotations

In 3DXRD, grain average orientations are directly obtained from the positions of the measured diffraction spots. Rotations then correspond to orientation changes from one state to another.

The first 3DXRD study of the rotations of individual bulk grains is published by Margulies *et al.* in 2001 [45]. They used a focused hard X-ray beam to illuminate a small region in a 3 mm thick specimen of high-purity Al. The sample was plastically deformed up to 11% and four grains were tracked, providing their respective rotation paths. The results were compared to the Taylor model, revealing clear inconsistencies between predictions and measurements. A similar study on a Cu specimen was published in 2002 by the same authors [46]. They deformed the sample up to 6%, measured the rotations of seven grains and noticed a strong influence of the orientation on the grain response.

As a result of these two feasibility studies, in 2003, Poulsen *et al.* proposed the first statistically-sound 3DXRD study of the rotations of 96 bulk grains in an Al polycrystal, deformed to 6% tension [47]. The experimental setup is schematically shown in Figure I.5. Represented in the stereographic triangle of an inverse pole figure, the rotations appeared as near-straight lines. The authors noted a strong correlation of the rotation paths with initial orientations, but also clear differences for a few grains of similar orientations (which were attributed to grain interaction). In a second publication, Winther *et al.* compared these results to the predictions of the Taylor model [8] and identified four regions in the orientation space with distinct trends, as shown in Figure I.6. A reasonable agreement between measurements and predictions was concluded, except in the $< 100 >$ corner region, where large variations among the experimental rotations were observed.

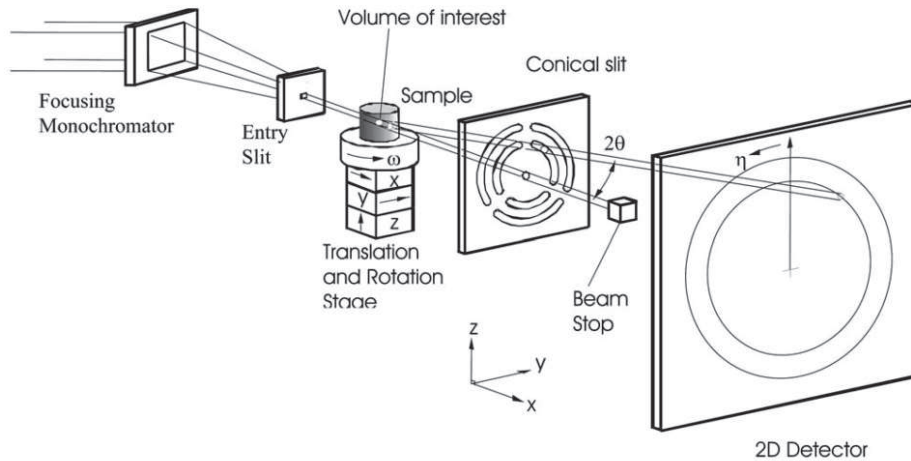


Figure I.5 – Sketch of the 3DXRD experimental setup, after Poulsen *et al.* [47]. The sample is positioned on an ω -rotation stage and probed with a focused monochromatic X-ray beam. Diffraction spots are recorded on a 2D detector.

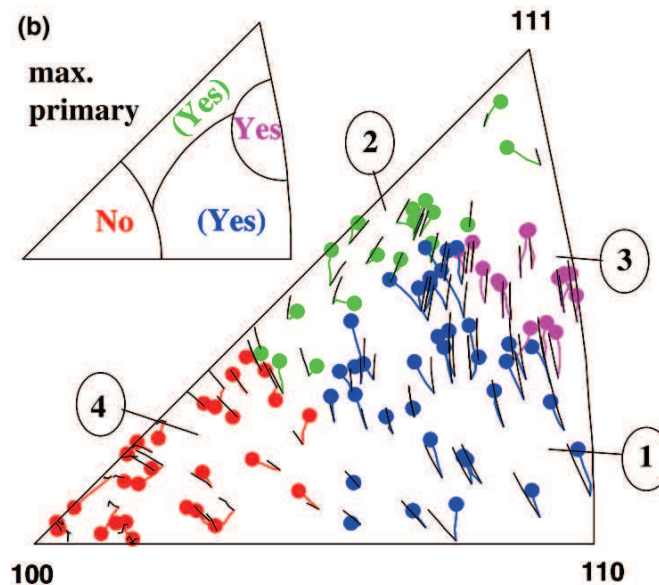


Figure I.6 – Lattice rotations of individual bulk grains in an Al polycrystal, after Winther *et al.* [8]. Inverse pole figure showing predictions of the Taylor model (black) and experimental rotations (colours) of 96 bulk grains. The final orientations are marked by dots. The colours indicate the different regions.

b) Intra-grain orientation spreads

The assessment of intra-grain orientation distributions is ideally based on spatial orientation maps such as those provided by the HEDM technique. A notable example is the work of Pokharel *et al.* [48], who followed the evolution of 5000 bulk grains during tensile deformation of pure Cu. The lattice orientations of a cylindrical volume with 0.8 mm in diameter and 0.5 mm in height was mapped with a spatial resolution of about 3-4 μm at five plastic strain levels up to 21%. Although such data sets provide detailed orientation maps, the authors mainly reported on grain average rotations.

The feasibility of assessing grain orientation distributions from 3DXRD measurements was demonstrated by Poulsen *et al.* [49]. The authors employed algebraic algorithm to re-

construct the orientation distribution functions of individual deformed grains from the diffracted intensity. More recently in 2015, the idea was exploited to some extent by Oddershede *et al.* [50], who studied by 3DXRD the rotation paths and intra-grain orientation spreads of three bulk grains in a sample of interstitial-free steel elongated to 9%. The grains had close initial orientations, but still different rotation behaviours, and were selected as being representative of the scatter observed near the $\langle 522 \rangle$ orientation. The different rotation paths were analysed through the Taylor model and explained by variations in the relative activities of the same four slip systems. By manually fitting simulated diffraction spots to the experimental ones, they reported that the observations could be explained by differences in the slip system activities. They concluded that, while the slip system selection was primarily related to the grain orientations, their respective activation rates had to be largely controlled by another factor, such as grain interaction.

c) Lattice strains and stresses

Lattice elastic strains can be evaluated from the displacements of the measured diffraction spots, by comparison between a reference (unloaded) and a current state (loaded).

Margulies *et al.* [51] presented in 2002 the first 3DXRD evaluation of the elastic strain state in a single bulk grain of Cu tensile specimen. The authors used a focused hard X-ray beam, centred the grain with respect to the diffractometer and deformed the sample elastically. Measurements were repeated for several load levels. Due to experimental constraints, only three components of the strain tensor could be determined, based on the variations of the Bragg angles of the diffraction spots. The estimated accuracy was about 10^{-4} . The results, shown in Figure I.7, revealed, as expected, a quite linear response of the grain. The apparent elastic modulus in the tensile direction was consistent with the theory. This same approach was later applied by Martins *et al.* [52] in 2004 and Aydiner *et al.* [53] in 2009. Martins *et al.* characterized ten individual bulk grains in a deformed tensile specimen of Al and noted some correlations between the elastic strain states and the orientations [52]. Aydiner *et al.* monitored the evolution of the full strain tensors of four grains embedded in a Mg-alloy compression specimen, in relation with mechanical twinning [53].

Although these three studies demonstrated the feasibility of monitoring grain average lattice strains, they were clearly limited by the small number of measured grains. Experimentally, this was due to the use of focused beams, which had cross-sections comparable in size to the grains. The authors were therefore restricted to the analysis of one or few grains at a time, which furthermore had to be centred as close as possible to the diffractometer rotation axis to facilitate data treatment.

The technique later evolved towards greater automation and robustness. As a result, in 2010, Oddershede *et al.* [54] proposed improvements, enabling the simultaneous and thorough characterization of hundreds of grains. Their method used a wider beam and included a twelve-parameter equation to fit the centroid, orientation and lattice parameters of each grain from the positions of the diffraction spots. The strain evaluation was based on the variations of the fitted lattice parameters, as detailed by Schlenker *et al.* [55]. The authors validated the procedure on simulations and experiments. By propagating the errors, they came out with achievable accuracies of about $10\ \mu\text{m}$, 0.05° and $1 - 2 \times 10^{-4}$ for grain positions, orientations, and strain components, respectively. In a subsequent publication, Oddershede *et al.* [9] applied the methodology on a Cu polycrystal deformed to 1.5% plastic strain. They were able to measure the full strain tensors of a thousand of randomly-oriented grains. Some of the results are illustrated in Figure I.8. The authors noted a clear dependence on the orientations, with a stiffer axial response for $\langle 111 \rangle$

orientations. They concluded that their observations could be partly explained by elastic anisotropy, but seemed also to indicate stress partitioning in the polycrystal.

More recently, Abdolvand *et al.* [56, 57] investigated the 3D stress development in parent and twin pairs of a Zircaloy-2 polycrystalline specimen, consisting of more than 6000 grains. This study, like most of the above-mentioned achievements, was based on the FABLE software suite [58], which is developed at ESRF on the materials science beamline ID11 for 3DXRD analysis.

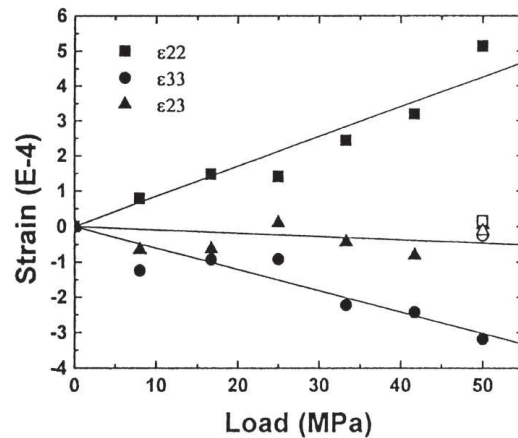


Figure I.7 – Elastic strains of a single bulk grain in a Cu polycrystal under loading, by Margulies *et al.* [51]. Evolution of the longitudinal ϵ_{22} , transverse ϵ_{33} and associated shear ϵ_{23} components as a function of applied load. Lines represent linear fits.

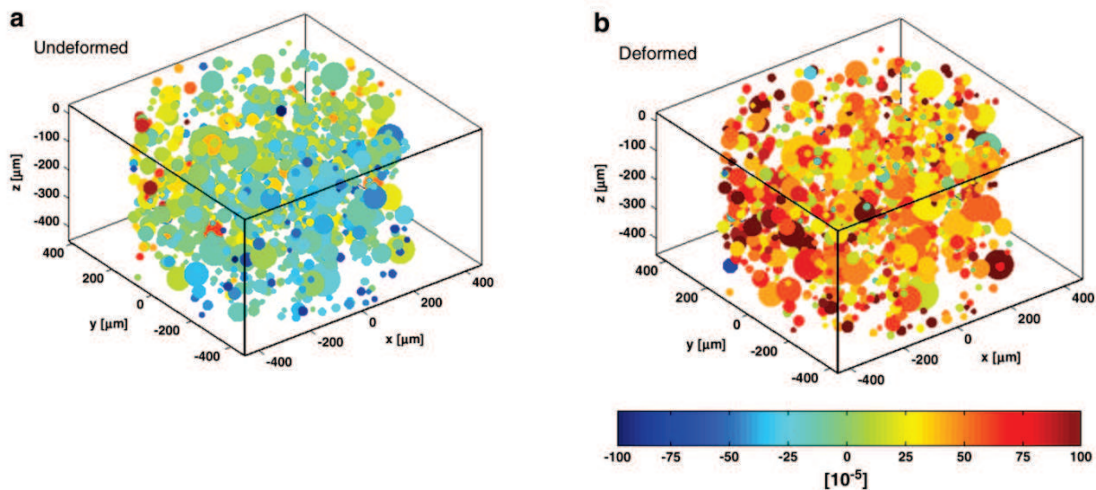


Figure I.8 – Elastic strains of 1118 grains in a cylindrical Cu polycrystal, after Oddershede *et al.* [9]. Grains are represented as equivalent spheres coloured according to their axial strain components at (a) the undeformed state and (b) 1.5% plastic strain.

I.3.4 Discussion

In this section, we have presented three different approaches to monitor individual grains during plastic deformation of polycrystals. While 2D microstructures allow for a full knowledge of the grain structure, they may not be representative of real 3D polycrystals. In contrast, split samples are designed to follow the evolution of bulk grains. The method enables to follow the rotations of a representative number of bulk grains up to large plastic strains ($\epsilon > 1$). The extended study of Quey *et al.* [13–15, 41, 42] provided detailed information on the average rotations and the development of orientation spreads inside grains. In particular, trends were established by analysis over the orientation space. However, grain-by-grain comparisons could not be carried out due to the surface analyses in the experiment.

The 3DXRD technique gives access to grains in a real 3D polycrystals. The technique was applied on various metallic materials. Its potential to monitor grain rotations and stress development was demonstrated by Poulsen, Winther, Oddershede and co-workers on statistically-sound grain sets [8, 9, 47, 54]. The assessment of intra-grain orientation distributions presents an evident interest for studies of metal deformation, but it has had only moderate fallouts so far. Oddershede *et al.* [50] used a manual fitting procedure to probe only three grains of the same orientation, which is an evident limitation. The technique would strongly benefit from greater automation, so as to characterize hundreds of grains in a reliable and reproducible manner. Poulsen, Hansen and co-workers [49, 59] proposed and detailed a method to reconstruct orientation distribution functions of individual grains from 3DXRD measurements using iterative algebraic algorithms. Their approach demonstrated the potential and feasibility of obtaining intra-grain orientation spreads from diffraction spot broadening.

As we have presented or mentioned most of the 3DXRD studies in the field of polycrystal plasticity, we note that the analyses generally remained qualitative or incomplete, as the authors dealt with small numbers of grains or focused on one measurable quantity. Oddershede *et al.* in Ref. [9], for example, rightly discarded the analysis of grain rotations, which were comparable in amplitude with the orientation accuracy and suffered therefore from large uncertainties. This emphasizes the need for sufficient levels of plastic strain to produce large enough grain responses. For experimental reasons, the technique is limited to deformation smaller than 10%. Indeed, when grains deform, the strain induces a spread of the intra-grain orientation distribution, which is observed in the measurements as an intensity loss and broadening of the diffraction spots. Depending on the material, the microstructure and the deformation, this can lead to the overlap of spots arising from different grains. A limit is reached when too much information is lost by broadening and overlapping. Intensity losses can be reasonably corrected by increasing exposure times. For spot overlaps, most of the above-mentioned works employed a relatively small beam size to reduce the number of grains probed simultaneously. Hence, to produce grain statistics, Oddershede *et al.* [9, 50] measured separate layers of the sample and eventually merged the results. This solution does not, however, seem fully satisfactory as it requires longer acquisition times and extra data processing.

It is worth discussing as well the accuracies of the technique. According to Oddershede *et al.* [9, 54], uncertainties of about 0.05° and $1 - 2 \times 10^{-4}$ can be achieved by 3DXRD on grain orientations and elastic strain components, respectively. For pure Al, the latter roughly results in an uncertainty of 7 MPa on stresses, which is of the same order of magnitude as the material yield strength. Hence, for such very soft materials, this value is not appropriate to capture a grain elastic regime, but it should allow to investigate plasticity. The issue of accuracy is closely related to the calibration of the experimental setup,

the importance of which seems to us to have been long overlooked in the literature. In Refs. [51, 52], attention was mainly paid to the determination of the sample-to-detector distance and the beam position on the detector, which would sufficiently described an ideal setup, but not an experimental one. Indeed, a 3DXRD diffractometer has imperfections and misalignments, which are detrimental for the accuracy and physical meaning of the measurements. The calibration aspect was better addressed by Oddershede *et al.* [54]. In their approach, a minimization procedure is applied to determine simultaneously the geometry parameters and grain properties, using the measurements of the undeformed state. Based on a large number of grains, a precise calibration can be achieved. The use of the same sample for both calibration and characterization is questionable though, as it fully depends on the investigated sample.

The results of the different studies have mainly been compared to the predictions of the Taylor model or its variants, leading to quite different observations depending on the authors. Kalidindi, Panchanadeswaran and coworkers [36, 40] concluded on a quasi-total failure of the Taylor model to predict the individual grain rotations. In contrast, Winther *et al.* [8] concluded on a reasonable agreement. In fact, many of these studies lacked quantitative measures of the actual discrepancies between experiment and simulation. From that viewpoint, the work of Quey *et al.* [13–15, 41, 42] seems to be the most complete.

Few studies have confronted experimental results on individual grains in 3D polycrystals and simulation results based on finite element calculations or other full-field simulation techniques. Only recently have actual comparisons been reported. Proudhon *et al.* published preliminary results comparing a finite element simulation with the grain average stresses in a Ti polycrystal measured by DCT and 3DXRD [32]. Pokharel *et al.* reported on rather qualitative comparisons of the grain average rotations measured by HEDM and simulated by fast Fourier transform [60, 61]. Abdolvand *et al.* compared 3DXRD measurements of the grain average stresses in a Zircaloy-2 polycrystal to a finite element simulation based on a Voronoi tessellation reproducing the experimental grain centroids and sizes [56, 57]. As a conclusion, to date, no detailed grain-by-grain analysis was reported, comparing individual grain rotations, orientation spreads and stresses between experiments and finite element simulations of the plastic deformation of a 3D polycrystal. Such studies are made entirely conceivable though by the combination of 3DXRD and DCT.

I.4 Objectives of the thesis

From the classical Taylor model to the more recent finite element simulations, substantial efforts have been made to predict the plastic behaviour of polycrystalline aggregates. Despite advances in modelling, important questions remain on the relative influence of grain orientation and grain interaction. The field has evidently suffered from a lack of experimental data to test out the different modelling assumptions. In contrast with the Taylor model, whose predictions can be compared to statistical measurements of X-ray or neutron diffraction, finite element models require ideally to measure the responses of individual bulk grains. The advent of 3DXRD opened the way to such studies, as demonstrated by the available literature, even if experiments are restricted to room temperature and axisymmetric loading with plastic deformation of a few percents.

In this work, we propose to combine *in situ* synchrotron experiments and simulations to study the individual responses of grains of an Al polycrystal during plastic deformation. To this end, we use several techniques: DCT, which gives access to the 3D grain structure of the undeformed state, and 3DXRD, which allows to follow grain responses during

deformation. The determination of grain positions and orientations by 3DXRD is well established in the literature. The evaluation of lattice strains was demonstrated as well, but requires careful data treatments to achieve reasonable accuracies. The orientation spreads are not directly accessible and will require the development of a new method.

We also dispose of two crystal plasticity models: the Taylor model, whose predictions only consider grain initial orientations, and a finite element elasto-visco-plastic model, which can account for the actual microstructure. The latter is provided by the DCT, but requires appropriate treatment and meshing to be used. The simulation results are qualitatively and quantitatively compared to experimental results, in terms of distributions and on a grain-by-grain basis. The comparison aims to address the question of how close finite element models are capable of reproducing experimental observations of polycrystal plasticity.

CHAPTER -II-

Experimental techniques

Contents

II.1 High-energy X-ray diffraction methods	22
II.1.1 3D X-ray diffraction microscopy	22
II.1.2 Diffraction contrast tomography	25
II.1.3 High energy diffraction microscopy	26
II.1.4 Experimental limits	28
II.2 Material and samples	29
II.2.1 Microstructure	29
II.2.2 Macroscopic behaviour	29
II.2.3 Sample preparation	31
II.3 Experiments at ID11/ESRF	32
II.3.1 DCT-HEDM comparison	32
II.3.2 In situ tensile test	33
II.4 Conclusion	35

This chapter first presents the experimental techniques used in this study: Three Dimensional X-Ray Diffraction (3DXRD), Diffraction Contrast Tomography (DCT) and High Energy Diffraction Microscopy (HEDM), all of which employ diffraction of high energy X-rays. Then, we describe our material, its microstructure and the sample preparation. Finally, we detail the *in situ* deformation experiments performed at the European Synchrotron Radiation Facility (ESRF), on beamline ID11.

II.1 High-energy X-ray diffraction methods

Since the late 90s, under the initiative of the Risø National Laboratory group, a set of techniques initially labelled as “Three Dimensional X-Ray Diffraction microscopy” (3DXRD) has been developed for structural characterization of (poly)crystalline matter [7]. In this document, for clarity and because “3DXRD” is now generally used for a specific instance of these methods, we will rather refer to the set of techniques as “High Energy X-Ray Diffraction” (HEXRD). This is in fact similar to “HEXD”, previously used by Miller *et al.* [62].

The core principle of HEXRD techniques derives from the “rotating crystal method” or “rotation method” developed for single crystal diffractometry [63]. As illustrated on Figure II.1, the sample is mounted on a ω -rotation stage and illuminated with a monochromatic, parallel X-ray beam, perpendicular to the rotation axis. A 2D, flat detector is positioned perpendicular to the beam at a specific distance from the sample. While the sample is rotated, any part of the illuminated region, which is in Bragg condition, will generate a diffracted beam resulting in a diffraction spot on the detector. For a complete characterization of the illuminated volume, the sample is continuously rotated (typically by 180° or 360°) and the diffracted intensity is integrated over successive rotation intervals with equal amplitudes, $\delta\omega$, referred as the “integration step”. This procedure, called a “scan”, results in a set of equally spaced and uniformly sampled images, from which the diffraction spots, or “reflections”, can be extracted. The main challenge then consists in associating the diffraction spots to the reciprocal space vectors of the illuminated grain lattices. In contrast with the rotating crystal method, the present measurements can involve many aggregated crystals, or grains, which can have different positions with respect to the rotation axis and different diffraction conditions. The process of identifying the diffracting grains and assigning the reflections to them is called “indexing”.

The high versatility of HEXRD techniques regarding their experimental setup (detector, sample-detector distance, etc.) has led to the development of different variants, such as far-field 3DXRD (3DXRD), Diffraction Contrast Tomography (DCT) and High Energy Diffraction Microscopy (HEDM).

II.1.1 3D X-ray diffraction microscopy

3DXRD is a fast and non-destructive technique that can be applied on millimetre-sized samples to simultaneously analyse the average properties of hundreds of grains, such as their centroids, average orientations, volumes and lattice strains. This section gives the main principles of the technique; a detailed analysis will be led in Chapter III.

a) Experimental setup

In 3DXRD, a detector of large pixel size (50 to 200 μm) is positioned at a relatively large distance from the sample (200 mm to 1 m depending on the detector). In these “far-field”

conditions, the grain positions and shapes have only a low influence on the diffraction spots. The latter appear on a set of rings resulting from the diffraction cones with half-opening 2θ , as given by Bragg's law. This experimental configuration favours the angular resolution over the spatial resolution.

b) Indexing approaches

While indexing diffraction spots is relatively straightforward for a single crystal, it becomes a complex combinatorial problem for polycrystals. This problem is generally addressed by the principles of completeness and uniqueness [7]. The completeness can be explained as follows: for given experimental conditions, a grain generates a maximum number of theoretically-observable reflections, M^{th} , depending on its orientation and position. An indexed grain should be considered as valid, in other words as a real grain, if the experimental number of reflections, M^{exp} , is sufficiently high with respect to M^{th} . The ratio $M^{\text{exp}}/M^{\text{th}}$ ranges from 0 to 1 and measures the grain completeness. The principle of uniqueness refers to the fact that a reflection should arise from one diffracting grain only. This implies, ideally, that any experimental spot should not be indexed more than once. In practice, however, this requirement is strongly weakened by the possibility of spot overlap.

Many approaches have been proposed to solve the indexing problem efficiently and reliably. They are generally based on either "forward" or "backward" projection. In the forward approaches, diffraction spots are first simulated for different orientations, which can be random or taken on a predefined grid of the orientation space. The simulated and experimental reflections are then compared and the orientations resulting in high enough completeness are marked as possible grains. While the far-field configuration makes it possible to assume initially that grains are located at the origin on the rotation axis, grain positions can also be taken into account by using a grid in the sample space, too. This is the approach used in Grainindex [64]. In backward approaches, the experimental reflections are directly used to determine the orientations of their corresponding grains. This is the approach adapted by Moscicki *et al.* [65] (symmetry properties of Friedel pairs), Bernier *et al.* [66, 67] (search through orientation fibres defined by the observed reflections) and by Schmidt in GrainSpotter [68] (search of vertices in the Rodrigues-Frank orientation space [69]).

c) Effects of deformation

For a loaded and deformed material, the measured diffraction spots are modified as illustrated on Figure II.2.

First, the elastic part of the deformation (or, equivalently, the stress) affects the interplanar distance between (hkl) lattice planes. The Bragg condition for the corresponding reflection is therefore modified, changing both the 2θ angle and the ω angle at which diffraction occurs. This results in a radial shift of the spot with respect to the diffraction rings and a shift in ω .

Second, the plastic part of the deformation affects the crystal orientation and mosaicity. The grain average rotation results in a similar effect as elastic strain and shifts the diffraction spot as a whole along the ring and in ω . The development of intra-grain mosaicity tends to spread the spot intensity along the diffraction ring and in ω over more and more successive images.

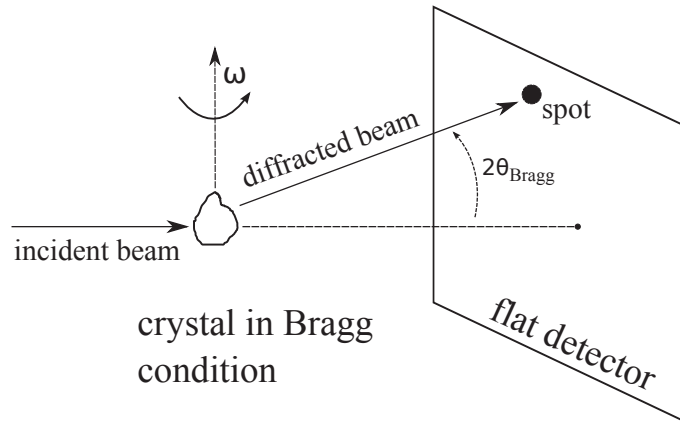


Figure II.1 – Rotating crystal method. A crystal is illuminated with a monochromatic, parallel, X-ray beam and rotated around a vertical axis. Diffraction occurs for ω angles that satisfy the Bragg condition. The beam is scattered at an angle 2θ given by Bragg's law, $2d_{hkl} \sin \theta = \lambda$, where λ is the X-ray wavelength and d_{hkl} the interplanar distance of (hkl) lattice planes. The diffracted beam is recorded as a spot on the flat detector, which is positioned at a given distance behind the sample and almost perpendicular to the incident beam.

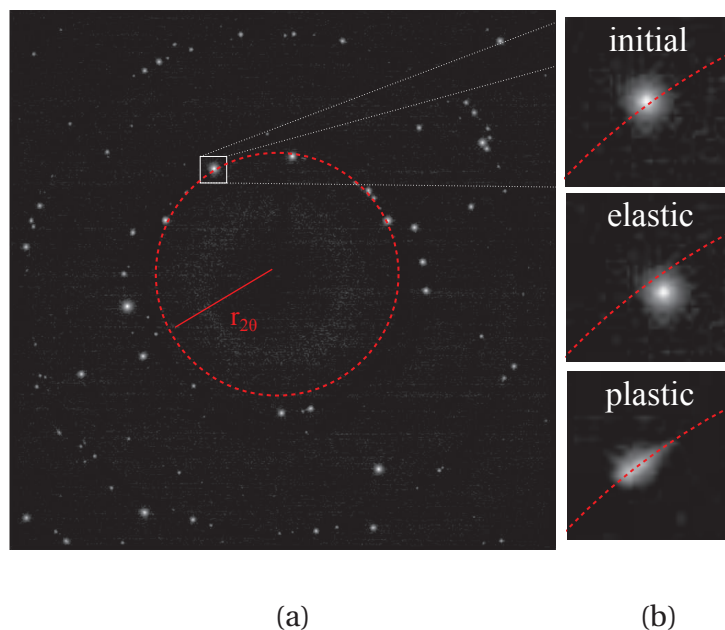


Figure II.2 – Effects of deformation on the far-field diffraction spots. (a) 3DXRD image showing the diffraction rings and spots at an undeformed, unloaded state. (b) Spot of interest represented after purely elastic deformation (radial shift, exaggerated for clarity) and plastic deformation (broadening along the ring).

II.1.2 Diffraction contrast tomography

Diffraction Contrast Tomography (DCT) is a technique for 3D mapping of grain structures. It was primarily applied on millimetre-sized samples containing up to a thousand undeformed/recrystallized grains [70, 71]. While a variant of HEXRD, DCT includes methods specific to X-ray computed tomography. This section provides the main principles of the technique only; detailed descriptions and applications can be found in the literature [43, 72, 73].

a) Acquisition geometry

The DCT technique is based on the simultaneous acquisition of the transmitted and the diffracted beams, as illustrated on Figure II.3-a. While the former is used for conventional absorption tomography of the sample, the latter gives access to the 3D shapes and orientations of the grains. The experimental setup includes a large, parallel, box beam and a high resolution 2D detector with a pixel size of about 1 μm . The detector is positioned closely behind the sample, at a distance of only a few millimetres. While the sample is continuously rotated by 360°, images are acquired with typical integration step $\delta\omega = 0.1^\circ$. A full scan may last from several minutes to several hours. The resulting stack of images then goes through processing operations to segment and extract the absorption tomogram and the diffraction spots (positions, shapes, sizes and intensities).

b) Friedel pair based indexing

Due to the perpendicularity between the beam and the rotation axis, each (hkl) reflection and its $(\bar{h}\bar{k}\bar{l})$ equivalent can be measured twice during a full ω -rotation. These four spots can be arranged in two pairs, called “Friedel pairs”, consisting each of an (hkl) and an $(\bar{h}\bar{k}\bar{l})$ reflection separated by 180° in ω . As illustrated on Figure II.3-b, we can represent the two paired spots in the same sample frame (detector planes at ω and $\omega + 180^\circ$) and notice that they define a line passing through the position of their grain of origin. Using this property and provided that two linearly independent Friedel pairs are available, we can determine both the grain position and average orientation.

In practice, Friedel pairs are identified using compatibility criteria in terms of position, shape and intensity. In particular, in the case of a grain with a low orientation spread, the paired spots are symmetrical with each other, which makes the detection quite reliable. Once Friedel pairs have been detected and associated to grains, the grain parameters can be refined. Then, forward projection can be used to predict the position of the missing spots and complete the indexing of each grain.

c) Reconstruction of grain shapes

The reconstruction of grain shapes is done grain by grain, using tomography algorithms, whose principle is to backproject the diffraction spot intensity into a box wrapping the grain of interest. During this process, the spots are treated as simple parallel projections of the grain shapes. This implies that the grains contain low orientation spread, typically below 1°.

The complete polycrystal is then obtained by assembling the reconstructed images of the individual grains. Possible overlaps and gaps between the grains are corrected by standard image processing (removal of intersections and dilation). Eventually, the absorption volume, computed from the transmitted intensity, can be superimposed on the 3D polycrystal to refine the shape of the sample.

II.1.3 High energy diffraction microscopy

High Energy Diffraction Microscopy (HEDM) was also developed for imaging 3D polycrystalline microstructures. However, the technique is based on different approaches for data acquisition and analysis, which makes it suitable for determining local orientations in plastically deformed samples (i.e., exhibiting intragranular orientation spreads). This section provides the main principles of the technique only; detailed descriptions and applications can be found in the literature [44, 48, 74–76]

a) Acquisition geometry

In HEDM, a layer-by-layer characterization of the sample is carried out with a planar focused beam. For each layer, scans over 180° or 360° are acquired at two or more detector distances, as shown in Figure II.4-a. This can be done simultaneously, by using semi-transparent detectors (as available at ID11/ESRF), or successively, by translating a unique detector. As the thickness of the beam (and therefore of the reconstructed layer) is of the order of $1\ \mu\text{m}$, several hundreds of scans may be needed to reconstruct volumes similar to those provided by DCT, which results in much greater acquisition and reconstruction times.

b) Forward modelling and Monte-Carlo optimization

The reconstruction is done on a predefined mesh (or grid) of the sample space and consists in determining the crystal orientation of triangle elements, as illustrated on Figure II.4-b. This results in an orientation field, where grains can be identified as clusters of elements with similar orientations.

HEDM is a “forward modelling technique”. For a given input orientation field, the diffraction spots are simulated by forward projection and compared to the experimental ones at all detector distances. The orientations that generate the best match are then determined by searching through the orientation space. The search is initially done on a predefined coarse grid and eventually refined by Monte-Carlo optimization. At the end of the procedure, each element is given an optimal orientation. In contrast with DCT, HEDM tends to fill up the input sample grid, leaving no or little empty space (i.e. without orientation). Another outcome of the reconstruction is the confidence value. It is similar to the completeness metric (Subsection II.1.1), but takes also into account the multiple detector distances and the ratio of overlap between simulated spots (projection of triangular elements) and experimental spots. The method, as described in Refs. [44, 74], works on binarized images, obtained after background subtraction and intensity thresholding; therefore the reconstruction process does not take into account the intensity distribution in the spots but only checks for the presence/absence of intensity. This allows the use of massive parallel optimization, by treating each element independently.

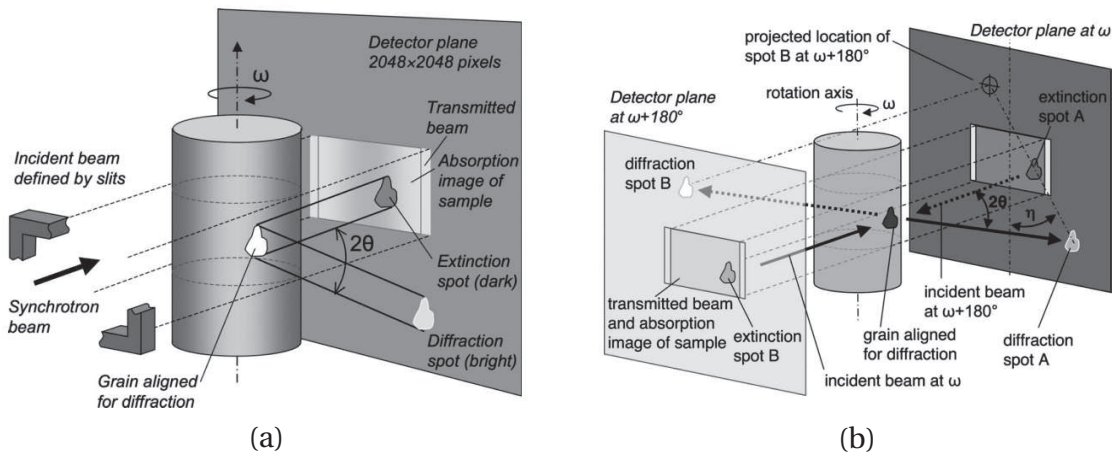


Figure II.3 – Principle of DCT, from Ref. [43]. (a) DCT setup, with the large box beam and the high-resolution detector, located close to the sample and recording both transmitted and diffracted intensities. (b) Friedel pair geometry represented in the sample frame, showing the paired diffraction spots at ω and $\omega + 180^\circ$, defining the beam path through the grain.

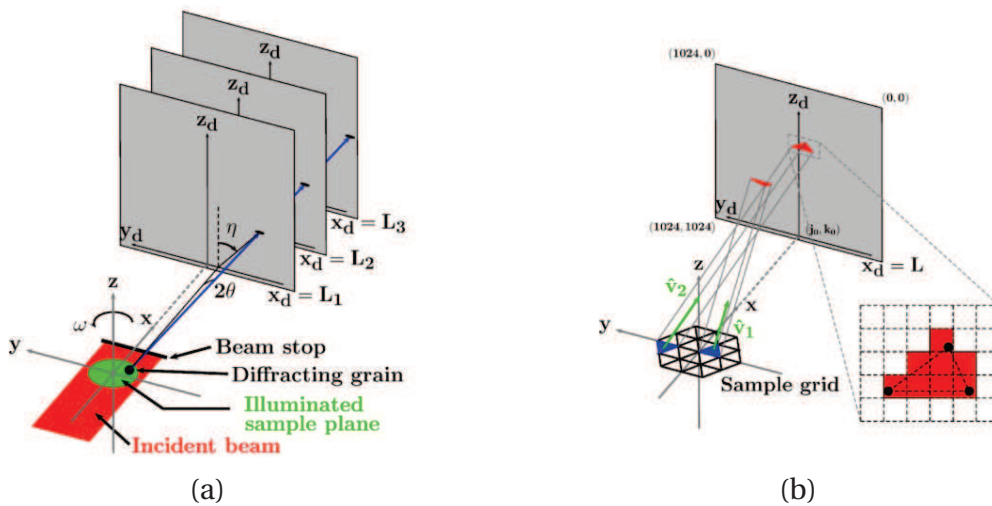


Figure II.4 – Principle of HEDM, from Ref. [44]. (a) The basic setup of HEDM includes a planar beam and a beam stop. Diffraction images acquired at multiple distances, using in the case of [44] one single detector moved sequentially. (b) Forward projection geometry, using a sample grid of triangular elements, each containing a local crystallographic orientation.

II.1.4 Experimental limits

The above descriptions of 3DXRD, DCT and HEDM allow us to draw experimental limits, in terms of sample and microstructure.

The three techniques are theoretically suited to millimetre-sized samples. In practice, the main limitation arises from DCT, since the size of the sample determines the size of the transmitted beam area. Therefore, the sample should not be too large (typically smaller than 1 mm) to provide sufficient field of view to record diffraction around the transmitted beam.

The applicability of HEXRD techniques then depends on the microstructure. In particular, the size distribution determines the minimum size of detectable grains, which is limited by the detector dynamic range to a fraction of the maximum grain size. Tighter distributions are therefore preferable. Nevertheless, the grains should be larger than the detector pixel size (typically 1-2 μm) to allow imaging by DCT or HEDM.

Other limiting aspects are the number of grains, the sample texture and the intra-grain orientation distributions. Indeed, from the point of view of data analysis and reconstruction, we saw that indexing is a crucial step. The main limitation of any indexing program/algorithm is related to the probability of spot overlap in the diffraction images, which increases with the the number of grains in the illuminated volume, the strength of the sample texture and the intra-grain orientation spread. This obviously affects DCT and HEDM, but it is even worse for 3DXRD. The latter technique is not very sensitive to grain relative positions and is therefore more prone to confuse reflections arising from grains with both close positions and orientations. However, in the absence of strong texture and intra-grain orientation spread, simulations showed that indexing up to a few thousands grains is possible [77]. This number then decreases with plastic deformation (Subsection II.1.1).

II.2 Material and samples

The material is a high purity Al-0.3% Mn alloy (Al-0.3Mn) used for previous studies in our laboratory [13, 78, 79]. It is comparable to the solid solution matrix of an AA3004 industrial alloy, without the intermetallic compounds (Al_6Mn) observed for saturated alloys ($> 1\%$ Mn). The presence of Mn in solid solution limits the recovery and recrystallization rates by solute-drag effect and increases strain hardening. This material deforms by crystallographic slip.

II.2.1 Microstructure

The as-cast microstructure consists of millimeter-sized grains [78]. Therefore, the material was cold rolled to 80% height reduction (logarithmic strain of 1.6) and heat-treated at 450°C for 25 min in an air furnace.

The recrystallized microstructure was characterized by EBSD mapping. Before observation, the sample surface was prepared as follows:

1. mechanical grinding using water lubricated, SiC discs with grit sizes of P800, P1200 and P2400,
2. mechanical polishing with 3 μm and 1 μm diamond pastes on felt discs,
3. electrolytic polishing in a Struers LectroPol-5 using the Struers electrolyte AII at a temperature of 12 °C, an applied voltage of 26 V and a time of 30s.

The EBSD measurements were done in a Zeiss Supra 55VP SEM, equipped with a high resolution NordlysNano camera (Oxford Instruments), using an acceleration voltage of 20 keV, a sample tilt of 70° and a working distance of 15 mm. The indexing was carried out with the AZtecHKL software suite, using a “refined accuracy” algorithm, which provides an angular resolution of about 0.1°.

The microstructure is shown in Figure II.5 and has an average grain size of 100-200 μm . Although no strong macrotexture was found in the recrystallized material, in agreement with previous results by Quey [13], microtextures can be observed in the presence of aggregates of grains disoriented by 5° to 15°. Figure II.6 shows the intra-grain orientation spread, which appears to be low, around 0.16°.

II.2.2 Macroscopic behaviour

The macroscopic mechanical behaviour of the material was characterized by uniaxial tensile testing. Round, standard specimens were prepared (ASTM-E8M, diameter of 4 mm, gage of 20 mm) and deformed until fracture at a rate of $5 \cdot 10^{-4} \text{ s}^{-1}$, while the gage length and applied force were monitored with an axial extensometer and a loadcell.

Figure II.7 shows the resulting strain-stress curve, computed against the initial gage length and cross-sectional area. We will later focus, for the experiments and the simulations, on the portion that lies between 0 and 5%, which suggests a yield strength of about 7 MPa.

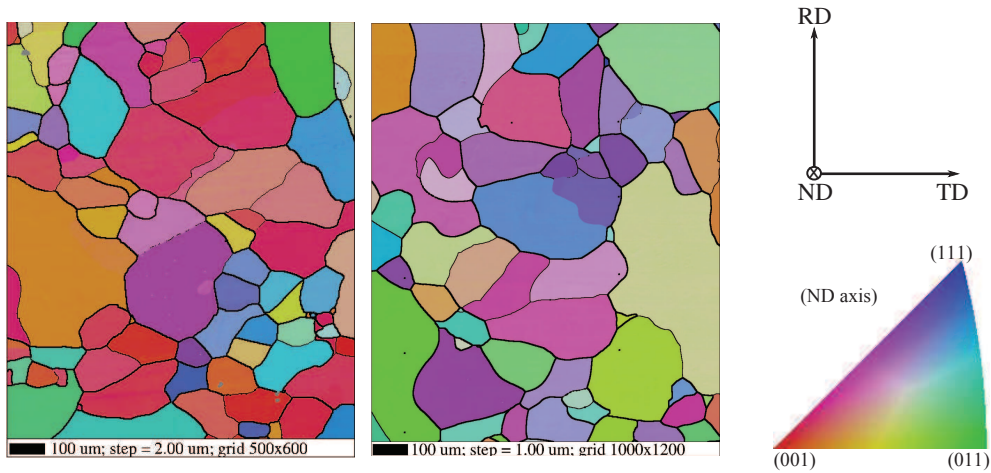


Figure II.5 – Recrystallized microstructures: two observations done on different samples. Inverse pole figure colouring, grain boundaries (bold lines $> 15^\circ$, thin lines $> 5^\circ$).

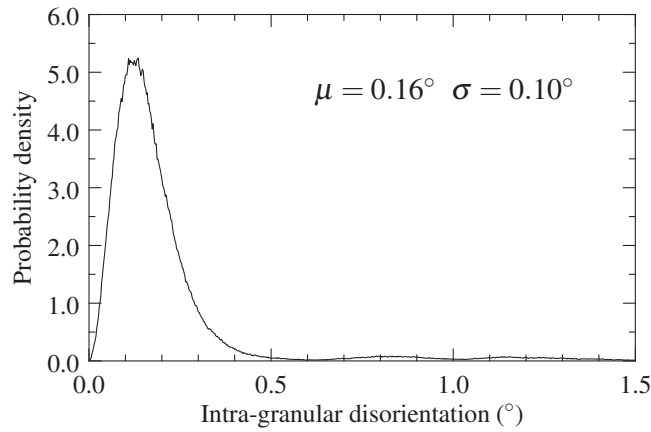


Figure II.6 – Distribution of intra-granular disorientations in the recrystallized material. The intra-granular disorientation is defined for each pixel as the disorientation angle with respect to the the average orientation of the corresponding grain. The distribution mean and standard deviation are provided as μ and σ .

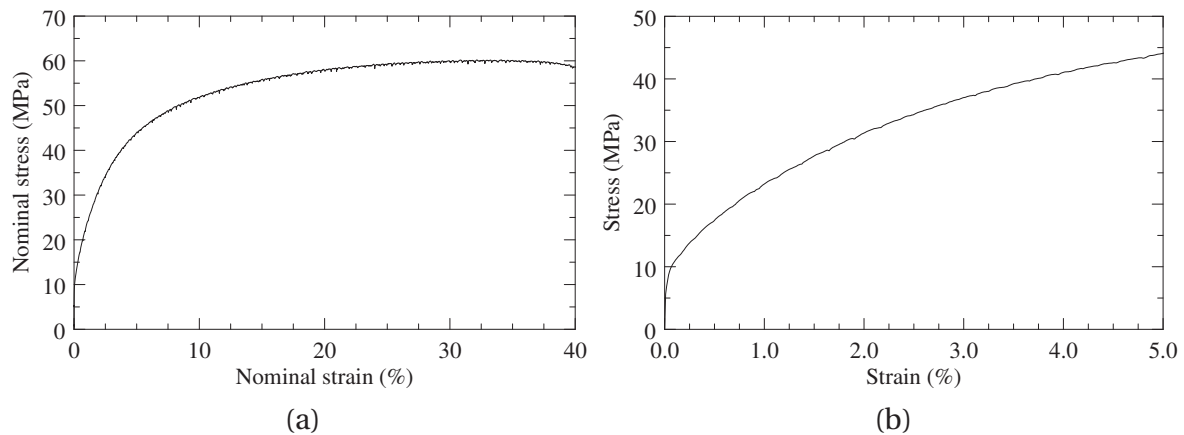


Figure II.7 – Tensile strain-stress curve of the material: (a) complete curve and (b) portion between 0 and 5%.

II.2.3 Sample preparation

The sample shape and dimensions for the *in situ* experiments are provided in Figure II.8. It consists of a flat, dog bone-shaped, tensile specimen, with a 1.5 mm long and 1 mm thick gage. The latter dimension is in agreement with the requirements for HEXRD experiments (Subsection II.1.4).

For sample preparation, two specimens were spark-machined out of the cold rolled material. Then, they were slightly polished to reduce the surface layer affected by machining and heat-treated to produce the final microstructure (Subsection II.2.1).

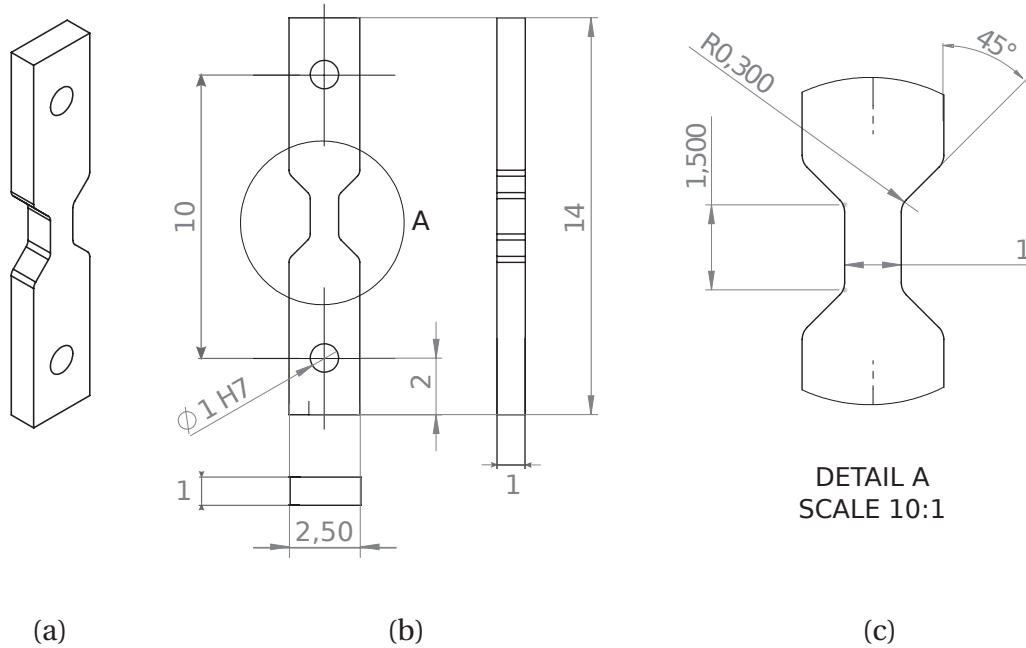


Figure II.8 – Shape and dimensions (mm) of the dog bone, tensile test specimens used for *in situ* experiments. (a) 3D view, (b) orthographic projections and (c) gage section of the specimen.

II.3 Experiments at ID11/ESRF

The experiments, done at ESRF on the beamline ID11, were organized around two samples. The first one, referred to as “Sample A”, was deformed to 1% plastic strain and measured by DCT and HEDM, with the aim of comparing the two techniques (Subsection II.3.1). The second sample, referred to as “Sample B”, was characterized by DCT at the initial undeformed state and *in situ* by 3DXRD at several levels of plastic strain, up to 4.5% (Subsection II.3.2).

II.3.1 DCT-HEDM comparison

Sample A was initially deformed to 1% plastic strain and the central part of the gage was then characterized by both DCT and HEDM. In addition, for comparison, the sample was later polished in our lab and mapped by EBSD (3 μm step) on a section parallel to the tensile axis and encompassing the region imaged by DCT and HEDM. The different regions characterized by the three techniques are schematically shown in Figure II.9.

a) DCT volume

For the DCT measurements, which involved the non-ideal case of a plastically deformed sample, the beam energy was reduced to 41.7 keV, to move the diffraction spots further away from the transmitted beam. The experimental setup included a 2048×2048 FReLoN camera [80] with a pixel size of 1.4 μm , positioned at 5 mm behind the sample, and a monochromatic beam, confined by slits to a rectangular cross-section of 350 μm in height and 1 mm in width. The acquisition was done for a complete rotation, an integration step of 0.1° and an exposure time of 2 s.

b) HEDM layers

For the HEDM measurements, the energy was set back to 60 keV and the beam was focused vertically using Kirkpatrick-Baez mirror optics to produce a 2 μm high and 1.5 mm wide, line cross-section. This allowed to illuminate only a thin layer of the sample, as required by the technique. The diffraction images were recorded using the so-called “3D detector” available at ID11/ESRF [81], which is made up of two semi-transparent 2048×2048 detectors with effective pixel sizes of 1.5 μm and 4.5 μm . The semi-transparency enabled the simultaneous acquisition at two distances of 5 mm and 15 mm. Fourteen layers could be measured in the region probed earlier by DCT, vertically spaced from each other with a 6 μm step. For each scan, we imposed a sample rotation of 180° , an integration step of 0.25° and an exposure time of 2 s.

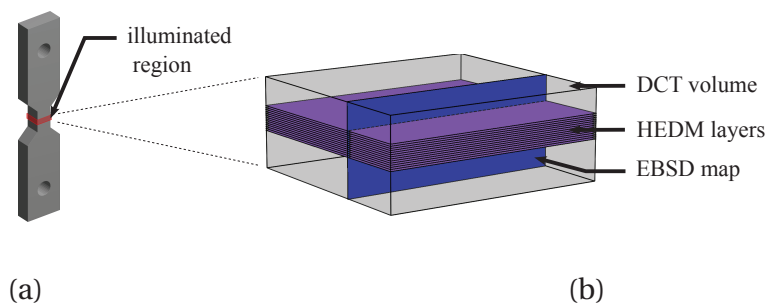


Figure II.9 – Schematic view of the investigated regions. (a) Illuminated region in the specimen. (b) Schematic positions of the HEDM layers and EBSD map in the DCT volume.

II.3.2 In situ tensile test

Sample B was first measured by DCT and 3DXRD in the initial undeformed state. Then, during *in situ* tensile test, it was measured by 3DXRD at five deformation levels up to 4.5% plastic strain. Before 3DXRD scans, calibration measurements were done on a reference powder of CeO₂ to assess the geometry of the far-field setup. The energy of the monochromatic beam was also calibrated and monitored throughout the experiment [82].

a) Deformation device

The tensile deformation device used during the experiment, called NanoX, is shown in Figure II.10-a. The device was developed at ID11 for *in situ* studies [83] and includes a glass tube, inside which the specimen is mounted between two anchoring pins. The upper grip section is fixed, standing on the glass tube, while the lower grip section applies the load. This design enables full rotation scans. For the experiment, the deformation was controlled in displacement and the load was monitored with a 500 N cell.

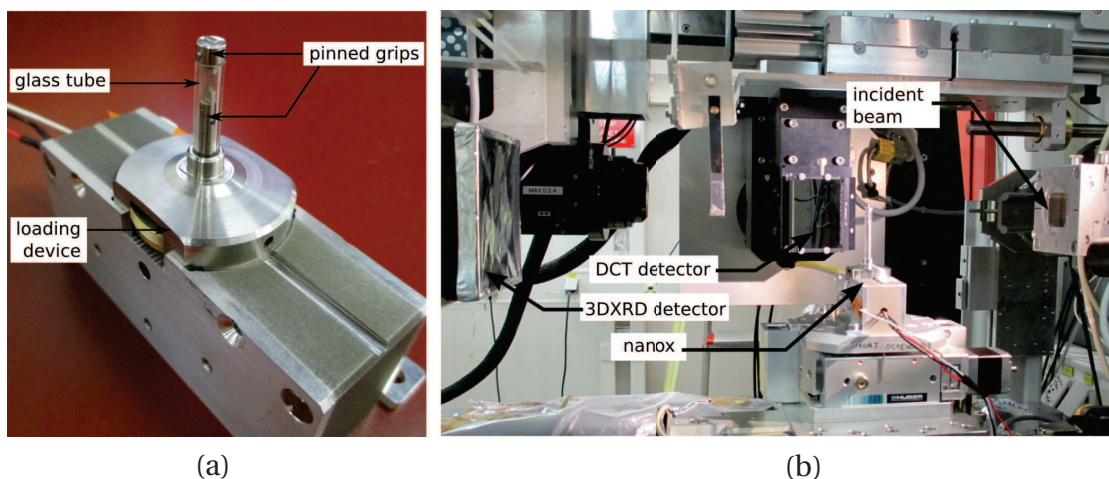


Figure II.10 – In situ deformation setup at ID11. (a) NanoX deformation device. The sample is mounted between two pinned grips inside a glass tube, allowing a full rotation of the goniometer. (b) Diffraction setup, with the Nanox rig mounted on the goniometer, DCT near-field and 3DXRD far-field detectors.

b) Calibration measurements

Detector: CeO₂ powder

Four diffraction images were recorded ($\omega = 0^\circ, 90^\circ, 135^\circ$ and 270°) using a Kapton capillary (inside diameter of 50 μm) filled up with a CeO₂ NIST certified powder. First the sample was centred on the rotation axis thanks to the high resolution detector used for DCT. Then, the beam height was reduced to 50 μm using the absorbing slits to illuminate a cylindrical volume with 50 μm in both height and diameter. Exposure time was 30 s.

Wavelength: Si wafer

ID11 is equipped with a wavelength monitoring device [82], which is made up of two photodiodes and a (100)-type silicon wafer on a rotation stage. To check the wavelength, the device can be inserted in the beam to scan the transmitted intensity while rotating the wafer. During rotation, (*hkl*) reflections lead to losses of intensity in the transmitted beam, called extinction peaks, whose positions are directly related to the wavelength.

The wafer was positioned with its surface normal to the beam and its flat cut along the horizontal direction. In practice, a first 180° scan is acquired with a step of 0.0016°, between the two positions where the wafer surface lies parallel to the beam. This scan provides an initial measure of the wavelength. Then, as long as the beam energy is not significantly changed, the variations of the wavelength can be monitored using the shifts of a few strong peaks in only 10°-wide scans.

c) Initial DCT characterization

The initial undeformed microstructure was characterized by DCT. The experimental setup included the same detector as in Subsection II.3.2 at the same distance of 5 mm and a box beam of 1 mm in width and 550 μm in height. The sample gage section, which is about 1.5 mm high, was therefore scanned in three, 550 μm high parts, with overlaps of 75 μm . The overlaps were used to facilitate merging of the three resulting volumes. For each scan, the measurements consisted of 3600 images acquired during a full rotation, with an integration step of 0.1° and an exposure time of 1 s.

d) In situ 3DXRD measurements

Far-field measurements were done on the central part of the DCT without changing the sample mounting. A FReLoN CCD camera [80] was positioned at a distance of 260 mm from the sample. This detector, coupled via fibre optics to a fluorescent screen, has an array of 2048 \times 2048 pixels with an effective size of 48.5 μm . Table II.1 details the parameters that were used for the successive scans. It can be seen that adjustments were made during the experiment to account for deformation. Up to 2% strain, no changes were made, since the spot broadening remained limited, as shown in Figure II.11. At 2.5% and 4.5% strain, the beam height was reduced to divide the probed volume into respectively two and three parts, with the aim of decreasing the number of grains in the beam. The integration step and exposure time were modified as well to account for intensity spread/loss due to plastic strain.

Table II.1 – Scan parameters used for 3DXRD during in situ tensile test.

strain (%)	ω -range (°)	ω -step (°)	exposure (s)	beam height (μm)	number of images
0	360	0.03	0.3	550	12000
1	360	0.03	0.3	550	12000
1.5	360	0.03	0.3	550	12000
2	360	0.03	0.3	550	12000
2.5	360	0.06	0.3	275	2 \times 6000
4.5	360	0.20	0.6	185	3 \times 1800

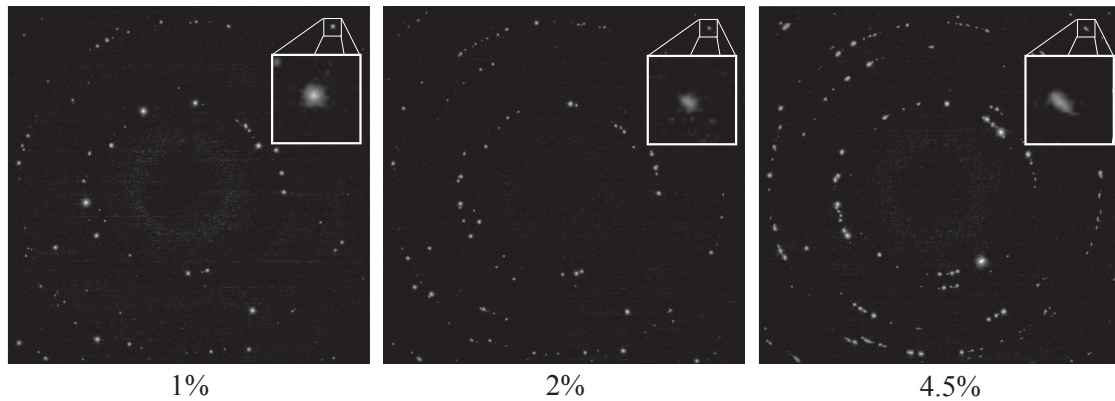


Figure II.11 – Spot broadening due to plastic strain (1%, 2% and 4.5%) observed during the experiment.

II.4 Conclusion

In this chapter, we have introduced the experimental techniques and the material of our study.

- Three different techniques were described, all based on the diffraction of hard X-rays recorded by flat detectors: 3DXRD, which enables to measure and follow grain average properties; DCT and HEDM, which are both imaging techniques, with different approaches.
- The material is a high-purity Al-0.3Mn alloy, which is single phased and deforms by crystallographic slip. The samples were machined and thermomechanically prepared to match the HEXRD requirements.
- The synchrotron experiments were organized around two samples. Sample A was deformed to 1% and imaged by DCT, HEDM, and later EBSD. Sample B was characterized at the initial state by DCT and *in situ* by 3DXRD during tensile testing up to 4.5% axial strain.

The subsequent analysis phase falls into two parts: data reconstruction for both imaging techniques and determination of grain average properties from 3DXRD.

CHAPTER -III-

Accurate measurement of grain average quantities

Contents

III.1 Geometry description	38
III.1.1 Diffraction images and spots	38
III.1.2 Coordinate systems	39
III.1.3 Parametrization	41
III.1.4 Projection equations	43
III.2 Geometry calibration	45
III.2.1 Detector tilt and distortions	45
III.2.2 Rotation axis	51
III.2.3 Complete geometry	54
III.2.4 Results	55
III.3 Calibration validation	58
III.3.1 Grain average quantities	58
III.3.2 Influence of the experimental uncertainties	59
III.3.3 Experimental results and validation	63
III.4 Conclusion	67

This chapter tackles the determination of grain average quantities, that is the calculation of the centroid, average crystal orientation and lattice properties of a grain, given a set of reflections indexed for that grain. We first provide a complete description and parametrization of the experimental geometry, which is then assessed through a calibration procedure (Sections III.1 and III.2). Finally, after having detailed the principles of the determination of grain average quantities, we discuss and validate the preliminary results obtained for the initial state of Sample B (Section III.3).

III.1 Geometry description

This section aims to mathematically describe the basic experimental setup of 3DXRD. The latter consists of very few elements. The sample is set on a rotation stage, which can rotate around a fixed axis ω and provides a measure of its angular position, ω . The sample is illuminated by a parallel, monochromatic X-ray beam, with an energy E (equivalent wavelength λ). The scattered intensity is recorded by a flat detector, positioned at a fixed distance downstream from the sample.

It has been long customary in the literature to assume a perfect setup, with a detector and a rotation axis perpendicular to the direction of the incident beam. Such an ideal configuration is very difficult to obtain in practice, but an accurate characterization requires to take into account any misalignment and imperfection.

III.1.1 Diffraction images and spots

Diffraction images are 16-bit images mapped on 2048×2048 pixel grids. The left-lower and right-upper pixels are respectively located at $(1, 1)$ and $(2048, 2048)$. Each diffraction image is assigned a corresponding ω angle, which is the mean angle of its integration interval. Hence, diffraction spot positions are described by coordinate triplets, (u, v, ω) .

In practice, due to grain size, mosaicity and instrumental broadening, diffraction spots consist of regions of connected pixels, usually chopped over several successive images. This is illustrated in Figure III.1. The detection and segmentation of these regions, largely discussed in the literature, are usually based on thresholding techniques. It results, for each spot, in a set of connected pixels p_i with their corresponding coordinates (u_i, v_i, ω_i) and intensity values I_i . We assume that the centre coordinates of the spot, also referred to “peak coordinates”, reflect the average properties of the grains. Therefore, before analysis, the spot information is reduced to the integral intensity I_{tot} and the centre of the intensity distribution (u, v, ω) as follows:

$$I_{\text{tot}} = \sum_{p_i} I_i \quad u = \sum_{p_i} \frac{I_i}{I_{\text{tot}}} u_i \quad v = \sum_{p_i} \frac{I_i}{I_{\text{tot}}} v_i \quad \omega = \sum_{p_i} \frac{I_i}{I_{\text{tot}}} \omega_i \quad (\text{III.1})$$

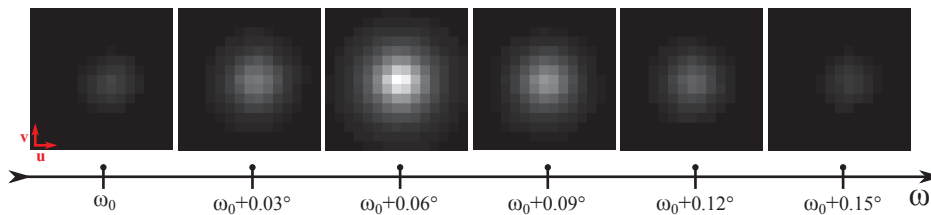


Figure III.1 – Diffraction spot, distributed over six successive images ($\delta\omega = 0.03^\circ$). The six images correspond to the same region of the detector (15×15 pixels).

III.1.2 Coordinate systems

We use six distinct sets of coordinate systems to relate a peak coordinates (u, v, ω) to its corresponding point in the reciprocal space of the grain lattice:

- the Cartesian system of the laboratory K_L ,
- the Cartesian system of the sample K_S ,
- the Cartesian system of the tilted detector K_D ,
- the Cartesian system of the ideal detector K_I ,
- the Cartesian system of the crystal K_C ,
- the affine system of the reciprocal lattice K_R .

The laboratory system, $K_L = (O, \mathbf{e}_1, \mathbf{e}_2, \mathbf{e}_3)$, is illustrated on Figure III.2. The laboratory origin, O , is located on the rotation axis ω . In principle, it can be arbitrarily chosen along the axis, but in practice, it is preferably chosen at mid-height of the beam section. The unit vector \mathbf{e}_1 is pointing downstream from the incident beam, along the direction of the incident wave vector \mathbf{k}_0 . The unit vector \mathbf{e}_2 is perpendicular to the vertical plane formed by \mathbf{e}_1 and ω .

The sample system, K_S , is entirely defined from the laboratory system. It coincides with K_L , when the angle ω equals zero. It is attached to the sample and rotates with the stage around ω .

The detector coordinate systems, $K_D = (C_B, \mathbf{n}, \mathbf{e}_u, \mathbf{e}_v)$ and $K_I = (C_B, \mathbf{e}_1, \mathbf{i}_u, \mathbf{i}_v)$, are illustrated on Figure III.2. The detector origin, C_B , is commonly called the “beam centre”. It is defined as the intersection between the beam axis (carried by \mathbf{e}_1 and passing through O) and the detector plane. The titled detector is described by its normal vector \mathbf{n} and two unit vectors, \mathbf{e}_u and \mathbf{e}_v , respectively aligned with the pixel rows and columns. Equivalently, the ideal detector is described by \mathbf{e}_1 , \mathbf{i}_u , and \mathbf{i}_v . For convenience, we impose that \mathbf{i}_v is contained in the plane formed by the beam axis and \mathbf{e}_v . As a consequence, K_I can be simply obtained by shifting K_L to C_B and rotating it around the beam axis. Then, the transformation from K_I to K_D solely results from the tilt of the detector plane.

Lastly, the crystal Cartesian system, K_C , and the reciprocal lattice affine system, K_R , are defined for each grain of the sample. For cubic crystals, K_C is simply defined by the three $[100]$, $[010]$ and $[001]$ direction vectors of the primitive unit cell. K_C is related to K_S via the grain lattice orientation. The reciprocal lattice space is built from the direct lattice space, depending on the crystal structure. For an ideal face-centred cubic crystal, the reciprocal lattice is body-centred cubic and K_R is defined by the three $[100]$, $[010]$ and $[001]$ direction vectors in the reciprocal lattice.

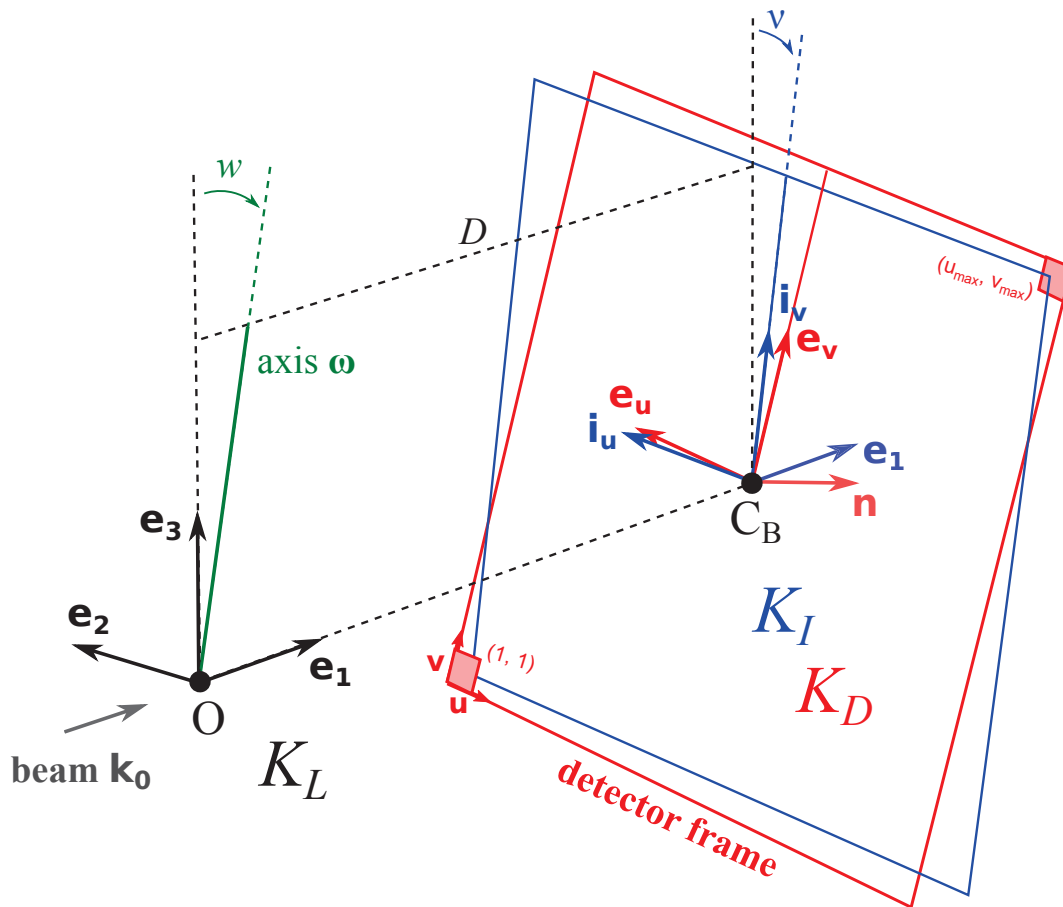


Figure III.2 – Laboratory and detector coordinate systems of the 3DXRD geometry: the laboratory system K_L (black), the ideal detector system K_I (blue) and the tilted detector system K_D (red). The misalignments are exaggerated for clarity.

III.1.3 Parametrization

We distinguish between “global parameters”, which only depend on the experimental conditions, and “grain parameters”, which define each grain. Our description uses nine global parameters and twelve grain parameters, summarized in Table III.1. We define them, one after the other, by considering the transformations between coordinate systems.

a) Global parameters

Sample to laboratory ($K_S \leftrightarrow K_L$)

We denote by w the angle between $\boldsymbol{\omega}$ and \mathbf{e}_3 , usually called the “wedge angle” (see Figure III.2). The transformation from K_S to K_L is thus given by:

$$\mathbf{r}_L = \boldsymbol{\Omega}_\omega \mathbf{r}_S \quad (\text{III.2})$$

where $\boldsymbol{\Omega}_\omega$ is a matrix describing the right-handed rotation by an angle ω around $\boldsymbol{\omega}$. The expression of $\boldsymbol{\Omega}_\omega$ is obtained from Rodrigues’ rotation formula as:

$$\boldsymbol{\Omega}_\omega = \begin{bmatrix} (1 - \cos \omega) \sin^2 w + \cos \omega & -\sin \omega \cos w & (1 - \cos \omega) \sin w \cos w \\ \sin \omega \cos w & \cos \omega & -\sin \omega \sin w \\ (1 - \cos \omega) \sin w \cos w & \sin \omega \sin w & (1 - \cos \omega) \cos^2 w + \cos \omega \end{bmatrix} \quad (\text{III.3})$$

Laboratory to ideal detector ($K_L \leftrightarrow K_I$)

We denote by D the distance OC_B , referred to as “detector distance”, and by ν the angle between the vertical plane and the pixel column direction, referred to as the “twist angle” (see Figure III.2). The transformation from K_L to K_I can be written as:

$$\mathbf{r}_L = \mathbf{T}_\nu \mathbf{r}_I + D \mathbf{e}_1 \quad (\text{III.4})$$

\mathbf{T}_ν denotes the right-handed rotation of angle ν around the beam axis, which we can write:

$$\mathbf{T}_\nu = \begin{bmatrix} 1 & 0 & 0 \\ 0 & \cos \nu & -\sin \nu \\ 0 & \sin \nu & \cos \nu \end{bmatrix} \quad (\text{III.5})$$

Ideal to tilted detector ($K_I \leftrightarrow K_D$)

The components of the unit vector \mathbf{n} are denoted by (n_1, n_2, n_3) in K_I . The transformation from K_I to K_D is:

$$\mathbf{r}_D = \mathbf{T}_n \mathbf{r}_I \quad (\text{III.6})$$

The transformation matrix, \mathbf{T}_n , is obtained by considering the constraint on \mathbf{i}_ν , as:

$$\mathbf{T}_n = \begin{bmatrix} n_1 & n_2 & n_3 \\ -\frac{n_1 n_2}{p} & p & -\frac{n_2 n_3}{p} \\ -\frac{n_3}{p} & 0 & \frac{n_1}{p} \end{bmatrix} \quad (\text{III.7})$$

where $p = \sqrt{n_1^2 + n_3^2}$.

Detector to image coordinates ($K_D \leftrightarrow (\mathbf{u}, \mathbf{v})$)

The image coordinates of the beam centre are denoted by (u_B, v_B) . For a pixel of coordinates (u, v) , we thus have:

$$\mathbf{r}_D = \begin{bmatrix} 0 \\ (u_B - u) \pi_u \\ (v - v_B) \pi_v \end{bmatrix} \quad (\text{III.8})$$

where π_u and π_v are the horizontal and vertical pixel sizes of the detector (considered as known).

b) Grain parameters

Each grain is defined, on average, by its position, orientation and unit cell. The position is assumed to be the grain centre of mass, or centroid, denoted by $\mathbf{r}_0 = (x_0, y_0, z_0)^T$ in K_S . The orientation is described by a Rodrigues vector, $\mathbf{R} = (R_1, R_2, R_3)^T$ or the corresponding orientation matrix \mathbf{U} . The unit cell is given by the six lattice parameters, $(a, b, c, \alpha, \beta, \gamma)$. The transformation of any reciprocal space vector \mathbf{g} to the crystal system K_C is given by:

$$\mathbf{g}_C = \mathbf{B} \mathbf{g} \quad (\text{III.9})$$

The orthogonalization matrix \mathbf{B} can be expressed in terms of the equivalent, reciprocal lattice parameters $(a^*, b^*, c^*, \alpha^*, \beta^*, \gamma^*)$ as [84]:

$$\mathbf{B} = \begin{bmatrix} a^* & b^* \cos \gamma^* & c^* \cos \beta^* \\ 0 & b^* \sin \gamma^* & -c^* \sin \beta^* \cos \alpha \\ 0 & 0 & c^* \sin \beta^* \sin \alpha \end{bmatrix} \quad (\text{III.10})$$

Finally, we relate K_C and K_S via the orientation matrix, \mathbf{U} . The latter is related to the Rodrigues vector components through the Rodrigues rotation formula. We thus have:

$$\mathbf{g}_S = \mathbf{U}^{-1} \mathbf{g}_C \quad (\text{III.11})$$

Table III.1 – Global and grain parameters describing the 3DXRD geometry.

parameter set	Symbol(s)	Feature
Global (9)	n_1, n_2, n_3	detector tilt
	v	twist angle
	u_B, v_B	beam centre
	D	detector distance
	w	wedge angle
	λ	beam wavelength
Grain (12)	x_0, y_0, z_0	centroid
	R_1, R_2, R_3	orientation
	$a, b, c, \alpha, \beta, \gamma$	unit cell

III.1.4 Projection equations

The introduced formalism allows us now to relate any diffraction peak to its corresponding point in the grain reciprocal lattice. This is done in one way or another, depending on the backward or forward approach. Let us consider a diffraction spot of coordinates (u, v, ω) which was indexed for a given grain under reciprocal lattice point (h, k, l) .

a) Forward approach

Combining Equations III.2, III.9 and III.11, the reciprocal space vector $\mathbf{g}_R = (h, k, l)^T$ becomes in K_L :

$$\mathbf{g}_L = \Omega_\omega \mathbf{U}^{-1} \mathbf{B} \mathbf{g}_R \quad (\text{III.12})$$

The diffraction condition is given by the Laue equation:

$$\mathbf{e}_k = \mathbf{e}_1 + \lambda \mathbf{g}_L \quad (\text{III.13})$$

where \mathbf{e}_1 and \mathbf{e}_k are the unit, direction vectors of the incident and diffracted beam, respectively. The prediction of the angle ω_F , for which Equation III.13 is satisfied, will be discussed in Subsection III.2.2.

As illustrated on Figure III.3, the diffracted beam originates from the grain position and intersects the detector plane at the spot position. This can be expressed in K_L , using Equation III.4, as:

$$\mathbf{T}_v \mathbf{T}_n^{-1} \mathbf{s}_D + D \mathbf{e}_1 = \xi \mathbf{e}_k + \Omega_\omega \mathbf{r}_0 \quad (\text{III.14})$$

where the unknown ξ is the length of the diffracted beam path. Since \mathbf{s}_D lies in the detector plane, it is perpendicular to \mathbf{n} . Thus, defining $\mathbf{T} = \mathbf{T}_n \mathbf{T}_v^{-1}$ and $\mathbf{n}_L = \mathbf{T}^{-1} \mathbf{n}$, we obtain:

$$\xi \mathbf{e}_k \cdot \mathbf{n}_L + (\Omega_\omega \mathbf{r}_0) \cdot \mathbf{n}_L - D n_1 = 0 \quad (\text{III.15})$$

The coordinate of the spot in K_D is then given by:

$$\mathbf{s}_D = \mathbf{T} \left(\frac{D n_1 - (\Omega_\omega \mathbf{r}_0) \cdot \mathbf{n}_L}{\mathbf{e}_k \cdot \mathbf{n}_L} \mathbf{e}_k + \Omega_\omega \mathbf{r}_0 - D \mathbf{e}_1 \right) \quad (\text{III.16})$$

Finally, using Equation III.8, we calculate the predicted image coordinates of the spot, (u_F, v_F) , where the subscript F stands for ‘‘forward’’.

b) Backward approach

Using Equation III.8 and Equation III.14, the diffracted beam vector \mathbf{e}_k is obtained from the peak coordinates, (u, v, ω) , as:

$$\mathbf{e}_k = \frac{\mathbf{T}^{-1} \mathbf{s}_D - \Omega_\omega \mathbf{r}_0 + D \mathbf{e}_1}{\|\mathbf{T}^{-1} \mathbf{s}_D - \Omega_\omega \mathbf{r}_0 + D \mathbf{e}_1\|} \quad (\text{III.17})$$

Then, the corresponding diffraction vector is, in the laboratory coordinate system:

$$\mathbf{g}_L = \frac{\mathbf{e}_k - \mathbf{e}_1}{\lambda} \quad (\text{III.18})$$

and, in the reciprocal lattice:

$$\mathbf{g}_R = \mathbf{B}^{-1} \mathbf{U} \Omega_\omega^{-1} \mathbf{g}_L = \begin{pmatrix} h_B \\ k_B \\ l_B \end{pmatrix} \quad (\text{III.19})$$

The backprojected indices are denoted by (h_B, k_B, l_B) , where the subscript B stands for ‘‘backward’’.

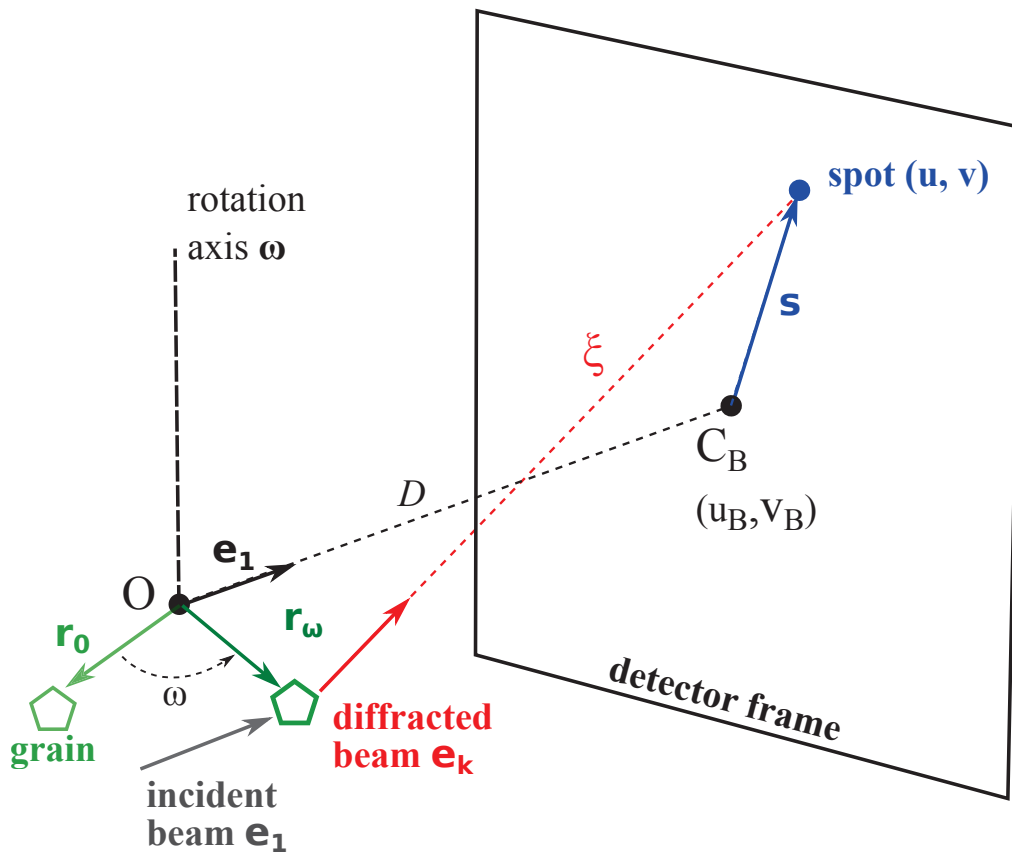


Figure III.3 – Schematic of a spot projection in the 3DXRD geometry. A grain is located at \mathbf{r}_0 in K_S (light green) and \mathbf{r}_ω in K_L after rotation (green). It produces a diffracted beam of direction \mathbf{e}_k (red), recorded on the detector as a spot (blue) of position \mathbf{s} or image coordinates (u,v) . The length of the diffracted beam path, between the grain and the detector, is denoted by ξ .

III.2 Geometry calibration

Like any scientific instrument, a 3DXRD diffractometer requires a preliminary calibration to allow for accurate and physically meaningful characterizations. The calibration refers to the determination of the global parameters, which are independent of the sample. At least two different approaches can be found in the literature: that of Oddershede *et al.* [54] and that of Bernier *et al.* [66].

The approach of Oddershede *et al.* consists in assessing the geometry from the measurements themselves [54]. As it depends on the investigated sample, it is not, strictly speaking, a calibration procedure. Besides, due to dependencies among the global and grain parameters, it cannot, *a priori*, ensure any acceptable level on the accuracy of the results.

The approach of Bernier *et al.* uses independent, calibration measurements on reference samples [66]. It is usually, and unfairly, criticized for being beamtime-consuming. However, it allows, in return for about twenty minutes, to achieve the best accuracy levels. This approach seems preferable to us for accurate data processing and strain measurements.

Our method is based on the simple observation that the tilt of the detector and the tilt of the rotation axis are unrelated. This allows a three-step calibration procedure, based on measurements on a reference powder sample and an undeformed single crystal. It proceeds as follows:

1. the tilt of the detector is obtained from measurements on the reference powder,
2. the tilt of the rotation axis is obtained from measurements on the single crystal,
3. the detector is linked to the rotation axis, using the single crystal data.

The approach was validated on measurements from ESRF and APS in Refs. [85, 86]. It was adapted and applied in this study to the 3DXRD measurements of Sample B.

III.2.1 Detector tilt and distortions

Area detectors have become state-of-the-art in various synchrotron-based characterization techniques. The determination of detector tilt and position is, in the literature, a well-known issue, which is generally treated using powder diffraction patterns.

a) Powder diffraction pattern

A powder consists of a large number of crystallites, randomly oriented. When a powder sample is irradiated, the beam is diffracted in many directions simultaneously, on a cone of solid angle $4\theta_{hkl}$, where θ_{hkl} is the Bragg angle corresponding to (hkl) lattice planes. The cone axis is parallel to the beam axis, and the cone apex is located in the irradiated volume at a distance D upstream from the detector. When the number of diffracting crystallites is large enough, the scattered intensity is uniformly distributed on the surface of the cone. This produces smooth, continuous rings on the detector. A powder diffraction pattern consists of several similar rings with different intensities and radii, called “Debye rings”, corresponding to different Bragg angles. An example is shown in Figure III.6-a.

The intersection of a cone with a tilted detector plane is not anymore a circle, but an ellipse, whose shape can be geometrically related to the tilt of the plane. This approach was proposed by Hammersley *et al.* [87], who described the tilt in terms of two angles:

an horizontal tilt, ϕ , with respect to the diffraction cone axis and a vertical tilt, β , around the tilted plane normal. Hart *et al.* [88] and, more recently, Borbely *et al.* [85] have shown that, due to the small ellipse eccentricity, the uncertainty on β strongly increases as ϕ decreases towards zero. This parametrization is ill-defined in a position close to the ideal detector. Therefore, we describe the tilt of the detector with the components (n_1, n_2, n_3) of its normal unit vector \mathbf{n} .

To relate the shape of a (hkl) Debye ring to (n_1, n_2, n_3) , we consider a point on that ring. In the ideal detector system K_I , we can write the tangent of the observed diffraction angle, $2\theta_{hkl}^{obs}$, as:

$$\tan\left(2\theta_{hkl}^{obs}\right) = \frac{\sqrt{y_I^2 + z_I^2}}{x_I + D} \quad (\text{III.20})$$

where (x_I, y_I, z_I) are the point coordinates in K_I . Using Equation III.6, we obtain:

$$\tan^2\left(2\theta_{hkl}^{obs}\right) = \frac{(n_1^2 + n_3^2)^2 y_D^2 + (n_1 z_D - n_2 n_3 y_D)^2}{\left(D\sqrt{n_1^2 - n_3^2} - n_1 n_2 y_D - n_3 z_D\right)^2}. \quad (\text{III.21})$$

where $(x_D = 0, y_D, z_D)$ are the point coordinates in K_D . The equation can be further transformed, using Equation III.8, to replace y_D and z_D by the image coordinates (u, v) .

b) Optimization problem

A calibration problem can be expressed as an optimization problem, with an objective function to be minimized over a set of variables, while accounting for inequality and equality constraints. Using Equation III.21, we can derive an objective function and formulate the problem as:

$$\begin{aligned} & \underset{\mathbf{n}, \tilde{D}, \tilde{u}_B, v_B}{\text{minimize}} & \mathcal{F}_1(\mathbf{n}, \tilde{D}, \tilde{u}_B, v_B) &= \sum_{i,j} \left(\tan^2 2\theta_{i,j}^{obs} - \tan^2 2\theta_j^{th} \right)^2 & (\text{III.22}) \\ & \text{subjected to} & & \left\{ \begin{array}{l} \|\mathbf{n}\| = 1 \\ n_1, \tilde{D} > 0 \end{array} \right. \end{aligned}$$

The summation in \mathcal{F}_1 runs over the points i of the Debye rings j . Theoretical diffraction angles θ_j^{th} are calculated using Bragg's law for a given wavelength λ and known lattice parameters (reference powder).

Solving Equation III.22 provides the maximum-likelihood values of the parameters in a non-linear least-squares sense. The goodness of the fit may be first assessed from the standard errors. Those can, however, be artificially reduced by increasing the number of points in the minimization. Therefore, we rather consider repeatability as a measure of the procedure error. This requires in practice to record and analyse multiple images.

The reader should note the use of \tilde{u}_B and \tilde{D} instead of u_B and D . Indeed, these parameters are related to the diffraction cone apex, which does not necessarily lie on the rotation axis (as required for the laboratory origin). On the contrary, v_B certainly defines a possible laboratory origin (as the rotation axis is near-vertical) and can, therefore, be reasonably retained thereafter.

c) Spatial distortions

An ideal, flat detector consists of a perfect, regular array of pixels. In real detectors, due to imperfections in the optics and the planarity of the detector area, the effective pixel

arrangement deviates from a perfect grid. This must be corrected to produce diffraction images with equidistant and accurate pixel coordinates.

In practice, spatial distortions can be assessed using a calibration grid, which includes accurately distributed pinholes. The detector phosphor screen is replaced with this plate and series of images are recorded in visible light. Then, the positions of the pinholes, as given by the images, can be compared to their real, known arrangement to interpolate distortion maps. An example, obtained for a CCD-based FReLoN detector, is shown in Figure III.5. In this case, the spatial distortions are attributed to the fibre optics between the scintillator and the CCD camera.

This approach, though, does not correct all kind of distortions. Diffraction images can also be affected by physical distortions, due to sample or scintillator absorption. Such effects can be either modelled or measured using reference powders. In the latter case, illustrated on Figure III.4, the experimental Debye rings are compared to the theoretical ones to compute the radial distortions as a function of the azimuthal angle η .

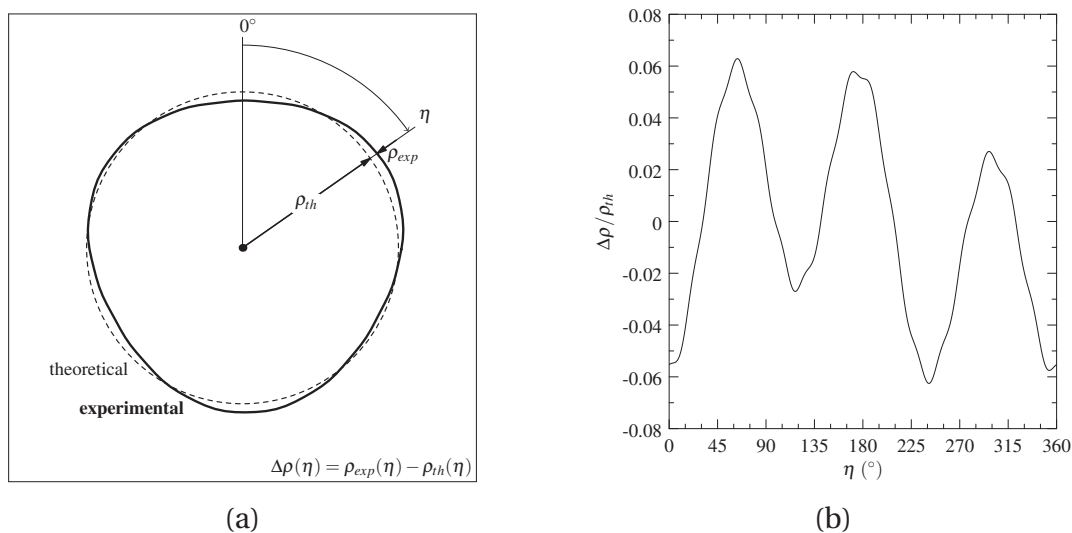


Figure III.4 – Principle of radial distortion assessment. (a) Schematic drawing of an experimental, distorted ring and the theoretical, ideal ring. (b) Resulting radial shifts, with respect to the beam centre, as a function of the azimuthal angle η .

d) Calibration work-flow

We proposed in Ref. [85] a tilt calibration framework taking distortions into account. The method is similar to that proposed by Lee *et al.* [89]. It can be applied to assess the detector distortions or check previous corrections obtained, for instance, with a calibration grid. The procedure comprises the following steps:

- 1 – Powder diffraction images are acquired with a reference sample (usually NIST¹ certified). The beam cross-section should be comparable to the detector pixel size and the powder should be fine enough to produce smooth, continuous Debye rings with uniformly distributed intensity over the circumference.
- 2 – For detectors with known spatial distortions, the distorted images should be projected on a distortion-free, pixel array [90].

¹U.S National Institute of Standards and Technology

- 3 – We consider, first, an arbitrary beam centre to compute the polar transforms of the images, as illustrated on Figure III.6-b. The new coordinates, denoted by (ρ, η) or, equivalently, $(2\theta, \eta)$, are consistent with the circular symmetry of powder diffraction patterns. The polar transformation associates to each η angle a 1D radial diffractogram. Then, Pseudo-Voigt functions can be fitted to the radial, peak profiles. This provides, in practice, sub-pixel precision for the determination of peak positions.
- 4 – The optimization problem of Equation III.22 is solved using the fitted peak positions, theoretical Bragg angles, and initial estimates of the parameters: $n_1 \simeq 1$, $n_2 \simeq 0$, $n_3 \simeq 0$, and \tilde{D} , \tilde{u}_B , v_B from experiment. To avoid any bias due to the polar transform, steps 3 and 4 are repeated, using the optimized beam centre.
- 5 – Several images are analysed to obtain the reproducibility errors of the parameters. Radial distortions are evaluated to detect, whether any other effect should be corrected.

The methodology was applied in Ref. [85] on data from the materials science beamline 1-ID (APS), measured with a GE Revolution 41RT flat-panel detector. The results revealed radial distortions having an azimuthal periodicity of 180° and a monotonic increase of the average offset with the radius. The latter were described analytically and included in the objective function \mathcal{F}_1 to obtain correct calibration parameters. Finally, the relative radial distortions were confined within $\pm 5 \times 10^{-5}$.

e) Results: FReLoN-4M and CeO₂ powder

The spatial distortions were assessed from independent optical measurements, using a calibration grid (Edmund Optics NT59-215). The resulting distortion map, illustrated on Figure III.5, provides the pixel shifts, $(\Delta u, \Delta v)$, with respect to an ideal grid. Distortion-free images were computed accordingly.

Four powder images were recorded at $\omega = 0^\circ, 90^\circ, 135^\circ$ and 270° . For each image, the calibration procedure was applied using, first, an estimated beam centre, and repeated, then, with the optimized beam centre. The corresponding polar transforms are shown in Figure III.6-b-c. The resulting parameter values are provided in Table III.2. A good repeatability is observed, suggesting, in particular, sub-pixel precisions on both detector distance and beam centre coordinates. The detector tilt appears to be independent of ω . We have also shown, in Ref. [85], that it neither depends on the beam energy nor on the measured sample.

The residual distortions are provided in Figure III.7. The relative radial offsets, $\Delta\rho/\rho$, are shown in Figure III.7-a, as a function of the azimuthal angle, η . A few spikes exceeding $\pm 1 \times 10^{-4}$ can be observed, but the residuals are mostly confined within $\pm 1 \times 10^{-4}$ and, even, $\pm 5 \times 10^{-5}$. This tendency is better emphasized in Figure III.7-b, which gives the average distortions of all rings as a function of the radius, ρ . The azimuthal averages fall between the limits of $\pm 5 \cdot 10^{-5}$. We can conclude that the spatial distortions were properly corrected.

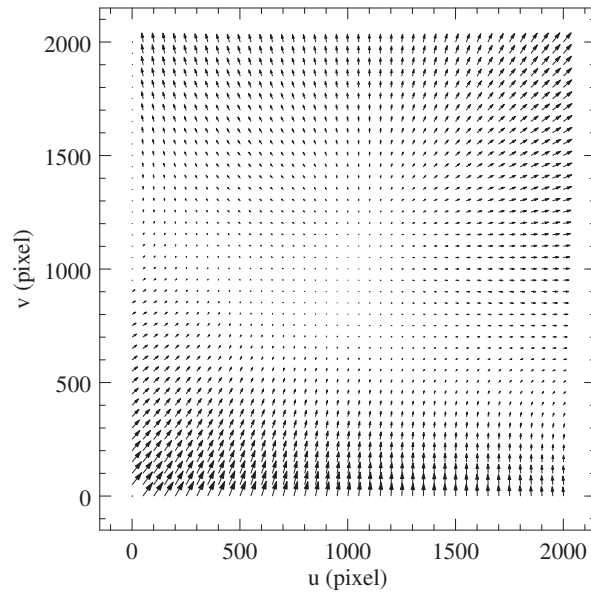
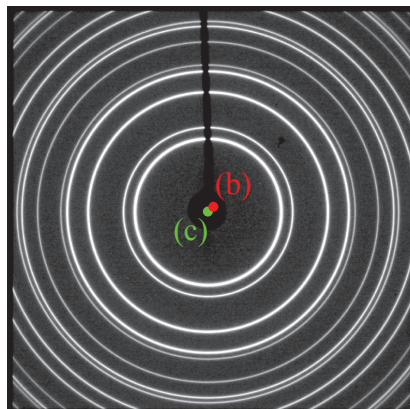
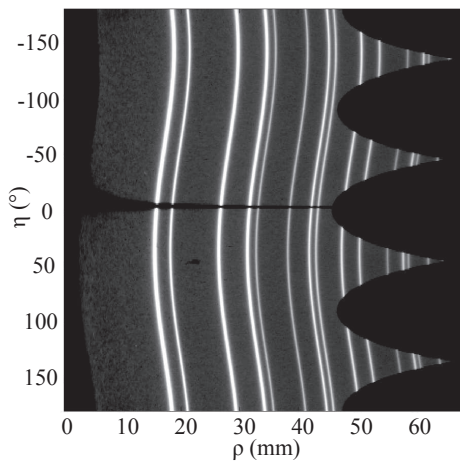


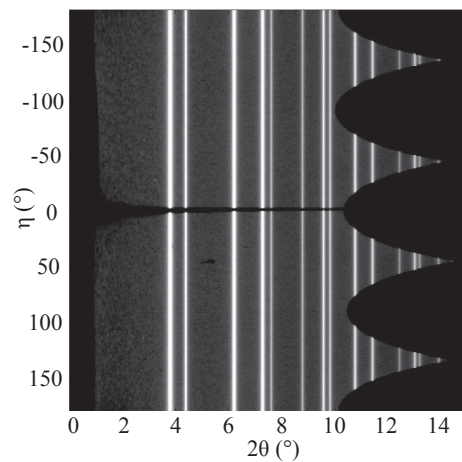
Figure III.5 – Distortion field of the FReLoN-4M, evaluated from optical measurements (J. Wright, ID11).



(a)



(b)

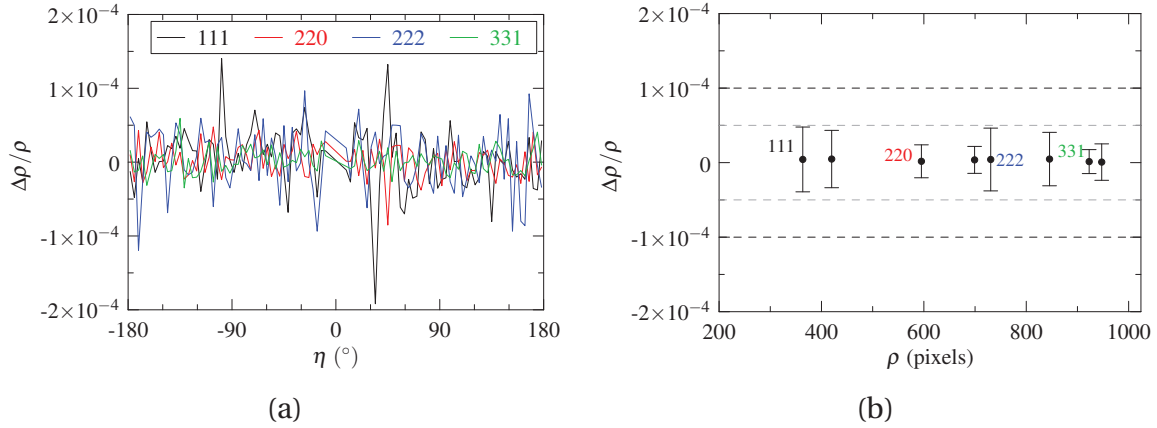


(c)

Figure III.6 – Polar transformation of a powder diffraction image. (a) Powder diffraction image measured at ID-11 using a CeO_2 powder sample. Polar transforms with respect to (b) the red centre and (c) the green centre .

Table III.2 – The detector tilt components (n_1, n_2, n_3), the detector distance D and the beam centre (u_B, v_B) obtained from the calibration of the FReLoN-4M.

ω ($^\circ$)	n_1	n_2	n_3	D (m)	u_B (pixel)	v_B (pixel)
0	0.9999499	-0.009927	0.0012625	0.258283	1003.575	995.898
90	0.9999502	-0.009881	0.0013928	0.258253	1003.571	995.894
135	0.9999488	-0.009991	0.0015926	0.258253	1003.579	995.954
270	0.9999489	-0.009986	0.0015803	0.256267	1003.581	995.960
Mean	0.9999494	-0.009946	0.0014570	0.258263	1003.577	995.927
STD	6×10^{-7}	5×10^{-5}	1×10^{-4}	1×10^{-5}	4×10^{-3}	3×10^{-2}


 Figure III.7 – Residual distortions of the FReLoN-4M after correction and calibration. (a) Relative radial shifts as a function of η for 111, 220, 222 and 331 Debye rings. (b) Azimuthal average of the radial shifts, as a function of ρ , for all the available rings (111, 200, 220, 311, 222, 400, 331 and 420). The error bars indicate the standard deviations.

III.2.2 Rotation axis

The second calibration step concerns the tilt of the rotation axis. The latter can be assessed regardless of the detector tilt or spatial distortions. Sharma *et al.* proposed such an approach, based on the difference in ω of Friedel pairs [67]. One may, indeed, observe from Equation III.13 that spot ω -coordinates only depend on the wavelength, the wedge angle, the crystal orientation and lattice parameters. Our method follows this principle and is based on the prediction of spot ω -coordinates.

a) Prediction of ω -coordinates

The Laue equation is given by Equations III.12 and III.13 as:

$$\mathbf{e}_k = \mathbf{e}_1 + \lambda \mathbf{g} = \mathbf{e}_1 + \lambda \Omega_\omega \mathbf{U}^{-1} \mathbf{B} \begin{pmatrix} h \\ k \\ l \end{pmatrix} \quad (\text{III.23})$$

This condition is equivalent to \mathbf{e}_1 and \mathbf{g} forming an angle of $\frac{\pi}{2} - \theta_{hkl}$, where θ_{hkl} is the corresponding Bragg angle. We can, therefore, modify Equation III.23 accordingly to obtain,

$$\mathbf{e}_1 \cdot \mathbf{e} = -\sin \theta_{hkl} \quad (\text{III.24})$$

with $\mathbf{e} = \mathbf{g} / \|\mathbf{g}\|$. Using the expression of Ω_ω given in Equation III.3, the condition can be further simplified to:

$$a_1 \sin \omega + a_2 \cos \omega + a_3 = 0 \quad (\text{III.25})$$

where the coefficients a_1 , a_2 and a_3 depend on the wedge angle and the crystal parameters. This equation is a well-known trigonometric form, which admits 0, 1 or 2 analytical solutions in $[0, 360^\circ[$ depending on the coefficient values. Hence, a given reciprocal lattice point (h, k, l) may produce 0, 1 or 2 reflections during a complete rotation.

b) Optimization problem

Equation III.25 allows to predict spot ω -coordinates, based on the global and grain parameters. It can also be used for the inverse procedure, that is the determination of the parameters, based on the experimental ω -coordinates. Although the method can be generalized to any crystal structure, we will restrict here to cubic crystals. These are described by one lattice parameter, a , leading to $\mathbf{B} = \frac{1}{a} \mathbf{I}$. Therefore, for a given spot, we can write the residual of Equation III.24, denoted by Φ , as:

$$\Phi = \left[\Omega_\omega \mathbf{U}^{-1} \begin{pmatrix} h \\ k \\ l \end{pmatrix} \right] \cdot \mathbf{e}_1 + \frac{\lambda}{a} \frac{h^2 + k^2 + l^2}{2} \quad (\text{III.26})$$

where the rotation matrix Ω_ω depends on the measured ω -coordinate. Thus defined, Φ must be equal to zero for any measured spot, when evaluated from the correct values of the parameters. Hence, for a single crystal, we can formulate an optimization problem as:

$$\underset{\mathbf{R}, w, a}{\text{minimize}} \quad \mathcal{F}_2(\mathbf{R}, w, a) = \sum_i \Phi_i^2 \quad (\text{III.27})$$

$$\text{subjected to} \quad a > 0$$

The summation runs over the spots i of the crystal. In practice, a first estimate of the orientation is provided by the indexing. The wedge angle is initially set to zero and the lattice parameter to a theoretical value.

c) Numerical simulations

We carried out numerical simulations to assess the influence of the number of available spots, N_s , and the size of the integration step, $\delta\omega$, on the parameter errors and accuracy. The choice of $\delta\omega$ in particular, limits the accuracy on the measured ω -coordinates.

We have considered 100 Al grains with random orientations. For each grain, a wedge angle was randomly chosen in the $[-0.5^\circ, 0.5^\circ]$ interval and Equation III.25 was solved for the ω -coordinates of 400 diffraction spots. Then, the influence of N_s was investigated by forming groups of 50, 100, 200 and 400 spots, while the influence of $\delta\omega$ was simulated by rounding the ω values to different decimal digits (from 0.001° to 1°). For each combination of N_s and $\delta\omega$ conditions, the calibration was applied to each individual grain.

The results are shown in Figure III.8. The “accuracy” refers to the absolute difference between the fitted and true values of the parameters. The “standard error” is an outcome of the optimization. For readability, the orientation accuracy is shown in terms of the disorientation angle with respect to the true orientation. The errors of the Rodrigues vector components were converted to a mean angular error (see Subsection III.3.3). For all the parameters, we observe a good agreement between the two quantities. Although the accuracy is not available experimentally, the simulations show that the standard errors provide good estimates of the actual errors.

Besides, we observe a linear relationship between the integration step and the accuracy, over three orders of magnitude. Evidently, decreasing the integration step and increasing the number of spots result in a gain in accuracy. The wedge angle error appears to be one to two orders of magnitude smaller than the chosen $\delta\omega$. The gain for the orientation, albeit slightly lower, is of the same order. In addition to simulations, the procedure was tested in Ref. [86] on experimental data concerning two single crystals of aluminium and tungsten. We can see from their standard errors, marked by black stars and squares, that the results are consistent with the expectations.

d) Results: monitoring the wavelength

The method can also be exploited to assess the beam wavelength. According to Equation III.26, λ and a solely intervene in the ratio λ/a . They cannot, therefore, be refined simultaneously. However, knowing λ , we can determine a , and vice versa. This principle was applied to monitor the wavelength throughout the *in situ* measurements of Sample B [82].

In practice, a Si wafer is inserted in the beam, between two successive 3DXRD scans, and measured in extinction diffraction, using two photodiodes. The data must be first corrected for the sample absorption, before extracting the extinction peak ω -coordinates. As the crystal orientation and structure are known from manufacturing, the extinction peaks can readily be indexed and used to solve Equation III.27, with λ as a parameter. The resulting standard errors are provided in Figure III.8. The relative standard error of λ is shown in Figure III.8-c. The results are in reasonable agreement with the simulations. The actual uncertainty on the wavelength is however limited by the relative uncertainty on the input cell parameter, which is 10^{-5} , higher than the error of 10^{-6} given by the fit.

As mentioned in Chapter II, a number of Si-wafer scans were acquired before and after each 3DXRD scans of Sample B. This enabled us to monitor the beam wavelength throughout the experiment. The results, presented in Figure III.9, reveal significant relative changes of the wavelength, of the order of 1×10^{-4} . The red squares indicate the successive values that were retained thereafter to analyse each 3DXRD scan.

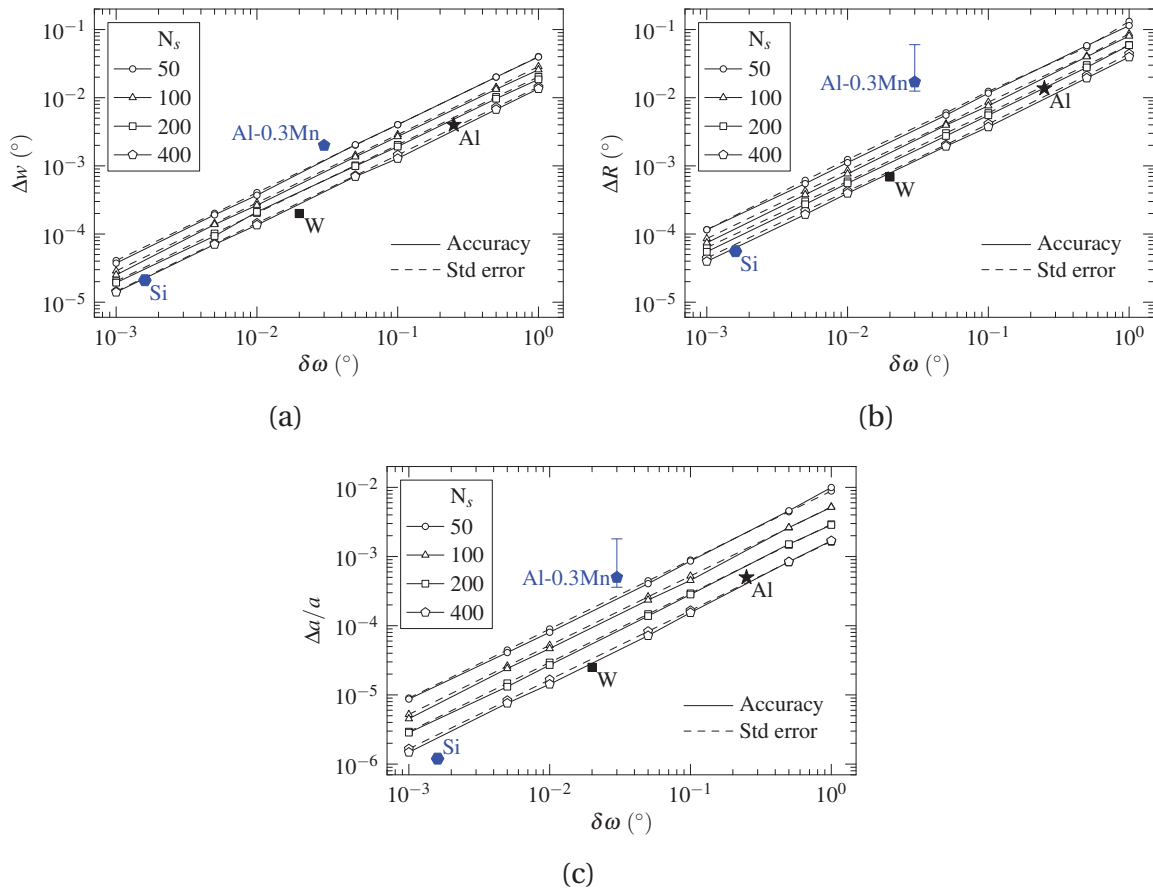


Figure III.8 – Numerical simulations of the fit errors and accuracies, resulting from the minimization of \mathcal{F}_2 , as a function of the integration step $\delta\omega$: (a) wedge angle, (b) orientation and (c) lattice parameter. ΔR is an equivalent angular error, calculated from the errors of the Rodrigues vector components [91]. Experimental results from Ref. [86] related to an Al single crystal (179 peaks) and a W single crystal (237 peaks), marked in black. Experimental results for the Si wafer (484 peaks) and Sample B (20 to 145 peaks, with an average at 100 peaks), shown in blue. The errorbars in (b) and (c) indicate the minimum and maximum standard errors for the grains of Sample B.

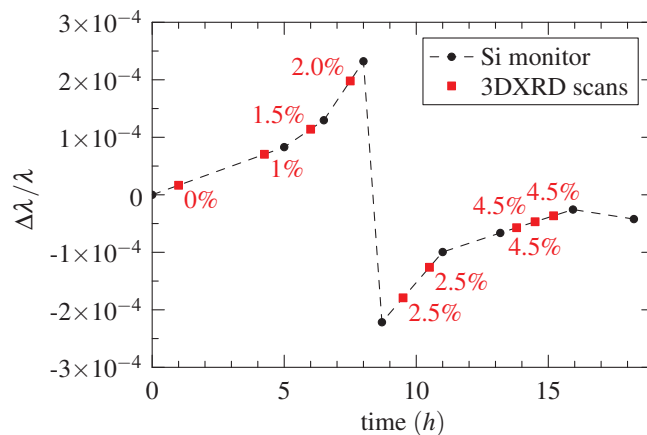


Figure III.9 – Variations of the wavelength during the 3DXRD measurements of Sample B. The continuous drift is attributed to temperature changes in the monochromator, resulting from the opening of the undulator gap before the experiment.

III.2.3 Complete geometry

In the previous sections, the detector and the rotation axis were treated separately to achieve independent and accurate determinations of their respective tilts. We have also proposed a method to assess the wavelength, which leaves three global parameters as unknowns: D , u_B , and v . The last calibration step consists in unifying the detector and the rotation axis in the laboratory system.

a) Basic diffractometer equation

We consider a diffraction spot of coordinates (u, v, ω) , which is associated to a given grain as an (hkl) reflection. The corresponding reciprocal space vector is $\mathbf{g} = (h, k, l)^T$. The spot position in K_D is obtained from (u, v, ω) through Equation III.8 and referred to as \mathbf{s}_D . From the projection equations, we can write, on one hand, using \mathbf{s}_D :

$$\mathbf{T}^{-1} \mathbf{s}_D = \frac{D n_1 - \Omega_\omega \mathbf{r}_0 \cdot \mathbf{n}_L}{\mathbf{e}_k \cdot \mathbf{n}_L} \mathbf{e}_k + \Omega_\omega \mathbf{r}_0 - D \mathbf{e}_1 \quad (\text{III.28})$$

and, on the other hand, using \mathbf{g} :

$$\mathbf{e}_k = \mathbf{e}_1 + \lambda \Omega_\omega \mathbf{U}^{-1} \mathbf{B} \mathbf{g} \quad (\text{III.29})$$

Combining the two equations and rearranging, we obtain the basic diffractometer equation:

$$\begin{aligned} \Psi = & (\mathbf{T}^{-1} \mathbf{s}_D - \Omega_\omega \mathbf{r}_0 + D \mathbf{e}_1) [(\mathbf{e}_1 + \lambda \Omega_\omega \mathbf{U}^{-1} \mathbf{B} \mathbf{g}) \cdot \mathbf{n}_L] \\ & + (\mathbf{e}_1 + \lambda \Omega_\omega \mathbf{U}^{-1} \mathbf{B} \mathbf{g}) [\Omega_\omega \mathbf{r}_0 \cdot \mathbf{n}_L - D n_1] = 0 \end{aligned} \quad (\text{III.30})$$

Thus defined, Ψ is a vectorial quantity that depends on the nine global parameters and the twelve grain parameters. It is equal to zero for any indexed spot, by definition, provided that the parameter values are correct.

b) Optimization problem

Using Equation III.30, we can readily derive an objective function and formulate the optimization problem, for a single crystal, as:

$$\begin{aligned} & \text{minimize} && \mathcal{F}_3 = \sum_i \|\Psi_i\|^2 \\ & \text{over} && \begin{cases} n_1, n_2, n_3, D, u_B, v_B, v, w, \lambda \\ x_0, y_0, z_0, R_1, R_2, R_3, a, b, c, \alpha, \beta, \gamma \end{cases} \\ & \text{subjected to} && \begin{cases} \|\mathbf{n}\| = 1 \\ n_1, D, \lambda, a, b, c, \alpha, \beta, \gamma > 0 \end{cases} \end{aligned} \quad (\text{III.31})$$

The summation in \mathcal{F}_3 runs over the indexed spots i of the crystal.

The function \mathcal{F}_3 is comparable to that used by Oddershede *et al.* [54]. This general, 21 parameter fit is in practice not fully reliable. Indeed, due to strong correlations among the parameters, the uniqueness of the solution is not ensured and the parameter standard errors may become large. The main difficulty lies in the quasi-linear relationship at high energies between D , λ and a , which cannot therefore be refined simultaneously. This emphasizes the need for preliminary, independent calibration procedures.

Here, from the previous two calibration steps and assuming a cubic crystal, we can fix six global parameters ($n_1, n_2, n_3, v_B, w, \lambda$) and nine grain parameters ($R_1, R_2, R_3, a, b, c, \alpha, \beta, \gamma$). We obtain a reduced set of six optimization parameters, consisting of: D, u_B, v, x_0, y_0 and z_0 . The first two were already estimated from powder diffraction, while the last four can reasonably start at zero.

To express the setup accuracy, we suggest to employ the finite Lagrangian strain tensor in the same line as Oddershede *et al.* [54]. Indeed, for an undeformed single crystal, the lattice strains should vanish on average and allow to characterize the diffractometer residual errors. We note however that the strain, as a symmetric tensor, does not fully describe the misalignments. This would be the case of a deformation gradient, which can be decomposed into a symmetric part (stretch) and a skew-symmetric part (rotation), as proposed by Edmiston *et al.* [92]. Here, the skew-symmetric part is contained in the errors of the crystal orientation.

The methodology was applied in Ref. [86] on experimental data concerning an Al single crystal (ID-11, ESRF) and a W single crystal (1-ID, APS). In both cases, it proved capable of properly assessing the diffractometer misalignments and reducing the strain errors below the 10^{-4} limit.

III.2.4 Results

The initial, undeformed state of Sample B was scanned over 360° by integration steps of 0.03° . The indexing is discussed in Section IV.2 and resulted in 824 individual grains, which were used to calibrate the 3DXRD diffractometer.

a) Polycrystal-based calibration

The calibration procedure is initially designed to use a perfect single crystal. It can, however, be readily adapted to an undeformed polycrystal. To do so, we have to extend the “*single-grain fits*”, defined by Equations III.27 and III.31, to “*multiple-grain fits*” for an arbitrary number of grains, N_g . The related objective functions, \mathcal{F}_2^P and \mathcal{F}_3^P , are:

$$\mathcal{F}_2^P = \sum_{i,j} \Phi_{i,j}^2 \quad (\text{III.32})$$

and,

$$\mathcal{F}_3^P = \sum_{i,j} \|\Psi_{i,j}\|^2 \quad (\text{III.33})$$

where the summations runs over the spots j of the grains i . As the global parameters are common to all the grains, these functions depend on $1 + N_g \times 4$ and $9 + N_g \times 12$ parameters, respectively. Applied on a large number of grains, we can expect the *multi-grain fits* to provide better estimates of the global parameters than the *single-grain fits*.

b) Detector and wavelength

As discussed in Subsection III.2.1, the spatial distortions of the FReLoN-4M detector were characterized through independent optical measurements with a calibration grid. After correction of the images, the detector tilt and residual distortions were assessed using a reference powder sample of CeO_2 . A good repeatability was observed for n_1, n_2, n_3 and v_B . The relative radial distortions were confined within $\pm 5 \times 10^{-5}$.

The beam wavelength, discussed in Subsection III.2.2, was obtained through independent measurements on a Si wafer, with a relative precision better than 10^{-5} .

c) Rotation axis

To determine the wedge angle, we performed the *multi-grain* fit of the rotation axis using the 100 most complete grains (more than 130 indexed reflections, i.e. completeness higher than 90%). The number of spots, thus considered, was 13,556. The refined value of the wedge angle was then used in the *single-grain* fits of the 824 individual grains, by allowing only the crystal orientation and the lattice parameter to vary.

The resulting standard errors are represented on Figure III.8. For w , it is higher than that expected with $\delta\omega = 0.03^\circ$ and $N_s = 13\,556$, by at least one order of magnitude. For the orientation and the lattice parameter, the errors are scattered due to the difference in the number of available spots from one grain to another (20 to 145 spots). As for the wedge angle, the standard is about one order of magnitude higher than expected.

The refined value of the wedge angle is given in Table III.3. The standard error is lower than 0.01° and corresponds to less than 10% of the angle magnitude. As this is acceptable and could not be improved by any means, it was retained for the further analyses. The individual grain orientations and lattice parameters, on the contrary, were not. The lattice parameters, in particular, exhibit relative standard errors higher than 10^{-4} , which prohibits using them as reference lattice parameters. These results suggest a significant scattering of the spot ω -coordinates with respect to ideal values, which must be related to a poorer crystal perfection than in the single crystal examples.

d) Complete geometry

To cope with the lack of reference lattice parameter, we performed laboratory X-ray diffraction measurements on a Al-0.3Mn powder sample. This provided a stress-free lattice parameter, $a_{\text{pow}} = 4.04830(10) \text{ \AA}$, which should be close to the average lattice parameter in an undeformed and unloaded polycrystal. Then, the optimization procedure was carried out as follows:

1. Fix n_1, n_2, n_3, v_B, w and λ
2. Set initially all the grain lattice parameters to a_{pow}
3. Run the *multi-grain* fit using the 100 most complete grains (varying D, u_B, v and, for each grain, $x_0, y_0, z_0, R_1, R_2, R_3$)
4. Run the *single-grain* fit on the 824 individual grains (varying only $x_0, y_0, z_0, R_1, R_2, R_3$ and a)
5. Repeat (3) and (4) until convergence of D .

The resulting parameters are presented in Table III.3. The iterative procedure enabled to reduce the standard error on D to $1 \mu\text{m}$, as well as to obtain a sub-pixel error on u_B . Both parameter values are different from those estimated with the detector tilt (using \mathcal{F}_1^P) and varied by $100 \mu\text{m}$ and 8 pixels, respectively. Regarding the twist angle v , the refined value exceeds three times the integration step and is therefore significant. Its standard error is about 0.3% in relative and is by one order of magnitude smaller than the wedge angle error. This better precision can be explained by the fact that v has the same effect on all the diffraction spots.

e) Pre-validation

The distribution of individual lattice parameters, shown in Figure III.10-a, has a mean value of 4.04820 \AA and a standard deviation of $8 \times 10^{-5} \text{ \AA}$. This is consistent with the initially assumed value of $a_{\text{pow}} = 4.04830(10) \text{ \AA}$. The distribution of relative standard errors, shown in Figure III.10-b, has a mean value of 2.5×10^{-5} (10^{-4} \AA). As the mean error is comparable to the width of the lattice parameter distribution, the latter must be partly attributed to the noise in the data. However, the distribution can not be properly described by a gaussian, which suggests that a physical phenomenon might also be involved. Indeed, these grain-to-grain variations of the lattice parameter could be explained by variations of the Mn content. In this case, the distribution lower and upper bounds would correspond to about 0.45wt% and 0.27wt% of Mn [93], respectively, which is not unrealistic.

Lastly, to validate the calibration, we must examine the results of the evaluation in terms of grain centroids, orientations and, in particular, residual lattice strains. This will be detailed in the next section.

Table III.3 – Calibration parameters: values of the global parameters after each calibration step. The numbers in parenthesis indicate the standard errors in the unit of the last decimal.

par.	Initial	\mathcal{F}_1 (CeO ₂)	\mathcal{F}_2 (Si)	\mathcal{F}_2^P (Sample B)	\mathcal{F}_3^P (Sample B)	Final
n_1	1	0.9999494 (6)	–	–	–	0.9999494 (6)
n_2	0	–0.0009946 (50)	–	–	–	–0.0009946 (50)
n_3	0	0.001457 (100)	–	–	–	0.001457 (100)
v_B (pixel)	1024	995.930 (30)	–	–	–	995.930 (30)
u_B (pixel)	1024	1003.577 (4)	–	–	995.857 (5)	995.857 (5)
D (m)	0.260000	0.258263 (10)	–	–	0.258179 (1)	0.258179 (1)
λ (Å)	0.206640	–	0.207189 (1)	–	–	0.207189 (1)
w (°)	0	–	–	0.0313 (20)	–	0.0313 (20)
v (°)	0	–	–	–	–0.1051 (3)	–0.1051 (3)

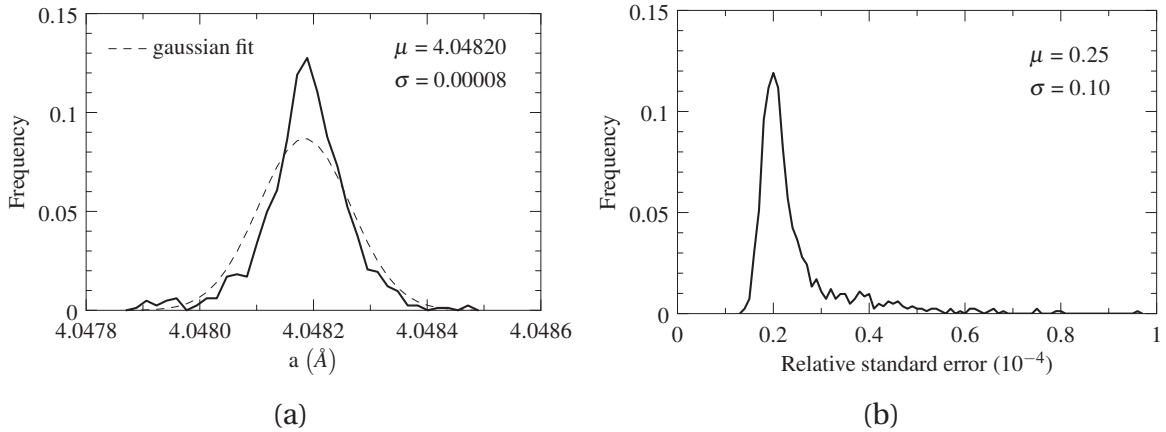


Figure III.10 – Distribution of grain lattice parameters in the initial state of Sample B: (a) lattice parameter values and (b) relative standard errors, for 824 individual grains.

III.3 Calibration validation

We have proposed in Sections III.1 and III.2 a general description and the related calibration procedure of the 3DXRD diffractometer. The reader may have noticed that the determination of grain properties is intricately linked to the calibration. In fact, part of the work has already been done by deriving the basic diffractometer equation and the related optimization problem of Equation III.31. The evaluation of lattice strains and stresses remains to be addressed, before validating the geometry calibration of Sample B.

III.3.1 Grain average quantities

a) Position, orientation and lattice parameters

Grain position, orientation and lattice parameters result from the resolution of Equation III.31. This is done grain by grain, by applying the *single-grain* fit and setting the global parameters to their calibrated values.

b) Lattice strains and stresses

We use as definition of elastic strain the finite Lagrangian strain tensor. For simplicity, it will be referred to as $\underline{\boldsymbol{\varepsilon}}^e$ (the superscript e stands for “elastic”). It is expressed in a crystallographic approach as the change of the metric tensor from a reference to a current state [63, 94]. This can be written in the crystal coordinate system, as:

$$\underline{\boldsymbol{\varepsilon}}^e = \frac{1}{2} \mathbf{B}_0 (\underline{\mathbf{G}} - \underline{\mathbf{G}}_0) \mathbf{B}_0^T \quad (\text{III.34})$$

where \mathbf{B}_0 is the orthogonalization matrix of the reference, undeformed lattice, $\underline{\mathbf{G}}_0$ is the metric tensor of the reference lattice and $\underline{\mathbf{G}}$ the metric tensor of the current, deformed lattice.

In practice, the undeformed state is described by the grain lattice parameter(s). For a cubic crystal of parameter a_0 , we simply have:

$$\mathbf{B}_0 = \frac{1}{a_0} \mathbf{I} \quad \text{and} \quad \underline{\mathbf{G}}_0 = a_0^2 \mathbf{I} \quad (\text{III.35})$$

Then, for the deformed state, we first determine the components of the contra-variant metric tensor, $\underline{\mathbf{G}}^*$, which is the inverse of $\underline{\mathbf{G}}$. This is done using:

$$\begin{pmatrix} h \\ k \\ l \end{pmatrix}^T \underline{\mathbf{G}}^* \begin{pmatrix} h \\ k \\ l \end{pmatrix} = \|\mathbf{g}\|^2 \quad (\text{III.36})$$

which relates the reciprocal lattice point (h, k, l) to the magnitude of the diffraction vector \mathbf{g} . The latter is given by Equation III.18 as $\mathbf{g} = (\mathbf{e}_k - \mathbf{e}_1)/\lambda$. Equation III.36 is defined for a single reflection. Using all the experimental spots of a grain, we obtain a system of N_s linear equations (number of spots) and six unknowns (symmetric tensor $\underline{\mathbf{G}}^*$). The system is usually overdetermined, which allows for least-squares estimates of $\underline{\mathbf{G}}^*$ components.

Finally, the strains can be converted to stresses using the elastic stiffness tensor:

$$\underline{\boldsymbol{\sigma}} = \underline{\mathbf{C}} : \underline{\boldsymbol{\varepsilon}}^e \quad (\text{III.37})$$

and both quantities can be transformed to the sample coordinate system using the crystal orientation matrix \mathbf{U} .

c) Volume and size

The grain volume, V_g , can be evaluated from the diffraction spot intensities. To do so, we assume that the total intensity diffracted by a grain, I_g , is proportional to its volume. This can also be expressed as the grain-to-sample volume ratio being equal to the grain-to-sample intensity ratio. We thus have:

$$V_g = \frac{I_g}{I_s} V_s \quad (\text{III.38})$$

I_s and V_s refer to the diffracted intensity and the volume of the illuminated region. Then, we define the equivalent grain size as the diameter of the sphere of volume V_g . In practice, I_s is calculated by summing the total intensities of all the diffraction spots, while I_g is restricted to the indexed spots of the grain. V_s can be roughly estimated from the sample dimensions or, more reliably, from tomographic measurements (e.g., DCT).

To be properly applicable, Equation III.38 requires to correct the spot intensities for a number of factors, related to the diffraction conditions and the incident beam. In this work, we have accounted for the structure and Lorentz factors, which affect the spot intensity as a function of the diffraction angles, 2θ and η . Other factors, such as the absorption phenomenon inside the sample or the incident beam inhomogeneities, are not readily accessible and were therefore neglected.

III.3.2 Influence of the experimental uncertainties

Numerical simulations were used to evaluate the effects of experimental uncertainties on the grain quantities. A set of 125 randomly orientation Al grains were arranged on a $1 \times 1 \times 1 \text{ mm}^3$ cubic grid, centred on the laboratory origin ($5 \times 5 \times 5$ grains). Each grain was assigned a set of 100 simulated peaks based on a *correct* geometrical setup, which was described by the global parameters evaluated for Sample B.

a) Influence of global parameters

The global parameters were treated separately, with the exception of n_1 , n_2 and n_3 , which were treated together. Considering for instance D, each simulation consisted in adding a random error to the value of D and comparing the resulting grain properties with the *correct* ones. This was repeated 100 times on each parameter for a total number of 700 simulations. For the parameter errors, we assumed normal distributions with a zero means and standard deviations equal to the experimental standard errors (see Table III.3). For the comparison between *erroneous* and *correct* grain properties, we examined the distances between grain centroids, Δr_0 , referred to as “position error”, and the disorientation angles between grain orientations, ΔR , referred to as “orientation error”. The lattice strains induced by the error of varied parameters were considered as residual strains.

The simulation results did not reveal any significant effects on grain positions with regard to the uncertainty levels involved. For the orientations, however, we identified three main correlations with the detector tilt n , the beam centre coordinate u_B and the wedge angle w .

In Figure III.11-a-b, the orientation errors are reported as a function of the error of n_1 and the angular error of n . We observe that the disorientation angles are mostly smaller than 0.01° . It is however remarkable that worst-case scenarios lead to orientation errors of about 0.01° . By extrapolating for $|\Delta n_1| = 10^{-5}$, we could expect errors of about 0.1° . This

emphasizes the need for a careful calibration of the detector tilt, which can be achieved at the best using a powder calibrant.

Figure III.11-c illustrates the influence of u_B . The errors, albeit being smaller than 0.01° , demonstrate the importance of a sub-pixel calibration of the beam-centre. Indeed, the beam centre is involved in the calculation of the diffraction vectors and directly influence their directions. The same statement can be drawn from Figure III.11-d, which highlights the strong influence of w . We clearly observe that a given variation of w can induce an identical angular error on grain orientations.

Lastly, regarding the lattice strains, we found that the normal components are linearly related to the variations of D and λ . This is illustrated on Figure III.12 for ε_{zz}^e . These results demonstrate that both parameters are critical, as their errors directly limit the strain resolution.

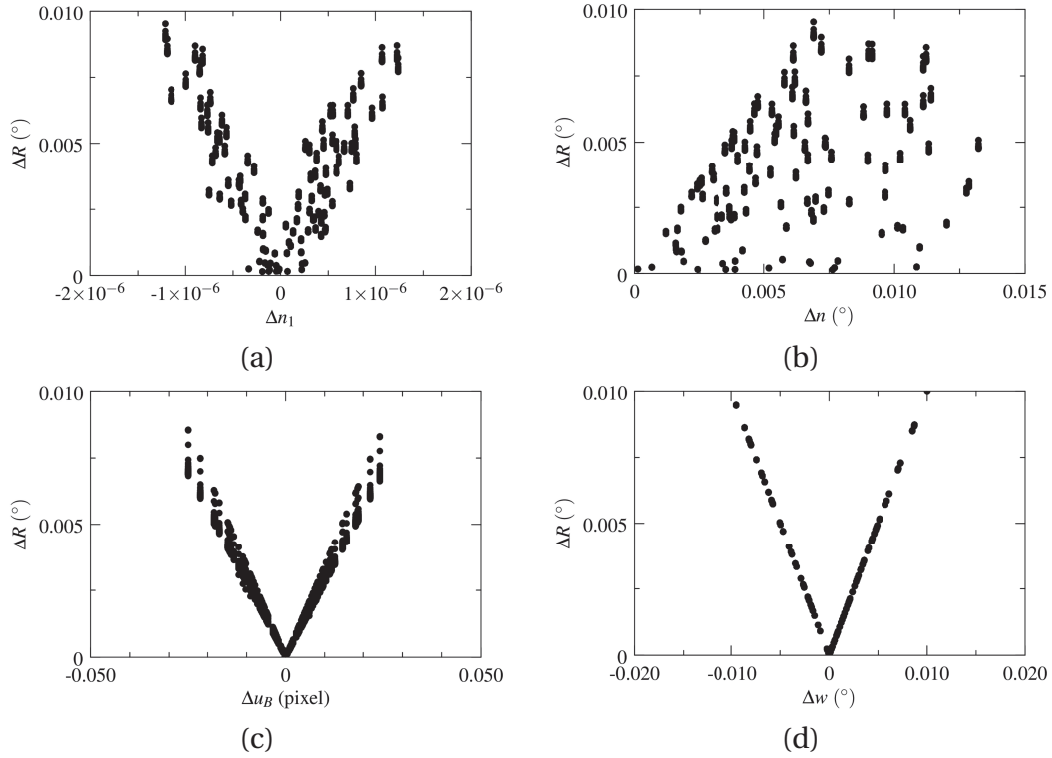


Figure III.11 – Effect of calibration errors on orientation accuracy: (a) principal detector-tilt component n_1 , (b) angular error of \mathbf{n} , (c) horizontal beam-centre coordinate u_B and (d) wedge angle.

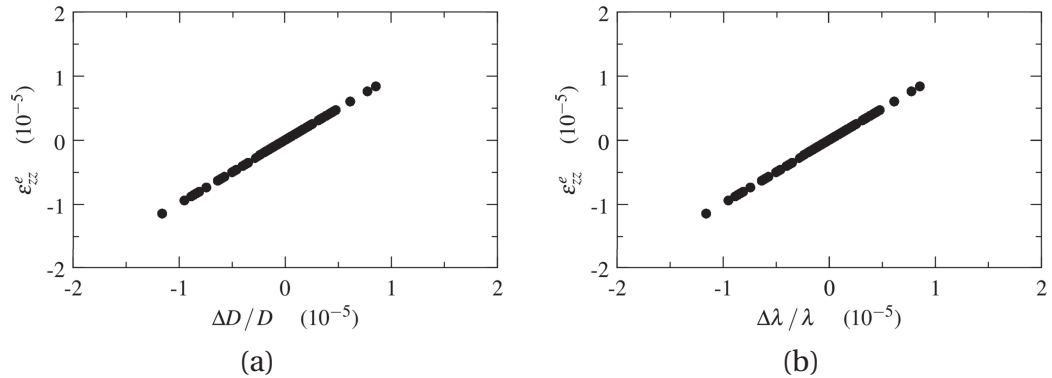


Figure III.12 – Residual lattice strains due to calibration errors. Influence of (a) the detector distance D and (b) the wavelength λ .

b) Influence of peak coordinates

The influence of spot position errors was also investigated, in the same way as for the global parameter errors. This time, for each simulation (100 in all), we kept the global parameters fixed and added random errors to the peak coordinates (u and v components only). Again, we assumed that the errors were normally distributed and with zero mean. For the standard deviation, referred to as σ_{uv} , we considered a variation over three orders of magnitude: 0.01, 0.1 and 1 pixel.

The results are reported in Figure III.13. We can observe that accuracies vary proportionally to σ_{uv} . This can be easily understood for the grain positions, where the average error is about $2 \times \sigma_{uv} \times N_s^{-1/2}$. The number of spots, N_s , is here equal to 100. For the orientations, the average error evolves roughly as $\sigma_{uv} \times \pi_{\theta\eta}$, where $\pi_{\theta\eta}$ is equal to 0.03° and refers to the mean angular extent² of the detector pixels. Surprisingly, contrarily to grain positions, the mitigation effect of N_s does not appear and might be compensated by another factor. Lastly, the spread of the residual strains increases linearly with σ_{uv} , as shown in Figure III.13-c with the distribution full widths at half maximum (FWHM). Indeed, the lattices strain are evaluated from the magnitude of the diffraction vectors, which vary with the peak radial errors. We can observe that the FWHM is already of about 1×10^{-4} for both normal and shear components at $\sigma_{uv} = 0.2$ pixel.

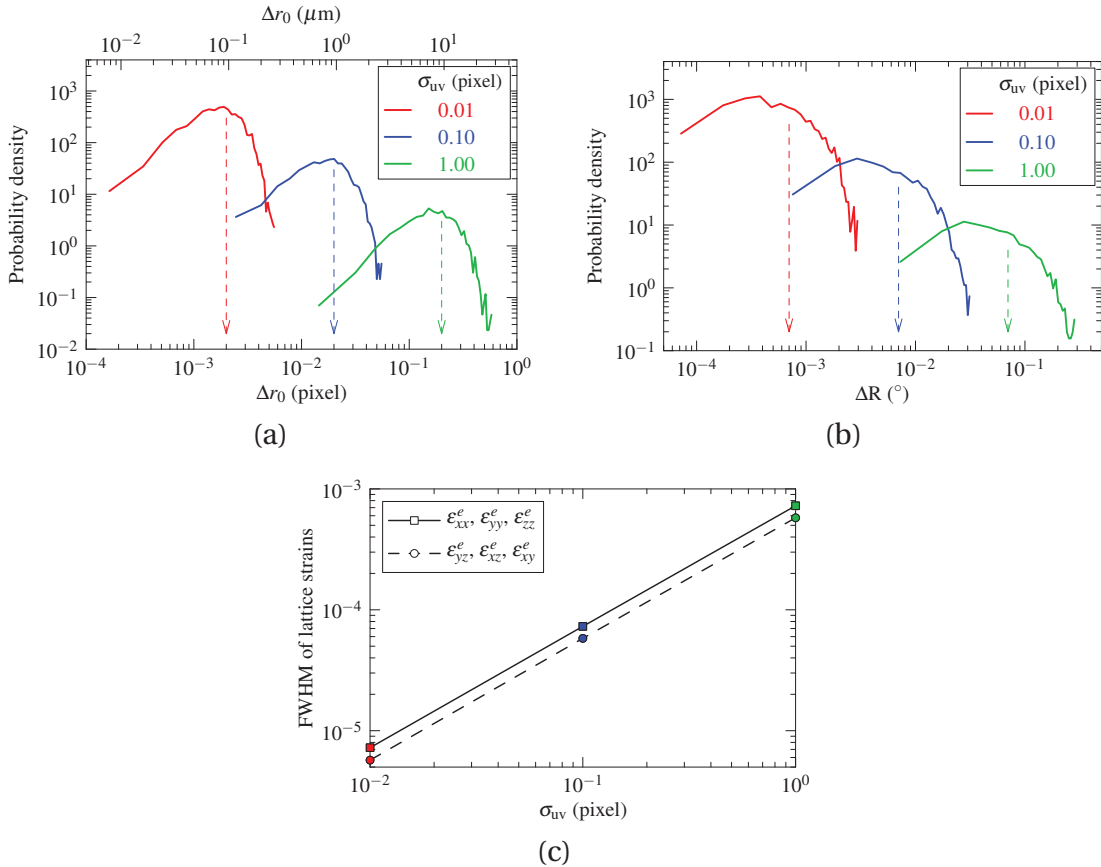


Figure III.13 – Effect of peak-coordinate errors on the accuracy of grain quantities: (a) position error (distance from the true position) and (b) orientation error (disorientation angle from the true orientation) and (c) lattice strains (full width at half maximum). σ_{uv} refers to the standard deviation of the peak-coordinate error distribution. The arrows in (a) and (b) indicate the mean values.

²Geometrical average between the mean radial extent (0.01°) and the mean azimuthal extent (0.1°).

c) Cumulated influence

Finally, the cumulated effects of the calibration and peak-coordinate errors were investigated, using the same 125 Al grains and geometry as previously. For each simulation (100 in all), the global parameters and peak-coordinates ($\sigma_{uv} = 0.1$ pixel) were varied simultaneously and the resulting grain properties were compared to the *correct* ones.

The results are reported in Figure III.14. The mean position and orientation errors are, respectively, 1 μm and 0.01° . The comparison with Figure III.13 reveals that the calibration errors do not significantly contribute to the position errors and are responsible only for about 20% of the orientation errors. The peak-coordinate errors are thus predominant with regard to the simulation assumptions. The same statement is valid for the residual lattice strains. The widths of the distributions are comparable to those reported in Figure III.13-c.

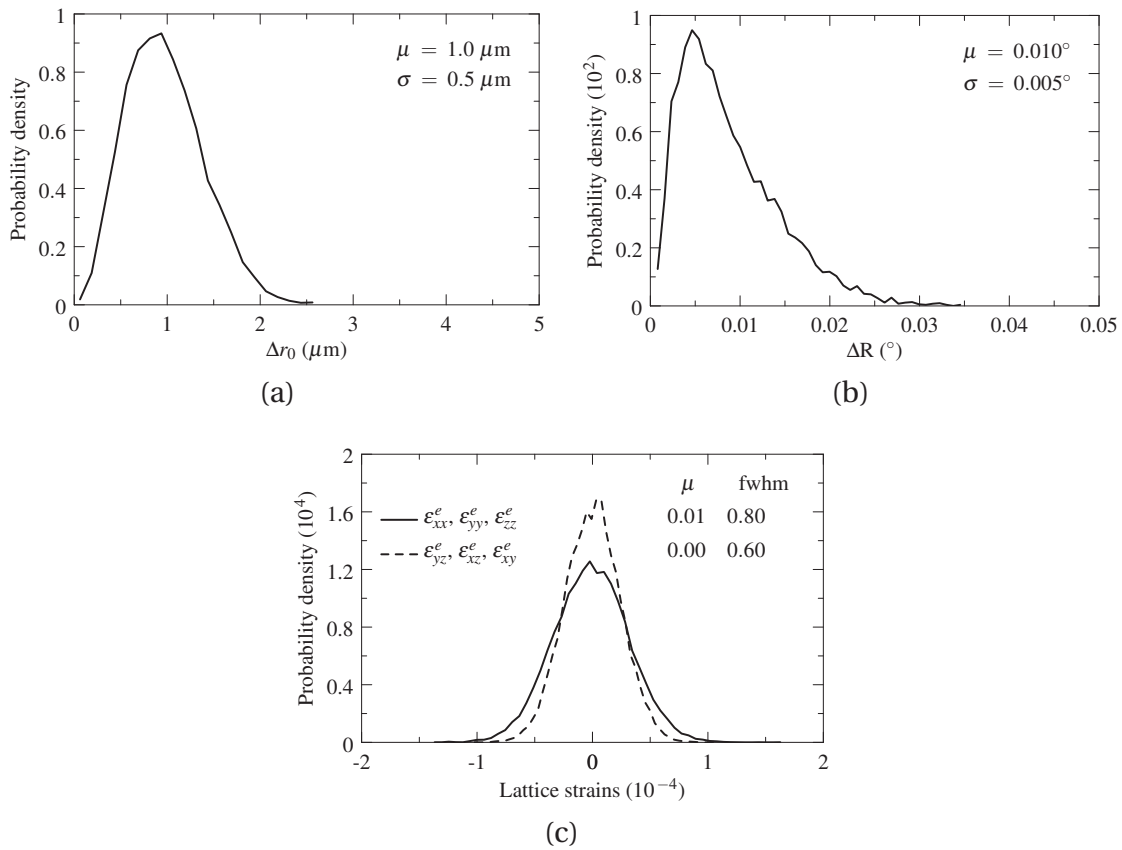


Figure III.14 – Cumulative effect of calibration and peak-coordinate errors on the accuracy of grain quantities. Distributions of (a) position errors (distance), (b) orientation errors (disorientation angle) and (c) residual strains. The distribution means (μ), standard deviations (σ) or FWHMs are provided.

III.3.3 Experimental results and validation

We started discussing the characterization of Sample B in Subsection III.2.4, in conjunction with the geometry calibration. In this section, we present the result for the grain centroids, orientations, sizes and lattices strains. This allows us to finally validate the calibration results.

a) Position, orientation and volume

The microstructure of Sample B is represented in Figure III.15 using equivalent spheres coloured by grain orientations. With large sub-structured grains, it looks typical of the structure of the Al-0.3Mn alloy, as shown in Subsection II.2.1. The volume height is almost 600 μm and is consistent with the nominal beam height of 550 μm . The volume thickness is about 800 μm , which is smaller than the initial gage dimensions and must be attributed to the polishing step after manufacturing.

The standard errors of the grain position and orientation components are shown in Figure III.16. Regarding the positions, the distributions of σ_{x_0} , σ_{y_0} and σ_{z_0} exhibit means of about 1 μm . We can see that the errors are generally smaller for σ_{z_0} . This is consistent with the fact that the grains rotate in a nearly horizontal plane. Regarding the orientations, the distributions of σ_{R_1} and σ_{R_2} have comparable means of about 0.005°. We can observe though, for σ_{R_3} , that the errors are five times as large. The analysis of the covariance matrix revealed strong correlations between u_B and R_3 , with coefficients ten times higher than between u_B and R_1 or R_2 . Although the reason remains unclear, this correlation reasonably explains the differences observed in the errors.

To provide more global measures of the precision, we assume normal distributions around zero for the individual component errors. Hence, the mean standard errors, $\langle\sigma_{r_0}\rangle$ and $\langle\sigma_R\rangle$, are well approximated by:

$$\langle\sigma_{r_0}\rangle \simeq \sqrt{\frac{8}{\pi}} \left(\frac{\sigma_{x_0} + \sigma_{y_0} + \sigma_{z_0}}{3} \right) \quad (\text{III.39})$$

$$\langle\sigma_R\rangle \simeq 2 \sqrt{\frac{8}{\pi}} \left(\frac{\sigma_{R_1} + \sigma_{R_2} + \sigma_{R_3}}{3} \right) \quad (\text{III.40})$$

Both quantities are provided in Figure III.16. The distributions are characterized by mean values of 1.5 μm and 0.018°, with tails extending up to about 5 μm and 0.06°, respectively. Most grains exhibit errors smaller than 3 μm and 0.03°.

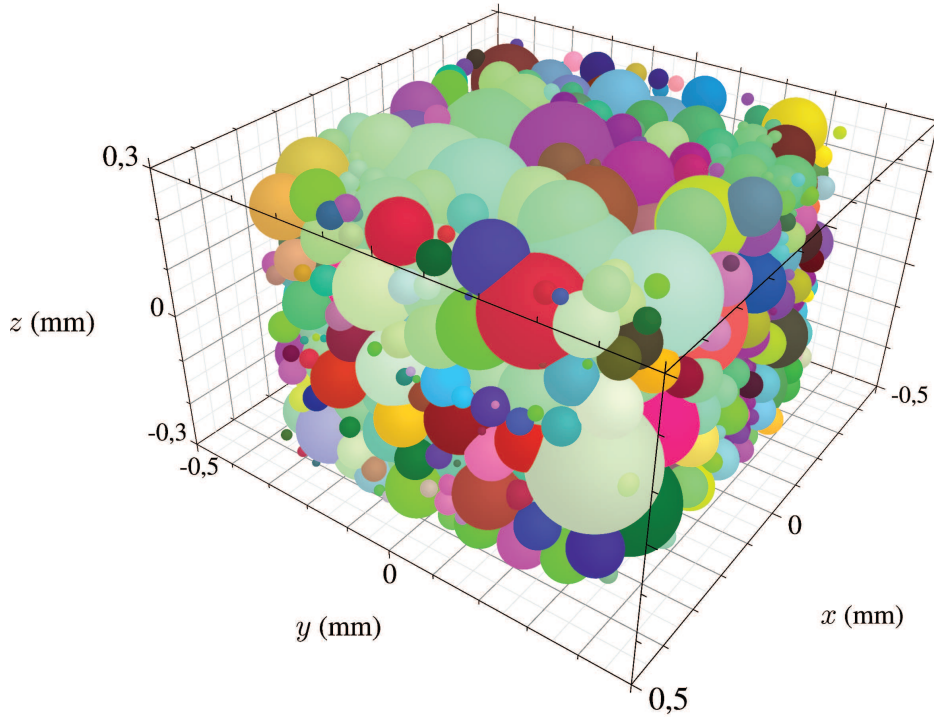


Figure III.15 – Initial microstructure of Sample B given by 3DXRD. The 824 grains are represented by equivalent spheres coloured by grain orientations. The RGB colour code is given by the Rodrigues vector components as $c_i = (R_i + \sqrt{2} - 1) / (2 \times (\sqrt{2} - 1))$, $i \in 1, 2, 3$.

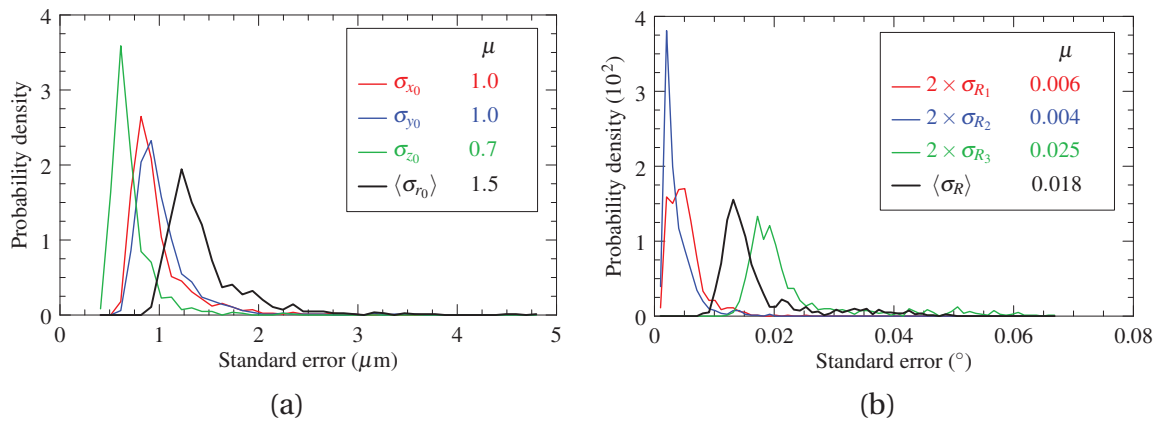


Figure III.16 – Standard errors for grain positions and orientations. Distributions of standard errors for grain (a) position and (b) orientation components. See the text for definitions.

b) Residual lattice strains and stresses

The lattice strains were evaluated using as reference lattice a non-distorted cube with a cell parameter equal to the average of the experimental distribution (Figure III.10). The results are expressed in the laboratory coordinate system and reveal residual strains confined within $\pm 10^{-4}$, as illustrated on Figure III.17. The distributions exhibit zero means and FWHM of about 1×10^{-4} and 0.6×10^{-4} for the normal and shear components, respectively.

The stresses were evaluated using the elastic constants of Ref. [18] and expressed in the laboratory coordinate system. The results reveal residual stresses mostly within ± 10 MPa, as illustrated on Figure III.18. The distributions exhibit FWHM of about 8 MPa and 4 MPa for the normal and shear components, respectively.

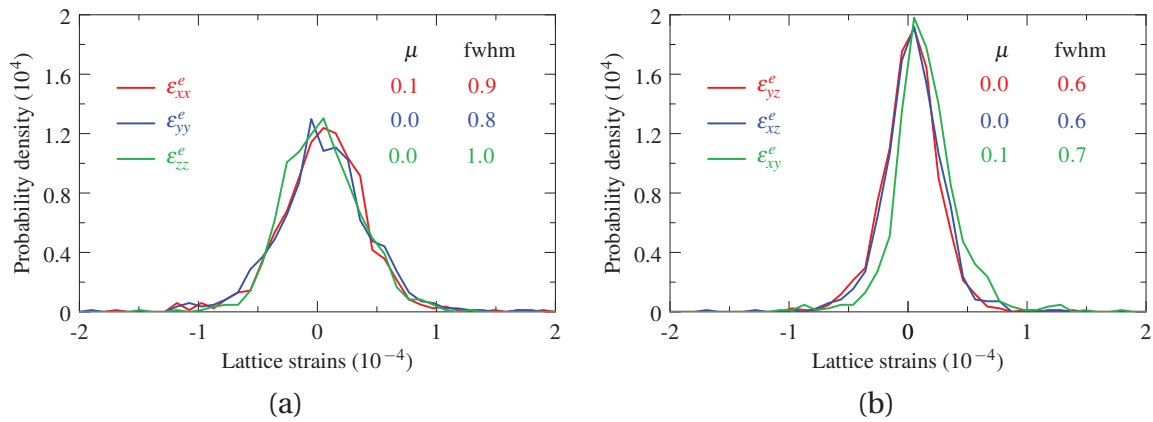


Figure III.17 – Residual lattice strains in Sample B. Distributions of (a) the normal components and (b) the shear components, expressed in the laboratory coordinate system. The mean and full-width-at-half-maximum are provided.

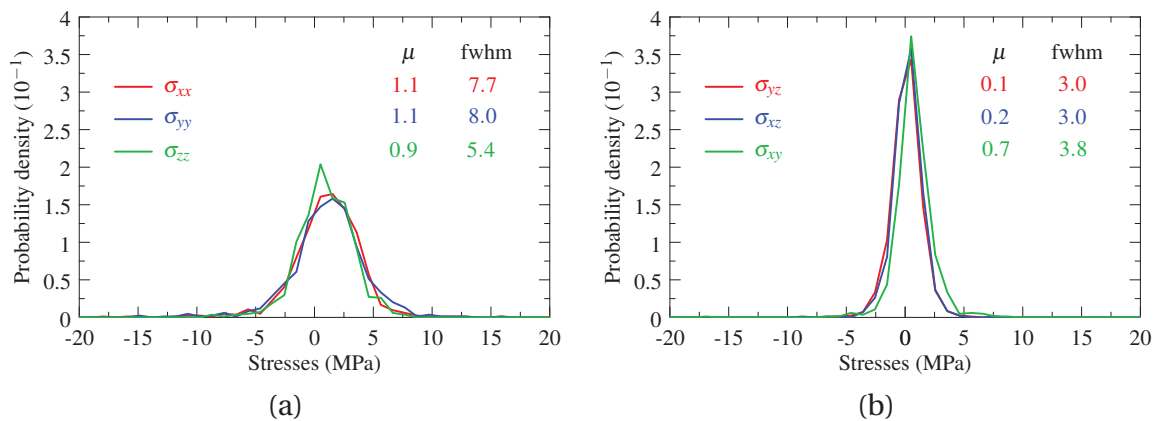


Figure III.18 – Residual stresses in Sample B. Distributions of (a) the normal components and (b) the shear components, expressed in the laboratory coordinate system. The mean and full-width-at-half-maximum are provided.

c) Discussion

These results can be discussed in light of the simulations of experimental uncertainties. On the calibration side, two parameters are equally crucial for strain evaluation: the detector distance D and the beam wavelength λ .

The determination of D was performed using Sample B and a stress-free lattice parameter, obtained from laboratory measurements. The grain lattice parameters were, on the average, within the measurement error of the stress-free value, which tends to validate the approach. The procedure also assumed that the sample was unloaded. So, the results reveal primarily residual lattice strains and do not, therefore, contradict this assumption.

The wavelength was obtained from independent measurements on a Si wafer. The latter revealed significant variations of λ throughout the experiment. For the analyses, we considered average values over the duration of each scan. Evidently, this does not allow to properly correct the continuous drift of λ . However, the difference, from the beginning to the end of each scan, appears to be smaller than 5×10^{-5} , suggesting that the issue should only have a limited impact on the results.

We also examined the influence of peak-coordinate errors, which arise in practice from the detector spatial distortions and the calculation of spots centroids. The distortions were assessed through independent optical measurements and radially confined within $\pm 5 \times 10^{-5}$ in relative around the expected peak positions. They should therefore have a limited influence, as the corresponding errors on peak-coordinates are between 0.02 and 0.05 pixels (for the smallest and largest Debye rings with radii of 460 pixels and 1000 pixels, respectively).

Regarding the calculation of spot centroids, it primarily depends on the spot segmentation, the grain size and the grain mosaicity. It is not readily measurable, though. The simulations enabled to partially close this gap. Indeed, we observed a quantitative agreement between the simulations of Figure III.14 ($\sigma_{uv} = 0.1$ pixels) and the results of Sample B. The experimental errors and FWHM are somewhat higher than the simulation ones, which suggests the value of 0.1–0.2 pixels as a reasonable upper-bound of the mean error.

Lastly, regarding the grain average quantities and related errors, we found that precisions of about 0.03° , 1×10^{-4} and 8 MPa could be achieved for grain orientations and lattice strains and stresses, respectively. These results concern the initial sample configuration and might, evidently, vary in the deformed states. Nevertheless, they allow validating the calibration results and considering the *in situ* study as feasible.

III.4 Conclusion

In this chapter, a general framework was introduced that allows for accurate determination of grain average quantities from 3DXRD measurements.

- The geometry of a 3DXRD diffractometer has been described and parametrized in a general way, based on several coordinate systems and taking into account any potential misalignment of the setup with respect to its ideal configuration.
- A three-step calibration procedure has been proposed to accurately estimate the global parameters and assess the detector spatial distortions, using independent measurements on a reference powder and a single crystal.
- The evaluation of grain average quantities has been discussed. The lattice strains, in particular, were described by the finite Lagrangian strain tensor, which can be obtained from the magnitude of the measured diffraction vectors.

Finally, the methodology has been used to characterize the initial, undeformed state of Sample B, consisting of 824 grains. The results indicate that accuracies of about 3 μm , 0.03°, 1×10^{-4} and 8 MPa can be met for the determination of grain positions, orientations, lattice strains and stresses, respectively. This is an improvement compared to the values proposed by Oddershede *et al.* [54].

CHAPTER -IV-

Cross-validation of the initial grain structure

Contents

IV.1	Comparison between DCT and HEDM	70
IV.1.1	Data sets	70
IV.1.2	Comparative methodology	71
IV.1.3	Results of the comparisons	74
IV.1.4	Discussion	78
IV.2	Comparison between DCT and 3DXRD	79
IV.2.1	Data sets	79
IV.2.2	Rigid body transform	83
IV.2.3	Results of the comparison	84
IV.2.4	Discussion	86
IV.3	Conclusion	87

This chapter is dedicated to the validation of the initial grain structure of Sample B and serves as a preliminary work for the comparison of experimental and numerical results. First, we compare the DCT and HEDM reconstructions of Sample A to validate the DCT method as applied on our material (Section IV.1). Second, we validate the initial, undeformed microstructure of Sample B by comparing the average grain structures given by DCT and 3DXRD (Section IV.2).

IV.1 Comparison between DCT and HEDM

Until very recently, the accuracy of 3D reconstructions was checked against data acquired with destructive laboratory techniques, especially by EBSD. However, due to the proliferation of HEXRD microscopy methods, a direct comparison between them is now possible.

DCT is currently limited to the analysis of materials with small intra-granular orientation spreads [43, 73, 95] and uses a wide-box beam and backward-modelling algorithms, which makes it a fast method. In contrast, HEDM is adapted for plastically deformed polycrystals, containing well-developed orientation spreads inside grains [48, 75, 76, 96, 97]. However, the use of a planar beam and thereby the requirement of a large series of acquisitions to build up representative 3D data sets, associated with a forward-modelling algorithm, makes the technique particularly time-consuming.

Since HEDM and DCT use similar detectors, their reconstructed microstructures should exhibit similar spatial resolutions. DCT reconstructions have already been checked against both phase contrast tomography [43] and EBSD mapping [98, 99]. However, both comparisons lack completeness, since crystallographic information is missing in phase-contrast tomography and an EBSD map contains only reduced spatial information (a slice in the three-dimensional structure). To overcome these limitations, we compare here a DCT reconstruction to a series of HEDM layers on the same region of Sample A. By using this slightly deformed polycrystal (of 1% tensile strain), the comparison can answer two questions related to the goodness of their reconstructions and the applicability of the current version of the *DCT* software package to slightly deformed crystals. For completeness, comparisons with EBSD will also be presented.

As part of this work, which was published in Ref. [100], I received a mobility grant from Région Rhône-Alpes to spend four months at Carnegie Mellon University (Pittsburgh, USA) and collaborate with Prof. Suter's team on the reconstruction of the HEDM measurements.

IV.1.1 Data sets

Diffraction acquisitions were done successively at beamline ID11 and EBSD analyses were carried out afterwards at the EMSE laboratory. Figure IV.1-b shows schematically the position of the data sets with respect to each other.

The DCT measurements were analysed with the *DCT* software package available at the beamline [101]. As described in Subsection II.1.2, the diffraction spots were used for reconstructing the grain shapes, while the transmitted intensity provided the specimen shape by absorption contrast tomography. The resulting microstructure is plotted on Figure IV.1-c. It is described on a cubic grid of voxels of size 1.4 μm and contains about 400 grains.

The HEDM measurements were analysed with the forward-modelling software *IceNine* [44, 96]. For each of the 14 layers, the sample space was meshed into about 390,000

equilateral triangle elements with an edge length of $2.5 \mu\text{m}$ and reconstructed as described in Subsection II.1.3. The results revealed lower-than-usual values of the confidence index, with an overall average of 0.5 and a maximum of 0.68, while a value of 1 here corresponds to about 50 matching spots. This can be explained by the relatively low signal-to-noise ratio of the images provided by the semi-transparent detectors and a slight misalignment of the sample rotation axis with respect to the direction perpendicular to the line-focused beam. Elements with confidence lower than 0.2 were considered to have non-indexed orientations.

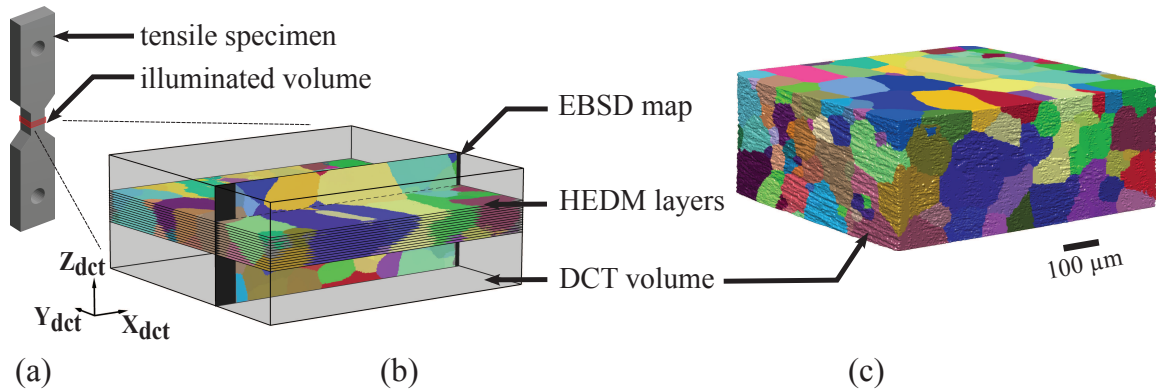


Figure IV.1 – Sample A and grain structure imaged with DCT, HEDM and EBSD. (a) Dog-bone shaped specimen, with the $350\text{-}\mu\text{m}$ -high illuminated volume shown in red. (b) Position of the HEDM and EBSD slices in the DCT volume. Black margins on the EBSD map indicate regions removed by electro-polishing. (c) DCT volume, which is about $350 \mu\text{m}$ high. Colouring according to Rodrigues vector components.

IV.1.2 Comparative methodology

a) Registration of orientation maps

A direct, unbiased comparison between the DCT, HEDM and EBSD microstructures can only be carried out if their respective locations are known accurately. The present experiment involves uncertainties associated, for example, to the vertical focusing of the beam for HEDM measurements and the use of different detectors, or to mechanical polishing for the preparation of the EBSD observation surface. While the relative positions of the data sets can be estimated by simple visual inspection (or, for HEDM, from the nominal acquisition coordinates), an automated registration method is required to refine them.

Registration between two data sets consists of determining the position of the first (HEDM or EBSD) with respect to the second (DCT) by maximizing the correspondance between the two, while accounting for potential distortions. This is carried out on a region which is located at the intersection between the DCT and HEDM (or EBSD) data sets, and referred to as “registration region”. For simplicity, each of the HEDM and EBSD data sets was re-mapped onto a grid of square pixels of the same size as in DCT ($1.4 \mu\text{m}$). The registration approach used here is based on a method developed previously for a comparison between X-ray nanotomography and SEM gray-level images [102] and extended to the more delicate case of crystal orientation data.

Let p be the pixel of interest in the layer data (HEDM or EBSD). Its position and crystal orientation are referred to as \mathbf{x}_{lay} and \mathbf{U}_{lay} in the coordinate system of the layer, respectively, and \mathbf{x}_{dct} and \mathbf{U}_{dct} in the coordinate system of the DCT volume, respectively. The

geometrical operator that relates \mathbf{x}_{lay} to \mathbf{x}_{dct} is an affine transformation that can be written as:

$$\mathbf{x}_{\text{dct}} = \mathbf{G}^{-1} \mathbf{F} \mathbf{x}_{\text{lay}} + \mathbf{s} \quad (\text{IV.1})$$

where \mathbf{F} is a matrix combining scaling and shear distortion, \mathbf{G} is a rotation matrix and \mathbf{s} is a shift vector. \mathbf{F} can be written as:

$$\mathbf{F} = m \begin{pmatrix} d_{12} & s_{12} & 0 \\ 0 & \frac{1}{d_{12}} & 0 \\ 0 & 0 & 1 \end{pmatrix} \quad (\text{IV.2})$$

where m is a magnification factor, d_{12} is a scaling ratio between directions 1 and 2 of the layer, and s_{12} is the in-plane shear. In contrast to the case of scalar data registration [102], the rotation \mathbf{G} involves a change of the pixel data values themselves (the crystal orientations), which can be written as:

$$\mathbf{U}_{\text{dct}} = \mathbf{U}_{\text{lay}} \mathbf{G}^{-1} \quad (\text{IV.3})$$

For specific values of the registration variables (\mathbf{F} , \mathbf{G} and \mathbf{s}), \mathbf{x}_{dct} and \mathbf{U}_{dct} are obtained using Equations IV.1 and IV.3. The corresponding crystal orientation in the DCT volume, $\tilde{\mathbf{U}}_{\text{dct}}$, is approximated by the orientation of the voxel at location \mathbf{x}_{dct} (in the absence of a simple, tri-linear interpolation scheme for crystal orientations).

The registration then consists in determining the values of \mathbf{F} , \mathbf{G} and \mathbf{s} that yield the best possible match between the layer and DCT data sets. The correspondence between the two is quantified by means of the local disorientations via the following function,

$$\Theta = \frac{1}{N} \sum_{p=1}^N \left[1 - \exp\left(-\frac{\theta_p}{\theta_c}\right) \right] \quad (\text{IV.4})$$

where θ_p is the disorientation angle between \mathbf{U}_{dct} and $\tilde{\mathbf{U}}_{\text{dct}}$. The reference angle θ_c is considered equal to 1° , and N is the number of pixels in the registration region. The expression of Θ and the value of θ_c are such that the influence of a local disorientation is zero at $\theta_p = 0^\circ$ and reaches 1 for $\theta_p > 5\theta_c$. The lower the value of Θ , the better the matching between the layer and its intersection with the DCT volume. The rotation matrix \mathbf{G} can be described by 3 independent variables, which is here done using the Rodrigues vector parameterization (R_1, R_2, R_3) [69]. Equations IV.1–IV.4 form a non-linear optimization problem of objective function Θ and variables $m, d_{12}, s_{12}, R_1, R_2, R_3$ and s_1, s_2 and s_3 (the components of \mathbf{s}). The minimization was performed using the NLOpt library (subplex algorithm) for local derivative-free optimization [98, 103] and the Orilib library for orientation and rotation calculations [104].

For HEDM registration, the magnification factor m , the three orientation variables (R_1, R_2, R_3) and the three shifts (s_1, s_2, s_3) were used while no distortions were allowed ($d_{12} = 1, s_{12} = 0$). The initial value of s_3 was estimated by visual inspection, while other parameters were set to default values ($m = 1, s_1 = 0, s_2 = 0, R_1 = 0, R_2 = 0, R_3 = 0$). The 14 HEDM layers were registered with respect to the DCT volume independently from each others. This resulted in magnifications m of 0.996 ± 0.003 and global rotations of $0.66 \pm 0.01^\circ$. Radial (x–y) shifts were of the order of 1. As shown by Figure IV.2, the axial (z) shifts of the different layers retrieved the expected vertical distribution, albeit with slightly smaller spacing between the layers ($5.8 \pm 0.15 \mu\text{m}$) than the imposed shift ($6 \mu\text{m}$). The error of the fit parameters represents the standard deviation over the 14 HEDM layers.

The same procedure was then applied to determine the location of the EBSD map inside the DCT volume, but this time allowing for scaling and shearing (d_{12} and s_{12}), to

account for sample misalignment in the SEM. As an initial guess, the EBSD microstructure was positioned in the radial, x - z plane ($R_1 = 1$, $R_2 = 1$, $R_3 = -1$) by visual inspection, while magnification and distortion parameters were set to default values ($m = 1$, $d_{12} = 1$, $s_{12} = 0$). The optimization resulted in a transformation of the EBSD map by a magnification m of 0.98, a global rotation of 4.4° , and distortions $d_{12} = 0.99$ and $s_{12} = 0.01$.

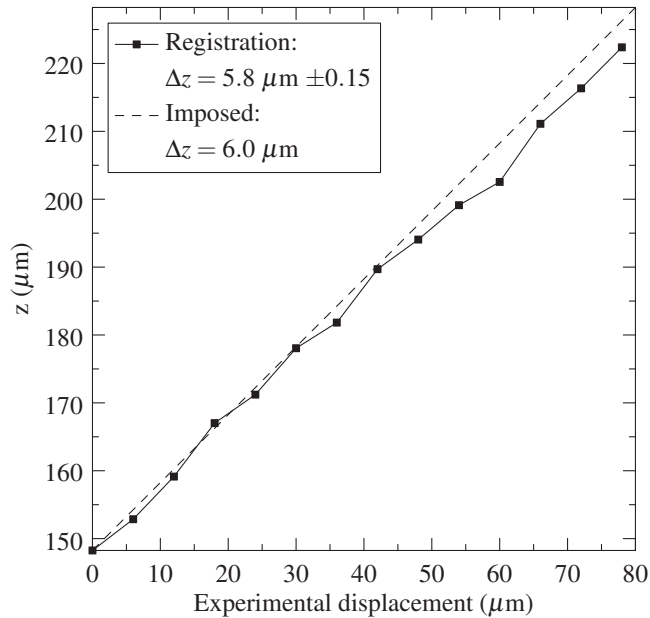


Figure IV.2 – Vertical distribution of the 14 HEDM layers, as given by the registration, plotted against the cumulated displacements imposed during measurements.

b) Comparison metrics

The registration parameters were used to extract sections of the DCT volume corresponding to the HEDM and EBSD data, as shown in Figure IV.4 and Figure IV.7. These maps can be used for an unbiased, quantitative comparison between the DCT, HEDM and EBSD data sets.

While grain (or subgrain) identification is intrinsic to the DCT method, it was performed by post-processing for HEDM and EBSD, using the grain boundaries. The latter were drawn considering a minimum disorientation angle of 1° . The comparisons were then based on the following metrics.

Microstructure overlap

The overlapping ratio between two grain maps can be evaluated once individual grains (or subgrains) are identified in the different data sets and paired between techniques, for example, by comparing their centres-of-mass and average orientations. Once the pairs have been formed, the overlap is calculated as the proportion of pixels that belong to the same grains.

Location of grain boundaries

The location of the grain boundaries can be compared by means of the Euclidean distance mapping [105]. The method indicates, for each pixel in the boundary network of a grain map (*e.g.* HEDM or EBSD), the shortest distance to the nearest pixel in the boundary network of the other reference grain map (*e.g.* DCT). Figure IV.3 shows the distribution of

boundary pixels per disorientation angles, in the DCT and HEDM grain maps. The overall quantity is about 20% higher for the HEDM data. This is mainly due to the significant difference below 5°, which led us to limit the Euclidean distance mapping to disorientation boundaries with angles higher than 5°. The same condition was applied for the comparison with EBSD. Lastly, it should be pointed out that the distances are computed on 2D maps and are therefore not fully representative of the 3D configuration. They provide, however, an upper bound that can be used for semi-quantitative analysis.

Local disorientation

The last metric concerns the local disorientation between corresponding pixels, which can be visualized either in the form of a disorientation map or in the form of an angle distribution. Since the DCT provides constant orientations per grain, variations can only be expected from HEDM or EBSD, and related to the intra-granular orientation spread in the respective data sets.

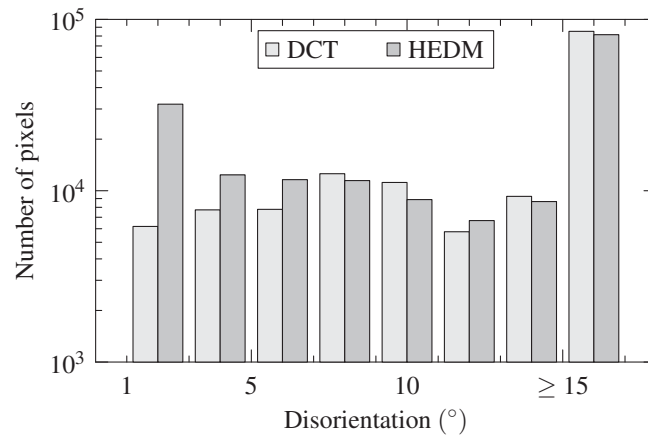


Figure IV.3 – Disorientation angle distribution of DCT and HEDM grain boundary pixels. The total number of boundary pixels is 145,658 for DCT, and 173,094 for HEDM.

IV.1.3 Results of the comparisons

a) DCT – HEDM

The microstructures as obtained by DCT and HEDM are provided in Figure IV.4 and are in appreciable general agreement. The microstructures exhibit a particularly large grain size dispersion, as expected from 2D layers within a 3D microstructure. Interestingly, while most grains are free from internal disorientation boundaries, others exhibit clear sub-structuring with internal disorientations of 1–5°, as expected from the preliminary characterizations of Al-0.3Mn. Such features result from the microstructure elaboration or, less likely, its subsequent plastic deformation. They were believed to be problematic for DCT because they involve regions of both similar locations and orientations, but they were in practice properly captured.

The grains and subgrains were paired between the two data sets, which led to about 80 pairs for each individual HEDM layer and 149 pairs when all 14 layers were considered (accounting for the duplication of grains across adjacent layers). This allowed to compute the overlapping ratio between DCT and HEDM microstructures, which reaches 87% and quantitatively confirms the previous observations.

The distribution of DCT-HEDM grain boundary distances is provided in Figure IV.5. It is characterized by an average value of 4 μm (3 pixels), which corresponds to about 4% of the average grain size, and a median value of 3 μm (2 pixels), which is similar to the element size used for the HEDM reconstruction. The agreement on the grain boundary positions is therefore remarkable.

Lastly, Figure IV.6-a provides the disorientation map corresponding to the microstructures of Figure IV.4. Regions above 5° disorientation appear in red and are located near grain boundaries, where grains do not necessarily overlap between the two data sets (13% of the maps). Elsewhere, grains overlap with disorientations mostly lower than 1°. The disorientation fields inside grains captured by HEDM, albeit weak, are typical of plastically deformed polycrystals. Figure IV.6-b provides the distribution of the disorientation angle (θ_p) over the overlapping regions, which has a mean of 0.38° and a standard deviation of 0.25°.

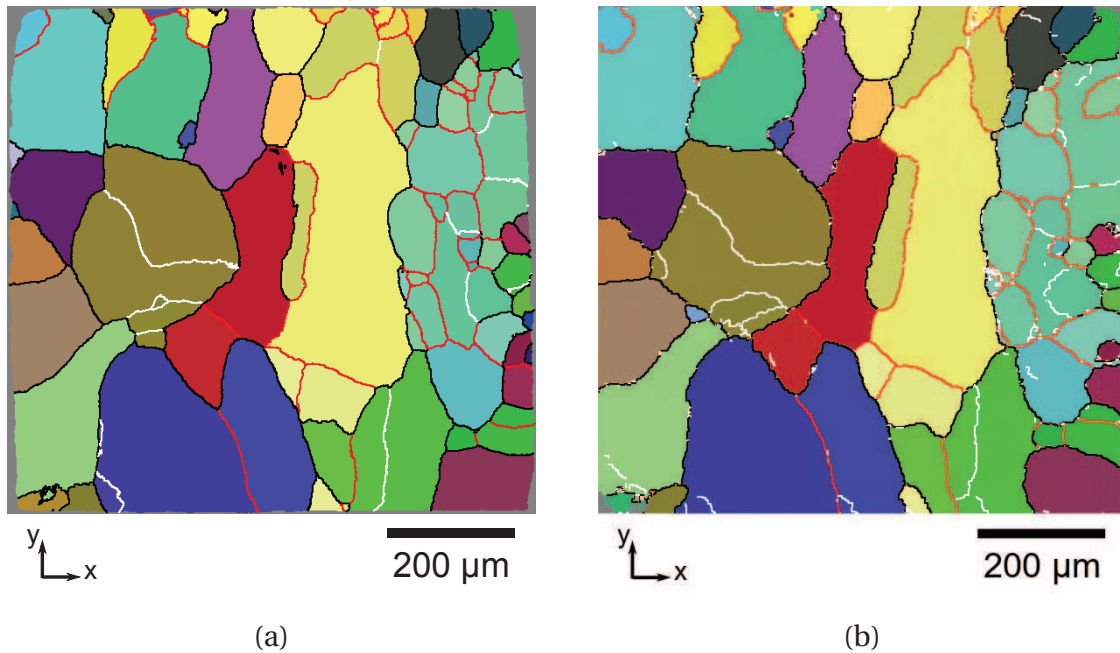


Figure IV.4 – Comparison between the (a) DCT and (b) HEDM microstructures on a single layer (HEDM layer #7). Orientation colouring as in Figure IV.1. Disorientation boundaries are plotted in black for $\theta > 15^\circ$, red for $5^\circ \leq \theta < 15^\circ$ and white for $1^\circ \leq \theta < 5^\circ$, where θ is the disorientation angle. The pixel size is 1.4 μm . Note the light blue, sub-structured region on the right hand side of the map, properly revealed by both methods.

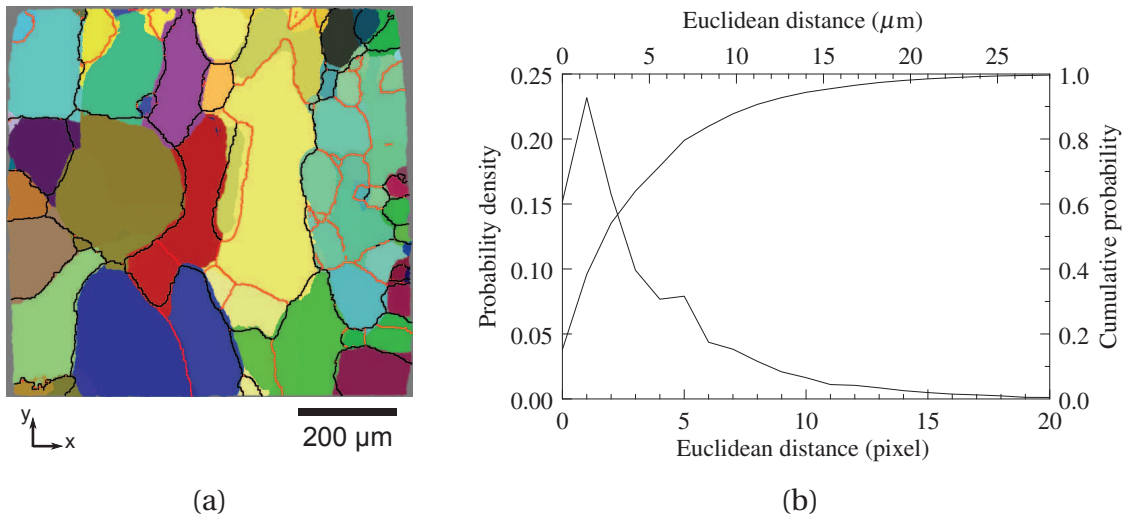


Figure IV.5 – Comparison between the positions of the grain boundaries of the DCT and HEDM microstructures of Figure IV.4. (a) DCT grain map, coloured as in Figure IV.4, with overlaid HEDM disorientation boundaries, plotted in black for $\theta > 15^\circ$ and red for $5^\circ \leq \theta < 15^\circ$. (b) Distribution of the distances between the grain boundaries.

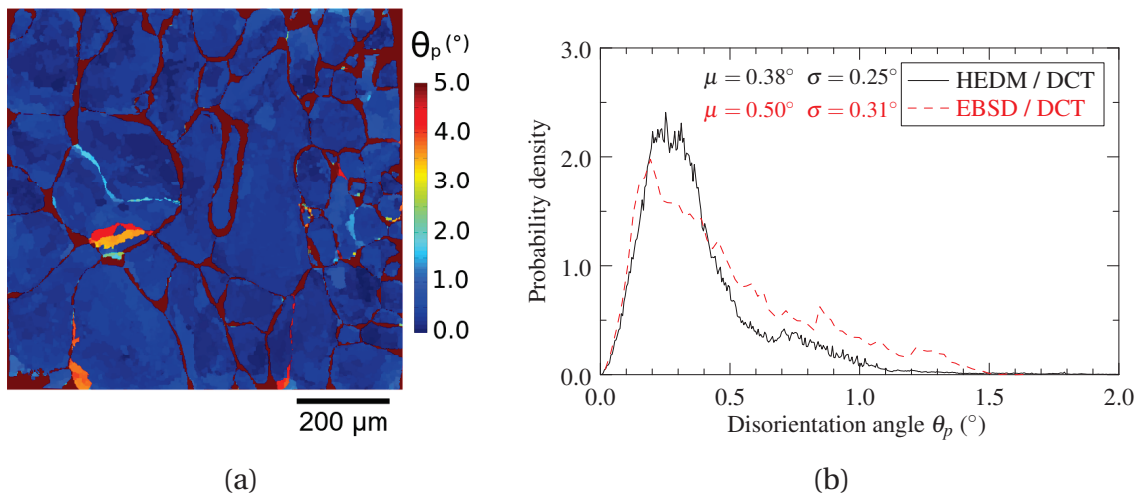


Figure IV.6 – Local disorientation between the DCT and HEDM microstructures of Figure IV.4, in terms of (a) map and (b) distribution. The distribution obtained from the comparison between DCT and EBSD is shown in (b) as well. θ_p is the disorientation angle.

b) DCT – EBSD

The DCT and EBSD microstructures are provided in Figure IV.7 and are also in good overall agreement. The overlapping ratio between the two microstructures, of 82%, is lower than for HEDM, which is partly due to a grain present on the EBSD image, but not indexed by DCT. The distribution of the Euclidean distance between the DCT and EBSD grain boundaries is plotted on Figure IV.8-b and shows an average of 5.6 μm (4 pixels), which again is slightly higher than for HEDM (5 μm). The distribution of θ_p in Figure IV.6-b is similar to that of HEDM, albeit slightly more intense in the upper tail, with an average value of 0.50° and a standard deviation of 0.31° .

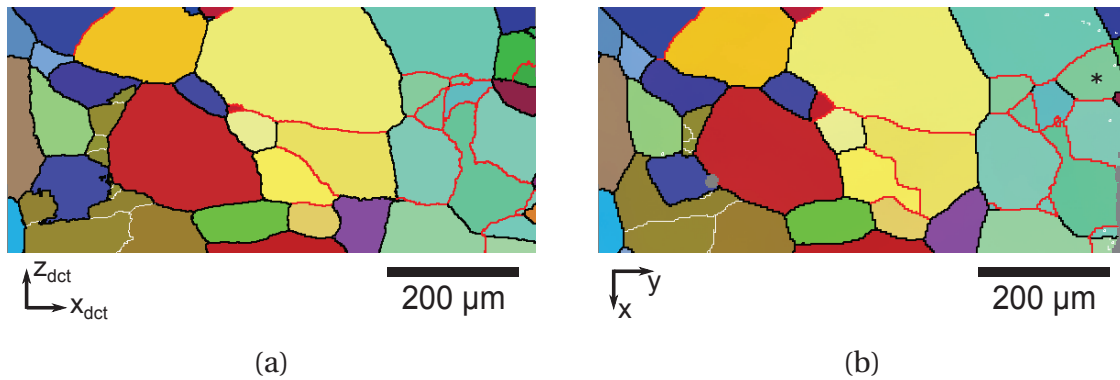


Figure IV.7 – Comparison between the DCT and EBSD microstructures. (a) DCT grain map and (b) EBSD orientation map. Orientation colouring as in Figure IV.1. Disorientation boundaries are plotted in black for $\theta > 15^\circ$, red for $5^\circ \leq \theta < 15^\circ$ and white for $1^\circ \leq \theta < 5^\circ$, where θ is the disorientation angle. The pixel size is 1.4 μm . Note the missing grain in the DCT map, marked by a black star on the right hand side of the EBSD map.

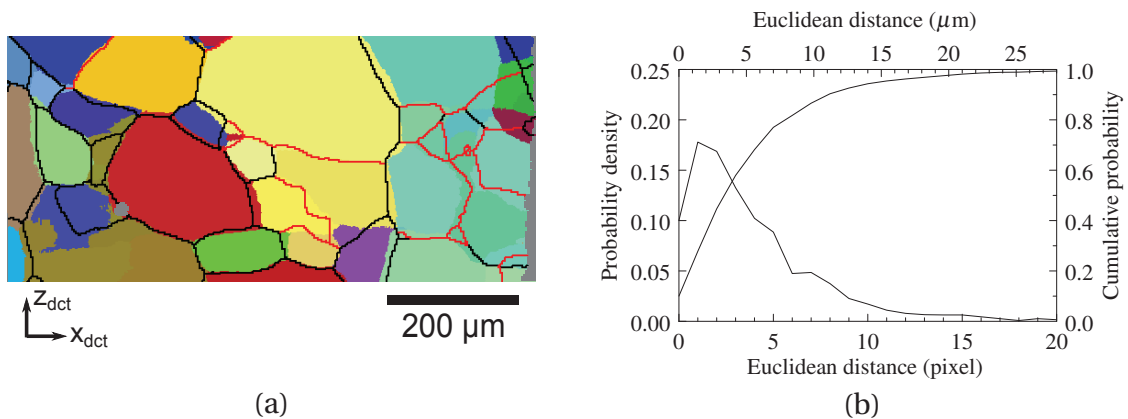


Figure IV.8 – Comparison between the positions of the grain boundaries of the DCT and EBSD microstructures of Figure IV.7. (a) DCT grain map, coloured as in Figure IV.7, with overlaid EBSD disorientation boundaries, plotted in black for $\theta > 15^\circ$ and red for $5^\circ \leq \theta < 15^\circ$. (b) Distribution of the distances between the grain boundaries.

IV.1.4 Discussion

The comparison between DCT and HEDM reveals that the two techniques deliver very similar microstructures. The agreement, albeit not perfect, is appreciable considering the potential sources of discrepancies.

On one hand, in the case of Sample A, DCT is expected to be influenced by the intra-granular orientation spread induced by plastic deformation, which is about 0.3° in average and is not consistent with the parallel beam assumption. This adds up to the well-known artefact of the technique (i.e., the back-projected grains being usually undersized), leading to gaps of a few voxels in the reconstructions, as shown in Figure IV.9-a. The latter are filled in using morphological dilation, which might introduce small errors (of a few voxels) in the final position of grains boundaries.

On the other hand, HEDM reconstructions of Sample A may have been influenced by the use of the *3D detector*, whose measurements showed lower signal-to-noise ratios than that of the DCT detector. This, combined with a slight misalignment of the rotation axis, has led to reduced resolution of grain shapes. This is shown in Figure IV.9-b by the confidence index of the reconstruction (i.e., completeness ratio) being capped at 0.6.

For both techniques, grain boundaries appear as regions of higher uncertainty, leading to gaps in the DCT and drops of the confidence values in the HEDM. These regions, of a few micrometers thick, are consistent with the average distance of $4\ \mu\text{m}$ between grain boundaries and the overlapping rate of 87%. Hence, in view of these elements, the present comparison can be seen as the first cross-validation of the two techniques, in terms of grain shapes.

The additional comparison, with EBSD, was done as a verification. It is still unclear whether the somewhat higher difference between DCT and EBSD than between DCT and HEDM is representative or due to the limited size of the EBSD region and the larger acquisition step of $3\ \mu\text{m}$. However, with an overlap of 82% and an average distance of $5.6\ \mu\text{m}$ between their respective grain boundaries, the agreement between DCT and EBSD remains acceptable and rather tends to further support the previous conclusion.

Furthermore, both comparisons provided valuable insights on the applicability of DCT on slightly deformed polycrystals and its ability to resolve sub-structured regions (see Figure IV.4 and IV.7), comparable to those commonly observed in the Al-0.3Mn alloy. It was found that the technique was able to detect subgrain boundaries with disorientation as low as 1° , this limit being certainly better for an undeformed sample.

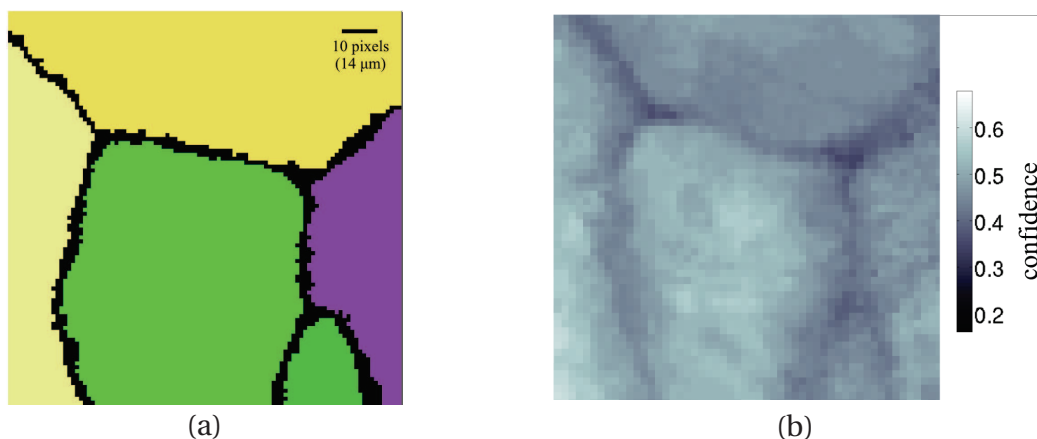


Figure IV.9 – Grain boundaries as uncertainty regions in DCT and HEDM reconstructions. (a) DCT map exhibiting inter-grain holes before the morphological dilation. (b) Confidence map of the HEDM reconstruction.

IV.2 Comparison between DCT and 3DXRD

The initial, undeformed state of Sample B was measured by both DCT and 3DXRD. In Section IV.2 we have assessed the validity of DCT when applied on Al-0.3Mn, whose microstructure commonly contains textured regions. We are now concerned with the similarity between DCT and 3DXRD results.

The two techniques employ different experimental setups and different strategies for data analysis. As mentioned before, DCT aims at producing 3D grain maps of the sample. Grain average properties only are accessible with 3DXRD, which limits the analysis to the grain centroids, orientations and volumes. As a near-field technique, DCT has a higher spatial resolution, while 3DXRD, as a far-field technique, is expected to have a higher angular resolution. This complementarity makes the comparison of real interest to cross-validate the initial configuration of Sample B.

IV.2.1 Data sets

As detailed in Subsection II.3.2, the gage of Sample B was scanned with a 550 μm high beam into three partially-overlapping parts, covering a total height of 1.4 mm. Subsequently, using the same beam configuration, the middle part of the gage (i.e. the middle part of the DCT measurements) was measured by 3DXRD.

a) Merging of DCT volumes

The DCT scans were analysed with the *DCT* software package. The three separate microstructures are shown in Figure IV.10-a-b-c. They are described on cubic grids of voxels of size 1.4 μm and contain respectively 829, 857 and 794 grains. The volumes are 560 μm -high, which is somewhat larger than the nominal beam height of 550 μm .

To merge the three volumes, it was first necessary to determine the offsets of the bottom and top parts with respect to the middle part. Vertical shifts of ± 425 μm were applied during the experiment. Slightly different values of ± 408 μm were determined based on the normalized cross-correlations between the absorption tomograms of the middle and the two other parts. This difference of 4% between experiment and cross-correlation, albeit significant, is consistent with the registration results of the HEDM layers, which seemed also to indicate a systematic bias of 3-4% in the vertical displacement of the goniometer stage (Subsection IV.1.2). Visual comparisons of characteristic details at the sample surface, as illustrated by Figure IV.11, tends to further support the cross-correlation results. They were therefore used to merge the three volumes.

To do so, the corresponding grains in the overlapping regions were matched manually to produce a list of 567 merging operations, which were then resolved in an automated way. Merging was done before the morphological dilation step. The shapes of the newly-formed grains were taken as the unions of their former merged parts. The morphological dilation was finally performed on the full volume to obtain the final DCT microstructure, in Figure IV.10-d, which is 1,384 μm high and contains 1,885 individual grains. During merging the grain orientations were also re-calculated as the average orientation of the merged parts, weighted by their volumes. The distribution of disorientation angles between the new and the former middle-part grain is provided in Figure IV.12. Orientation changes can be expected owing to grain mosaicity. We observe that they are small and mostly confined below 0.05° , which can be explained by the use of relatively large overlapping regions for merging.

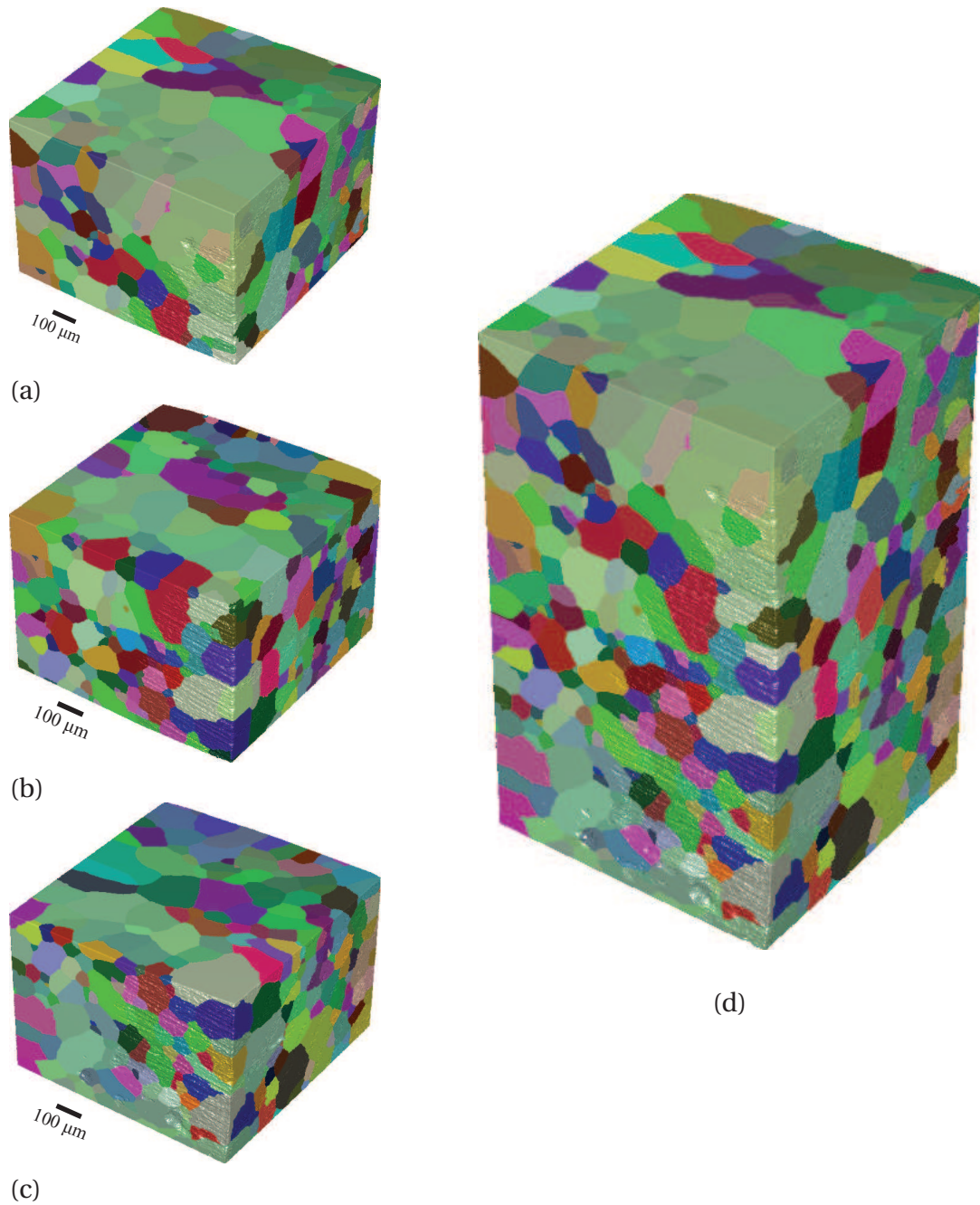


Figure IV.10 – Grain structure of Sample B as imaged by DCT: (a) top part with 829 grains, (b) middle part with 857 grains, (c) bottom part with 794 grains and (d) full, merged map containing 1,885 individual grains. The three sub-volumes are about 560 μm high, while the full volume is 1,384 μm high. Orientation colouring according to Rodrigues vector components.

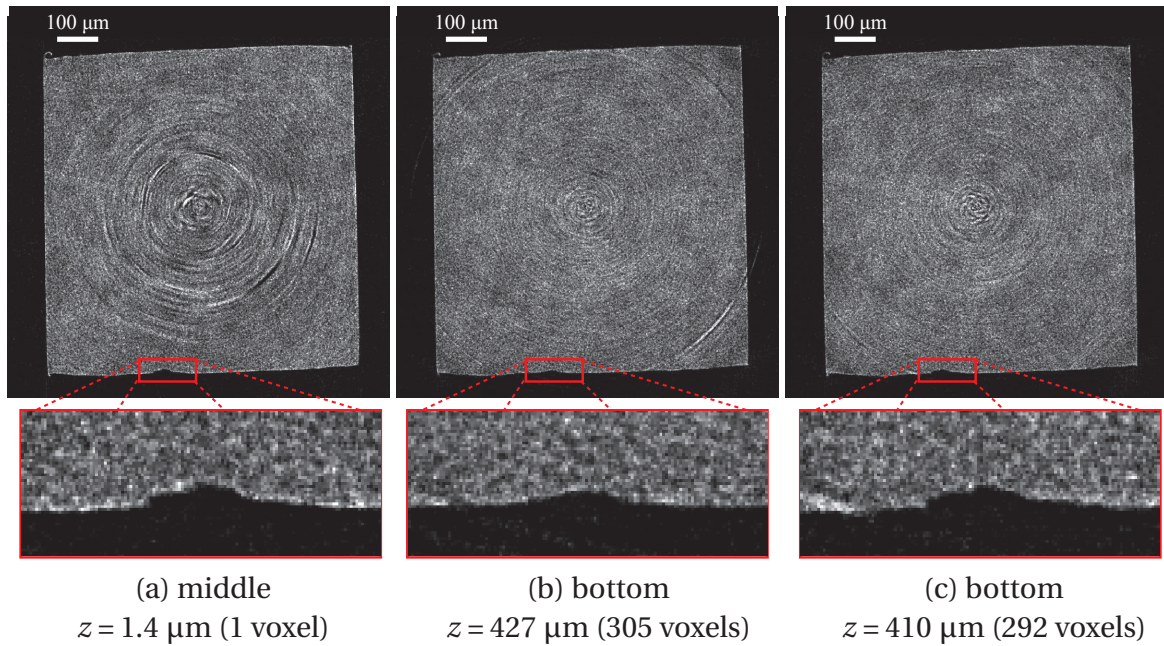


Figure IV.11 – Comparison between the middle-part and bottom-part absorption tomograms. (a) Horizontal section of the middle-part tomogram at $z = 1$ voxel. (b) Corresponding section of the bottom-part tomogram at $z = 305$ voxels, as expected from the experimental conditions. (c) Corresponding section of the bottom-part tomogram at $z = 292$ voxels, as determined by the cross-correlation. Note the comparison of the same detail on the sample surface, which shows a better similarity between a) and c) than between a) and b).

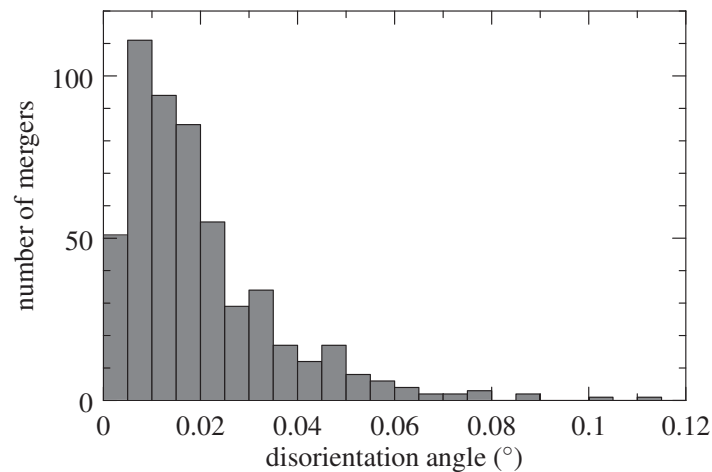


Figure IV.12 – Distribution of orientation changes caused by merging. The disorientation angle measures the orientation change of a middle-part grain when merged with top-part or bottom-part grains. The total number of merged grains is 567.

b) Indexing of 3DXRD

DCT and 3DXRD data are generally indexed separately. This adds an extra layer of difficulty to the comparison, which is the need for matching grains between the two data sets. We propose here to directly use the properties of the DCT grains to index the 3DXRD spots. To do so, we considered the 560 μm -high middle section of the DCT map and extracted the properties of the grains (or grain parts) found in that region. A number of 860 grains were thus identified. Their centroids and orientations were used to index the 3DXRD diffraction spots.

The resulting completeness ratios for the 860 grains are shown in Figure IV.13-a as a function of DCT grain sizes. We can observe that the completeness tends to improve with the grain size, certainly due to the increase of counting statistics. For grains larger than 50 μm , the average completeness reaches 0.84, equivalent to about 120 indexed spots. For grains smaller than 50 μm , the completeness ratios are significantly lower, with an average of 0.48. Thereafter, only the grains with at least 20 spots were accepted, resulting in a final number of 824 grains for the comparison. The remaining 54 grains are small, with completeness lower than 0.2. As shown in Figure IV.13-b, they are mostly located at the sample surface or at the upper and lower limits of the volume. In the former case, they may be more difficult to index due to their eccentric positions, while, in the latter case, they may have got in and out of the beam during the 3DXRD scan because of the non-zero wedge angle.

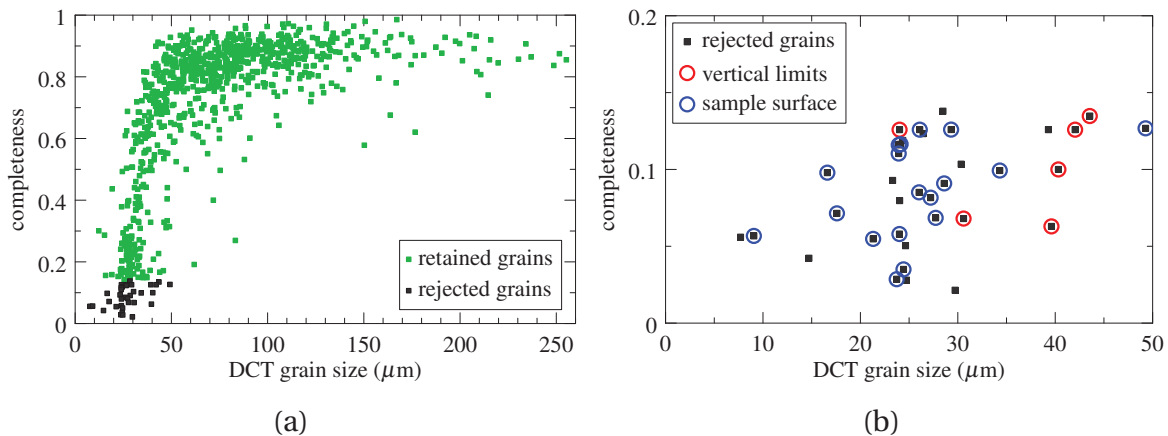


Figure IV.13 – Completeness ratios resulting from the indexing of 3DXRD spots: (a) complete set of 860 grains and (b) focus on the 36 rejected grains, with less than 20 assigned spots. The completeness ratio is defined for each grain as the ratio of the number of assigned spots and the maximum number of expected theoretical reflections. The latter number is estimated by forward simulation. In (b), we have marked the six grains lying on the upper/lower limits of the middle-part map (red) and the 17 grains in contact with the sample surface (blue).

IV.2.2 Rigid body transform

The comparison consists in assessing the differences in terms of grain average properties given by the DCT and 3DXRD analysis. The two microstructures are represented in Figure IV.14 and show an appreciable overall agreement. A closer look at the data revealed though significant differences in both grain positions and orientations, particularly a systematic shift of the 3DXRD grains of about $10\ \mu\text{m}$ downwards along Z with respect to the corresponding DCT grains. This must be attributed to the use of a different beam centre for the analysis and, more generally, different descriptions of the geometry. This difference can be seen as a purely rigid body motion and must be compensated for an unbiased comparison between the two techniques. In fact, this is very similar to the registration problem addressed in Subsection IV.1.2, albeit much simpler, since it consists in determining the optimal rotation and translation that minimize the distance between the corresponding DCT and 3DXRD grain centroids.

It resulted here in a translation of $(-5\ \mu\text{m}, -5\ \mu\text{m}, -11\ \mu\text{m})$ and a rotation of 0.11° . These parameters were used to correct the 3DXRD data (grain positions and orientations) before being compared to DCT.

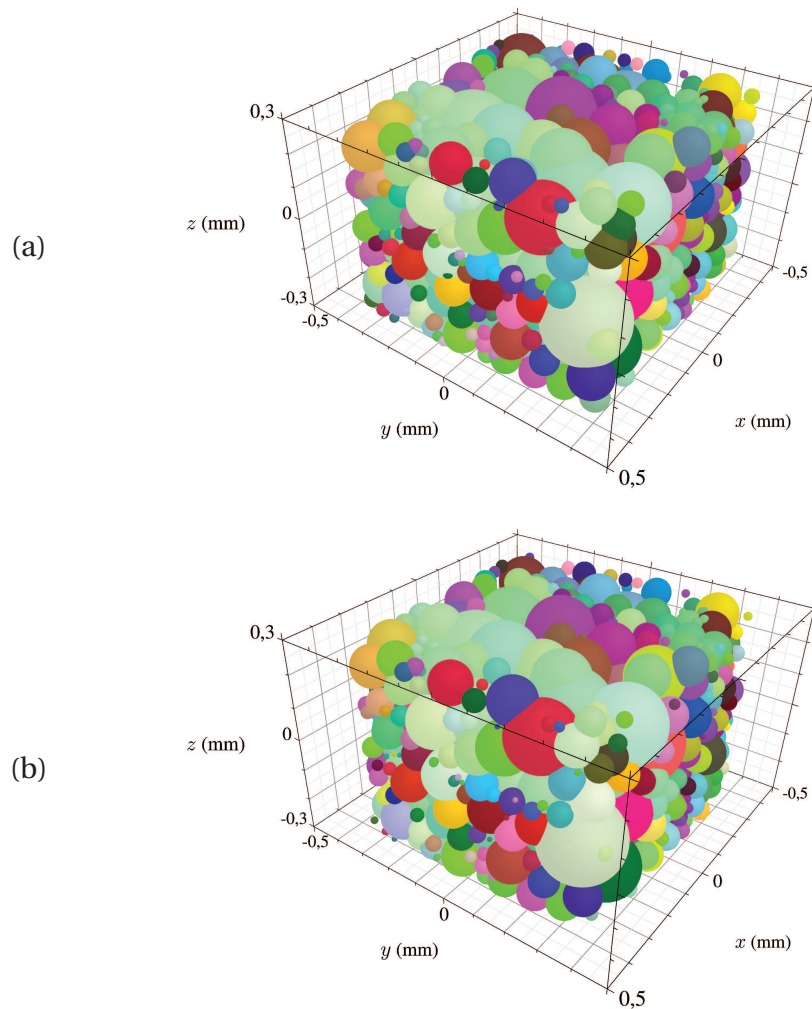


Figure IV.14 – Average representation of the microstructure of Sample B given by (a) DCT and (b) 3DXRD. Grains are represented by spheres of diameters equal to the grain sizes, centred on the grain positions and coloured by grain orientations. Colouring according to the components of Rodrigues vectors.

IV.2.3 Results of the comparison

a) Position

The distributions of the three shift components, given in Figure IV.15-a, are centred on zero and have comparable standard deviations of 3.5, 4.9 and 3.7 μm , respectively.

Figure IV.15-b plots the distance between DCT and 3DXRD grain centroids against the DCT grain size. We observe that most of the errors are lower than 10% of the grain size. Very few grains have position errors larger than 20% of the grain size. Two grains of size 80 μm and 200 μm show remarkably high errors, above 50 μm . Both are, however, surface grains lying on the upper limit of the volume, which might explain the large difference observed.

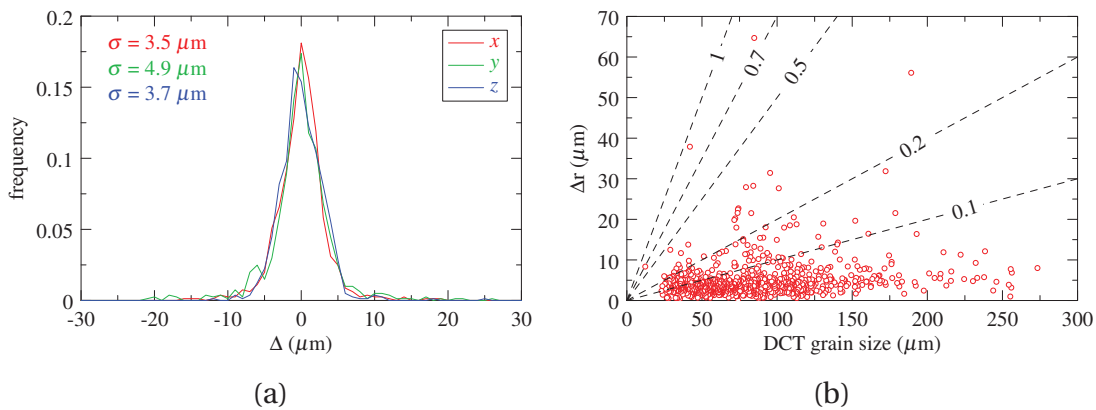


Figure IV.15 – Difference in grain position between the DCT and 3DXRD data, considering the 824 retained grains. (a) The distributions of the three shift components and corresponding standard deviations, shown in different colours. (b) Distance between DCT and 3DXRD grains as a function of the grain size evaluated by DCT. The straight lines represent different distance-to-size ratios.

b) Orientation

The distributions of disorientation angles between DCT and 3DXRD grains, with and without applying the rigid body transform, are given in Figure IV.16. We can observe a clear difference between the two distributions, the average angle being 0.1° before and 0.03° after correction. Given that the grain orientations were not taken into account to determine the rigid rotation, this result is remarkable.

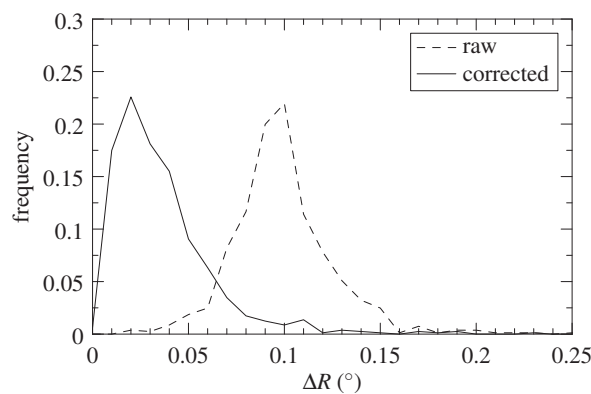


Figure IV.16 – Distribution of disorientation angles between DCT and 3DXRD data, based on 824 grains, before (raw) and after accounting for the rigid body motion (corrected). The distributions have respective means of 0.1° and 0.03° .

c) Size

The DCT and 3DXRD grain sizes are calculated in two different manners. In DCT, they are obtained from the 3D grain maps as the number of voxels making up each grain, while in 3DXRD, they are estimated from the intensities of the diffraction spots (Section III.3). The grain sizes given by the two procedures, compared in Figure IV.17, are in good agreement. A deviation from the $y = x$ line is observed for grains smaller than 100 μm , which consistently appear smaller in the 3DXRD than in the DCT results. This difference is also visible in Figure IV.14-a-b, where the 3DXRD polycrystal looks somewhat smaller than the DCT one, and in Figure IV.18, where the lower tail of the grain size distribution is more populated for 3DXRD. This yields an average size of about 69 μm , compared to 74 μm in the full DCT and 77 μm in the middle DCT volume. The similarity between the latter two distributions suggests that the investigated middle section is representative of the full sample gage, at least in terms of grain size.

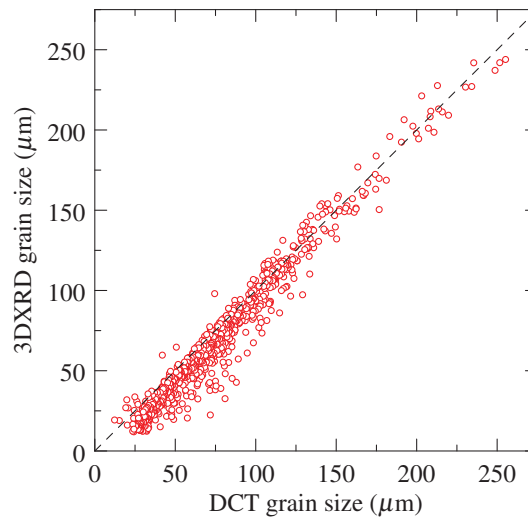


Figure IV.17 – Comparison of DCT and 3DXRD grain sizes, based on 824 grains. The DCT grain sizes are obtained from the grain 3D shapes, while the 3DXRD grain sizes are calculated from spot intensities. In the latter case, the reference volume of the illuminated region was given by the DCT reconstruction and was equal to 0.3822 mm^3 .

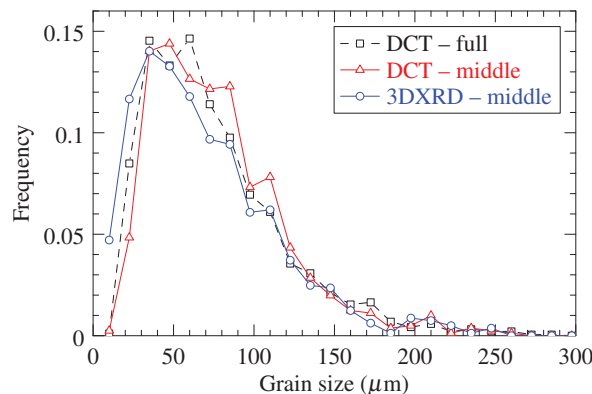


Figure IV.18 – Distribution of grain size in Sample B, as given by DCT and 3DXRD. The average sizes are 74 μm (full DCT), 77 μm (middle DCT) and 69 μm (3DXRD).

IV.2.4 Discussion

A similar comparison was already done by Nervo *et al.* in Ref. [71] using a sample of commercially pure titanium containing about 1,800 grains. The DCT and 3DXRD measurements were analysed with the *DCT* and *ImageD11* software packages, respectively. Matching the grains between the data sets resulted in about 1,500 pairs (84% of all indexed grains) which were compared in terms of position, orientation and size. The overall agreement between the two techniques, albeit not perfect, was remarkable. The main discrepancies were attributed to the differences in spatial resolution, quantum efficiency and dynamic range of the near-field and far-field detectors, and were observed in the lower tail of the grain-size distribution for small grains with lower completenesses and reduced counting statistics.

Our study was carried out in a similar manner as Nervo *et al.* [71]. The main difference was the use of the DCT results to index the 3DXRD spots, which avoided matching the data sets. It resulted in 824 pairs, about 95% of the initial, 860 DCT grains. The remaining 36 grains were small grains, with less than 20 spots in the 3DXRD indexing results; they were therefore not retained for the comparison. The 3DXRD data initially contained 93,031 spots, among which 5,903 only remained unindexed (6%). Running a separate grain search on these spots did not yield any additional grain, which suggests that the DCT analysis did not miss any significant grains.

Another difference with Nervo *et al.* [71] was the need for a rigid body correction. The transform was determined based on the grain positions only and applied on both 3DXRD grain positions and orientations. We observed that the discrepancies in grain orientations between the two data sets were significantly reduced, which tends to validate the correction. The rigid rotation of 0.11° can be reasonably attributed to slightly different definitions of the laboratory coordinate system (i.e., DCT and 3DXRD employ different detectors, geometry descriptions and calibration procedures).

The comparison between DCT and 3DXRD results revealed that the two techniques deliver very close grain centroids, with standard deviations of 3-5 μm on the three shift components. In the comparison of Nervo *et al.*, larger shifts were found in the horizontal components than in the vertical component of the grain positions. Indeed, we would expect the z component to be more accurate, as it is nearly constant during a scan. This was however not what we observed. Since both comparisons are based on the same experimental means and both used the *DCT* software package, this difference may arise from the 3DXRD analysis. It is however unclear which stage of data processing is the source of it. Concerning the difference in grain orientations, the results are very similar to those of Nervo *et al.* [71]. The distribution of disorientation angles shows a close agreement between DCT and 3DXRD, with a maximum at 0.02° , a mean at 0.03° (3DXRD integration step) and with most of the angles below 0.1° (DCT integration step).

Lastly, we have compared the DCT and 3DXRD grain sizes. The former were obtained from the DCT map, while the latter were evaluated from the spot intensities. In that sense, our comparison is different to that of Nervo *et al.*, who applied the intensity approach for both DCT and 3DXRD. The two techniques are in good agreement. The main discrepancies concerned the lower tail of the grain size distribution, where grains consistently appear smaller in the 3DXRD than in the DCT results. Nervo *et al.* attributed this to the use of a constant threshold to segment 3DXRD spots, while it is scaled by the spot maximum intensity in DCT. The same statement could be made here, but it is unclear how the DCT grain volumes are affected by the intensity back-projection.

IV.3 Conclusion

In this chapter, we have proposed a multi-technique cross-validation of the initial grain structure of Sample B, as a preparatory work for further investigations.

Regarding Sample A, we carried out the first direct comparison between the two imaging techniques, DCT and HEDM. It revealed, in particular, a 87% correspondence between the microstructures and an average distance of 4 μm between their respective grain boundary networks. This allowed us to cross-validate the reconstructions in terms of grain shapes and also to check the applicability of DCT on the Al-0.3Mn alloy.

Regarding Sample B, we compared the initial, undeformed grain structures given by DCT and 3DXRD. The analysis was based on 824 individual grains, initially identified by the DCT reconstruction and then retrieved in the 3DXRD data. The results suggest that the DCT did not miss any significant grains, which tends to validate the approach. A close agreement was found between the two data sets, in terms of grain centroids and orientations. The differences are clearly smaller than the pixel size of the 3DXRD detector (47.5 μm) and the DCT integration step (0.1°), respectively.

CHAPTER -V-

In-situ 3DXRD analyses of individual grain responses

Contents

V.1	In-situ grain monitoring throughout straining	90
V.1.1	Tracking of individual grains	90
V.1.2	Monitoring of grain average quantities	92
V.2	Assessment of intra-grain orientation distributions	94
V.2.1	Experimental data: azimuthal projection of diffraction spots	94
V.2.2	Simulated data: generation of spots from the grain ODF	96
V.2.3	Optimization problem	99
V.2.4	Application example	100
V.3	Experimental results	102
V.3.1	Representativeness	102
V.3.2	Grain rotations	102
V.3.3	Intra-grain orientation spreads	110
V.3.4	Grain elastic strains and stresses	115
V.4	Summary and discussion	120

This chapter deals with the experimental results concerning the *in situ* measurements of Sample B during uniaxial tensile loading up to 4.5% of plastic strain. First, we present the methodology for tracking and characterizing the individual grains from the initial state to the last deformed state (Section V.1). Then, we describe the methodology developed for determining intra-grain orientation distributions from 3DXRD measurements (Section V.2). Lastly, the results are presented and analysed in terms of grain rotations, intra-grain orientation spreads, elastic strains and stresses (Section V.3).

V.1 In-situ grain monitoring throughout straining

During the *in situ* experiments at ID11, the sample was measured by 3DXRD at six successive levels of plastic strains: $\epsilon = 0, 1.0, 1.5, 2.0, 2.5$ and 4.5% . Our study involves following the same individual grains throughout straining and monitoring their responses to the applied load. Since the 3DXRD scans were acquired separately without any *a priori* knowledge of the visible grains, specific data treatments are required, especially at $\epsilon = 2.5\%$ and 4.5% , which were acquired in two and three sub-volumes, respectively.

V.1.1 Tracking of individual grains

The data analysis of 3DXRD measurements was carried out separately for each scan using in-house MATLAB[®] routines. The procedure involved correcting the diffraction images for spatial distortions, subtracting background intensities and searching for individual diffraction spots. As a result of plastic deformation, we observed a progressive decay and broadening of spots intensities over the successive scans. This was accompanied by a significant raise of spot overlap, making simple thresholding inappropriate. The software DIGIgrain [106] was therefore employed. Based on a multi-threshold painting algorithm, it investigates coherently the 3D intensity distributions in the (u, v, ω) space to detect and separate slightly overlapping spots. This is illustrated on Figure V.1. The results revealed an increase of overlap from about 9% ($\epsilon = 0\%$) to 43% of the spots ($\epsilon = 4.5\%$), as well as a decrease of the number of individual spots from about 93,000 ($\epsilon = 0\%$) to 76,000 ($\epsilon = 2.0\%$). The latter observation was associated to the difficulty of isolating strongly overlapping spots and to the decay of spot intensities below a detectable level for small grains.

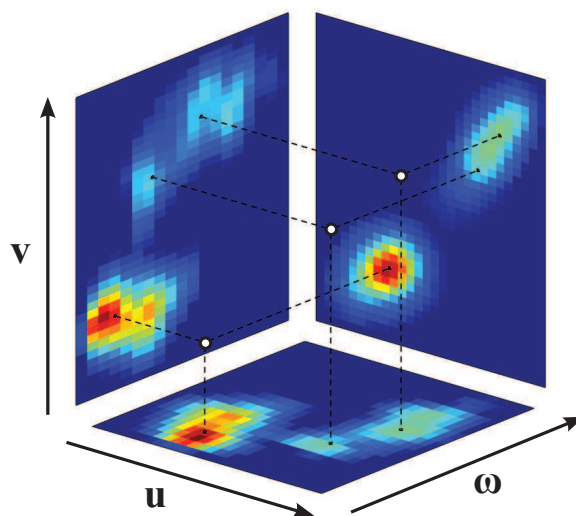


Figure V.1 – Example of three overlapping spots at $\epsilon = 2.0\%$. Projections of the intensity distribution along u, v and ω coordinates. The individual centroids were calculated by DIGIgrain.

The indexing stage was described in Subsection II.1.1 and consists in assigning the diffraction spots to their grains of origin. This is usually done separately for each scan, with no *a priori* knowledge of the grains inside the illuminated region. Then, to achieve grain tracking, the grains must be matched between the successive scans, following tedious procedures based on similarity criteria (distance, disorientation and size difference). This is even more difficult when the microstructure contains grains of both close positions and orientations (which is the case here). Furthermore, due to spot broadening and overlapping, the risk of erroneous indexing increases with plastic strain. This led us to consider the initial state of the specimen as a reference for grain indexing in the subsequent states. The initial state was analysed and cross-validated in Chapter IV. It consists of 824 grains, originally identified in the DCT reconstruction and retrieved in the 3DXRD measurements.

Due to the asymmetric loading conditions (the specimen is fixed at one end and deformed at the other end), grains may move in and out of the beam as strain increases. Hence, while the grains which are visible in the scanning area may not be the same at all strain levels, only the grains which are present at the initial state are analysed. This allowed a simple procedure for grain detection and tracking, where the grains of each state were indexed using the grains from the previous state. This approach is allowed by the small plastic strain increments involved, which result in only small displacements and rotations of the grains. At $\varepsilon = 2.5\%$ and $\varepsilon = 4.5\%$, grain positions were corrected by the appropriate vertical shifts before indexing the grains in the two and three sub-volumes, respectively.

Indexing statistics are illustrated on Figure V.2. The number of spots per grain ranges from 20 (minimum threshold imposed) to 141 (maximum theoretical value of observable reflections). Figure V.2 shows that it is initially 100 on average and decreases down to 77 as strain increases, with large variations between grains. This progressive decay of indexing statistics, attributed to the asymmetric loading conditions and the decrease in the number of detected spots, results in a progressive loss of tracked grains, as shown in Table V.1. We observe that 5 to 10% of the grain of the initial set are lost at every increment, resulting in a final number of 466 grains. Hence, 57% of the initially indexed grains could be followed throughout straining.

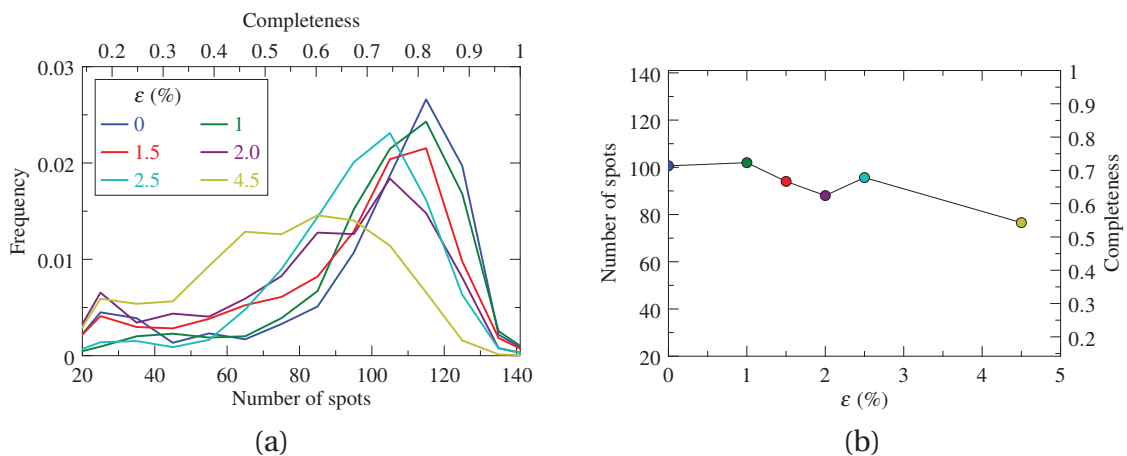


Figure V.2 – Evolution of grain completenesses with strain: (a) distributions and (b) mean values.

Table V.1 – Evolution of grain indexing and tracking with strain.

	0.0%	1.0%	1.5%	2.0%	2.5%	4.5%
Indexed grains	824	748	694	623	570	466
Tracking rate (%)	100	91	84	76	69	57

V.1.2 Monitoring of grain average quantities

The determination of the grain average quantities is carried out with respect to a given geometry of the setup. The latter was calibrated along with the characterization of the initial, undeformed state, in Chapter III. As the setup remained unchanged throughout the *in situ* experiment, we do not expect the global parameters to vary significantly. Hence, the initially calibrated values were used to characterize the subsequent deformation states. The only modifications concerned the drifting wavelength, which was varied according to the wavelength monitor.

The methodology described in Chapter III was applied to characterize each grain at each strain level. The *single-grain* fit provided the grain positions and orientations, based on the calibrated global parameters and the coordinates of the diffraction spots. The volumes were estimated from the scattered intensities. The lattice elastic strains and stresses were evaluated with respect to the initial, undeformed state. The different quantities and their standard errors were expressed in the laboratory coordinate system. At $\epsilon = 2.5\%$ and 4.5% , the sub-volumes were first treated separately and later assembled. This required re-calculating volume-weighted properties for the partly illuminated grains, visible over several sub-volumes.

Lastly, due to the imperfections in the loading conditions, we expected the specimen to slightly translate and rotate rigidly throughout straining. The rotation component, in particular, can be detrimental to the analysis, as it adds up to the *small* lattice rotations induced by the plastic deformation. Hence, the data had to be corrected for rigid body motions between the successive strain levels. This was done in the same way as for the DCT – 3DXRD comparison of Chapter IV. The motions were evaluated from the displacements of the grain centroids and the appropriate corrections were applied to transform each property back into the configuration of the initial state. The procedure revealed in particular that during the first strain increment, the sample horizontally shifted by almost $200\ \mu\text{m}$ and rotated by a non-negligible angle of $0.65(1)^\circ$. This motion can be easily explained by typical adjustments of the sample in the deformation rig upon loading. The vertical shift was only $56\ \mu\text{m}$ though, which limited the grain loss. The subsequent increments caused only negligible displacements with respect to $\epsilon = 1.0\%$.

The final grain sets are represented in Figure V.3, where it clearly appears that the same region of the sample was probed from $\epsilon = 0.0\%$ to 4.5% , although some grains were progressively lost throughout the analysis.

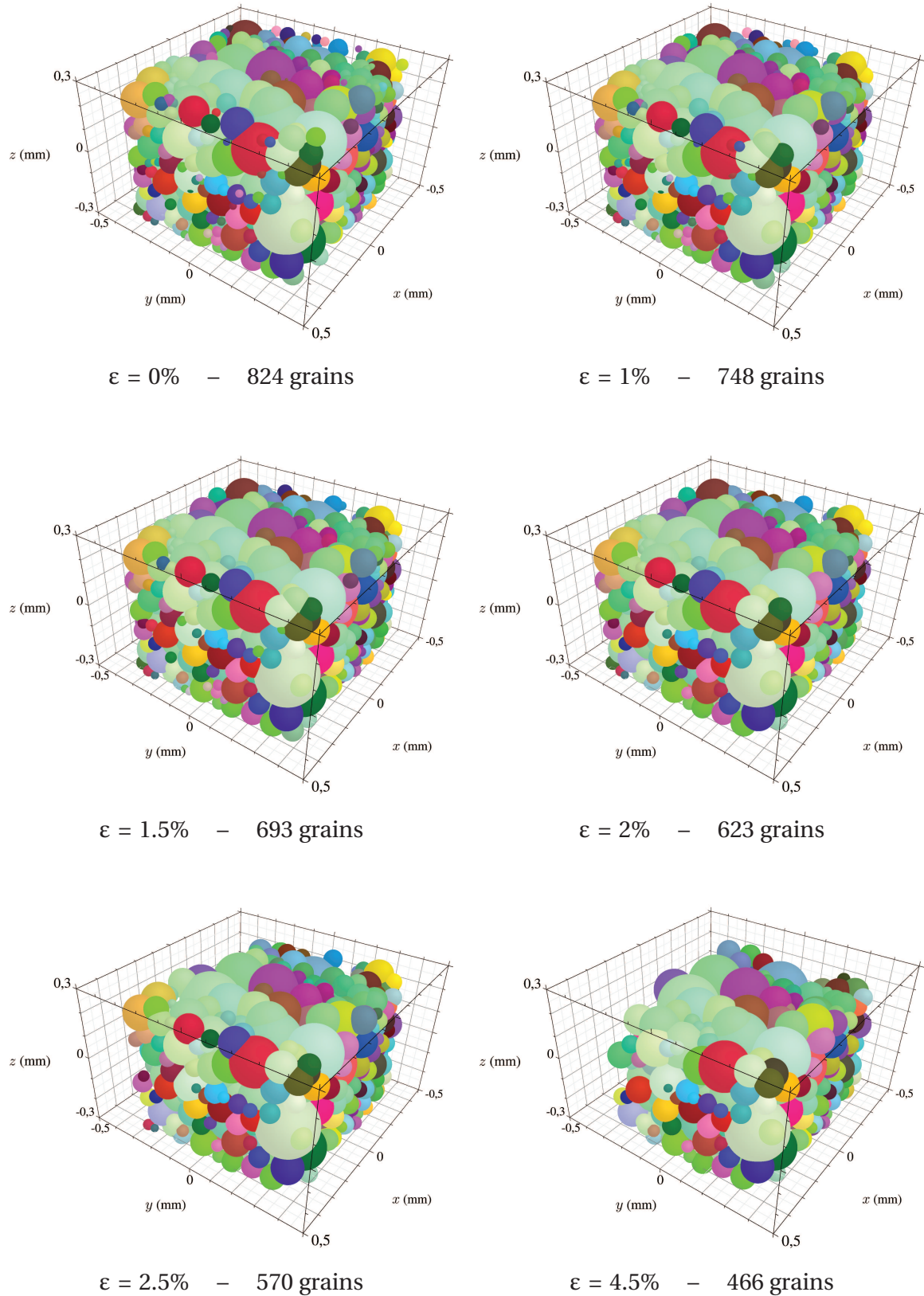


Figure V.3 – Representation of the grains indexed in the successive deformed states. Grains are represented by equivalent spheres, coloured by grain orientations. Colouring according to the Rodrigues vector components. Note the clear matching in terms of positions, orientations and sizes, and the progressive loss of grains with strain.

V.2 Assessment of intra-grain orientation distributions

The intra-grain orientation distribution can be mathematically described by an orientation distribution function (ODF). For a grain having a perfect lattice, this is a delta function. In the presence of an orientation distribution, the function can take different forms. The knowledge of grain ODFs is particularly useful in plasticity, as it is directly related to the deformation mechanisms inside the individual grains [50].

3DXRD data are usually employed to obtain average properties of grains, but as demonstrated by Poulsen *et al.* [49], it also gives access to individual grain ODFs. Hansen *et al.* [59] proposed an algebraic method to reconstruct ODFs from 3DXRD data, by solving a system of linear equations,

$$\mathbf{A}\mathbf{x} = \mathbf{b}$$

where \mathbf{b} denotes the measured data (pixel intensities), \mathbf{x} denotes the unknown ODF (discretized function) and \mathbf{A} is a forward projection matrix relating \mathbf{b} and \mathbf{x} . Depending on the amount of data and unknowns, the system can become computationally very large and thus requires the use of iterative regularization methods. Besides, although the knowledge of the full distributions is of interest, it seems that knowing their main attributes (i.e., anisotropy, principal directions and spreads) would be sufficient for analyses and comparisons to simulations.

In the present work, we developed and applied a new automated fitting procedure, which allows to directly assess the principal directions and spreads of intra-grain orientation distributions. The grain ODF is described by a predefined model with a small number of unknown parameters. The latter are then determined by maximizing the similarity between the experimental data (measured spots) and simulated data (generated spots from the ODF).

V.2.1 Experimental data: azimuthal projection of diffraction spots

a) System of coordinates

Various system of coordinates can be employed to represent diffraction spots. The most natural one consists of the (u, v, ω) triplet and is directly related to the detector frame. For a fixed geometry, it can be seen that u , v and ω vary with the grain orientation. Hence a non-delta distribution of the intra-grain orientations may result in non-delta distributions of all-three coordinates. Another commonly-used coordinate system consists of the $(2\theta, \eta, \omega)$, which is consistent with the configuration of concentric rings and is therefore more representative of the diffraction geometry. Furthermore, as a result of Bragg's law, 2θ does not depend on the orientation. A non-delta distribution of the intra-grain orientations may only result in non-delta distributions of η and ω coordinates. Hence, we can conclude from this analysis that the $(2\theta, \eta, \omega)$ representation shows some advantages over the (u, v, ω) one for the determination of intra-grain orientation spreads. It allows reducing the experimental data to 2D spots (η and ω coordinates), which can be more easily visualized and computationally handled.

b) Azimuthal projection

The intensity distribution of a diffraction spot is simply a projection of the intra-grain orientation field, which can be described as a 6D space combining position and orientation. Here, the grain shape and size are neglected, so that the positional component is reduced

to the grain centroid, \mathbf{r}_0 . This is a reasonable approximation in 3DXRD, as the detector is located far from the sample (small angular error) and the detector pixel size is of the same order as the grain size (low spatial resolution).

A spot is described as a collection of pixels p_i of coordinates (u_i, v_i, ω_i) and intensity values I_i . The transformation from (u, v, ω) to (η, ω) coordinates is thereafter referred to as *azimuthal projection*. For a given pixel, the corresponding diffraction vector, \mathbf{g}_L^i is given, in the laboratory coordinate system, by the backward projection equations (see Subsection III.1.4 for the notations):

$$\mathbf{g}_L^i = \frac{1}{\lambda} \frac{\mathbf{T}^{-1} \mathbf{s}_D^i - \boldsymbol{\Omega}_\omega \mathbf{r}_0 + D \mathbf{e}_1}{\|\mathbf{T}^{-1} \mathbf{s}_D^i - \boldsymbol{\Omega}_\omega \mathbf{r}_0 + D \mathbf{e}_1\|} - \frac{\mathbf{e}_1}{\lambda} \quad \text{with} \quad \mathbf{s}_D^i = \begin{bmatrix} 0 \\ (u_B - u_i) \pi_u \\ (v_i - v_B) \pi_v \end{bmatrix}$$

Then, the η coordinate is obtained as:

$$\eta_i = \text{atan2}\left(-\mathbf{g}_L^i \cdot \mathbf{e}_2, \mathbf{g}_L^i \cdot \mathbf{e}_3\right) \quad (\text{V.1})$$

Interestingly, this definition makes η independent of the grain position. We will show later that this allows for a more direct generation of the simulated diffraction spots. The azimuthal projection is however not independent of the grain size and shape, which will have to be accounted for in the fitting procedure.

The azimuthal projection is illustrated on Figure V.4. The procedure consists in projecting and integrating the intensity of a 3D spot onto a specific 2D plane. The (u, v) -coordinates are transformed to η -coordinates using Equation V.1, while the ω -coordinates are not affected by the projection. Hence, each pixel column in Figure V.4-b corresponds to a 2D image in Figure V.4-a and represents the integrated intensity distribution along the η direction. The η range is divided into equal-sized bins. For consistency with the detector pixel size, the η -bin size can vary from one spot to another and is chosen equal to the local η extent of the detector pixels. The latter is roughly given by $1/r$, where r is the radius in pixels of the corresponding diffraction ring. Depending on the η_i coordinates, the pixel intensities, I_i , are added up to the “nearest” bins in the (η, ω) projection.

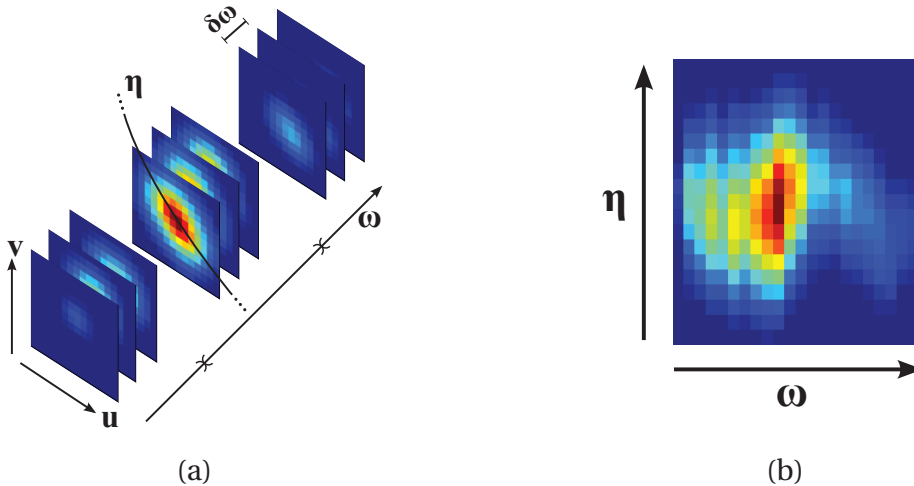


Figure V.4 – Illustration of azimuthal projection: (a) experimental diffraction spot in (u, v, ω) coordinates and (b) azimuthal projection in (η, ω) coordinates.

V.2.2 Simulated data: generation of spots from the grain ODF

a) Description of the ODF

In general, at relatively low strains, most grains develop “unimodal” orientation distributions, composed of an average rotation and an orientation spread [14]. Therefore, a grain ODF can be conveniently decomposed into an average orientation, \mathbf{R}_0 , and a disorientation distribution function, $\mathcal{P}(\Delta\mathbf{R})$, where $\Delta\mathbf{R}$ denotes a disorientation with respect to \mathbf{R}_0 . This description is evidently very general and holds for any kind of orientation descriptor. In this work, we use Rodrigues vectors. For cubic crystals, the fundamental region of the Rodrigues orientation space, shown in Figure V.6-a, is a truncated cube, where orientation fibres appear as straight lines. Compared to the usual Euler space, it offers the advantages of exhibiting relatively low distortions and no degeneracy [107].

It was observed experimentally that typical unimodal orientation spreads induced by plastic deformation exhibit nearly Gaussian distributions along the three principal axes [14, 91]. This can be mathematically described by a tri-Gaussian law:

$$\mathcal{P}(\Delta\mathbf{R}) = \prod_{i=1}^3 \frac{1}{\sqrt{2\pi}\lambda_i} \exp\left[-\frac{1}{2}\left(\frac{\Delta R'_i}{\lambda_i}\right)^2\right] \quad (\text{V.2})$$

where $\Delta R'_i$ is the disorientation component along the i^{th} principal axis. The three principal axes are related to the three laboratory directions using:

$$\Delta\mathbf{R}' = \mathbf{K} \Delta\mathbf{R}$$

where \mathbf{K} is a rotation matrix, $\Delta\mathbf{R}$ is a disorientation expressed in the laboratory coordinate system and $\Delta\mathbf{R}'$ is expressed in a coordinate system depending on the distribution axes. It follows that \mathcal{P} depends on six parameters, including the three standard deviations ($\lambda_1 \geq \lambda_2 \geq \lambda_3$) and three parameters describing \mathbf{K} .

For visualization purposes, we can represent such a distribution in the Rodrigues space as an ellipsoid, of semi-axes aligned with the distribution principal axes and radii equal to the distribution standard deviations. The ellipsoid is centred on the corresponding grain orientation to represent the orientation distribution, while it is rather centred on zero to represent only the disorientation part¹. Figure V.5 illustrates the cases of an isotropic distribution ($\lambda_1 = \lambda_2 = \lambda_3$), an anisotropic distribution with principal axes aligned with the laboratory directions ($\lambda_1 > \lambda_2 \geq \lambda_3$, $\mathbf{K} = \mathbf{I}$) and an arbitrary distribution ($\lambda_1 \geq \lambda_2 \geq \lambda_3$, $\mathbf{K} \neq \mathbf{I}$).

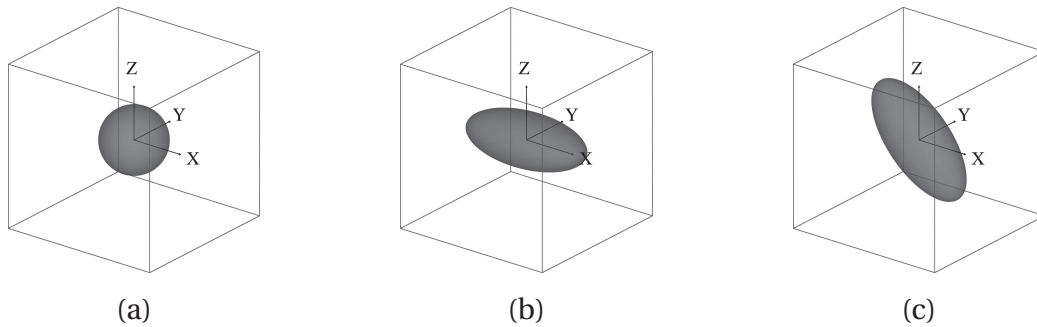


Figure V.5 – Representation of tri-Gaussian ODFs by ellipsoids. Illustration of (a) an isotropic distribution ($\lambda_1 = \lambda_2 = \lambda_3$), (b) an anisotropic distribution with principal axes aligned with the laboratory directions ($\lambda_1 > \lambda_2 \geq \lambda_3$, $\mathbf{K} = \mathbf{I}$) and (c) an arbitrary distribution ($\lambda_1 \geq \lambda_2 \geq \lambda_3$, $\mathbf{K} \neq \mathbf{I}$).

¹Note that the distortion of Rodrigues orientation space, albeit low, implies not only a shift, but also a rotation of the ellipsoid as it is moved from the grain average orientation to the origin.

b) Truncation and discretization of the ODF

Prior to the generation of spots, the grain ODF must be discretized. At low plastic strains, we can expect the orientation spreads to be small. This allows not to sample the disorientation distribution on the full fundamental region of the Rodrigues space, but only on a relatively small box of size Δr and centred on zero. The value of Δr must be chosen so that only a negligible part of the information is lost due to this truncation. For normal laws, it is known that $> 99\%$ of the data are contained within $\mu \pm 3\sigma$, where μ is the mean and σ is the standard error. We can therefore reasonably impose that $\Delta r/2 = 3\lambda_1$. Knowing the size, the box can be discretized as a volume of $N \times N \times N$ voxels with the origin in the central voxel. This results in a set of N^3 sampling disorientations, $\{\Delta \mathbf{R}_i\}$, arranged on a cubic grid. The corresponding probability densities (or, equivalently, grain volume fractions) are given by:

$$P_i = \frac{\mathcal{P}(\Delta \mathbf{R}_i)}{\sum_j \mathcal{P}(\Delta \mathbf{R}_j)} \quad (\text{V.3})$$

The voxel size, $\delta r = \Delta r/N$, must be chosen as a compromise between quality and quantity. Indeed, when δr is too large (typically $> \lambda_i$), the ODF is undersampled and may not allow to produce smooth, continuous spots. To avoid that problem, δr is taken smaller than $2\lambda_3$, where λ_3 was defined as the lowest standard deviation of the tri-Gaussian. This condition allows for a reasonable description of the ODF. However, decreasing δr increases N^3 , which might rapidly become computationally costly and thus inappropriate for the fitting procedure. In practice, we observed that the optimization could be solved in reasonable times up to $N^3 \approx 500,000$ (i.e., $N \approx 80$). The discretization is illustrated on Figure V.6 for an arbitrary ODF.

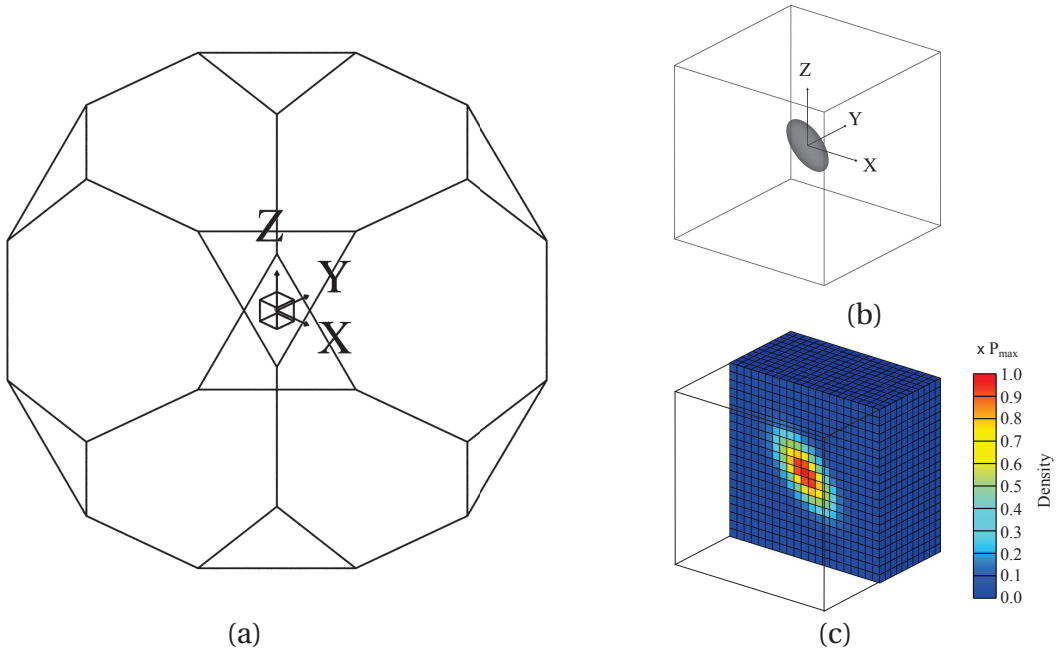


Figure V.6 – Truncation and discretization of a grain ODF. The parameter values are $\lambda_1 = 0.0087$ ($\approx 1^\circ$) and $\lambda_2 = \lambda_3 = 0.0044$ ($\approx 0.5^\circ$). For the truncation and discretization, $\Delta r = 0.0524$ ($\approx 6^\circ$) and $N = 23$, resulting in $\delta r = 0.0022$ ($\approx 0.25^\circ$). The disorientation distribution is represented (a) in the Rodrigues orientation space, (b) as an ellipsoid in the truncation box and (c) as a discrete volume containing 12167 voxels.

c) Generation of the spots

Let us consider an ODF, described by an average orientation \mathbf{R}_0 , a set of disorientations $\{\Delta\mathbf{R}_i\}$ and the associated probability densities $\{P_i\}$. Using Rodrigues vectors, the actual orientation of each ODF voxel is obtained as [69]:

$$\mathbf{R}_i = (\mathbf{R}_0, \Delta\mathbf{R}_i) = \frac{\mathbf{R}_0 + \Delta\mathbf{R}_i - \mathbf{R}_0 \times \Delta\mathbf{R}_i}{1 - \mathbf{R}_0 \cdot \Delta\mathbf{R}_i} \quad (\text{V.4})$$

From the discrete ODF, the aim is to generate the spot intensity distribution corresponding to a given (hkl) reflection, measured experimentally. This requires the use of a *virtual diffractometer*, which was developed based on the forward projection equations of Subsection III.1.4. The method involves three steps:

1. **Calculation of the (η, ω) coordinates.** For each ODF voxel of orientation \mathbf{R}_i , the corresponding ω_i coordinate is the solution of the trigonometric form of Equation III.25. The diffraction vector, \mathbf{g}_L^i , is given by (see Subsection III.1.4 for the notations):

$$\mathbf{g}_L = \Omega_{\omega_i} \mathbf{U}_i^{-1} \mathbf{B} \begin{pmatrix} h \\ k \\ l \end{pmatrix} \quad (\text{V.5})$$

where \mathbf{U}_i is the orientation in matrix notation. Then, the η_i coordinate is provided by Equation V.1. As a result of the choice of the azimuthal projection to represent the experimental spots, we can observe that the simulation is remarkably straightforward and does not involve any use of the grain position or the detector configuration.

2. **Calculation of the spot intensity distribution.** We use the same (η, ω) grid for the simulated spot as for the experimental one (azimuthal projection) to later facilitate the comparison between the two. The points falling outside the grid are ignored. Otherwise, depending of the (η_i, ω_i) coordinates, the densities values, P_i , are added up to the intensity values of the “nearest” bins in the grid.
3. **Correction for the ODF discretization and the grain size.** The discretization of the ODF induces errors in the generated spots and, when it is too coarse, can even leads to strong discontinuities in the intensity distributions. Furthermore, as mentioned earlier, the azimuthal projection is not insensitive to the grain shape and size, which participate to the spot broadening along η . This must be taken into account to capture the actual spread and anisotropy of the grain orientation distribution. Therefore, the simulated spot is corrected by convolving its image with two Gaussian filters. The first one concerns the angular extent of the ODF voxels and is defined as:

$$G_1(\eta, \omega) = \frac{1}{2\pi\theta^2} \exp\left(-\frac{\eta^2 + \omega^2}{2\theta^2}\right) \quad (\text{V.6})$$

with,

$$\theta = \text{atan}\delta r \simeq \delta r$$

The second filter is 1D only and acts along η to correct the spatial extent of the grain. It is defined as:

$$G_2(\eta) = \frac{1}{\sqrt{2\pi}\sigma^2} \exp\left(-\frac{\eta^2}{2\sigma^2}\right) \quad (\text{V.7})$$

where σ is taken equal to the grain equivalent radius. These two filters are applied successively to produce the final intensity distribution of the spot.

V.2.3 Optimization problem

The present approach consists in determining the ODF that provides the best fit between the experimental and simulated diffraction data. This is formulated as an optimization problem, where the objective function measures the similarity between the experimental spots (azimuthal projection) and simulated spots (virtual diffractometer) and has to be maximized over the six parameters of the tri-Gaussian ODF.

a) Comparison of experimental and simulated spots

The similarity between experimental and simulated spots is quantified by the Pearson product-moment correlation coefficient, defined as:

$$r = \frac{\frac{1}{N_\eta N_\omega - 1} \sum_{i=1}^{N_\eta} \sum_{j=1}^{N_\omega} (I_{\text{exp}}^{ij} - I_{\text{exp}}) (I_{\text{sim}}^{ij} - I_{\text{sim}})}{\sqrt{\frac{1}{N_\eta N_\omega - 1} \sum_{i=1}^{N_\eta} \sum_{j=1}^{N_\omega} (I_{\text{exp}}^{ij} - I_{\text{exp}})^2} \sqrt{\frac{1}{N_\eta N_\omega - 1} \sum_{i=1}^{N_\eta} \sum_{j=1}^{N_\omega} (I_{\text{sim}}^{ij} - I_{\text{sim}})^2}} \quad (\text{V.8})$$

where I_{exp}^{ij} and I_{sim}^{ij} are the intensities in the experiment and simulation azimuthal projections, respectively. N_η and N_ω are the number of bins along η and ω coordinates. I_{exp} and I_{sim} represent the averages of I_{exp}^{ij} and I_{sim}^{ij} . The correlation coefficient is insensitive to the difference in average values, so that the comparison does not require to normalize the intensities. The higher the value of r (ranging from 0 to 1), the better the similarity between the experimental and simulated spots.

b) Objective function

The objective function depends on the six parameters of the tri-Gaussian model: the three standard deviations $\lambda_{i=1,2,3}$ and three parameters describing the rotation matrix, \mathbf{K} . Initially, the standard deviations can be set to an arbitrary (but realistic) positive value (for example, $\delta\omega$). The three rotation parameters can be chosen so that the principal axes of the distribution are initially aligned with the laboratory axes ($\mathbf{K} = \mathbf{I}$).

Then, given a current state of the parameters, the ODF is truncated, discretized and submitted to the virtual diffractometer to generate simulated spots. The latter are compared with the experimental ones using Equation V.8. The similarity between the two is thus defined as:

$$\mathcal{O} = \sum_k r_k \quad (\text{V.9})$$

where r_k is the correlation coefficient and k runs over the available spots for the grain. Thus defined, \mathcal{O} is a non-linear function that must be maximized with respect to the six ODF parameters.

The complete method (azimuthal projection, virtual diffractometer and optimization) was implemented in C, using in particular the NLOpt library (subplex algorithm) for local derivative-free optimization [98, 103] and the Orilib library for orientation and rotation calculations [104].

V.2.4 Application example

The method is exemplified here on a selected bulk grain out of the 466 grains that were tracked up to $\epsilon = 4.5\%$. The grain has an average size of 60 μm and an arbitrary orientation (26° away from Cube).

a) Experimental data

The experimental data initially consisted of 123 spots at $\epsilon = 1.0\%$ and 83 spots at $\epsilon = 4.5\%$. The overlapping spots were removed to avoid any influence of the intensity arising from other grains. This resulted in a number of 91 available spots at $\epsilon = 1.0\%$ and 47 available spots at $\epsilon = 4.5\%$, which were submitted to the azimuthal projection. Only 24 spots could be retrieved in the five deformed states. The evolutions of eight of them are shown Figure V.7-a. We can observe that the spots tend to broaden along specific directions in the (η, ω) space, revealing that both the angular extent and the anisotropy of the orientation distribution developed throughout straining.

b) Results of the optimization

The final simulated spots resulting from the optimization are shown in Figure V.7-b. Numerical results are provided as well in Table V.2. For all spots, a good agreement is found between experiment and simulation in terms of broadening directions and extents. The similarity is measured by the Pearson correlation coefficient, which is on average 0.80 at $\epsilon = 1.0\%$ and reaches 0.95 at $\epsilon = 4.5\%$. The final results reveal that the grain develops an anisotropic orientation distribution throughout straining, with $\lambda_1 \simeq 2\lambda_2$. The major principal axis, associated to λ_1 , appears to be close to the X direction of the laboratory.

Table V.2 – Assessment of intra-grain orientation spreads: results of the fitting procedure for a selected grain. The principal axis is the longest axis (corresponding to λ_1).

ϵ (%)	Nb of spots	λ_1 (°)	λ_2 (°)	λ_3 (°)	Principal axis			$\langle r \rangle$
					x	y	z	
1.0	91	0.08	0.04	0.02	0.836	0.119	-0.536	0.80
1.5	83	0.16	0.08	0.05	0.936	0.194	-0.292	0.86
2.0	78	0.22	0.09	0.07	0.946	0.147	-0.288	0.88
2.5	44	0.30	0.13	0.09	0.963	0.050	-0.266	0.93
4.5	47	0.56	0.25	0.15	0.962	0.060	-0.267	0.95

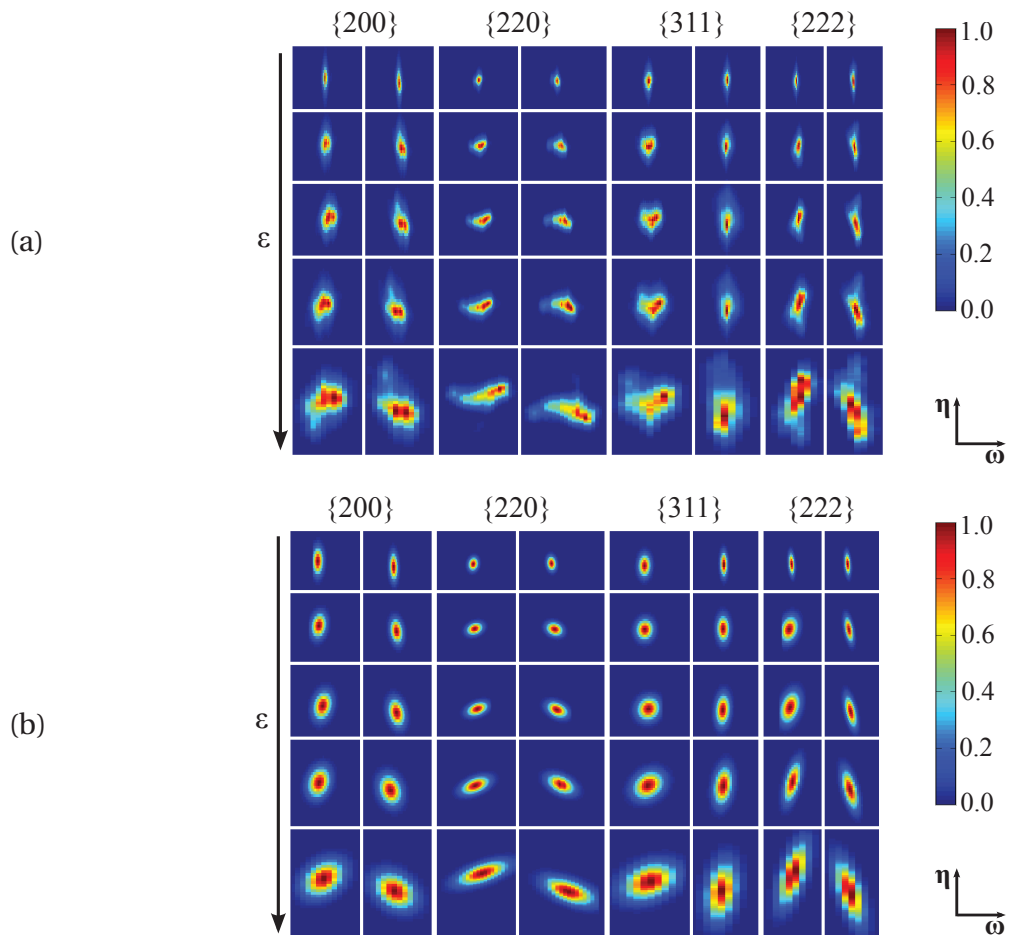


Figure V.7 – Comparison between experimental and simulation spots for a selected grain: (a) Experimental and (b) Simulation. The spots are grouped by types of reflection (columns) and ordered by increasing strain (rows). The first and last rows correspond to $\epsilon = 1.0\%$ and $\epsilon = 4.5\%$, respectively. The true hkl indices are (from left to right): 200 , $\bar{2}00$, 220 , $2\bar{2}0$, $31\bar{1}$, $\bar{1}3\bar{1}$, $2\bar{2}2$ and $\bar{2}\bar{2}\bar{2}$. The spot intensities are coloured using a linear scale in arbitrary unit with the maximum equal to 1.

V.3 Experimental results

This section presents the results of the *in situ* monitoring of 466 individual grains from the initial undeformed state to 4.5% of plastic strain. The measured grain behaviours are analysed in terms of rotations, orientation spreads, elastic strains and stresses, using different metrics and representations.

V.3.1 Representativeness

The 466 individual grains that were tracked up to 4.5%, represent a sub-set of the initial set of 824 indexed grains. The statistical representativeness must be preserved though and ensured by the significant number of remaining grains. This can be ascertained with regard to the grain distributions. The spatial distribution was already illustrated on Figure V.3, showing that the 466 grains span the same region of space as the 824 grains. The average grain sizes were also found to be close: 76 μm for the 426 grains and 91 μm for the 824 grains. This difference of 15 μm is due to small grains, with diameters smaller than 50 μm , which were present in the initial state and were not retrieved in the subsequent ones. The orientation distributions are shown in Figure V.8. We observe a clear correspondence between the two $\{111\}$ pole figures. Although a relatively strong texture can be noticed (attributed to the material and sample preparations), the data provide a good coverage of orientation space (Figure V.9).

V.3.2 Grain rotations

As mentioned in the literature review, previous works on plastic deformation explored individual grain rotations using different approaches. Winther *et al.* [8] in particular relied on the inverse pole figure (IPF) representation, which is commonly used to visualize and investigate grain orientations and rotations in uniaxial tension. The authors identified a relation to the initial orientation of the rotation paths, according to which they proposed a division of the stereographic triangle into four regions. As a first step, the present results can be analysed with regard to that division. This is done in Figure V.9, showing an agreement with the observations of Winther *et al.* [8] in region 1 (notable tendency to rotate towards the $[100]$ - $[111]$ line) and region 3 (tendency to rotate along the $[110]$ - $[111]$ line towards the $[111]$ pole). In regions 2 and 4, we can observe that the rotations are generally smaller and also more variable, even for grains of close orientations.

Although the IPF representation allows for quantitative studies of texture evolution, it remains only qualitative for individual grain rotations, since it leaves out the rotation component around the tensile axis. In fact, the study of rotations is in general problematic, as these quantities are not readily manipulable and comparable. Hence, Quey *et al.* [13, 41] largely based their analysis on the decomposition of rotations into axis / angle pairs, which allows for simple and palpable metrics. Here, we propose to adapt and apply their approach (used for plane strain compression) to the case of uniaxial tension. Thereafter, each rotation is described as an axis / angle pair, (\mathbf{r}, θ) , where \mathbf{r} is a unit vector expressed in the laboratory coordinate system and θ is positive. The rotations can be analysed with regard to the consecutive strain increments or with respect to the initial orientation.

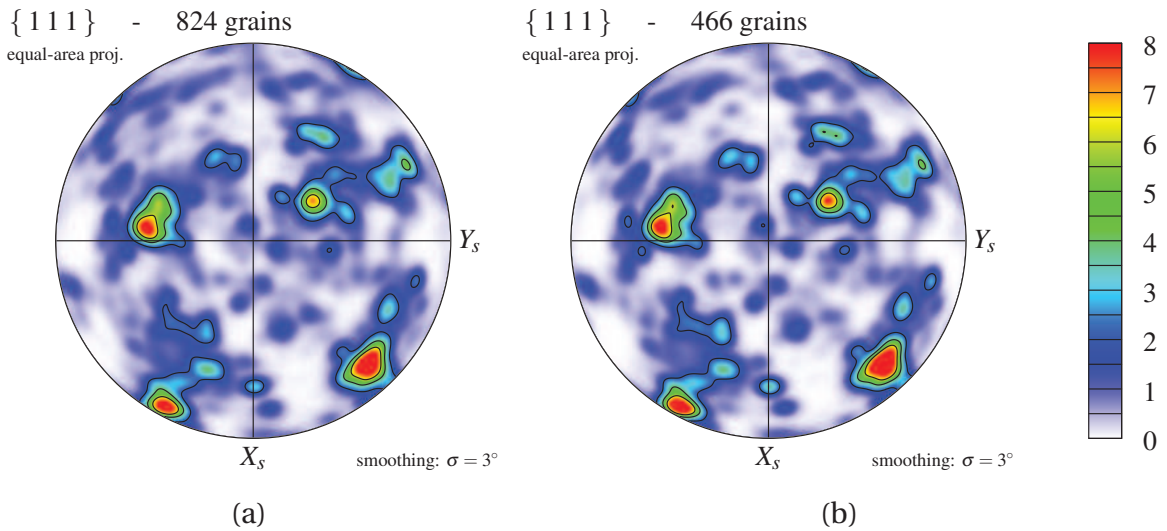


Figure V.8 – Macrotecture of Sample B. $\{111\}$ pole figures (equal-area projection) showing the orientation distribution of (a) the 824 initial grains and (b) the 466 tracked grains, as a density field with contour lines.

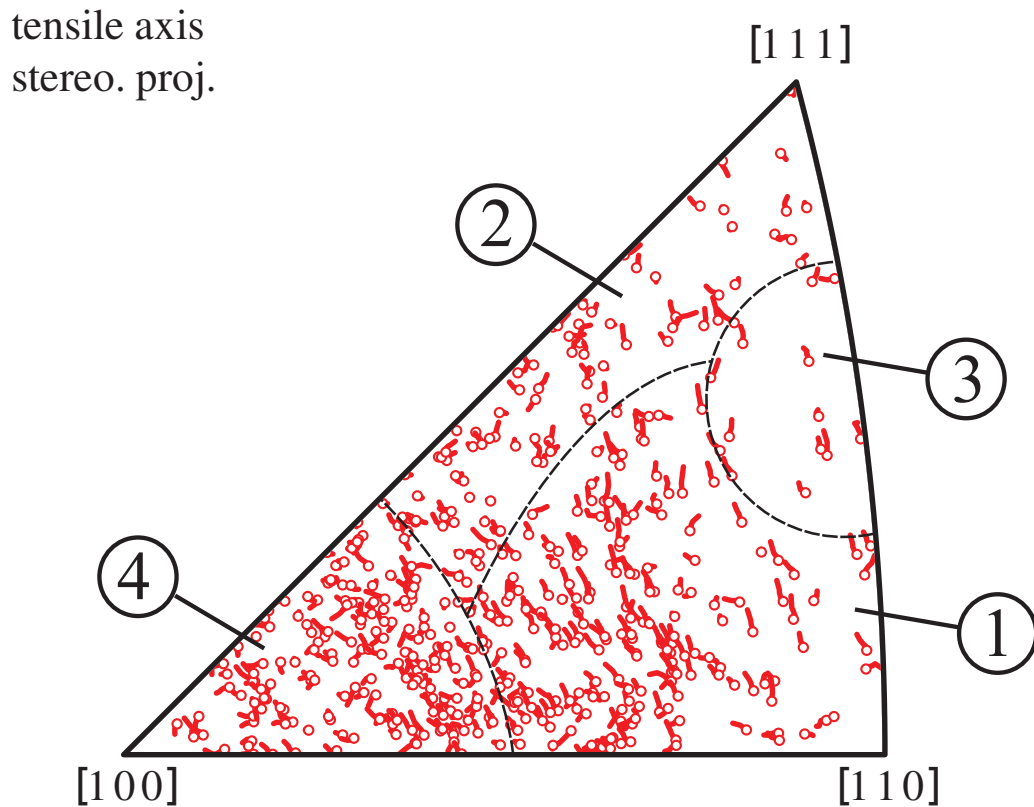


Figure V.9 – Orientation and rotation of the tensile axis per individual grain. Inverse pole figure (stereographic projection) showing the initial orientations (red circle) and rotation paths (red lines) of the grains. The triangle is divided in four regions, as proposed by Winther *et al.* [8]. Region 4 covers all orientations within 24° of $[100]$. Region 3 covers all orientations within 8° of $[221]$. Region 1 covers all the remaining orientations within 24° of $[110]$. Region 2 covers all the rest of the triangle.

a) Incremental rotations

The incremental rotations are the rotations from one deformation state to the next. The incremental rotation angles are referred to as θ_i . To allow for comparisons between the successive θ_i , the angles are scaled to correspond to the same strain increment of 1%. The corrected angles are referred to as $\hat{\theta}_i$ and calculated as $\hat{\theta}_i = \theta_i \times 0.01 / \Delta\varepsilon$, where $\Delta\varepsilon$ is the corresponding strain increment. Figure V.10 plots the distributions of incremental rotation angles. We can observe that $\hat{\theta}_i$ increases from $\varepsilon = 1.0\%$ to $\varepsilon = 1.5\%$, remains stable up to $\varepsilon = 2.5\%$ and then decreases in the last increment.

The successive $\hat{\theta}_i$ are compared in Figure V.11. The Pearson correlation coefficient, ρ , is a measure of the linear correlation between two variables. A value of 0 indicates no correlation, 1 is for a total correlation and -1 for a total anti-correlation. We can observe that the increase and decrease in θ_i come with a loss of correlation. Hence, the highest value of ρ reaches 0.9 and is found between $\theta_i^{1.5}$ and $\theta_i^{2.0}$, within the plateau observed in Figure V.10. The lowest value of ρ is 0.36 and indicates a poor correlation between $\theta_i^{1.0}$ and $\theta_i^{1.5}$. The first increment might be affected by late and different onsets of plasticity, from grain to grain, which would be consistent with both the small angles and the low correlation observed.

Overall, the rotations are rather small. Up to 2.5% in particular, the average θ_0 is about 0.13 (in absolute) and represents only four to five times the angular precision achieved on grain orientations. This raises the question on the error in the determination of the rotation axes. Indeed, it was shown by Bate *et al.* [108] that an error δ in determining the rotation angle θ , results in an angular error β in the rotation axis, of:

$$\beta = \text{atan}\left(\frac{\delta}{\theta}\right) \quad (\text{V.10})$$

This yields $\beta = 20^\circ$ in the present case. Hence, a significant part of the rotation axes are poorly determined. This led us not to consider the incremental rotation axis in the analysis.

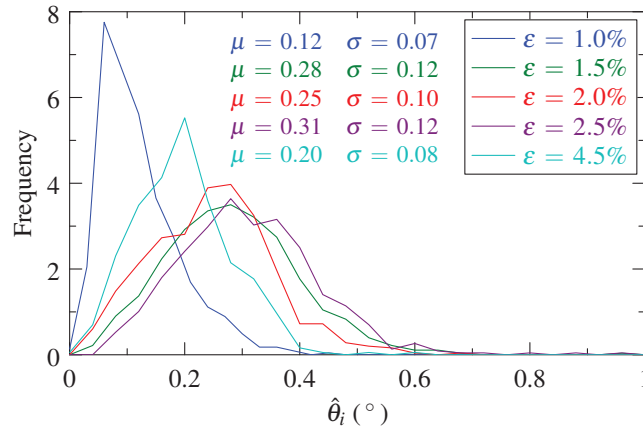


Figure V.10 – Rotation angles of the successive strain increments, $\hat{\theta}_i$. Distribution mean values, μ , and standard deviations, σ .

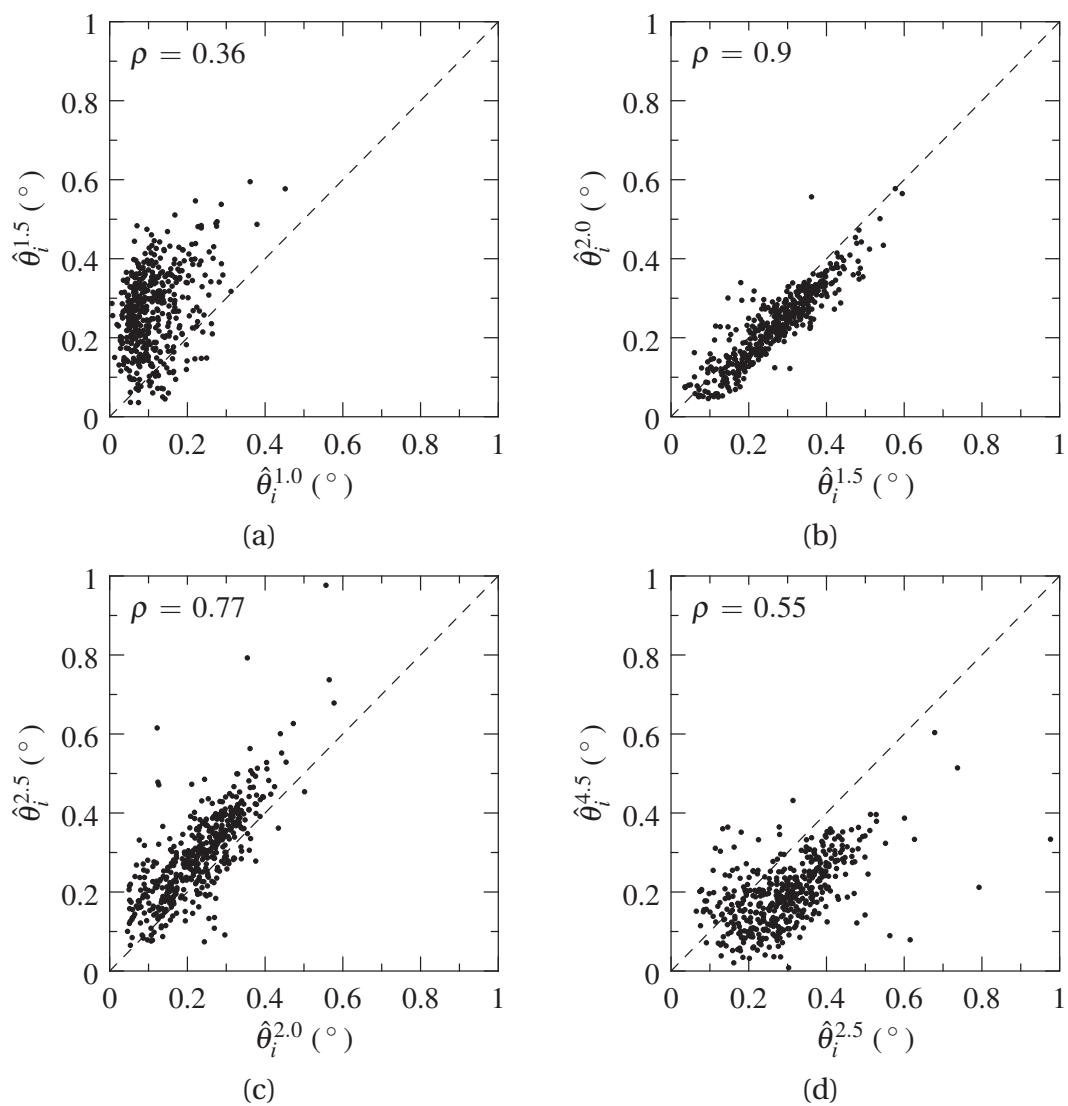


Figure V.11 – Correlation between the rotation angles of the successive strain increments, $\hat{\theta}_i$. ρ is the Pearson correlation coefficient.

b) Rotations with respect to the initial orientation

The rotation angles with respect to the initial orientations, referred to as θ_0 , are presented in Figure V.12. We can clearly observe that the rotations increase with strain, up to an average value of 0.80° . Along with this increase, the distribution broadens as well, which shows that the grains are not equally affected and rotate at different rates. The final angles range from 0.1° to 1.6° and denote a high variability of the rotations, which is consistent with the observations of Figure V.9.

The rotation axes with respect to the initial orientations, referred to as \mathbf{r}_0 , are shown in Figure V.13. Only the last strain level is considered to minimize the angular errors on the determination of the axes. The distribution indicates a high concentration close to the periphery of the circle, with higher levels about the X direction, which are attributed to the sample texture. The results suggest a tendency of the rotation axes to lie perpendicular to the tensile direction, Z. This can be understood from the viewpoint of crystallographic slip. In uniaxial tension of fcc crystals, the most highly stressed slip system is $(1\ 1\ \bar{1})\ [1\ 0\ 1]$ (when the tensile axis falls in the basic IPF triangle). The corresponding rotation axis, also referred to as spin vector, is $(1\ \bar{1}\ \bar{1})$. As shown in Figure V.14, depending on the crystal orientation, the angle $\alpha(\mathbf{r}_0, \mathbf{z})$ between the spin vectors and the tensile axis varies between 62° and 90° . The distribution of $\alpha(\mathbf{r}_0, \mathbf{z})$ for a uniform orientation distribution, shown in Figure V.15, indicates that the spin vectors are more frequently perpendicular to the tensile axis; this is accentuated when considering the experimental distribution. Obviously, this provides only a first-order explanation of the experimental distribution, as the plastic deformation results from the combined activities of several slip systems.

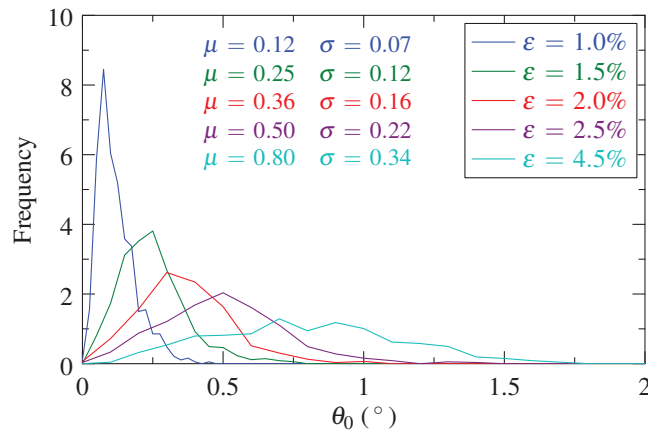


Figure V.12 – Rotation angles with respect to the initial orientations, θ_0 , for the successive deformation states. The distribution mean values (μ) and standard deviations (σ) are provided.

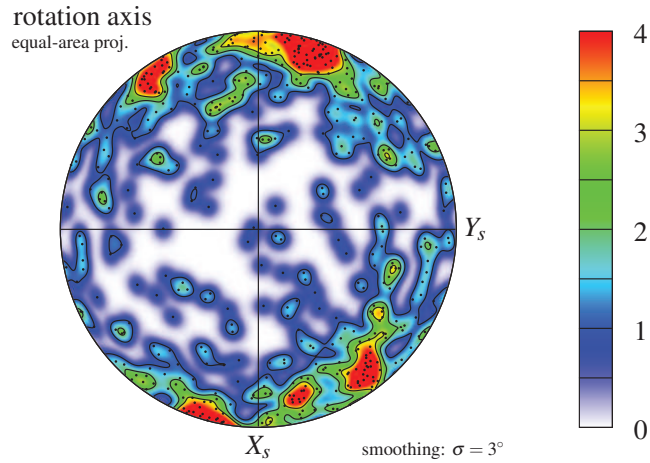


Figure V.13 – Rotation axes with respect to the initial orientations, \mathbf{r}_0 , for $\epsilon = 4.5\%$. Pole figure (equal-area projection) showing the individual rotation axes (black dots), with a density field and contour lines added.

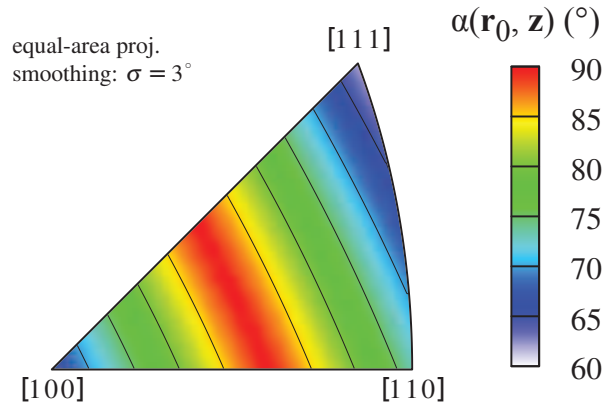


Figure V.14 – Orientation dependency of the angle α between the tensile axis \mathbf{z} and the spin vector \mathbf{r}_0 of the most highly stressed slip system $(11\bar{1})[101]$.

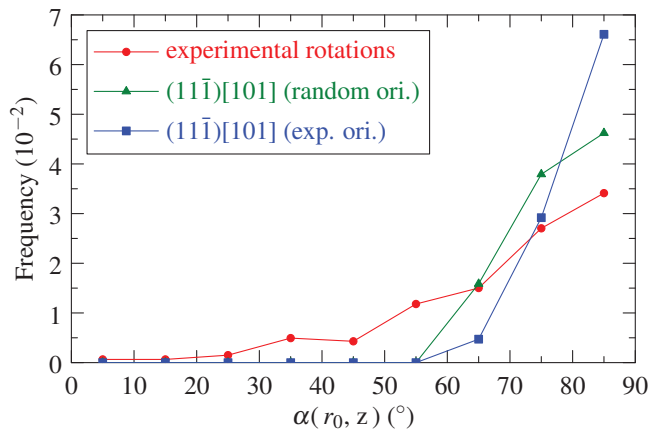


Figure V.15 – Distribution of angles α between the tensile axis and the rotation axes \mathbf{r}_0 , considering the most highly stressed slip system $(11\bar{1})[101]$ for uniformly-distributed random orientations (green) and the experimental orientations (blue). The red curve shows the actual experimental distribution of $\alpha(\mathbf{r}_0, \mathbf{z})$.

c) Relation to the grain orientations

As illustrated on Figure V.9, the results show that two grains of close orientations can either exhibit similar rotation paths or rotate in two very different manners. Quey *et al.* [41] referred to this orientation dependency as the variability at constant orientation (VCO) of the rotations. Ideally, the VCO should be evaluated by comparing the rotations of several grains of identical orientations and for several different orientations to span all the orientation space. This is however not possible, due to the finite number of grains.

An alternate approach was proposed by Quey *et al.* [41] to determine the average VCO over all orientations. This is done by comparing the rotations of all pairs of grains. The differences in rotation between (\mathbf{r}_1, θ_1) and (\mathbf{r}_2, θ_2) can be quantified by the angle between the axes:

$$\alpha = \text{acos}(\mathbf{r}_1 \cdot \mathbf{r}_2) \tag{V.11}$$

and the relative difference between the angles:

$$\Delta_r\theta = 2 \left| \frac{\theta_1 - \theta_2}{\theta_1 + \theta_2} \right| \tag{V.12}$$

Then, by considering the disorientation angle of the pairs, α and $\Delta_r\theta$ can be plotted as functions of the disorientation angle. The VCO is calculated by extrapolating at zero disorientation the average variability tendency over given intervals.

Due to the axial symmetry of loading, the influence of the grain orientation is only related to the orientation with respect to the tensile axis. Hence, for the comparison of (\mathbf{r}_1, θ_1) and (\mathbf{r}_2, θ_2) , one grain of the pair must be rotated until it reaches the minimum disorientation between the two. The grain rotation axis is then transformed accordingly, while the rotation angle remains unchanged. Figure V.16 shows the distribution of the disorientations of the pairs, with and without symmetry considerations. We can observe that axial symmetry displaces the distribution towards lower disorientations and thus enables to enrich the interval used for the determination of the VCO.

The evaluation of the VCO is illustrated in Figure V.17. Intervals of 3° were considered to compute the average tendencies. The smooth variations reasonably allows for extrapolating the VCO at zero. The values obtained are 49° and 0.44 for the rotation axes and rotation angles, respectively. These non-zero values indicate that the rotations are controlled not only by the orientations, but also by grain interactions.

The overall variability (V) is defined as the average variability over all pairs. The values obtained are 78° and 0.5 for the rotation axes and rotation angles, respectively. The VCO values can be compared to the V values. The ratio VCO/V ranges from 0 to 1. The higher the value, the stronger the effect of grain interaction compared to the effect of the orientation. The ratios obtained are 0.63 for the rotation axes and 0.88 for the rotation angles, suggesting a notable influence of grain interaction on rotation axes and a relatively strong influence on rotation angles.

These results provide a global measure of the variability. However, as pointed out by Winther *et al.* [8] and also observed in Figure V.9, the variability appears to vary from one region of the orientation space to another (*e.g.*, region 1 seems to exhibit less variability than region 4). Although local values of the VCO cannot be obtained, we can still conceive evaluating it over specific regions of the orientation space, such as those proposed by Winther *et al.* [8]. The results, shown in Figure V.18, are in agreement with the observations of Winther *et al.* Regions 2 and 3 exhibit high variabilities in terms of both rotation axis and angle. Region 1 exhibits the lowest variability, especially in terms of rotation axis, which explains the well pronounced rotation direction in this region.

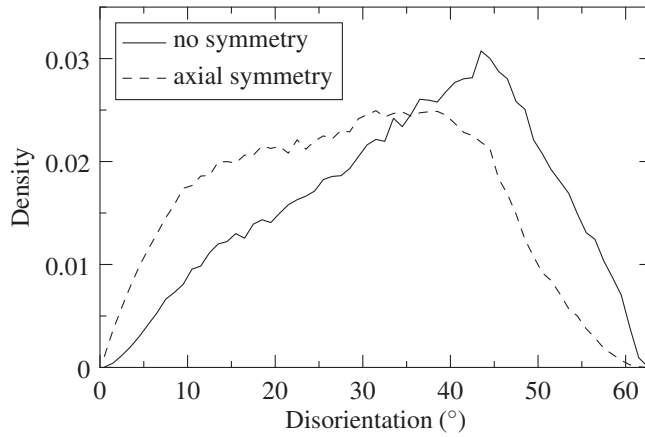


Figure V.16 – Influence of axial symmetry on the disorientation of grain pairs.

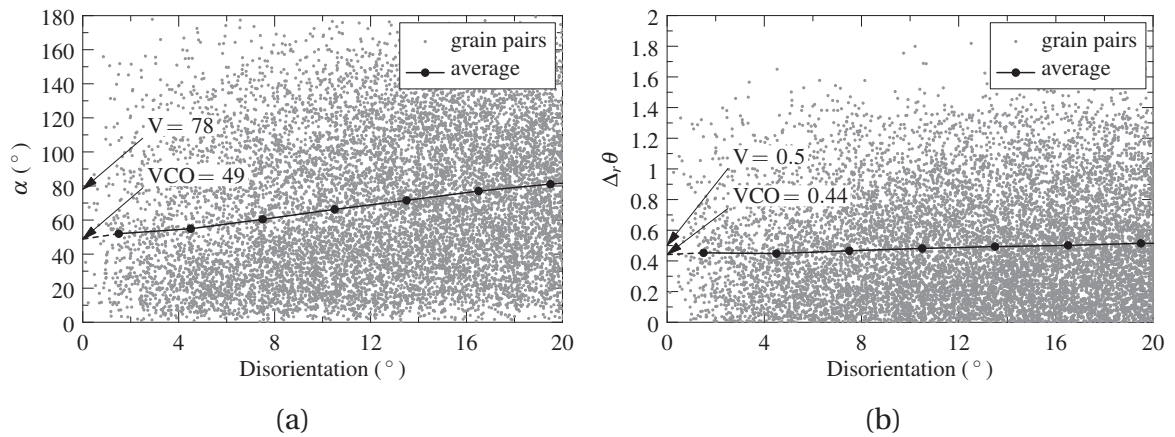


Figure V.17 – Variability at constant orientation (VCO) of the grain rotations, $(r_0^{4.5}, \theta_0^{4.5})$: rotation (a) axes and (b) angles. See the definitions of α and $\Delta_r\theta$ in the text. The grain pairs are plotted as dots. The continuous line gives the tendency averaged on 3° intervals. The dashed line represents the extrapolation at zero. V is the overall variability.

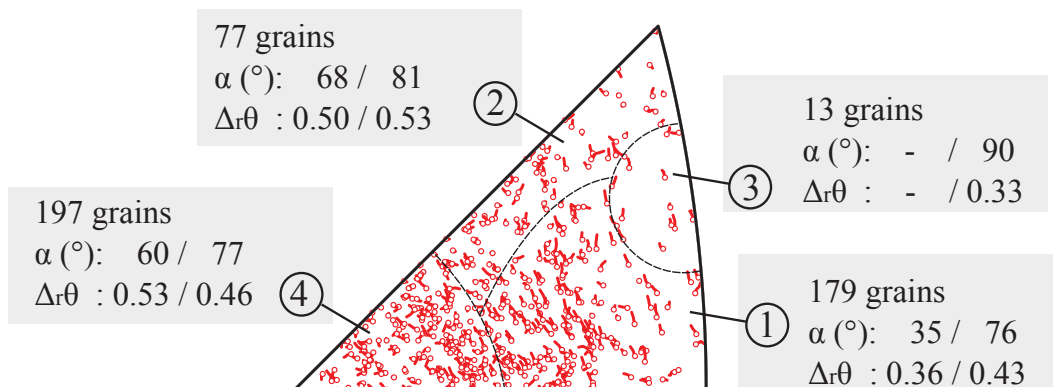


Figure V.18 – Variability at constant orientation of the grain rotations in the four IPF regions defined by Winther *et al.* [8]. The values are provided as (VCO / V) pairs, except for region 3, where there was too few grains to determine the VCO.

V.3.3 Intra-grain orientation spreads

The intra-grain orientation spreads were assessed from the diffraction spots, following the approaching presented in Section V.2. For each of the 466 tracked grains and at each successive deformed states, we assumed simple tri-Gaussian distributions about the average orientations. Each spread is thus described by three principal axes ($\mathbf{r}_1^d, \mathbf{r}_2^d, \mathbf{r}_3^d$) and three characteristic widths along these axes ($\lambda_1, \lambda_2, \lambda_3$). The preferential disorientation axis, \mathbf{r}_1^d (or equivalently $-\mathbf{r}_1^d$), corresponds to the largest width, λ_1 . In the following, we analyse the spreads in terms of widths (average disorientation and anisotropy) and directions (preferential axes) separately, before looking for relations to the grain orientations.

a) Average disorientation

An intra-grain orientation spread can be first characterized in terms of its angular extent. The latter is described by the “average disorientation angle”, θ_d , with respect to the average orientation. This is a common measure in EBSD [15] or HEDM [48], but it is not directly available from 3DXRD data. An estimator is therefore required.

For an isotropic distribution (i.e. $\lambda_1 = \lambda_2 = \lambda_3$) with small angular extents, a good estimator was proposed by Glez and Driver [91]:

$$\theta_d^{\text{iso}} \simeq \sqrt{\left(\frac{8}{\pi}\right)} \times 2\lambda_1 \quad (\text{V.13})$$

Similarly, for an anisotropic distribution with small angular extents, we propose to use:

$$\theta_d \simeq \sqrt{\left(\frac{8}{\pi}\right)} \times 2 \left(\frac{\lambda_1 + \lambda_2 + \lambda_3}{3} \right) \quad (\text{V.14})$$

This estimator was tested on random distributions, as shown in Figure V.19. Despite a systematic underestimation, we can expect the error to be smaller than 20% and on the average of 10%, which is very satisfactory for this study.

The distributions of average disorientation angles are provided in Figure V.20 with the average values for the successive strain levels. We can observe a gradual spread of the distributions and an increase of the average θ_d from 0.18° to 0.61° . At $\varepsilon = 4.5\%$, the distribution extends up to 1.56° . The distributions of θ_d are comparable with the successive distributions of θ_0 in Figure V.12.

b) Anisotropy

The intra-grain orientation spread can also be characterized in terms of its anisotropy. The latter is described by its strength using the “anisotropy factor”, λ_a , which is related to the λ_i as:

$$\lambda_a = \lambda_1 / \sqrt[3]{\lambda_1 \lambda_2 \lambda_3} \quad (\text{V.15})$$

The anisotropy factor is minimum and equal to 1 for an isotropic distribution.

The distributions of anisotropy factors are provided in Figure V.21 with the average values for the successive strain levels. We can observe that the anisotropy tends to increase throughout straining. The mean value increases from 1.7 to 2.0. The highest value is observed at $\varepsilon = 4.5\%$ and reaches 4.8.

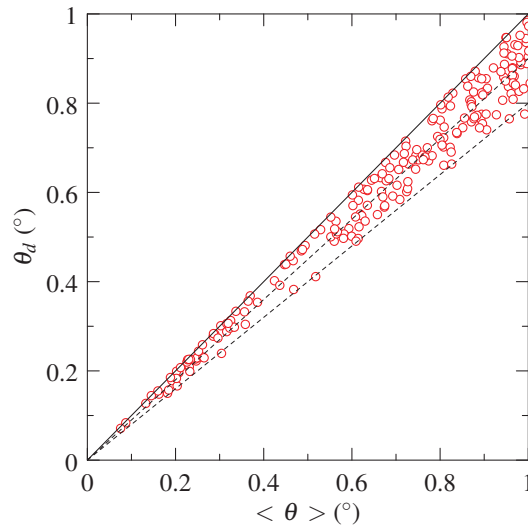


Figure V.19 – Estimation of the average disorientation angle of a tri-Gaussian ODE. The tests were performed on 500 random distributions. For each, the standard deviations $\lambda_{i=1,2,3}$ were chosen randomly and a list of 10,000 pseudo-random points was drawn from the distribution. $\langle \theta \rangle$ is the average disorientation angle calculated over these points, while θ_d is estimated from $\lambda_{i=1,2,3}$ using Equation V.14. The comparison indicates that θ_d underestimates $\langle \theta \rangle$ with an error smaller than 20% and on average of 10%.

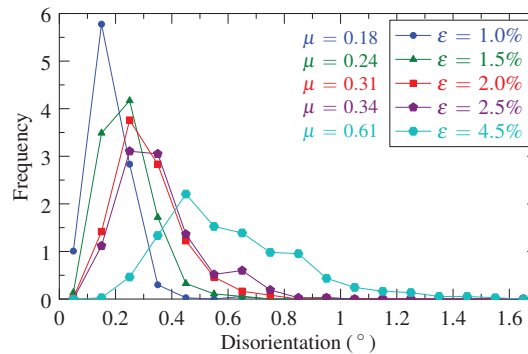


Figure V.20 – Evolution with strain of the average disorientation the intra-grain orientation spreads. Distribution mean values given by μ .

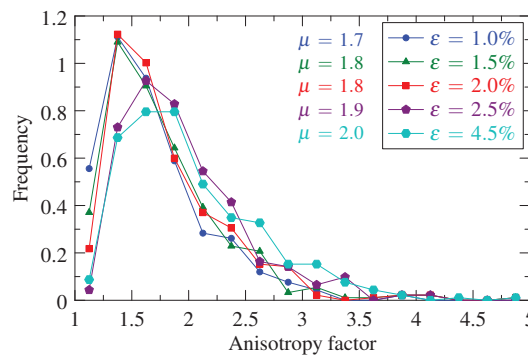


Figure V.21 – Evolution with strain of the anisotropy of the intra-grain orientation spreads. Distribution mean values given by μ .

c) Preferential disorientation axis

The distributions of preferential disorientation axes are represented in Figure V.22 as pole figures for the successive strain levels. At $\varepsilon = 1.0\%$, the axes are close to the tensile direction, Z. As strain increases, a transition occurs from $\varepsilon = 1.0\%$ to $\varepsilon = 2.5\%$ that leads to a progressive migration towards the periphery of the circle. Then, from $\varepsilon = 2.5\%$ to $\varepsilon = 4.5\%$, the distribution remains stable. The migration and the final distribution indicate a tendency of the rotation axes to align in the sample X-Y plane, i.e. perpendicular to the tensile direction. This is also illustrated on Figure V.22-f, where axes initially on the periphery of the stereographic circle vary much less than the others. Considering the loading symmetry, these results seem to indicate a relation to the tensile axis. We will see thereafter that the higher concentration about X can be explained by the sample texture.

The distribution of preferential disorientation axes is similar to the distribution of rotation axes shown in Figure V.13. In both, the axes preferably lie on the periphery of the circle, with a higher concentration about the X direction. The distribution can thus be analysed with regard to the grain rotation axes. However, no relation could be identified by examining the differences between the preferential disorientation axes and the rotation axes. Another possibility is to compare the preferential disorientation axes with crystal directions, since we observed an influence of the sample texture. Again, no relation could be identified.

d) Relation to the grain orientations

The intra-grain orientation distributions are represented in the fundamental region of the Rodrigues orientation space. In the left-hand column of Figure V.23, the orientation distributions are represented as ellipsoids, with semi-axes and radii equal to the distribution principal axes and standard deviations, respectively. The ellipsoids are centred on the corresponding grain orientations and coloured according to the components of the preferential disorientation axes, r_1^d . In the right-hand column of Figure V.23, the orientation distributions are represented on a top-view as batons of constant radius and length, centred on the corresponding grain orientations and aligned with the preferential disorientation axes, r_1^d . The same colour scheme is used.

This was done for $\varepsilon = 1.0\%$, $\varepsilon = 2.0\%$ and $\varepsilon = 4.5\%$ to illustrate the transition observed in Figure V.22. From the top-view distribution, at $\varepsilon = 1.0\%$, the batons seem to be randomly oriented and show no clear pattern. We know from Figure V.20-b that the preferential axes are close to Z and tends towards X, resulting here in dominant red-blue colors. At $\varepsilon = 2.0\%$, we can see that many batons have rotated and lie in the X-Y plane. Finally at $\varepsilon = 4.5\%$, most of the batons are aligned with X, Y or a combination of the two, resulting near-exclusively in red-green colors. However, the arrangement indicates a strong influence of grain orientations: on the top-view plots, the preferential disorientation axes appear to be perpendicular to the "projection of the orientation vectors" (going from the origin to the centroid of the batons). This relationship will be further investigated in Chapter VI, with the comparison to simulation.

Furthermore, the higher concentration of axes about the X direction, observed in Figure V.22, can be explained from Figure V.20-c. Indeed, we can observe that, due to the sample texture and the orientation dependency, most of the batons are aligned with X. This can be seen from the dominant red color.

Regarding the angular extents of the distributions, we evaluated the VCO and V values of θ_d , which revealed a low influence of grain orientations (VCO / V = 0.92).

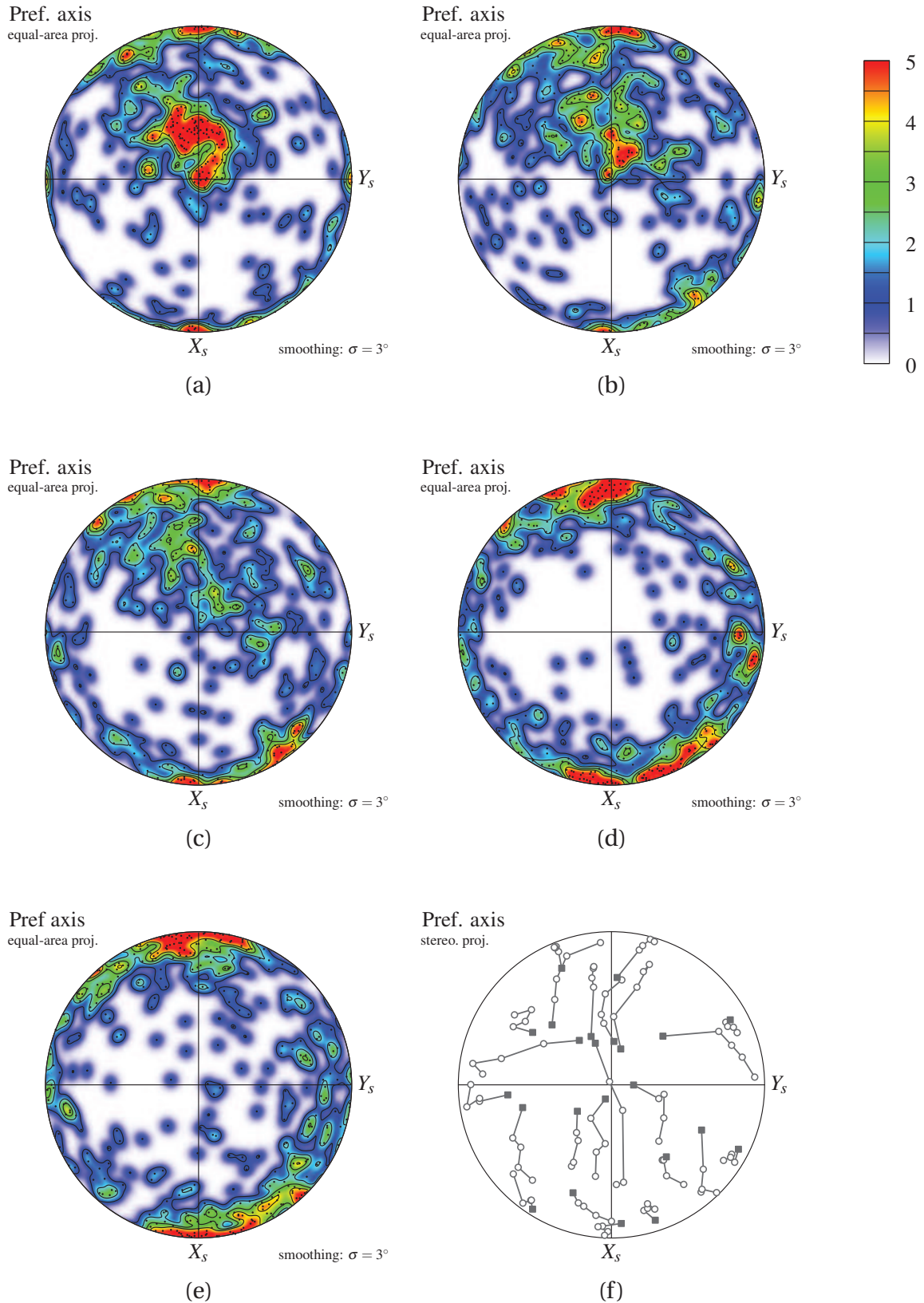


Figure V.22 – Evolution of the preferential disorientation axes with strain. (a-e) Equal-area projections showing the preferential disorientation axes as dots, with a density field and contour lines added. (a) $\epsilon = 1.0\%$, (b) $\epsilon = 1.5\%$, (c) $\epsilon = 2.0\%$, (d) $\epsilon = 2.5\%$, (d) $\epsilon = 4.5\%$. (f) Stereographic projection showing the paths of the preferential axes of 24 grains, starting from $\epsilon = 1.0\%$ (square).

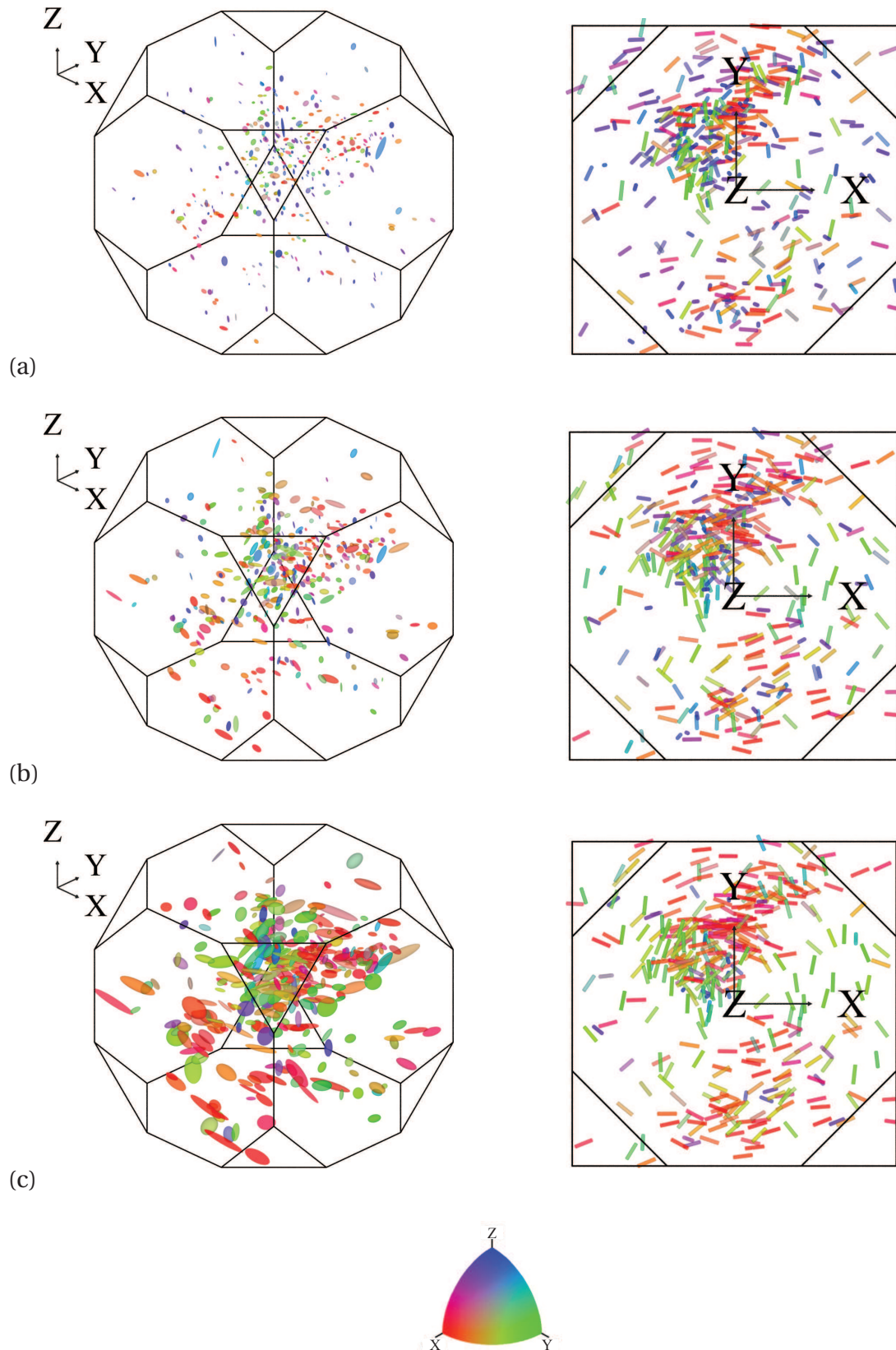


Figure V.23 – Correlation between the orientation spreads and the orientation of the grains, illustrated in the Rodrigues fundamental region for (a) $\epsilon = 1.0\%$, (b) $\epsilon = 2.0\%$ and (c) $\epsilon = 4.5\%$. Intra-grain orientation spreads are represented as (Left) equivalent ellipsoids or (Right) batons aligned with the preferential axes. The colour is related to the direction of the preferential axis. For visibility, the ellipsoids were magnified by a factor of 10.

V.3.4 Grain elastic strains and stresses

We dispose for each grain and each strain level of the six components of the lattice elastic strain tensor, $\underline{\epsilon}^e$, and the six components of the stress tensor, $\underline{\sigma}$. This is illustrated on Figure V.24 for two selected grains. The quantities are expressed in the laboratory coordinate system and plotted against the applied macroscopic stress.

For both grains, we can observe a monotonic and near-linear increase of the strain along the tensile direction up to about 6×10^{-4} . Along with this, the axial stress components increase up to about 40 MPa, which is consistent with the applied stress. The main differences between grain (a) and (b) can be observe for the other components. For grain (b), the transverse and shear components remain low, within $\pm 2 \times 10^{-4}$ for the elastic strain and ± 10 MPa for the stress. In contrast, grain (a) exhibits significant variations of the transverse components.

These variations among the grain mechanical responses lead to distributions of the strain and stress components. Figure V.25 represents the evolution of the distributions of the axial strain and stress components. As a result of the sample deformation, the mean values increase, which reflects the overall response of the material. In addition, the distributions progressively spread out. In the final state, the full width at half maximum (FWHM) of the σ_{zz} distribution reaches 30 MPa, which is of the same order as the mean value. Such a scattering might be partly attributed to the measurement errors, but should also be related to variabilities in the grain mechanical responses.

a) Macroscopic response

The results were first validated against the macroscopic response of the specimen. To do so, the volume-weighted averages of the strain and stress components in the successive states were calculated over all available grains. The standard errors were propagated and are indicated as error bars.

Figure V.26 presents the comparison between the material behaviour (continuous test in laboratory), the loads displayed by the stress rig (NanoX) and the averages over all the grains (3DXRD). Regarding the first two, a reasonable agreement is observed. The *in situ* stress-strain curve is though slightly below the continuous curve, which might be attributed either to relaxation effects or to the material texture. Besides, there is a good agreement between the two *in situ* curves.

Figure V.27 details the comparisons between the average components and the applied stress. The latter must correspond in Figure V.27-a to the axial component, σ_{zz} . As already pointed out, the agreement is found to be good and within the errors. The other components are expected to be zero, which is satisfied by the shear, but not by the transverse components. The latter exhibit values and errors of about 5 MPa in the final state, reflecting the accumulation of measurement errors. Regarding the strain components in Figure V.27-b, we can observe near-linear relations with respect to the applied load. The Young's modulus can be estimated from the slope of the axial response. The value obtained is 81 ± 3 GPa, which is about 15% larger than expected for Al (70 GPa).

The transverse components, ϵ_{xx}^e and ϵ_{yy}^e , decrease linearly along with the increase of ϵ_{zz}^e , which can be attributed to the Poisson effect. Figure V.28 shows the Poisson ratios, ν_x and ν_y , obtained separately for both transverse components. The ratios are distributed about 0.3 and ranges from 0.26 to 0.34. This is comparable to a typical value of 0.35 for pure Al [16]. The systematic difference between ν_x and ν_y may however indicate a systematic bias in the analysis.

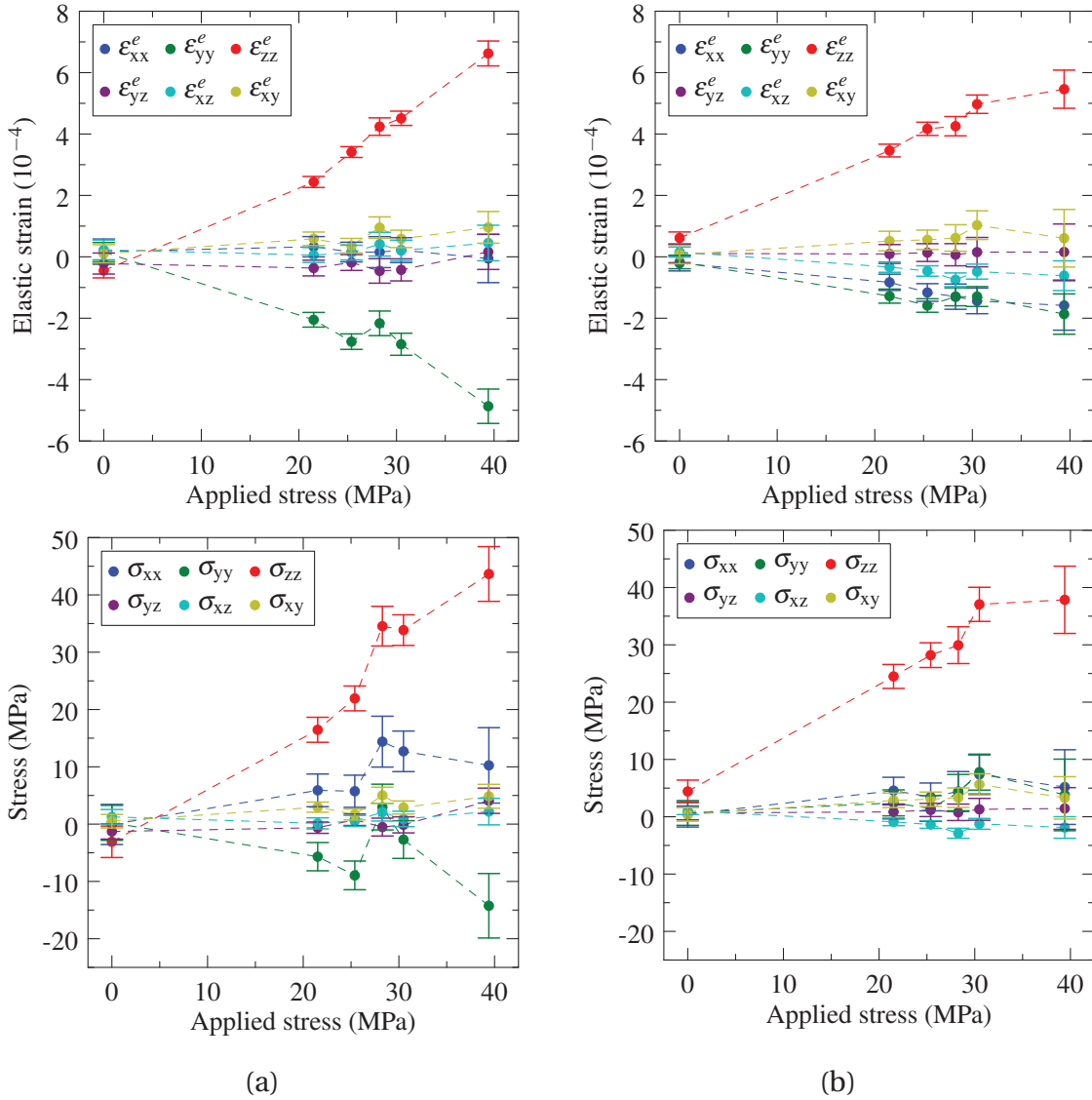


Figure V.24 – Mechanical responses against the applied stress of two selected grains. Evolution of lattice elastic strain components and stress components for grain (a) and grain (b). The errorbars represent the standard errors.

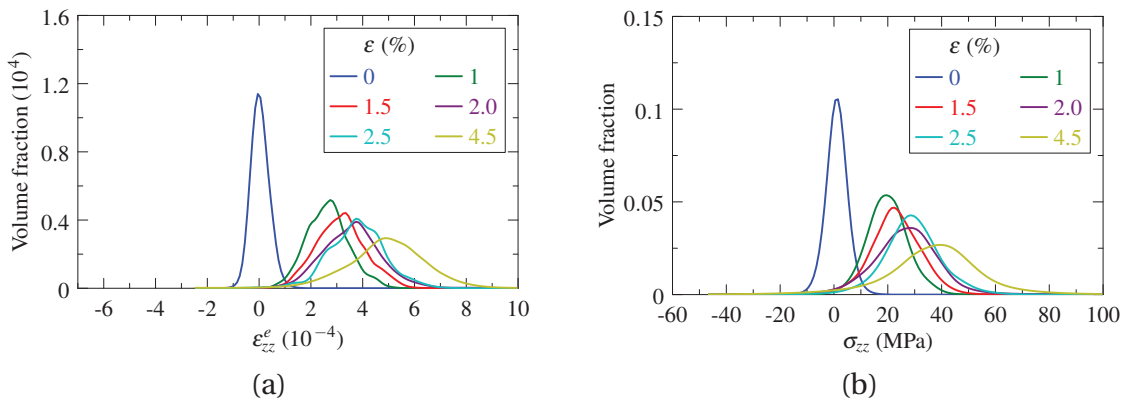


Figure V.25 – Evolution of the distribution of axial elastic strains and stresses. (a) Axial elastic strain, ϵ_{zz}^e , and (b) axial stress, σ_{zz} .

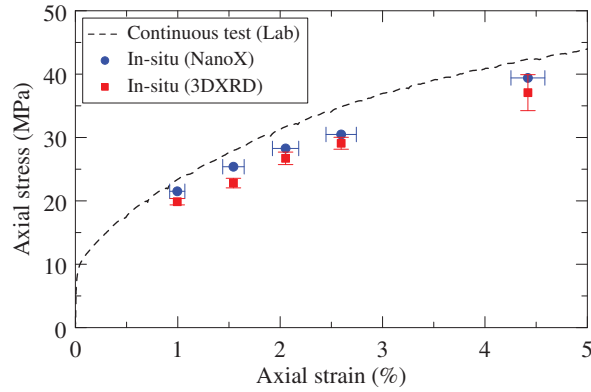


Figure V.26 – Macroscopic stress-strain curve. Comparison between (a) continuous laboratory test and (b-c) in situ experiment on Sample B. The vertical error bars (3DXRD) are the propagated standard errors. The horizontal error bars (NanoX) represent the experimental uncertainties on the axial displacement, which was applied manually for technical reasons.

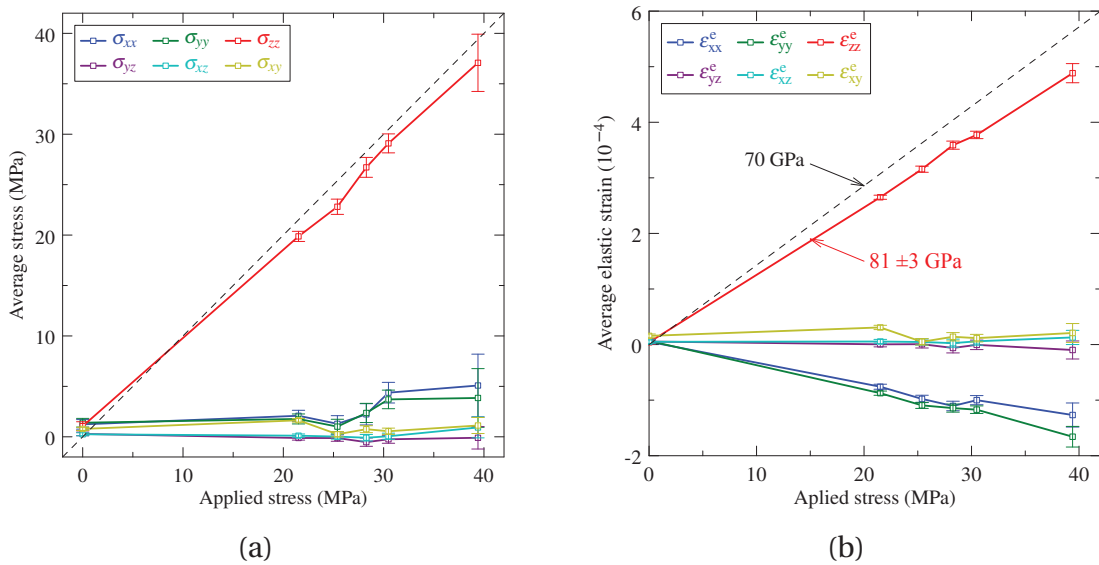


Figure V.27 – Average mechanical response of Sample B during in situ tensile test, in terms of (a) stress components, σ_{ij} , and (b) elastic strain components, ϵ_{ij}^e . The averages were calculated over all the available grains and weighted by their volumes. The error bars represent the propagated standard errors.

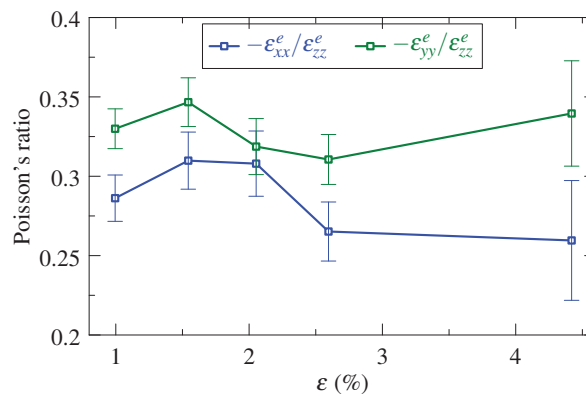


Figure V.28 – Poisson effect of Sample B during tensile loading, obtained from the average axial and transverse elastic components.

b) Relation to the grain orientations

Figure V.29 shows the repartition of the axial stress in the first deformed state as a function of orientation. Variations suggest a dependency of the axial response on the grain orientation. Close to the $[111]$ corner, the grains appear to carry more strain and stress than in other regions of the triangle.

To further explore these variations, we considered three grain subsets, respectively consisting of 30 grains within 10° of $[100]$, 30 grains within 10° of $[110]$ and 29 grains within 15° of $[111]$. The mean and standard deviations of the axial strain and stress components were calculated. The axial responses of the three subsets are represented on Figure V.30 as a function of the applied stress. Differences can be observed, with, in particular, slightly larger strains and stresses for the $[111]$ direction on average. This observation is however limited by the large errors, which do not allow to draw clear distinctions between the subsets and, again, indicate a significant scattering among the grains. We can reasonably say though that, on the average, the grains close to $[111]$ appear to carry more stress, as already pointed out in Figure V.29.

This tendency can be related to the difference between hard and soft grain responses. For a grain in uni-axial tension, the critical shear stress for slip, τ_c , affects the flow stress, σ , as:

$$\sigma = M \tau_c \quad (\text{V.16})$$

where τ_c is assumed to be the same on all slip systems. M is referred to as the ‘‘Taylor factor’’. It depends on the grain orientation and, in tension, varies from 2.3 (soft grain) to about 3.7 (hard grain). The determination of M is known from the theory of Taylor-Bishop-Hill and is treated in detail in Ref. [16]. The orientation dependency of M is shown on Figure V.31-a.

Figure V.31-b plots the axial stress components of all the available bulk grains at $\epsilon = 1.0\%$ as a function of the Taylor factor. A large scattering of the data can be observed, which at first sight does not allow to identify any relation. A linear fit seem though to indicate that the stress tends to increase with the Taylor factor. The tendency, albeit weak, is present, as revealed by the errors, which are smaller than the slope. Hence, this suggests that, on average, harder grains carry more load. This effect seems to remain stable along the deformation, but with an increasing scattering.

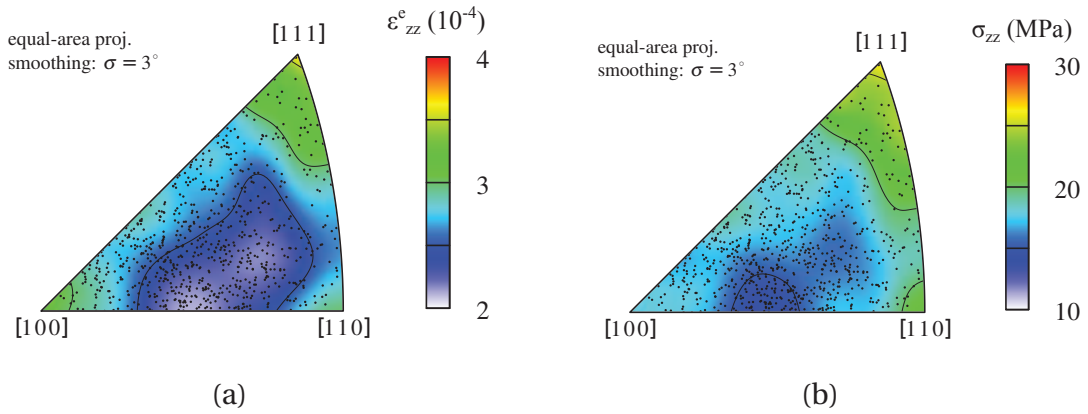


Figure V.29 – Relation to orientation of the grain (a) axial elastic strains and (b) axial stresses at $\epsilon = 1.0\%$. Inverse pole figure (equal-area projection) showing the tensile axis per individual grain (dots) and the corresponding average strain and stress distributions.

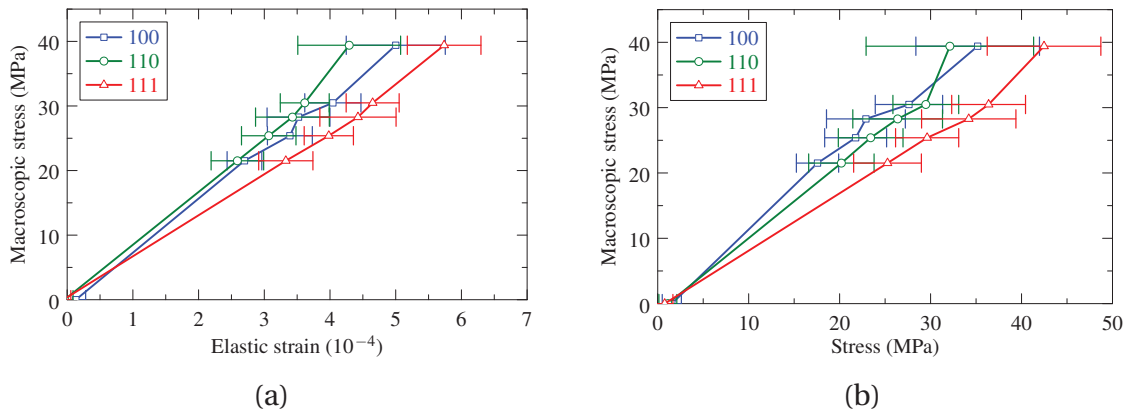


Figure V.30 – Axial mechanical response close to [1 0 0], [1 1 0] and [1 1 1] orientations, considering 30 grains within 10° of [1 0 0], 30 grains within 10° of [1 1 0] and 29 grains within 15° of [1 1 1].

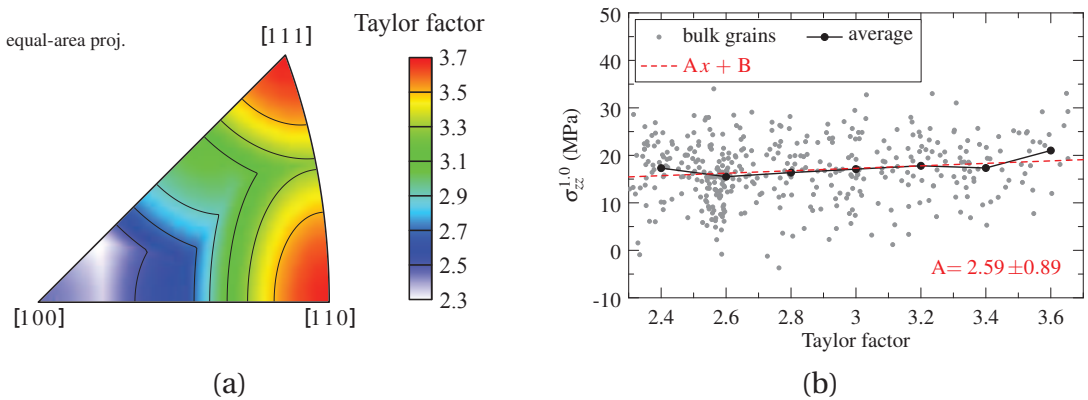


Figure V.31 – Influence of the Taylor factor on the axial stress. (a) Orientation dependence of the Taylor factor, according to Ref. [16]. (b) σ_{zz} against the Taylor factor, considering all available bulk grains at $\epsilon = 1.0\%$.

V.4 Summary and discussion

In this chapter, 466 grains were monitored *in situ* during uniaxial loading at six successive plastic strain levels up to 4.5%. This grain set corresponds to a representative subset containing 57% of the initial 824 grains. For each strain level, the 3DXRD measurements allowed to determine the centroid, average orientation and volume of each individual grain. The grain average elastic strain tensors were evaluated with respect to the initial undeformed state. The grain average stress tensors were derived using the elastic stiffness tensor of Al.

To complete the characterization, a new original method was proposed to assess the principal axes and standard deviations of the intra-grain orientation spreads. Consistent with experimental observations, the grain disorientation distribution is assumed to follow a simple tri-Gaussian function, described in the Rodrigues orientation space by six parameters. The latter values are determined by maximizing the similarity between the experimental spots (azimuthal projection) and simulated spots (virtual diffractometer), generated from the ODF.

The *grain average rotations* were described by rotation axis / angle pairs and studied with respect to the initial grain orientations and with regard to the successive strain increments. We observed some variability from grain to grain in the rotation angles, as well as strong correlations between the successive increments. The rotation angles were generally small, ranging on average from 0.12° at $\varepsilon = 1.0\%$ to 0.8° at $\varepsilon = 4.5\%$. This led us, for uncertainty reasons, to consider only the final rotation axes. The latter revealed to be near-perpendicular to the tensile axis, Z. We examined the relation of the rotations to the grain orientations using the variability at constant orientation (VCO) and the overall variability (V). The determination of the VCO requires in principle to dispose of many grains of close orientations, which was not our case. Instead, we employed the approach of Ref. [42] to determine the average VCO over all orientations. The ratio VCO/V allows to characterize the orientation dependency compared to grain interactions and ranges from 0 (strong influence of orientations) to 1 (strong influence of grain interactions). This was done for the rotation axes and the rotation angles, while taking account of the axial symmetry of loading. The results revealed (VCO, V) values of (49° , 78°) and (44%, 50%), respectively and indicate a strong influence of grain interactions on the rotation axes and an even stronger influence on the rotation angles. Overall, the results confirm the qualitative observations of Winther *et al.* [8].

The *intra-grain orientation spreads* were described by average disorientation angles, anisotropy factors and preferential disorientation axes. The angles were relatively small, comparable to the grain rotation angles and of about 0.6° on average at $\varepsilon = 4.5\%$. The anisotropy appeared to have already developed at $\varepsilon = 1.0\%$ and only slightly increased beyond to an average of 2. The preferential disorientation axes were initially gathered close to Z and appeared to migrate toward the X-Y plane from $\varepsilon = 1.5\%$ to $\varepsilon = 2.5\%$. This suggested the tendency of the axes to be perpendicular to the tensile axis. A denser distribution was observed close to X, which was attributed to sample texture and gave a first hint of the dependency on grain orientations. No relation could be identified between the preferential disorientation axes and the grain rotation axis, or any crystal directions. Regarding the relation between intra-grain orientation spreads and grain orientation, it was investigated in the fundamental region of the Rodrigues orientation space. At $\varepsilon = 4.5\%$, the preferential disorientation axes appeared strongly correlated to the grain orientations. On

the opposite, the average disorientation angles did not show any dependency on the grain orientations, as confirmed by the variability at constant orientation.

The *lattice strains and stresses* were examined on average at the macroscopic scale, as a function of crystallographic orientation and for the individual grains. Regarding the macroscopic response of the sample, it was calculated as the volume-weighted average over all available grains at each strain level. The average axial stress appeared to correspond within the errors to the axial stress measured by the deformation rig. The effective Young modulus and Poisson ratio were consistent with typical values for Al. These results allowed for a preliminary validation of the strain evaluations before deeper analyses.

The distributions of strain and stress components revealed a significant variability among the grain responses. At $\epsilon = 4.5\%$, the grain axial stresses were distributed from about -5 MPa to 80 MPa, with an average of 40 MPa and a FWHM of 30 MPa. This spread is questionable with regard to the measurement errors. From the conclusions of Chapter III, accuracies of about 10^{-4} can be expected for the determination of lattice elastic strains. This evidently holds for the initial state and may deteriorate along with strain. Hence, we clearly observed that the standard errors increased to reach 1.5×10^{-4} and 10 MPa in the last deformed state. This indicates an increase of data scatter, which strongly limits the analysis of variations from grain to grain. The uncertainties can however be reduced by considering grain populations to identify average tendencies.

The distribution of axial stress in the stereographic triangle revealed some dependency on the orientation. It also indicated that grains closer to the $[111]$ orientation seemed to carry more load on average. This was confirmed by considering three subsets, consisting of grains within 10° of $[100]$, 10° of $[110]$ and 15° of $[111]$, respectively. The results showed differences between them, but with relatively large errors. The stresses were also compared to the Taylor factors, suggesting that harder grains carried more load, on average.

As a conclusion, we were able to follow and characterize 466 grains in Sample B from the undeformed state to $\epsilon = 4.5\%$ of tensile deformation. The individual rotations, orientation spreads and mechanical responses were qualitatively and quantitatively investigated using different representations and metrics. The influence of grain interactions could be highlighted, as well as relations to the grain orientations. The rotations, in particular, exhibit a relatively high variability at constant orientation, which brings to light a significant influence of grain interactions. These results form a representative dataset for the comparison with the predictions of polycrystal plasticity models.

CHAPTER -VI-

Comparison between experiment and crystal plasticity modelling

Contents

VI.1 Finite element model	124
VI.1.1 Polycrystal representation and meshing	124
VI.1.2 Constitutive equations	130
VI.1.3 Determination of material parameters	131
VI.1.4 Data analysis	132
VI.2 Grain average rotations	135
VI.2.1 Distributions	135
VI.2.2 Variability at constant orientation	138
VI.2.3 Grain-by-grain comparisons	139
VI.3 Intra-grain orientation spreads	141
VI.3.1 Distributions	141
VI.3.2 Relation to deformation mechanisms	145
VI.3.3 Grain-by-grain comparisons	146
VI.4 Grain average elastic strains and stresses	149
VI.4.1 Distributions	149
VI.4.2 Macroscopic response	152
VI.4.3 Relation to the grain orientations	153
VI.4.4 Grain-by-grain comparisons	154
VI.5 Summary and discussion	158

This chapter tackles the comparison between the experimental results and simulation results from crystal plasticity modelling. First, we describe the finite element model and the simulation reproducing the *in situ* tensile test (Section VI.1). Then, we present the results and compare them to the measurements, in terms of grains rotations (Section VI.2), intra-grain orientation spreads (Section VI.3), elastic strains and stresses (Section VI.4).

VI.1 Finite element model

A finite element simulation reproducing the experimental conditions was carried out. The input mesh was obtained from the experimental data using a new approach, implemented in the free software package Neper [102, 109] developed at the laboratory. The finite element calculations of polycrystal plasticity were performed using FEpX [26, 110].

VI.1.1 Polycrystal representation and meshing

The simulation required the construction of a realistic mesh from the DCT data. As mentioned in Subsection I.2.2, direct free meshing of experimental polycrystals is a non-trivial procedure, strongly sensitive to imaging artefacts and likely to provide inhomogeneous mesh attributes. Alternative strategies include the use of *Voronoi tessellation* or *Laguerre tessellation*, which are largely employed to generate realistic virtual polycrystals, as they can be automatically meshed into good-quality elements [4].

Recently, simple procedures were proposed to iteratively determine the Laguerre tessellation that reproduces at best the grain centroids and volumes of a given polycrystal [33]. However, when applied on experimental data, the resulting tessellations often show significant discrepancies with the actual microstructure. In the present work, we developed an approach that aims at finding the Laguerre tessellation that approximates at best the experimental morphology¹. This is solved as an optimization problem, which is defined thereafter.

a) Approximation of experimental microstructures

Principle of Laguerre tessellations

Let us consider a spatial domain \mathcal{C}_0 of \mathbb{R}^3 and a finite set of generating points and weights, $\{(\mathbf{x}_i, w_i)\}_{i=1\dots n}$. The Laguerre tessellation of \mathcal{C}_0 consists of a collection of space-filling and non-overlapping cells, $\{\mathcal{C}_i\}_{i=1\dots n}$, which are mathematically defined as follows:

$$\mathcal{C}_i = \{\mathbf{y} \in \mathcal{C}_0 \mid d(\mathbf{y}, (\mathbf{x}_i, w_i)) \leq d(\mathbf{y}, (\mathbf{x}_j, w_j)) \quad \forall j \neq i\} \quad (\text{VI.1})$$

where $d(\bullet, \bullet)$ is the power distance, defined as:

$$d(\mathbf{y}, (\mathbf{x}, w)) = \|\mathbf{y} - \mathbf{x}\|^2 - w^2 \quad (\text{VI.2})$$

The Laguerre tessellation is a weighted variation of the Voronoi tessellation. Both produce convex cells, but the seed weights used in the Laguerre tessellation provide much more flexibility in cell sizes and shapes. In fact, any tessellation into convex cells can be represented as a Laguerre tessellation [111]. Figure VI.1 provides an example of a Laguerre tessellation generated from random seed positions and weights.

¹These developments were made in the context of a wider effort to develop a general method to generate virtual polycrystalline structures from various types of experimental data: grain size/sphericity distributions, grain centroids/volumes (3DXRD) or grain shapes.

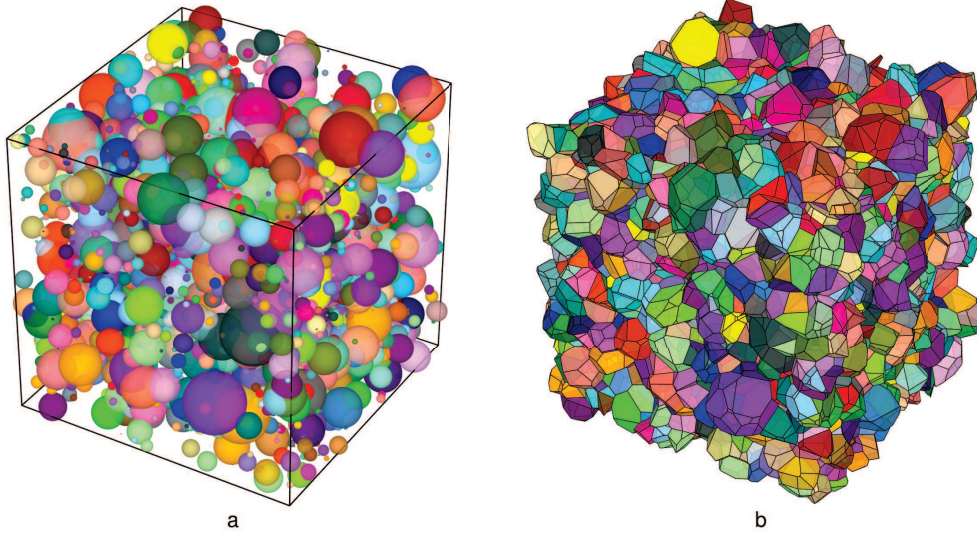


Figure VI.1 – Example of a polycrystal generated by Laguerre tessellation using Neper. (a) Seeds represented by equivalent spheres and (b) resulting cells.

Experimental data

Because Neper only works with convex domains, the sample domain must also be convex or near convex. This applies to testing specimens, as their gage sections can generally be represented either by cuboids or by cylinders. In the sample domain, the experimental microstructure is described by a set \mathcal{M} of cubic voxels \mathbf{v} , arranged in a regular grid of coordinates and labelled by their corresponding grains. Let $I(\bullet)$ refer to the labelling function. The experimental grain \mathcal{G}_i can be defined as:

$$\mathcal{G}_i = \{ \mathbf{v} \in \mathcal{M} \mid I(\mathbf{v}) = i \} \quad (\text{VI.3})$$

Then, let $I_c(\mathbf{v}, j)$ be the function that provides the grain label of the j^{th} voxel (out of 26) connected to \mathbf{v} . The layer of voxels at the boundary of the grain \mathcal{G}_i is referred to as \mathcal{G}_i^{B} and satisfies:

$$\mathcal{G}_i^{\text{B}} = \{ \mathbf{v} \in \mathcal{G}_i \mid \exists j \mid I_c(\mathbf{v}, j) \neq i \} \quad (\text{VI.4})$$

Lastly, the grain centroids and equivalent radii are given by:

$$\mathbf{c}_i = \frac{1}{\#\mathcal{G}_i} \sum_{\mathcal{G}_i} \mathbf{v} \quad \text{and} \quad r_i = \Delta v \sqrt[3]{\frac{3}{4\pi} \#\mathcal{G}_i} \quad (\text{VI.5})$$

where $\#\bullet$ represents the set cardinality and Δv refers to the voxel length.

Discrepancy measure

The method aims at finding the Laguerre tessellation that approximates at the best the experimental data, that is, the set of cells \mathcal{C}_i that approximates at best the experimental grains \mathcal{G}_i . This requires a measure of the discrepancy between the two.

A simple approach consists in counting the number of experimental voxels falling in the wrong cell in the tessellation:

$$N_{\text{wrong}} = \#\{ \mathbf{v} \in \mathcal{M} \mid \mathbf{v} \notin \mathcal{C}_{I(\mathbf{v})} \} \quad (\text{VI.6})$$

which can vary from 0 (perfect match) to $\#\mathcal{M}$. This function is however desirable for optimization, since it takes only integer values.

A more appropriate metric is based on the Euclidean distance that separates each voxel, \mathbf{v} , to its corresponding cell in the tessellation, $\mathcal{C}_{I(\mathbf{v})}$. Hence, the overall discrepancy can be measured by:

$$\chi = \frac{1}{n} \sum_{\mathbf{v} \in \mathcal{M}} \frac{1}{\#\mathcal{G}_{I(\mathbf{v})}} \left[\frac{d_E(\mathbf{v}, \mathcal{C}_{I(\mathbf{v})})}{r_{I(\mathbf{v})}} \right]^2 \quad (\text{VI.7})$$

In Equation VI.7, the squared distance is normalized by the squared equivalent radius and the number of voxels in the corresponding grain. This prevents favouring the large grains against the small ones. It follows that χ provides an average measure of the overall discrepancy, independently of the grain sizes and voxel length.

Given the complex shape of $\mathcal{C}_{I(\mathbf{v})}$, the calculation of $d_E(\mathbf{v}, \mathcal{C}_{I(\mathbf{v})})$ is quite costly. Therefore, for large experimental volumes, the evaluation of Equation VI.7 can become very expensive, as it implies testing a very large number of voxels. A less expensive measure can be obtained by reducing the experimental data to the grain-boundary voxels. Indeed, a Laguerre tessellation that reproduces at the best the experimental grain boundaries will also be a good volumic approximation of the experimental microstructure. The discrepancy measure is easily derived from Equation VI.7 as:

$$\chi_B = \frac{1}{n} \sum_{\mathbf{v} \in \mathcal{M}_B} \frac{1}{\#\mathcal{G}_{I(\mathbf{v})}^B} \left[\frac{d_E(\mathbf{v}, \mathcal{C}_{I(\mathbf{v})})}{r_{I(\mathbf{v})}} \right]^2 \quad (\text{VI.8})$$

where \mathcal{M}_B refers to the subset of \mathcal{M} containing the grain boundary voxels. Here, the experimental data of Sample B contain more than 336,000,000 voxels ($593 \times 573 \times 989$) among which about 10% only are at the grain boundaries. As a consequence, using Equation VI.8 instead of Equation VI.7 allows to reduce computation time by a factor of 10.

Optimization procedure

The optimization problem consists in finding the seed positions and weights ($4 \times n$ variables) that provide the best approximation of the experimental data according to Equation VI.8 (objective function). The procedure comprises three steps.

1. Data reduction: the experimental data are reduced to the subset \mathcal{M}_B of grain boundary voxels. This is done by going through \mathcal{M} and checking the neighbourhood of each voxel.
2. Initialization: the seed positions and weights, $\{(\mathbf{x}_i, w_i)\}_{i=1 \dots n}$, are initially set to the experimental grain centroids and equivalent radii, $\{(\mathbf{c}_i, r_i)\}_{i=1 \dots n}$, as given by Equation VI.5. This initial solution is in general close to the optimal one and enables thus employing local optimization algorithms.
3. Optimization: the objective function, χ_B , is minimized over the set of $4 \times n$ variables defining the Laguerre tessellation. The resulting seed positions and weights provide the best approximation of the experimental data according to the discrepancy measure.

This procedure is illustrated on Figure VI.2 for the simple case of a 2D microstructure containing three grains.

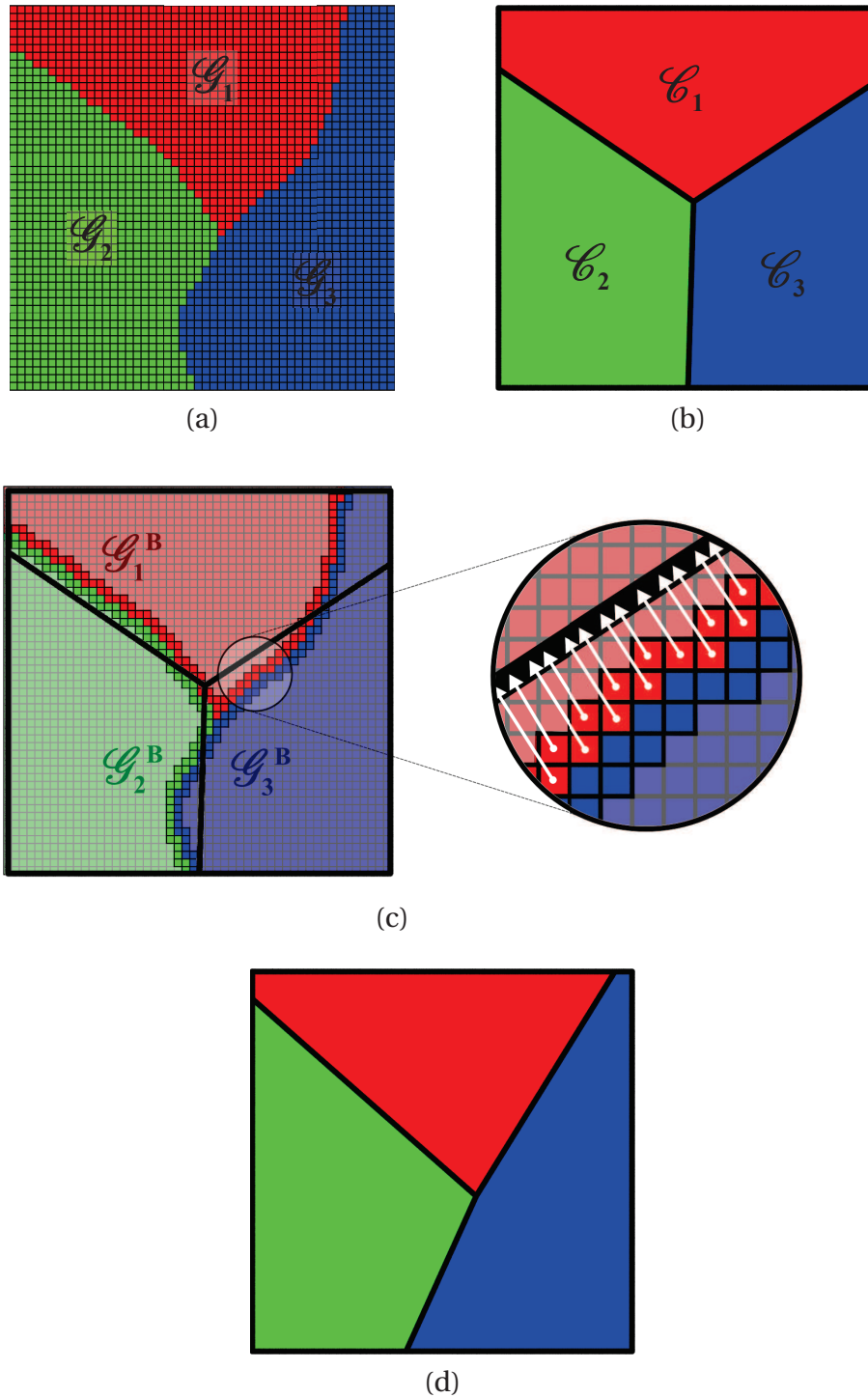


Figure VI.2 – Optimization procedure exemplified for a 2D microstructure. (a) Experimental microstructure containing three grains (voxel sets \mathcal{G}_1 , \mathcal{G}_2 and \mathcal{G}_3). (b) Initial Laguerre tessellation based on the experimental grain centroids and radii. (c) Comparison between the experimental grain boundaries (\mathcal{G}_1^B , \mathcal{G}_2^B and \mathcal{G}_3^B) and tessellation boundaries. (d) Optimized Laguerre tessellation after minimization of χ_B .

b) Approximation and meshing of Sample B

The approximation method was implemented in the free software package Neper [109], using the free library NLOpt (subplex algorithm) for non-linear derivative-free optimization [98, 103] and the free library Open MPI for parallel computing [112]. It was then applied on the experimental data of Sample B. To define a convex domain for Neper, the sample domain was slightly cropped to obtain a cuboid of dimensions $0.83 \text{ mm} \times 0.81 \text{ mm} \times 1.384 \text{ mm}$. The optimization involved more than 500,000 iterations and, using multi-processing on a standard parallel computer (2 nodes with 8 cores each), the calculation time was roughly 10 hours. The experimental microstructure and the optimized tessellation are shown in Figure VI.3.

Due to the presence of non-convex grains in the experimental polycrystal, the latter can not be perfectly described by a Laguerre tessellation. A good qualitative agreement is observed though between the two. This can be quantitatively ascertained by examining the discrepancy measure ($10 \text{ }\mu\text{m}$ on average between the cell and grain boundaries) and by counting the number of incorrectly described voxels (18% of the total number).

Finally, the polycrystal was meshed into equiaxed 10-node tetrahedral elements with an element size of about $10 \text{ }\mu\text{m}$. The mesh density was about 700 elements per grain on average. The complete mesh, shown in Figure VI.4, contains 1,256,000 elements.

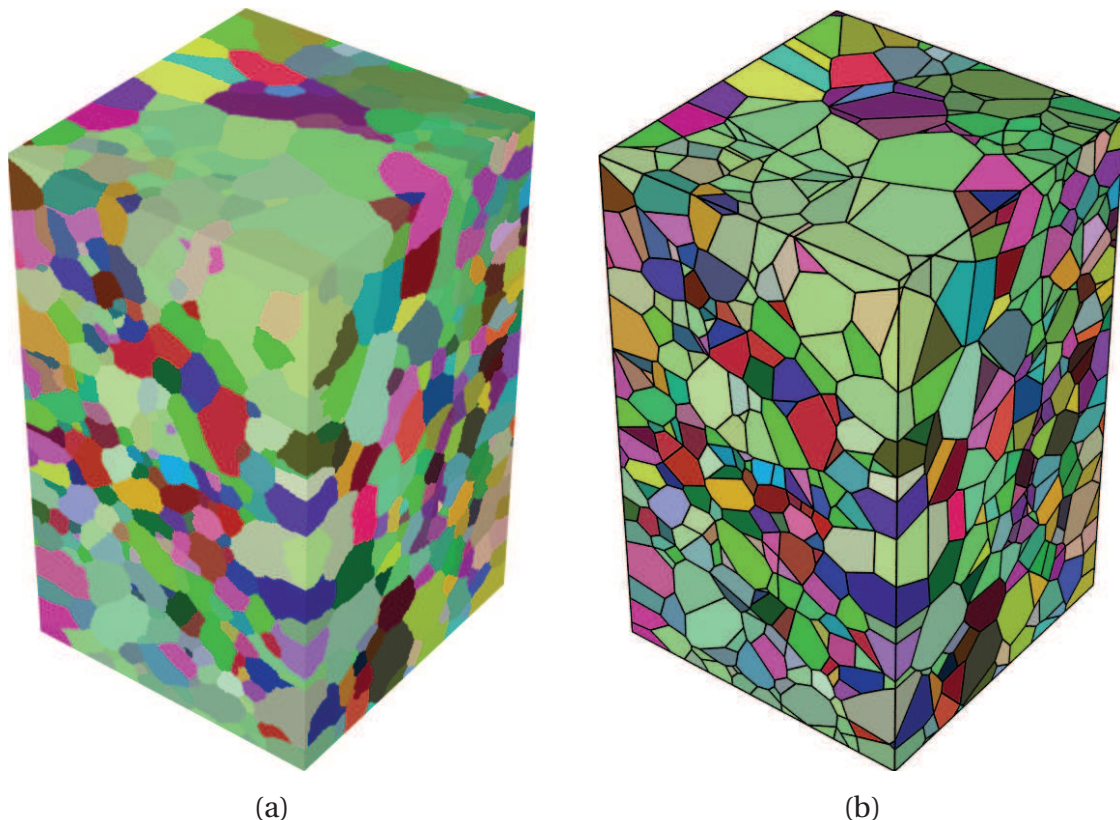


Figure VI.3 – Approximation of the experimental microstructure of Sample B. (a) Experimental microstructure cropped to a cuboid of dimensions $0.83 \text{ mm} \times 0.81 \text{ mm} \times 1.384 \text{ mm}$. (b) Laguerre tessellation after optimization. Orientation colouring related to Rodrigues vector components.

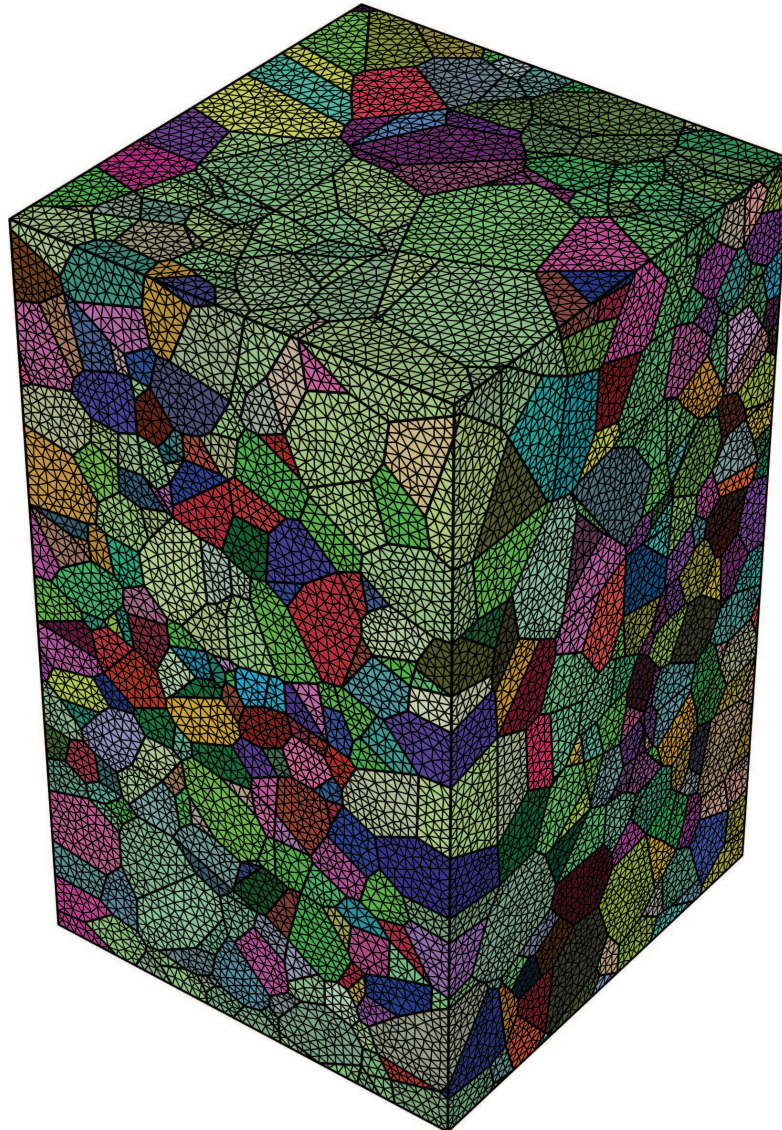


Figure VI.4 – Finite element mesh of Sample B containing 1,256,000 tetrahedral elements. Orientation colouring related to Rodrigues vector components.

VI.1.2 Constitutive equations

The simulations were performed with the finite element code FEpX [110]. The main features of the implemented elasto-visco-plastic theory are summarized thereafter, based on the detailed description of Marin and Dawson in Ref. [26].

Kinematic decomposition

The crystal mechanical response includes both anisotropic elasticity and plastic deformation by crystallographic slip on given systems (here, the twelve octahedral $\{111\} \langle 110 \rangle$ systems). The deformation gradient, $\underline{\mathbf{F}}$, is decomposed as,

$$\underline{\mathbf{F}} = \underline{\mathbf{V}}^e \underline{\mathbf{R}}^* \underline{\mathbf{F}}^p \quad (\text{VI.9})$$

where $\underline{\mathbf{F}}^p$ is the plastic part resulting from slip, $\underline{\mathbf{R}}^*$ represents the lattice rotation and $\underline{\mathbf{V}}^e$ is the elastic stretch. Let \mathcal{B}_0 and \mathcal{B} be the initial undeformed configuration and the current deformed configuration, respectively. We denote by $\hat{\mathcal{B}}$ the intermediate, relaxed configuration obtained by elastically unloading without rotation from \mathcal{B} .

Under the assumption of small elastic strain, $\underline{\mathbf{V}}^e$ can be written,

$$\underline{\mathbf{V}}^e = \underline{\mathbf{I}} + \underline{\boldsymbol{\varepsilon}}^e \quad (\text{VI.10})$$

where $\underline{\mathbf{I}}$ is the second-rank identity tensor. The infinitesimal strain tensor, $\underline{\boldsymbol{\varepsilon}}^e$, is related in the crystal coordinate system to the Kirchhoff stress tensor through the fourth-order stiffness tensor, $\underline{\mathbf{C}}$, as:

$$\underline{\boldsymbol{\tau}} = \underline{\mathbf{C}} : \underline{\boldsymbol{\varepsilon}}^e \quad (\text{VI.11})$$

and the Kirchhoff stress relates to the Cauchy stress based on the material point volume in $\hat{\mathcal{B}}$ as:

$$\underline{\boldsymbol{\tau}} = \det(\underline{\mathbf{V}}^e) \underline{\boldsymbol{\sigma}} \quad (\text{VI.12})$$

The plastic velocity gradient, $\hat{\underline{\mathbf{L}}}^p$, written in the $\hat{\mathcal{B}}$ configuration, can be expressed as:

$$\hat{\underline{\mathbf{L}}}^p = \dot{\underline{\mathbf{F}}}^p \underline{\mathbf{F}}^{p-1} = \hat{\underline{\mathbf{D}}}^p + \hat{\underline{\mathbf{W}}}^p \quad (\text{VI.13})$$

where $\hat{\underline{\mathbf{D}}}^p$ and $\hat{\underline{\mathbf{W}}}^p$ refers to its symmetric and skew-symmetric parts. The latter directly relate to crystallographic slip, as:

$$\hat{\underline{\mathbf{D}}}^p = \sum_s \hat{\underline{\mathbf{M}}}^s \dot{\gamma}^s \quad (\text{VI.14})$$

and,

$$\hat{\underline{\mathbf{W}}}^p = \sum_s \hat{\underline{\mathbf{Q}}}^s \dot{\gamma}^s + \dot{\underline{\mathbf{R}}}^* \underline{\mathbf{R}}^{*T} \quad (\text{VI.15})$$

where $\hat{\underline{\mathbf{M}}}^s$ and $\hat{\underline{\mathbf{Q}}}^s$ are respectively the symmetric and skew-symmetric parts of the Schmid tensor of the system s , written in the configuration $\hat{\mathcal{B}}$.

Behaviour laws

Slip is assumed to follow a viscoplastic behaviour, where the slip rate of the system s , $\dot{\gamma}^s$, is related to the resolved shear stress, τ_s , through a power law:

$$\dot{\gamma}^s = \dot{\gamma}_0 \left| \frac{\tau_s}{g^s} \right|^{\frac{1}{m}} \text{sign}(\tau_s) \quad (\text{VI.16})$$

and the resolved shear stress is the projection of the Kirchhoff stress on s ,

$$\tau^s = \hat{\mathbf{M}}^s : \underline{\boldsymbol{\tau}} \quad (\text{VI.17})$$

Lastly, the slip system hardness evolves according to a saturation hardening law and is described by:

$$\dot{g}^s = h_0 \left(\frac{g_\infty - g^s}{g_\infty - g_0} \right)^{n'} \sum_s |\dot{\gamma}^s| \quad (\text{VI.18})$$

The viscoplastic parameters, $\dot{\gamma}_0$ and m , and the hardening parameters, h_0 , g_0 , g_∞ and n' , are considered to be identical for the twelve octahedral slip system (isotropic hardening).

These constitutive equations of the crystal behaviour are used in a finite element formulation which solves for the motion of the polycrystal mesh based on the weak form of the equilibrium equations [110].

VI.1.3 Determination of material parameters

The material behaviour (at the crystal scale) was determined by fitting (at the macroscopic scale) the experimental stress-strain curve obtained in laboratory with a larger polycrystal (see Subsection II.2.2). In the simulation, we used a large random polycrystal generated by Poisson-Voronoi tessellation and made of 2000 grains. The latter were assigned random orientations, uniformly distributed over the orientation space. The polycrystal was meshed into 1,400,000 tetrahedral elements, yielding a mesh density of about 700 elements per grains (consistent with the mesh density used in the simulation of Sample B).

Boundary conditions were chosen to reproduce the loading conditions of a tensile test. The upper face was submitted to a constant axial velocity, while the lower face was fixed for axial translation. The polycrystal was kept from rigidly translating and rotating about the tensile axis by fixing the (0, 0, 0) corner and fixing along x the (0, 0.81, 0) corner. The four lateral faces were loading-free.

Material parameters were adjusted manually to get the best possible match between experiment and simulation. The final parameter values are provided in Table VI.1. The stress-strain curves are shown in Figure VI.5. We observe a good agreement between the curve measured in laboratory and the curve corresponding to the finite element simulation of the random polycrystal. This indicates that the chosen material parameters allow for a good description of the macroscopic behaviour of the material in the selected deformation range ($\epsilon \leq 4.5\%$). They also seem reasonable for a good description of the grain-scale behaviour.

The same parameters were used to run the finite element simulation of Sample B. The stress-strain curve, shown in Figure VI.5, reveals somewhat smaller stresses than in the laboratory stress-strain curve. This tendency is consistent with the experimental curves of Sample B and can be attributed to the sample texture. A good agreement between experiment and finite element simulation is observed for Sample B.

Table VI.1 – Material parameters determined from the laboratory test and used in the finite element simulation.

$\dot{\gamma}_0$ (s^{-1})	m	h_0 (MPa)	g_0 (MPa)	g_∞ (MPa)	n'
1	0.03	47	6	455	2.6

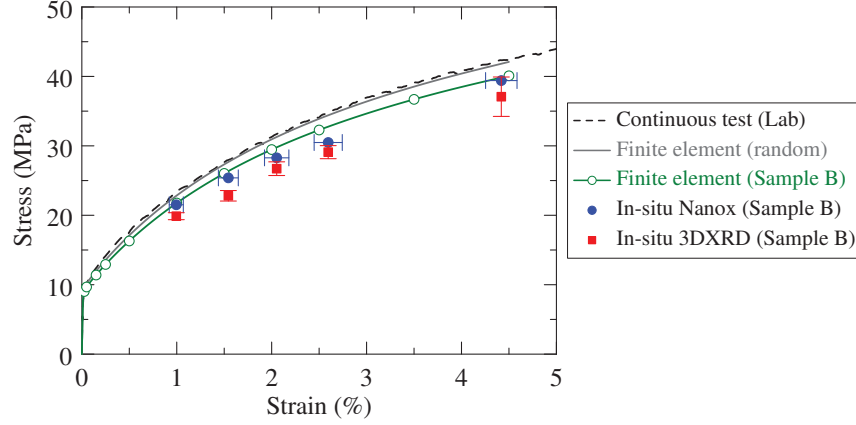


Figure VI.5 – Macroscopic stress-strain curves, as obtained from the continuous laboratory test, the in situ tensile test on Sample B and the finite element simulations. The material parameters were adjusted to make the gray curve (simulation on a random polycrystal) coincide with the black curve (continuous laboratory test).

VI.1.4 Data analysis

The development of heterogeneous strain and stress fields at the grain and intra-granular scales is illustrated at $\epsilon = 4.5\%$ in Figure VI.6 for the lattice rotation angles, the axial elastic strain and the axial stress components. Each grain is described by a set of tetrahedral elements i of volume fractions ϕ_i , orientations \mathbf{R}_i , elastic strain tensors $\underline{\epsilon}_i^e$ and stress tensors $\underline{\sigma}_i$. All quantities are expressed in the sample coordinate system. Consistent with the experimental results from 3DXRD, the heterogeneities are examined as frequency distributions, without taking account of the spatial information. The comparison with 3DXRD measurements also requires to average the physical quantities over the grain volumes.

For the elastic strains and the stresses, averaging is straightforward and consists in computing the volume-weighted mean values over the grain elements. For the orientations, each discrete distribution is decomposed into a mean orientation and a discrete set of disorientations, $\{\Delta\mathbf{R}_i\}$, with respect to the mean orientation. The latter was obtained by quaternion averaging, while accounting for the crystal symmetries and eliminating the *umklapp* effect [91]. All calculations were performed using the free library Orilib [104]. The disorientation sets were examined in the Rodrigues orientation space, revealing mostly unimodal distributions. This is illustrated on Figure VI.7 for a selected grain at $\epsilon = 4.5\%$. Consistent with the experimental results, each distribution was characterized by an average disorientation angle:

$$\theta_d = 2 \sum_i \phi_i \operatorname{atan} \|\Delta\mathbf{R}_i\| \quad (\text{VI.19})$$

as well as three principal axes ($\mathbf{r}_1^d, \mathbf{r}_2^d, \mathbf{r}_3^d$) and three characteristic lengths along the principal axes ($\lambda_1 \leq \lambda_2 \leq \lambda_3$), provided by the singular value decomposition of $\{\Delta\mathbf{R}_i\}$. Again, the first principal axis, \mathbf{r}_1^d , corresponds to the direction of higher disorientation angles and is referred to as “preferential disorientation axis”. Lastly, the intensity of the anisotropy is measured by the anisotropy factor, $\lambda_a = \lambda_1 / \sqrt[3]{\lambda_1 \lambda_2 \lambda_3}$.

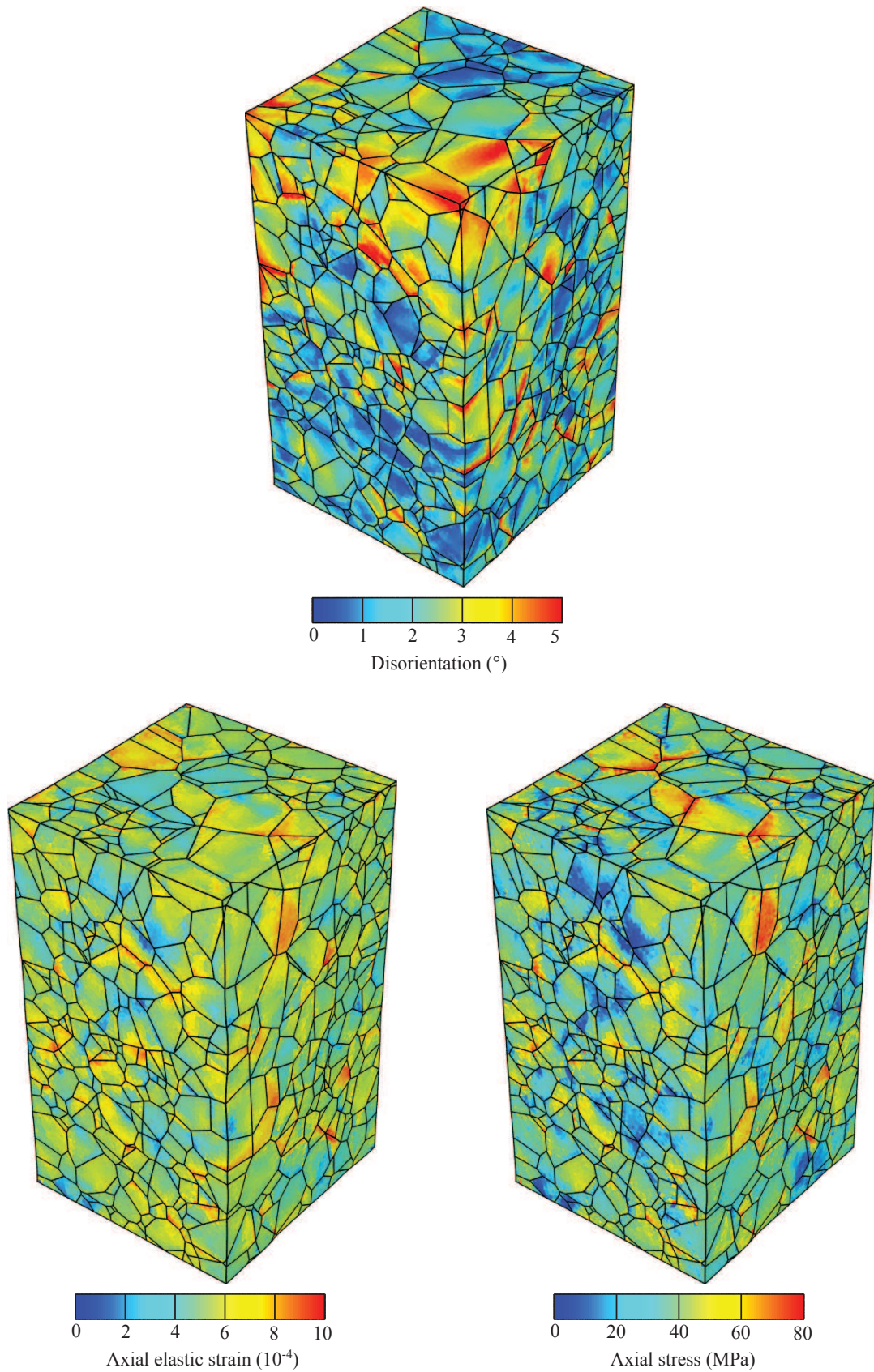
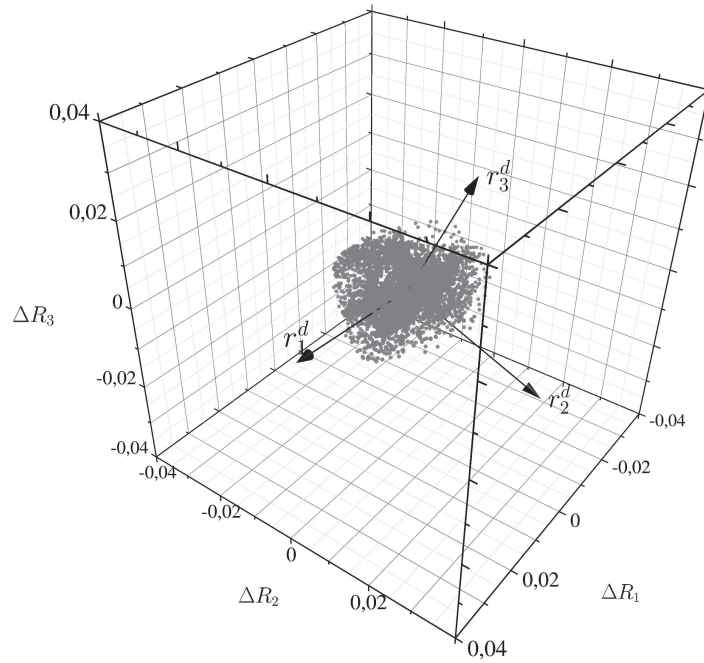
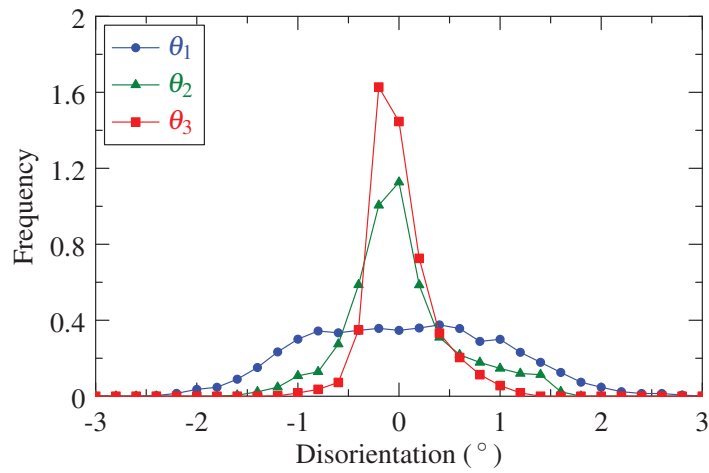


Figure VI.6 – Disorientation, axial elastic strain and axial stress fields in the finite element simulation after $\epsilon = 4.5\%$. The disorientation angle is calculated with respect to the initial orientation.



(a)



(b)

Figure VI.7 – Analysis of the orientation distribution in a finite element grain. (a) Disorientation distribution in the fundamental region of the Rodrigues space and (b) disorientation distributions (θ_1 , θ_2 , θ_3) along the 3 principal axes (r_1^d , r_2^d , r_3^d).

VI.2 Grain average rotations

The simulated grain rotations are compared to the experimental ones, in terms of distribution, variability and on a grain-by-grain basis. As mentioned previously, each rotation is described by an axis / angle pair, (\mathbf{r}, θ) , where \mathbf{r} is a unit vector and θ is positive.

The predictions of the Taylor model are also considered in the comparison. The main principles of Taylor's approach were presented in Section I.1: the model neglects the elastic strains and considers that all the grains are subjected to the same plastic strain (the macroscopic strain). The same crystal behaviour is used.

VI.2.1 Distributions

a) Rotation angles

The distributions of rotations angles are provided in Figure VI.8 for the successive strain increments. The incremental angles, $\hat{\theta}_i$, are normalized to correspond to a deformation increment of 1%. We observe that the grains rotate at a near-constant rate in both simulations, with average $\hat{\theta}_i$ of about 0.35° and 0.18° for the finite element method and the Taylor model, respectively. These results differ from the experiment, shown in Figure VI.8-a, where $\hat{\theta}_i$ increases from $\epsilon = 1.0\%$ (0.12°) to $\epsilon = 1.5\%$ (0.28°), remains stable up to $\epsilon = 2.5\%$ (0.31°) and then decreases in the last increment (0.20°). The overestimation of $\hat{\theta}_i$ by the finite element simulation remains to be explained.

Overall, we observe that the rotation rates are overestimated on average by the finite element simulation and somewhat underestimated by the Taylor model in all but the first increment. As a result, in Figure VI.9, the full rotation angles are overestimated in both simulations, with a smaller difference between the experiment and Taylor. The experimental angles appear to be less scattered. The finite element and Taylor distributions exhibit higher frequencies in the upper tails, extending up to about 3.5° and 2.3° , respectively, while the frequencies above 1.9° are already negligible in the experiment.

b) Rotation axes

The distributions of rotation axes are provided in Figure VI.10. We observe noticeable differences between the experiment and the simulations. The experimental axes are preferably distributed on the periphery of the stereographic circle and in particular near the X direction. The finite element simulation reveals a concentration of axes near the -X pole, which suggests some agreement with the experiment. However, the distribution exhibits overall lower densities and appears to be more uniform by nature. In fact, the best qualitative agreement is found between the experiment and the Taylor model, where the axes also tend to lie on the periphery of the stereographic circle.

The distributions of angles α between the rotation axes and the tensile axis are shown in Figure VI.11. Due to the axial symmetry, the range of values can be reduced and α varies from 0° (parallel to Z) to 90° (perpendicular to Z). The case of a random, uniform distribution of axes is represented as well and consists in a sine function. For the analysis of the complete distributions, the frequencies must be corrected for the increase of "area fraction" with α and thus normalized by the frequencies corresponding to the uniform case. This is illustrated in Figure VI.11-b, which confirms the observations made from the pole figures. The finite element distribution appear to be close to the uniform one, while the experimental and Taylor distributions clearly exhibit higher frequencies near to 90° . Above 35° , a reasonable agreement is found between the experimental results and the

Taylor model. Below 35°, the frequencies are strictly equal to zero for the Taylor model, while it is not the case in the experiment. Indeed, we can observe in Figure VI.10-c a clearly-defined region within 35° about the tensile axis where the Taylor model does not predict any rotation axes.

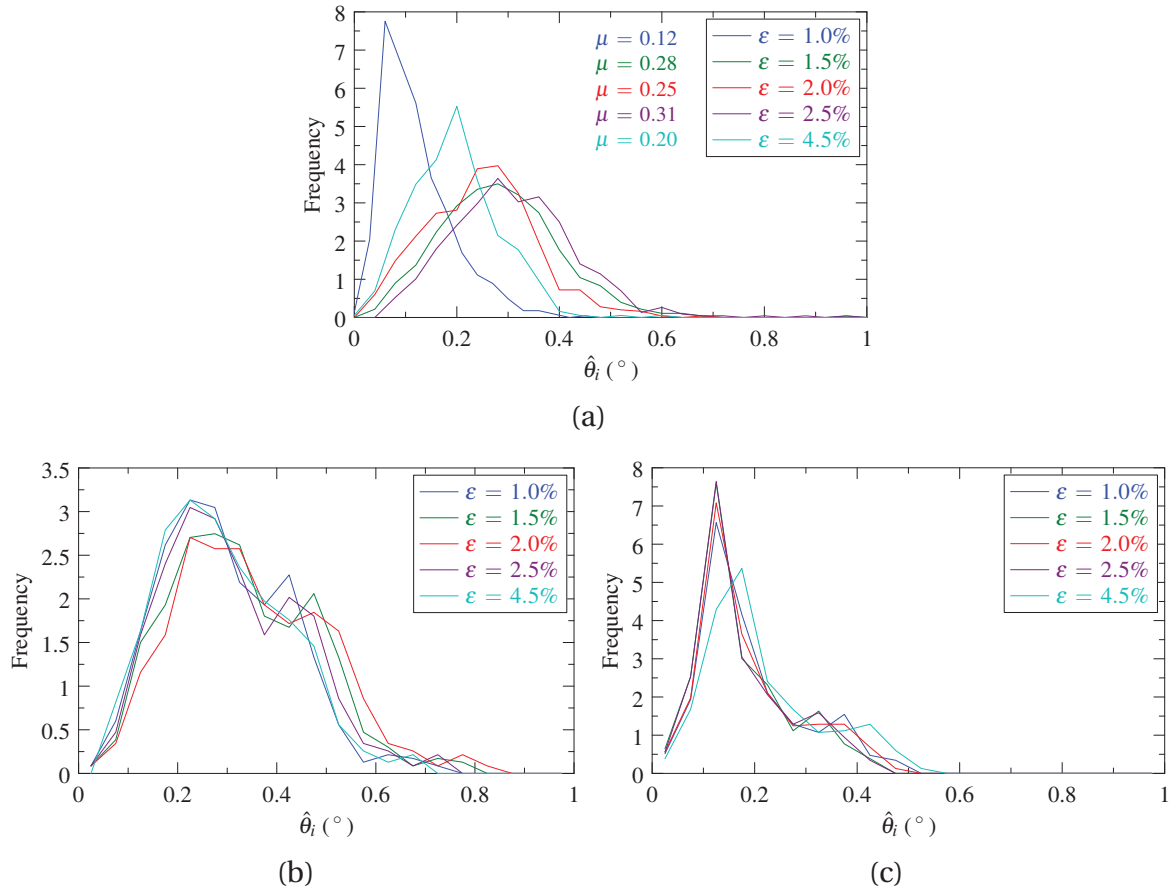


Figure VI.8 – Experimental and simulated rotation angles: distributions of incremental angles ($\hat{\theta}_i$) in (a) the experiment, (b) the finite element simulation and (c) the Taylor model.

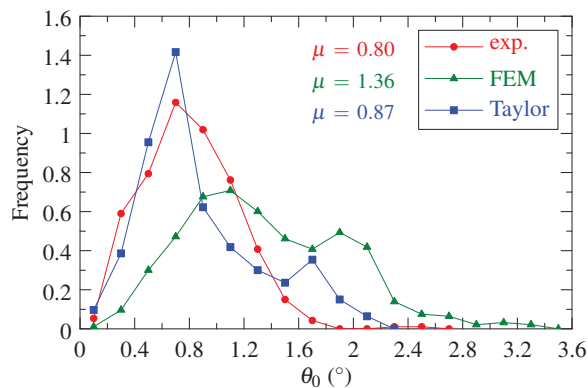


Figure VI.9 – Experimental and simulated rotation angles: distributions of rotation angles from the initial state to $\epsilon = 4.5\%$ (θ_0).

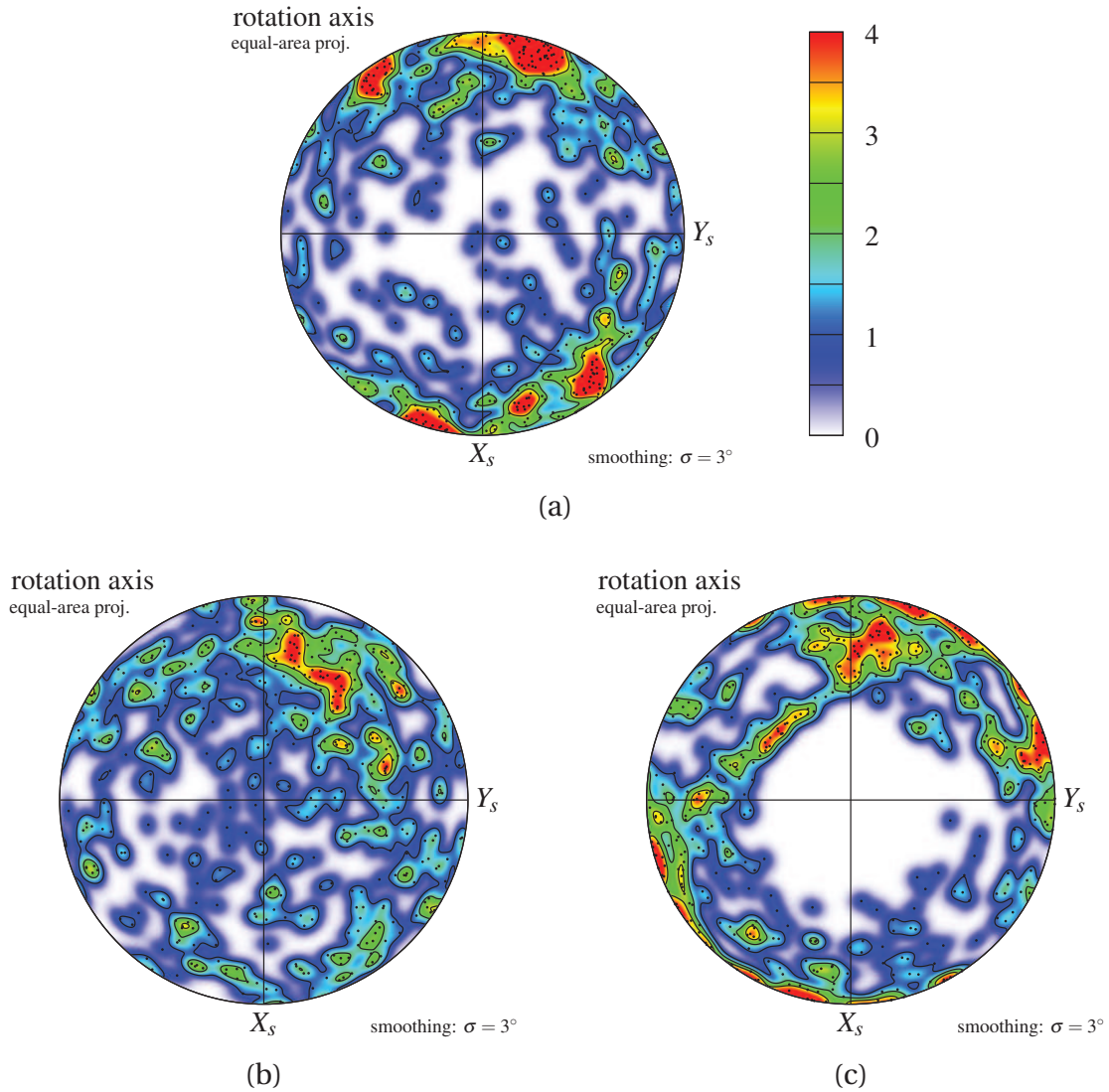


Figure VI.10 – Experimental and simulated rotation axes: (a) experiment, (b) finite element simulation and (c) Taylor model, from the initial state to $\epsilon = 4.5\%$. The pole figures are equal-area projections of the rotation axes onto the sample X-Y plane. The rotation axes are plotted as points on a density field with contour lines.

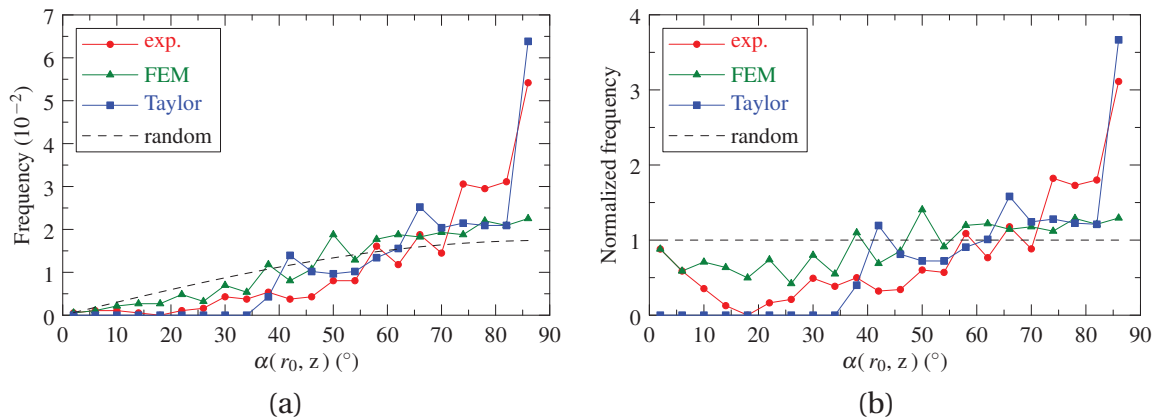


Figure VI.11 – Experimental and simulated rotation axes: correlation with the tensile direction Z. (a) Frequency and (b) normalized frequency distributions of the angles α between the rotation axes and Z.

VI.2.2 Variability at constant orientation

The variabilities at constant orientation (VCO) and overall variabilities (V) of the full rotations, obtained experimentally and in the simulations, are compared in Figure VI.12 and Table VI.2.

For the Taylor model, Quey *et al.* [42] observed that the zero-extrapolation approach provides variabilities close to zero for large enough grain sets (>2000). This demonstrates the validity of the method, as the Taylor predictions only depend on the grain orientations. Here, due to the limited number of grains (466), the VCO is not strictly equal to zero. The values remain however small, at 4° and 0.1 for the rotation axes and angles respectively. They corresponds to the uncertainties that can be expected for the evaluation of the experimental and finite element variabilities.

In the finite element simulation, for two grains of identical orientation, the rotation axes are disoriented on the average by 53° and the rotation angles differ on the average by 36%. These VCO values can be compared to the V values. The ratios of 64% and 88% for the rotation axes and angles, respectively, suggest a notable influence of the grain interaction on the rotations, compared to the influence of grain orientations. We observe that the finite element variabilities are in remarkable agreement with the experimental ones, thus indicating that the finite element model successfully reproduced the influence of grain interaction on the rotation variabilities.

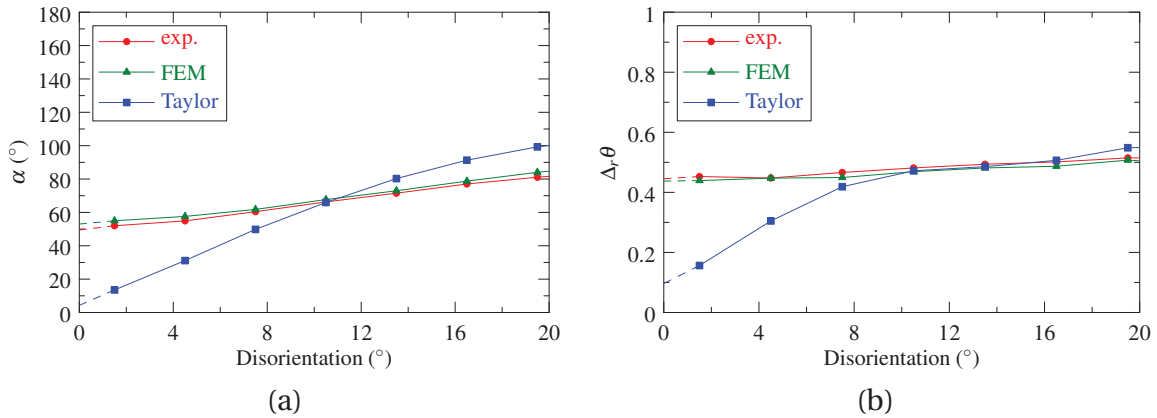


Figure VI.12 – Variability at constant orientation of the experimental and simulated rotations. (a) Rotation angles and (b) rotation axes.

Table VI.2 – Variabilities at constant orientation and overall variabilities of the experimental and simulated rotations.

	α (°)			$\Delta_r \theta$		
	VCO	V	ratio	VCO	V	ratio
Exp.	49	78	63%	0.45	0.50	90%
FEM	53	83	64%	0.44	0.50	88%
Taylor	4	88	5%	0.10	0.55	18%

VI.2.3 Grain-by-grain comparisons

The experimental and simulated rotation angles are compared in Figure VI.13. The correlation, quantified by the Pearson correlation coefficient, appears to be moderate with the finite element simulation and near absent with the Taylor model.

The experimental and simulated rotation axes are compared in Figure VI.13 in terms of the α angles between them. The case of a random, uniform distribution is also represented and corresponds to a sine function. The normalized frequencies are provided in Figure VI.13-b. We can observe the tendency of both models to predict rotation axes close to the experimental ones. The distributions appear to be relatively broad and extend up to 130° for the finite element method and even 180° for the Taylor model. The agreement is clearly better with the finite element simulation. The mean deviations are 40° (finite element model) and 54° (Taylor model). This indicates that, on the average, the rotation axes predicted by the finite element simulation are closer to the experimental ones by an angle of 14° .

The differences between the experiment and the Taylor model can be attributed to the variability of the experimental rotations, which cannot be reproduced by the Taylor model. The average angle between their respective rotation axes is 54° and the average relative difference between the rotation angles is 51%. This is comparable to the experimental VCO values of 49° and 45%, respectively, thus highlighting the important influence of grain interactions on the grain rotations. The finite element method improves the prediction of the rotation axes compared to the Taylor model by incorporating those interactions. The remaining discrepancies are to be attributed to the approximate morphology and the crystal behaviour.

For a finer analysis, the differences can be examined with regard to the grain orientations using, for example, the division of the orientation space defined by Winther *et al.* [8]. Figure VI.15 shows the average α deviations and the correlation coefficients ρ in the four regions. The results are consistent with the observations of Winther *et al.*: apart from Region 3 (which contains only 13 grains), the best agreement between experiment and simulations is found in Region 1. Besides, we can observe that in all regions the finite element predictions are closer (or better correlated) to the experiment than the Taylor ones.

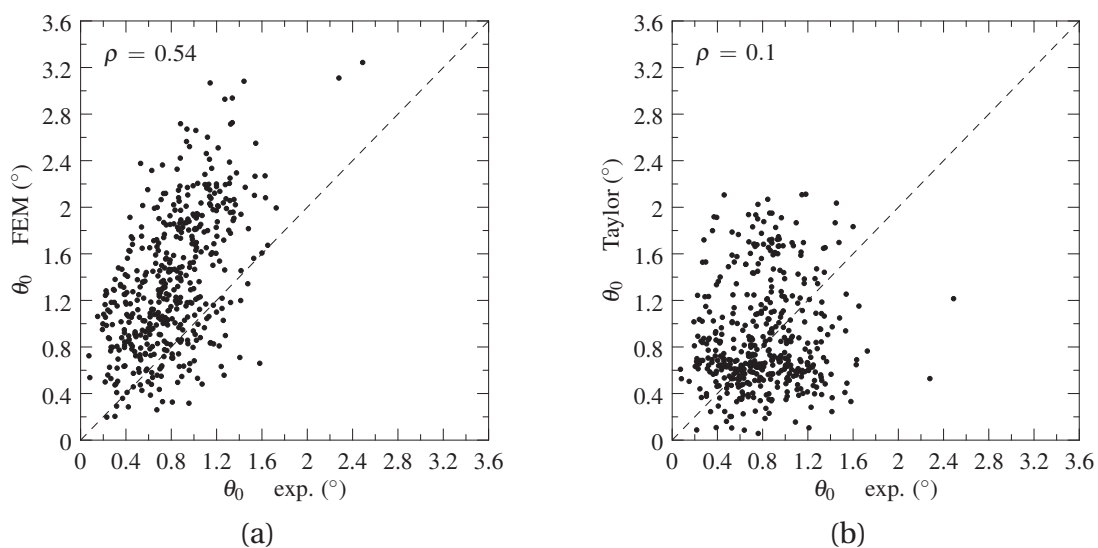


Figure VI.13 – Correlation between the experimental and simulated rotation angles. (a) Comparison between the experiment and the finite element simulation. (b) Comparison between the experiment and the Taylor model. ρ is the correlation coefficient.

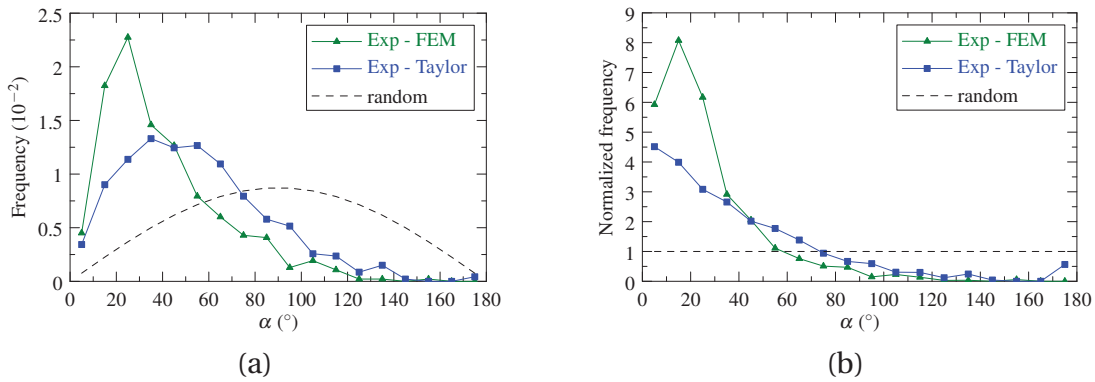


Figure VI.14 – Deviation between the experimental and simulated rotation axes. (a) Frequency and (b) normalized frequency distributions of the angles α between the experimental and simulated axes.

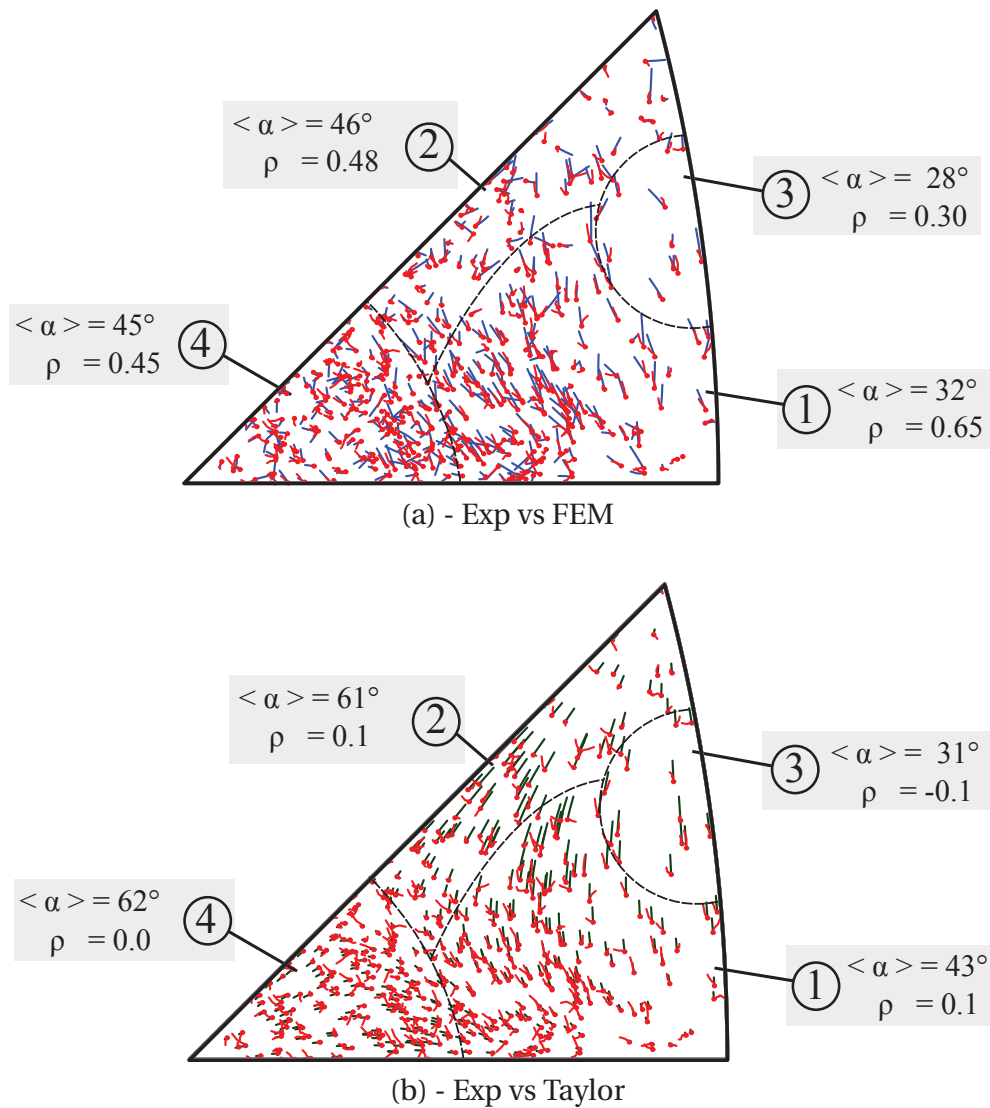


Figure VI.15 – Comparison of experimental and simulated rotations in the four IPF regions defined by Winther *et al.* [8]. The experimental rotations appear in red, while the finite element and Taylor ones are shown in blue and green, respectively. $\langle \alpha \rangle$ is the average deviation angle between experimental and simulated rotation axes. ρ is the correlation coefficient between experimental and simulated rotation angles. Regions 1, 2, and 4 contain 179, 77, 13 and 197 grains, respectively

VI.3 Intra-grain orientation spreads

The simulated intra-grain orientation spreads are compared to the experimental ones in terms of distribution and grain by grain. As mentioned previously, each spread is described by an average disorientation angle θ_d , an anisotropy factor λ_a and a preferential disorientation axis r_1^d (or equivalently $-r_1^d$).

In addition to the finite element simulation, we also considered in the comparison a new Taylor-based approach proposed by Quey *et al.* in Ref. [15]. Based on the simple assumption of an isotropic stress distribution about the grain nominal stress state, the model infers the anisotropy attributes (but not the angular extent) of the resulting reorientation distribution. A detailed description is provided in Appendix A. Thereafter, this simplified model will be referred to as Isotropic Stress Model (ISM).

VI.3.1 Distributions

a) Disorientation angles

The distributions of the average disorientation angles are shown in Figure VI.16 for the experiment and the finite element simulation. The average values corresponding to the successive strain levels are provided in Table VI.3. For both experiment and simulation, the average disorientation angles are monotonically increasing from 0.18° and 0.17° ($\epsilon = 1.0\%$) to comparable values of 0.61° and 0.77° ($\epsilon = 4.5\%$). The increase rates, albeit being somewhat smaller in the experiment, are in reasonable agreement. The distributions at 4.5% are directly compared in Figure VI.16-c. We observe that the angles vary from 0.1° to 1.8° . Although they are larger in the simulation by 0.16° on average, the agreement remains substantial.

b) Anisotropy factors

The distributions of the anisotropy factors are shown in Figure VI.17 for experiment and simulations. The average values corresponding to the successive strain levels are provided in Table VI.3. We observe that the anisotropy is stable in the finite element simulation at 1.75 and relatively stable as well in the simulation at comparable values of 1.7-2.0. Although a slight increase with strain of the average value is observed in the experiment, the changes in the distribution remain limited. The distributions at 4.5% are shown in Figure VI.16-c and compared to the ISM distribution. The latter exhibits a comparable average values of 2.12. We observe that the anisotropy factor ranges from 1.2 to about 5.7 in the ISM results, while it ranges from 1 to 4.9 in the experiment, and from 1 to 2.9 in the finite element simulation. Despite these differences, a reasonable agreement can be reported between experiment and simulation.

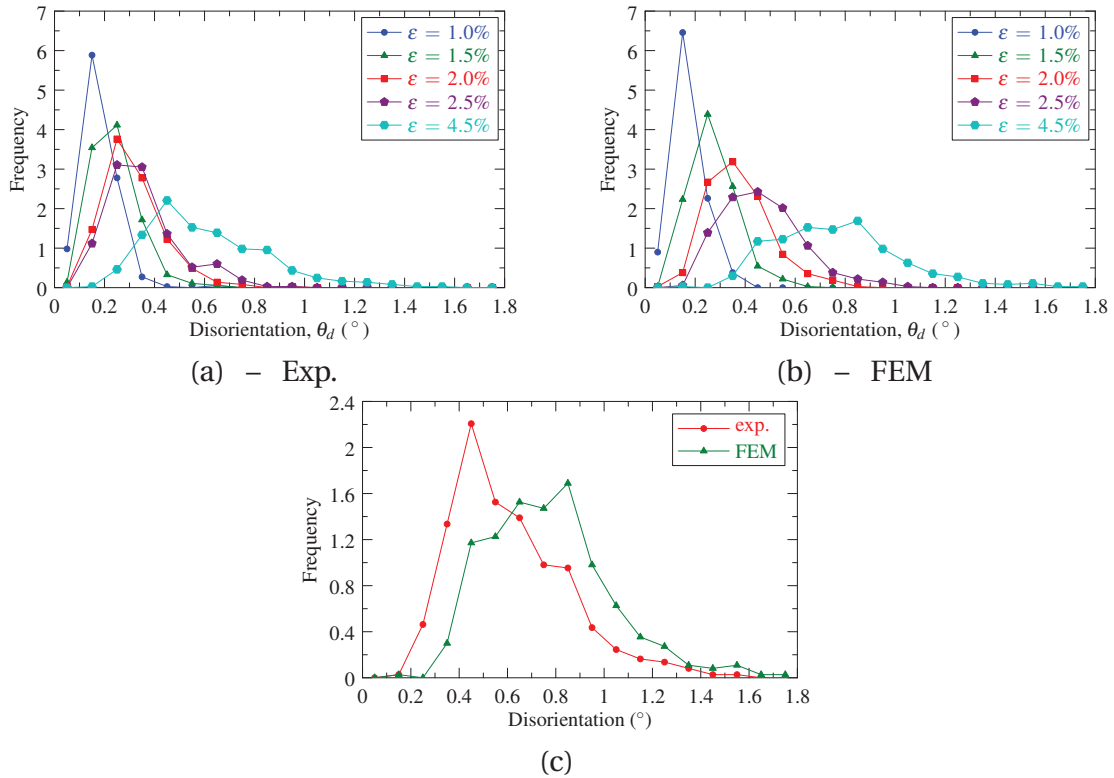


Figure VI.16 – Experimental and simulated average disorientation angles (θ_d). Evolution with strain in (a) the experiment and (b) the finite element simulation. (c) Direct comparison at 4.5%. Average values are provided in Table VI.3

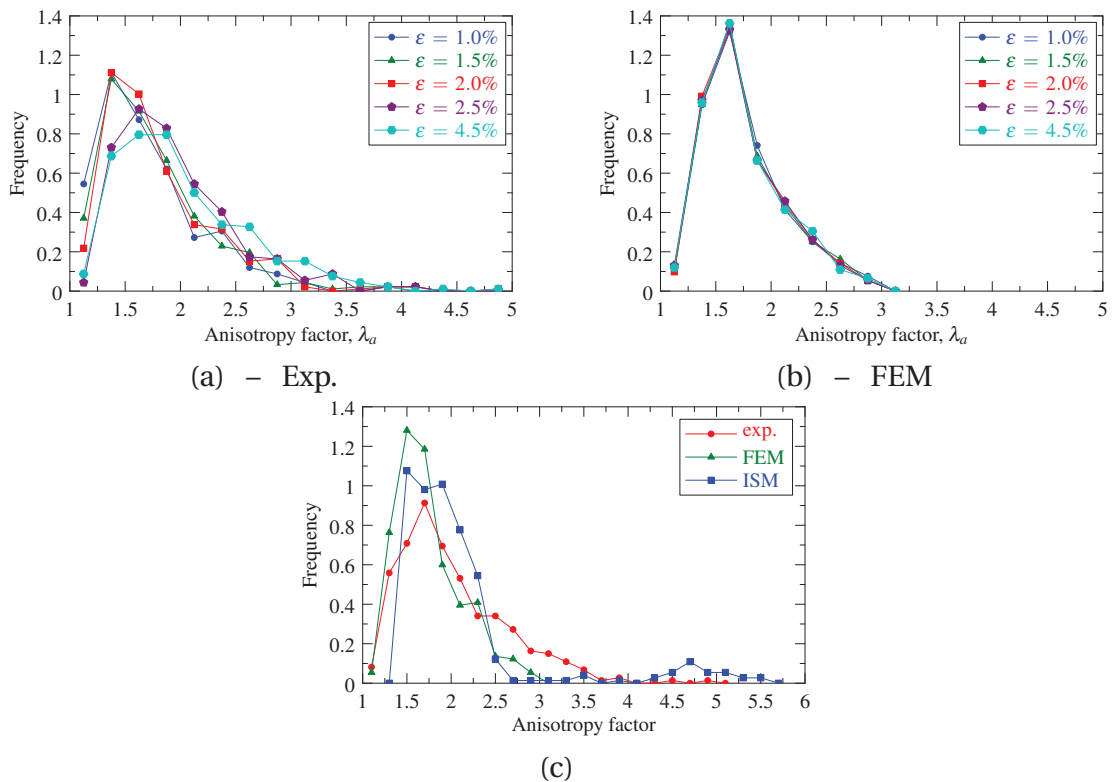


Figure VI.17 – Experimental and simulated anisotropy factors (λ_a). Evolution with strain in (a) the experiment and (b) the finite element simulation. (c) Direct comparison at 4.5%. Average values are provided in Table VI.3

Table VI.3 – Evolution of the average disorientation angles and anisotropy factors with strain in the experiment and the simulations.

strain (%)	Disorientation angle, θ_d (°)		Anisotropy factor, λ_a		
	Exp.	FEM	Exp.	FEM	ISM
1.0	0.18	0.17	1.70	1.75	2.12
1.5	0.24	0.27	1.77	1.75	2.12
2.0	0.31	0.37	1.81	1.75	2.12
2.5	0.34	0.46	1.95	1.75	2.12
4.5	0.61	0.77	2.00	1.75	2.12

c) Preferential disorientation axes

We observed experimentally that the preferential disorientation axes migrate between $\varepsilon = 1.0\%$ and 2.5% and tend to be perpendicular to the tensile axis. Then, they remain stable beyond $\varepsilon = 2.5\%$ (Subsection V.3.3). In contrast, we observe in the finite element simulation that the preferential disorientation axes are already developed at $\varepsilon = 0.5\%$ and slightly vary up to $\varepsilon = 4.5\%$. The ISM provides one prediction regardless of the strain level. Hence, as the grain rotation angles are small, and considering that the experimental spreads are better assessed for the last strain level (larger spot broadening), we will restrict the comparison to $\varepsilon = 4.5\%$.

The distributions of preferential disorientation axes at $\varepsilon = 4.5\%$ are presented in Figure VI.18, for experiment and simulations, as equal-projections onto the sample X-Y plane. We observe that the experimental and simulation axes are strongly distributed on the periphery of the pole figures, that is, in the X-Y plane. This tendency can be further examined by taking into account the axial loading symmetry and thus considering only the angles α between the disorientation axes and the tensile axis Z. This is illustrated on Figure VI.19. We observe a good quantitative agreement between the three distributions, which show a clear increase of the frequencies close to 90° . The tendency is much stronger for the ISM distribution, where there is not any preferential disorientation axis within 45° of Z. The increase appears to be more regular for the experiment and the finite element simulation. In terms of pole figure distributions, a better qualitative agreement is found between the experiment and the finite element simulation. Both reveal disorientation axes preferentially distributed about the X direction, while they are more evenly distributed along the circle periphery for ISM.

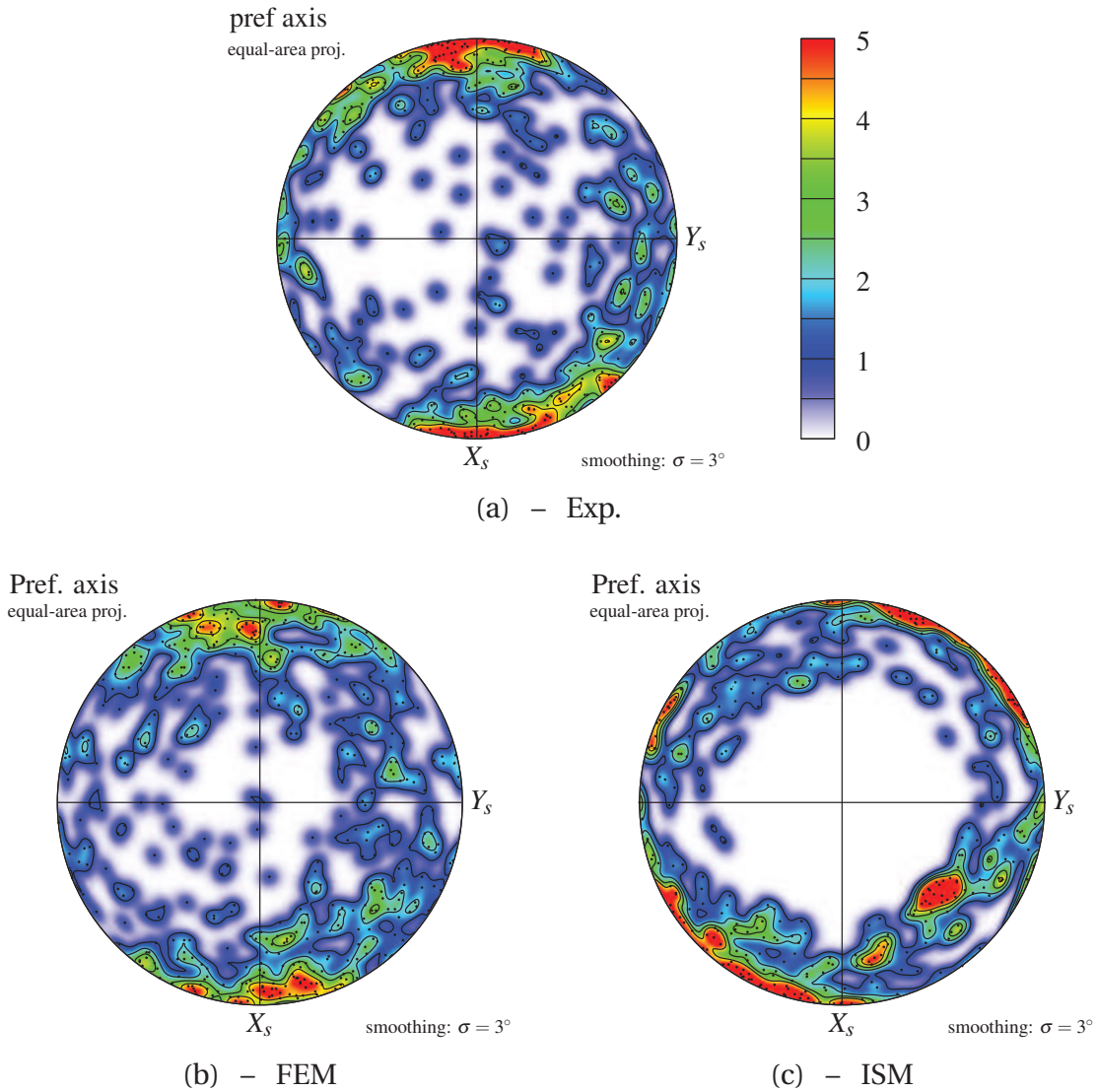


Figure VI.18 – Experimental and simulated preferential disorientation axes after 4.5%: (a) experimental, (b) finite element simulation and (c) ISM. The pole figures are equal-area projections of the preferential axes onto the sample X-Y plane. The axes are plotted as points on a density field with contour lines.

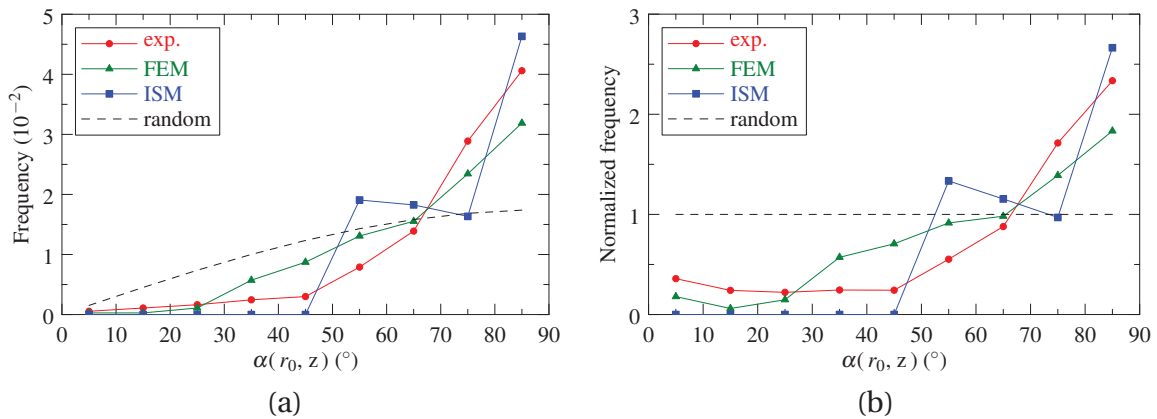


Figure VI.19 – Experimental and simulated preferential disorientation axes after 4.5%: correlation with the tensile direction Z. (a) Frequency and (b) normalized frequency distributions of the angles α between the preferential disorientation axes and Z.

VI.3.2 Relation to deformation mechanisms

The development of the intra-grain orientations spreads results from spatial fluctuations of the lattice rotations and indicates differences in the local slip system activities. This can be analysed based on the finite element simulation results, as was done in Ref. [15].

A crystal rotation is controlled by the crystal slip geometry, which consists for each slip system s of a plane normal \mathbf{n}^s , a slip direction \mathbf{b}^s and a spin direction \mathbf{t}^s . A particular attention is paid to the spin directions, which determine the crystal rotation axis depending on the slip rates $\dot{\gamma}^s$. The latter are available in the finite element simulation for each element and each slip system. It is generally observed that two or three systems have dominant activities during straining. This can be assessed for each grain by averaging the absolute slip rates over the grain elements. The higher the average absolute slip rate $|\overline{\dot{\gamma}^s}|$, the higher the activity of the slip system s .

The distribution of spin vectors weighted by the average absolute slip rates ($|\overline{\dot{\gamma}^s}| \mathbf{t}^s$) is provided in Figure VI.20 for $\epsilon = 1.0\%$. We can observe that the most activated systems have spin vectors that lie preferentially in the X-Y plane. The distribution appears to be very similar to those obtained for the grain rotation axes in Figure VI.10 and the preferential disorientation axes in Figure VI.18. Although these observations are consistent with our analysis, they alone are not sufficient to explain the observed distribution of preferential disorientation axes.

This requires to examine the intra-grain variability of the slip rates in the simulation. This is done again for $\epsilon = 1.0\%$, in relation with the distribution of spin directions. For each slip system, the variability of the slip rates is given by the standard deviation of the slip rates over the grain elements. The obtained variabilities are plotted against the average absolute slip rates in Figure VI.21. We can observe that non-active systems exhibit low variabilities. The variability then increases with the activity and is higher for the most activated slip systems. Combined with the slip geometry, this variability leads to a higher variability of the reorientation rates about the spin vectors of the most activated systems. In the end, the preferential disorientation axes are distributed accordingly, which explains the similarity in the finite element simulation between the distribution of preferential disorientation axes in Figure VI.21 and the distribution of spin directions in Figure VI.18-b.

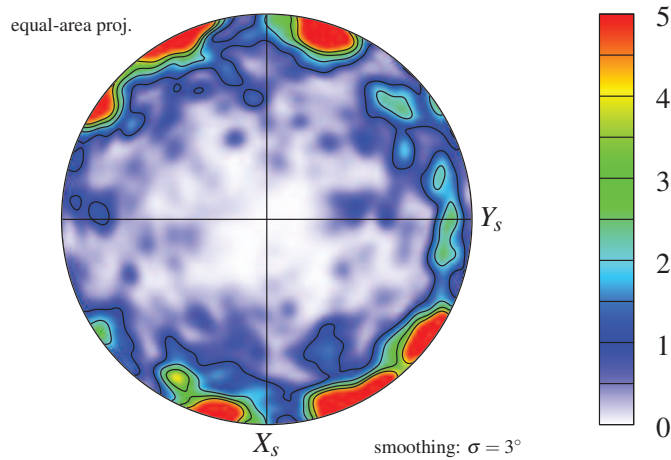


Figure VI.20 – Distribution of active spin vectors in the finite element simulation at $\epsilon = 1.0\%$: equal-area projection of $|\overline{\dot{\gamma}^s}| \mathbf{t}^s$.

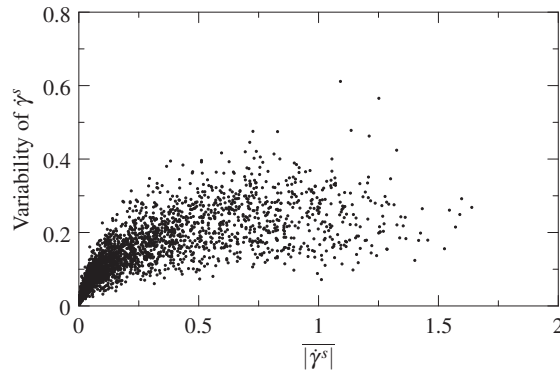


Figure VI.21 – Relation between slip rate variability and slip activity. For each grain, the slip rate variabilities (standard deviation) of the twelve octahedral systems are plotted against the slip activity (average absolute rates).

VI.3.3 Grain-by-grain comparisons

a) Disorientation angles

The average disorientation angles are compared in Figure VI.22 for the experiment and the finite element simulation. As already observed, the distributions are of comparable extent, with somewhat larger angles in the simulation. The correlation between the individual, experimental and simulated, disorientation angles appears to be relatively low, the coefficient value being 0.41.

b) Anisotropy factors

Low to very low correlations were found on the anisotropy factors either between the experiment and the finite element simulation (0.21), or between the experiment and ISM predictions (0.01). For the ISM in particular, the anisotropy factors are almost uniformly distributed within 1.5 to 2.5, and any relation with respect to the experimental angles.

c) Preferential disorientation axis

The deviation between the experimental and the simulated preferential axes can be quantified from the angles α between them. The corresponding distributions are shown in Figure VI.23. In both plots, the finite element simulation exhibits higher frequencies between 0 and 45°. The ISM distribution is rather uniform (this can be seen in particular from the normalized frequencies). These results indicate a correlation between the experiment and the finite element simulation, but no correlation between the experiment and the ISM. The respective average α angles between the preferential axes are 37° and 50°, which are comparable to the average α angles between the rotations axes (40° and 54°). The apparent absence of correlation between the experiment and the ISM model can however be investigated by further analyses.

The preferential disorientation axes are plotted in the fundamental region of the Rodrigues orientation space, as shown for $\epsilon = 4.5\%$ in Figure VI.24. The preferential disorientation axes are represented by batons (constant radius and length), centred on the corresponding grain orientations and aligned along the preferential disorientation directions. The colours indicate the sample directions, with which the preferential disorientation directions are aligned.

We can see from the distributions that the batons are mostly aligned with X (red), Y (green) or intermediate positions. The alignment is clearly orientation dependent and varies smoothly in the orientation space. This is shown in particular by the projections along the tensile axis Z. Similar trends can be identified between the three distributions. The best overall agreement is found between the experiment and the finite element simulation. Away from the Z-axis, a good agreement can also be observed between the experiment and ISM. Close to the Z-axis, the alignments evolves very smoothly in the ISM predictions and are rather variables in the experiment (and the finite element simulation). The region close to the Z-axis would corresponds in an IPF to the region close to the [1 0 0] corner (tensile axis along [1 0 0]), where a high variability of the experimental grain rotations is observed. This can explain the significant differences observed between the experiment and the ISM predictions, as the Taylor model usually fail in this part of the orientation space to reproduce the variability and predict the grain rotations. The strong texture in this region can therefore explain that no overall correlation could be identified from the α angles between the experiment and the ISM axes (Figure VI.23).

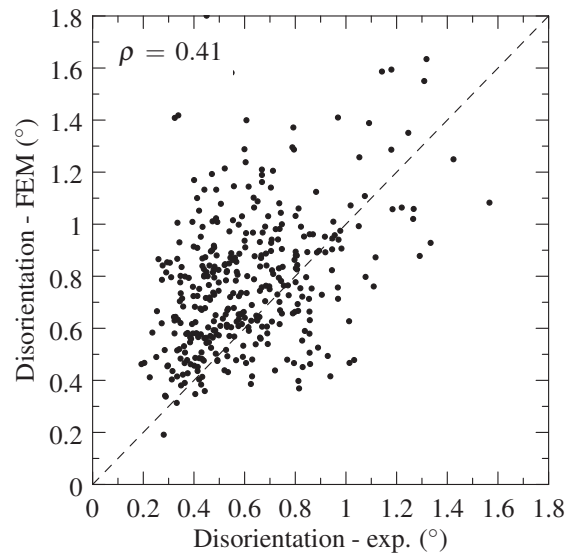


Figure VI.22 – Correlation between the experimental and simulated (FEM) average disorientation angles. ρ is the correlation coefficient.

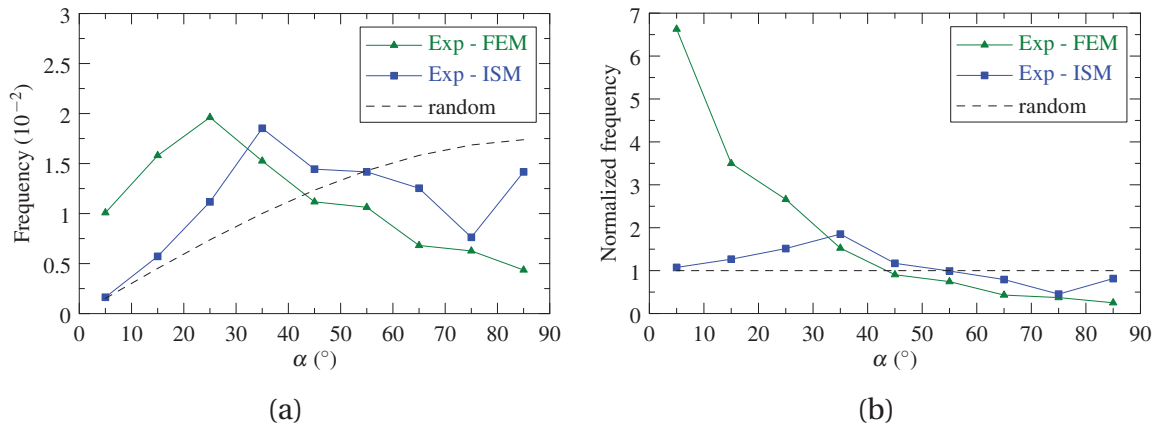


Figure VI.23 – Deviation between experimental and simulated preferential disorientation axes. (a) Frequency and (b) normalized frequency distributions of the angles α between the preferential disorientation axes.

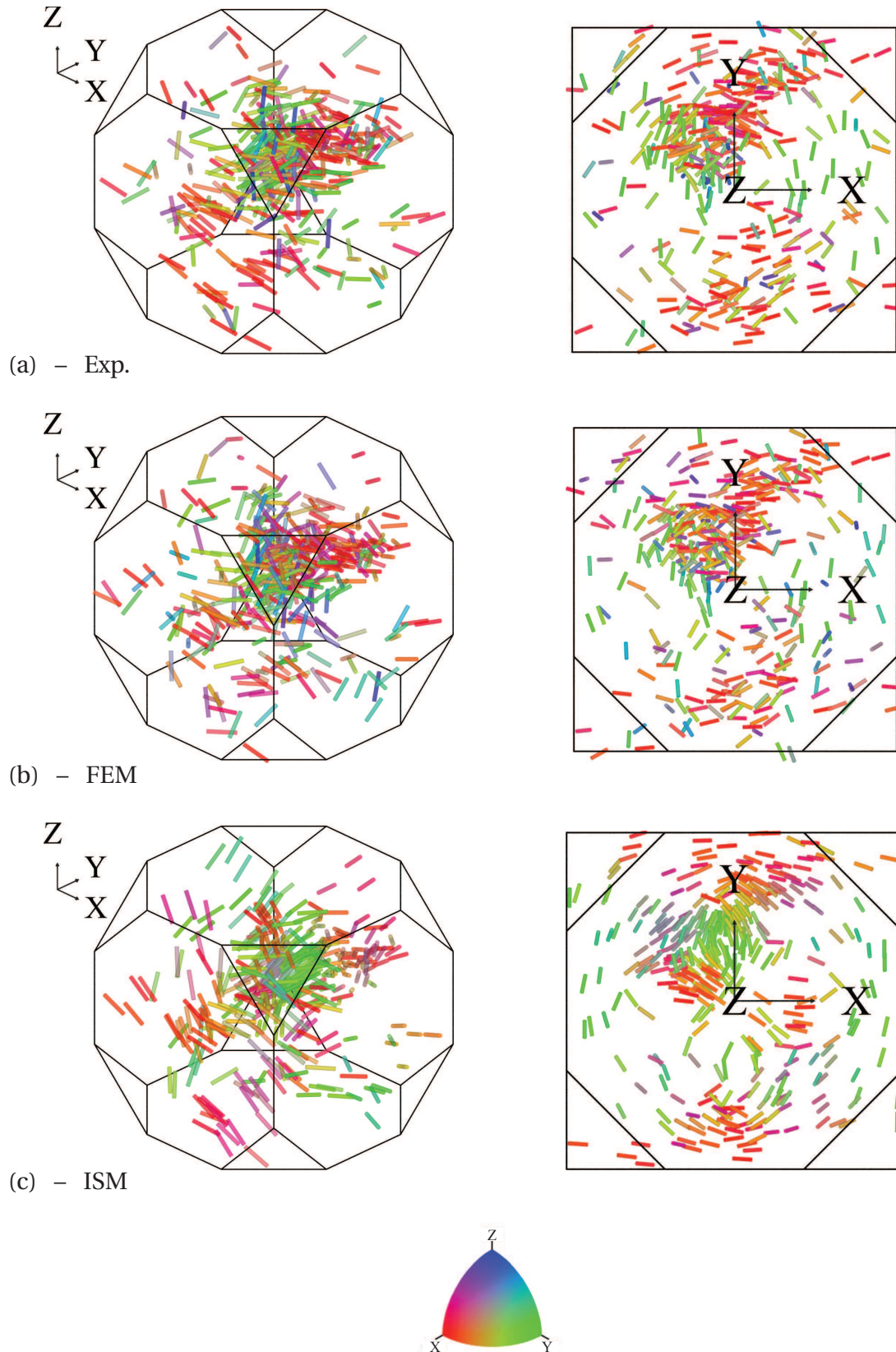


Figure VI.24 – Experimental and simulated disorientation axes: relation to the grain orientations, shown in the Rodrigues fundamental region for (a) experiment, (b) finite element simulation and (c) ISM. Each grain is represented by a baton centred on the grain orientation and aligned with the preferential disorientation axis. The colour is related to the axis components.

VI.4 Grain average elastic strains and stresses

The elastic strains and stresses obtained from the finite element simulation are compared to the experimental ones, in terms of distribution and grain by grain. In the experiment, a single, average elastic strain tensor $\underline{\epsilon}^e$ and a single, average stress tensor $\underline{\sigma}$ are measured for each grain. Hence, for the comparison, the simulated elastic strain and stress fields are averaged over each grain volume. The quantities are expressed and examined in the sample coordinate system.

VI.4.1 Distributions

The distributions of elastic strain and stress components are provided in Figures VI.25 and VI.26, and were computed using the same grains in experiment and simulation. The densities represent volume fractions, which were obtained by weighting the strain and stress values by the corresponding grain volumes. The mean and full-width-at-half-maximum (FWHM) of the experimental distributions were obtained from Gaussian fits. For comparability, the same procedure was applied to the simulation data, although this could also be calculated based on the distributions over all the mesh elements.

Regarding the elastic strains in Figure VI.25, we can observe a reasonable agreement between the evolutions of the distributions in the experiment and the simulation. It can be seen for the transverse component ϵ_{xx}^e (shifting from 0 to about -2×10^{-4}), the axial component ϵ_{zz}^e (shifting from 0 to about 5×10^{-4}) and the shear component ϵ_{xz}^e (steady about zero). The remaining transverse and shear components exhibit similar trends as ϵ_{xx}^e and ϵ_{xz}^e . The shift of the transverse components toward negative values is characteristic of the Poisson effect, as the material tends to contract along the directions perpendicular to the stretching direction. This effect was already assessed in the experiment, yielding Poisson's ratios of $\nu_x = 0.28 \pm 0.03$ and $\nu_y = 0.34 \pm 0.03$ at $\epsilon = 1.0\%$. In the simulation, we obtain values of $\nu_y = 0.33$ and $\nu_z = 0.36$, which both are consistent with the theoretical value of pure Al (0.35, [16]) and the experimental values. Besides, we observe the same tendency of the ϵ_{xx}^e component to be smaller than ϵ_{yy}^e . Although this seemed to indicate a systematic bias in the measurements, the simulation rather suggests that this difference is due to the texture.

Regarding the stresses in Figure VI.26, similar evolutions are observed as well. The axial stress component is shifted with straining from 0 to about 40 MPa. The transverse and shear components remain steady about zero, as it can be expected on the macro-scale for uni-axial tension. A slight deviation is observed though in the experiment, where the transverse components exhibit mean values of about 5 MPa at $\epsilon = 4.5\%$. This can be attributed to the measurements errors, which are at least of the same order.

Both in experiment and simulation, the strain and stress distributions broaden with plastic deformation. This affects all the six components, as their amplitudes progressively decrease from the initial to the final state. This indicates a variability among the grain mechanical responses. The broadening are similar for the transverse and shear components, but appear to be very different for the axial components. Indeed, regarding ϵ_{zz}^e and σ_{zz} , the experimental FWHMs are almost twice as large as in the simulation. One could attribute this to the measurement errors; however, such a difference should be observed as well on the transverse and shear components, which is clearly not the case. These results thus rather suggest a higher variability of the grain responses in the experiment than in the simulation.

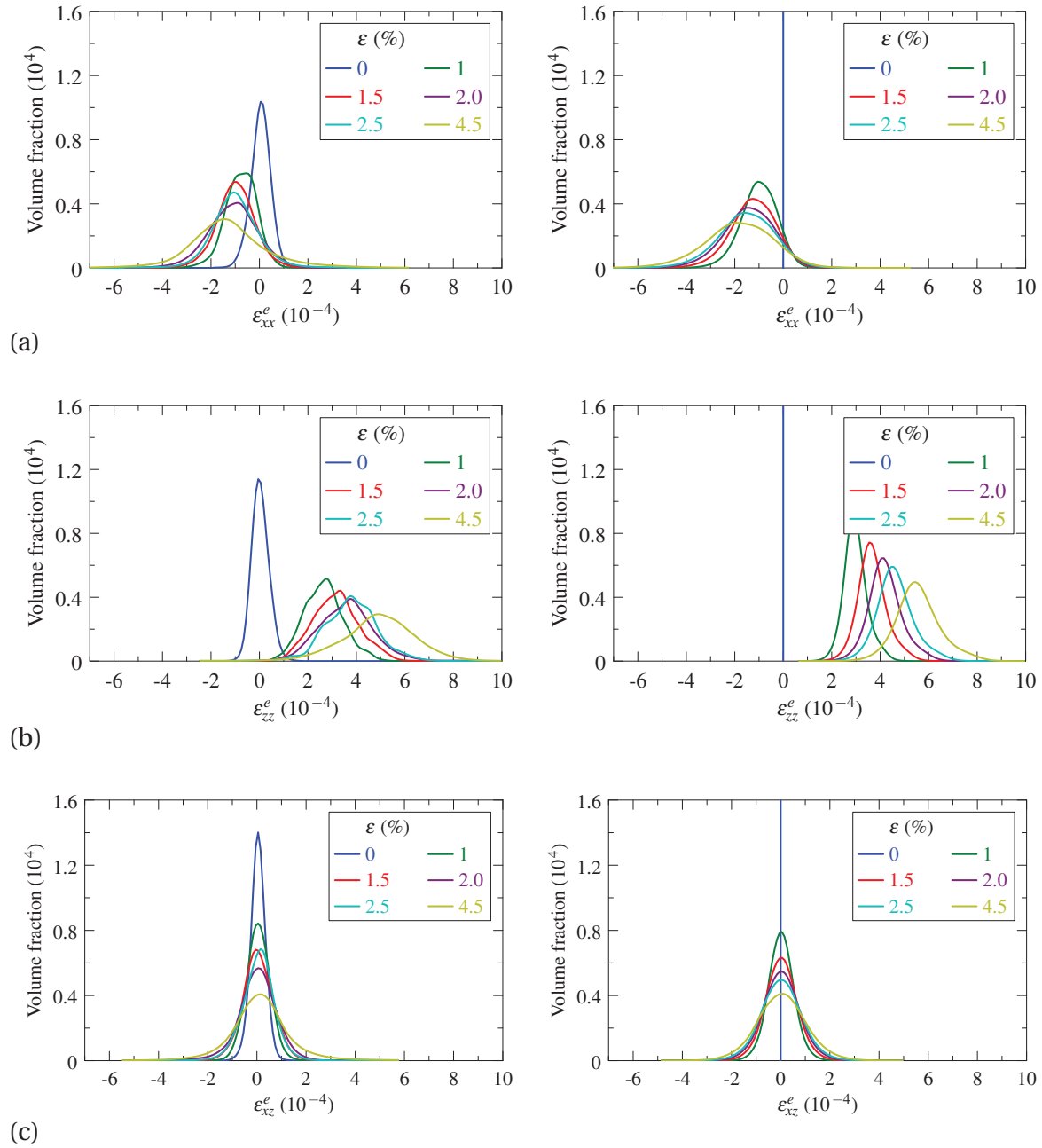


Figure VI.25 – Evolution of the experimental (left) and simulated (right) elastic strain distributions with plastic strain, illustrated for the xx-transverse component, the zz-axial component and the xy-shear component.

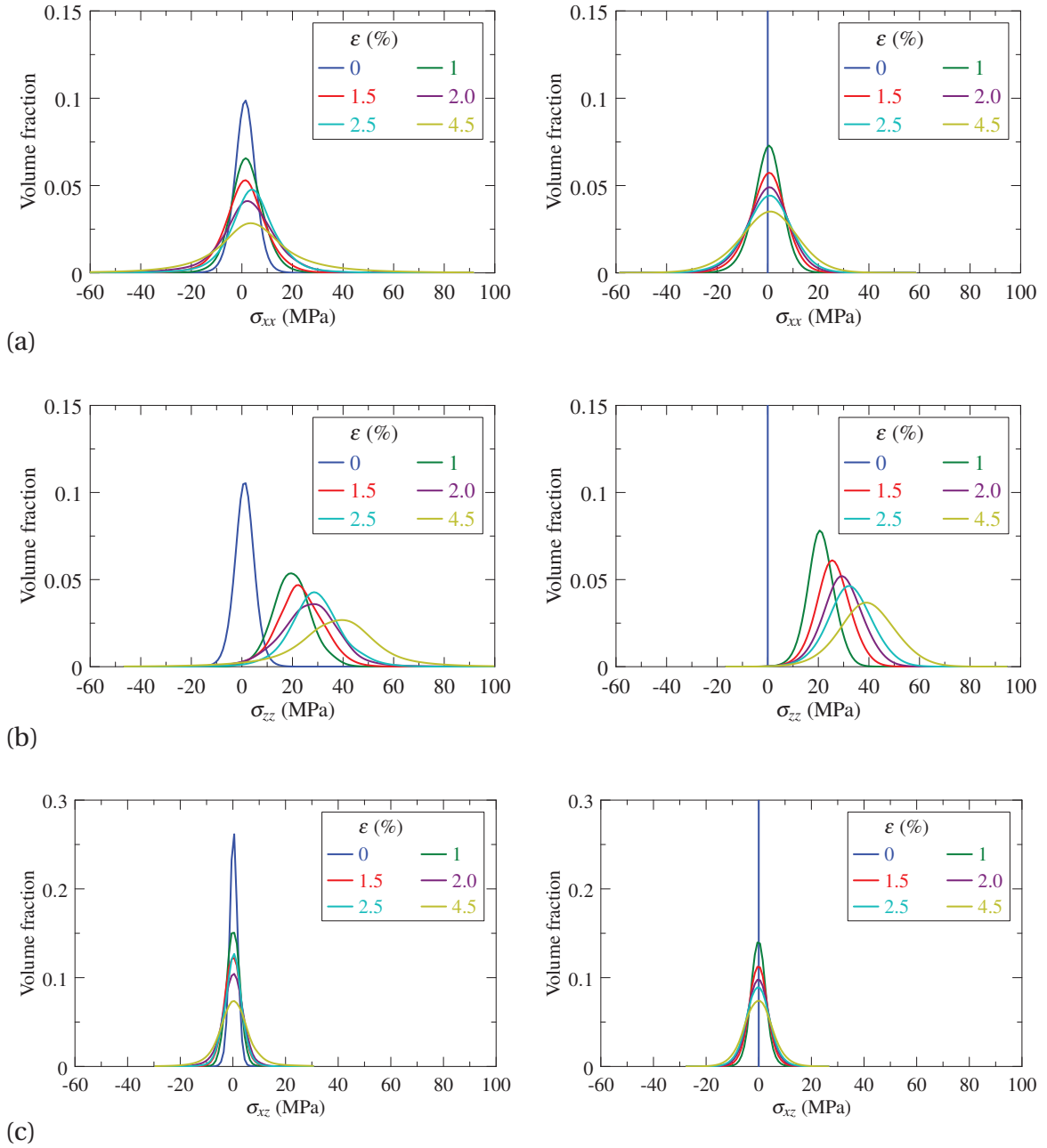


Figure VI.26 – Evolution of the experimental (left) and simulated (right) stress distributions with plastic strain, illustrated for the xx-transverse component, the zz-axial component and the xy-shear component.

VI.4.2 Macroscopic response

The mean, axial, elastic strain and stress values are compared in Figure VI.27. The experimental error bars correspond to standard errors, which were calculated by propagating the individual grain standard errors. We observe that both quantities are found larger in the simulation than in the experiment. The difference is less severe for the stress and within the error at $\epsilon = 4.5\%$, but it is much larger than the errors for the elastic strain. This seems to indicate either that the sample slightly relaxed during the *in situ* measurements, or that the plastic strain levels were slightly overestimated. Although this makes the comparison more delicate, it does not prevent from examining the correlations between experiment and simulation results.

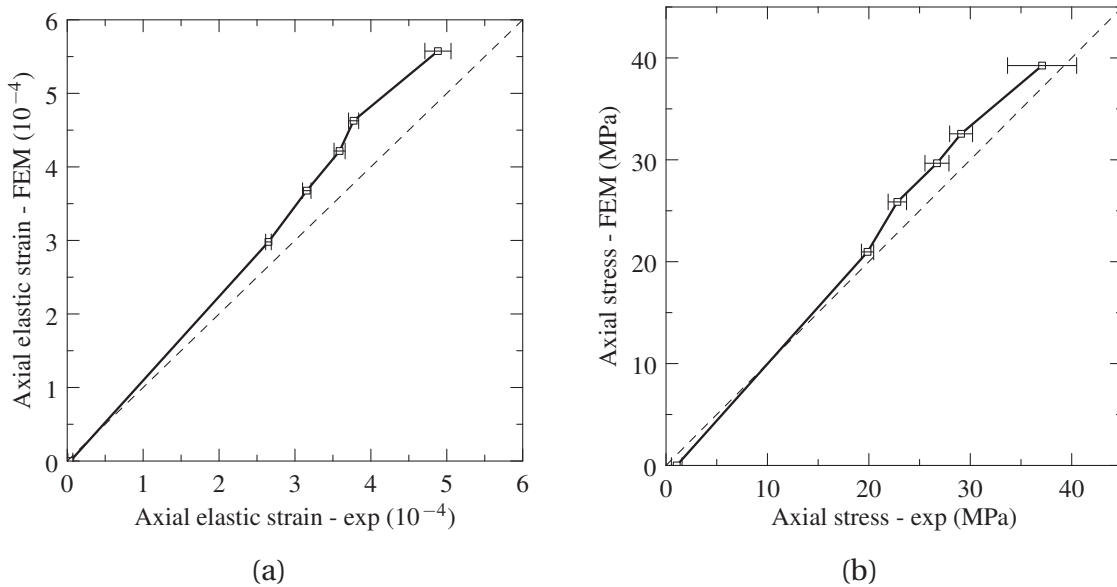


Figure VI.27 – Average axial elastic strain and stress: correlation between experiment and finite element simulation (volume-weighted averages). The experimental error bars correspond to the propagated standard errors.

VI.4.3 Relation to the grain orientations

The repartitions of axial elastic strain and axial stress, as a function of the orientation, are represented in Figure VI.28 for $\epsilon = 1.0\%$. Both experiment and simulation show a dependency on crystallographic orientation, which results on average that grains close $[1\ 1\ 1]$ exhibit higher values of axial elastic strain and stress. As already mentioned, we observe in the experiment a significant drop of the average grain response in a large region of the orientation space, near the centre of the stereographic triangle. This is not reproduced in the finite element simulation.

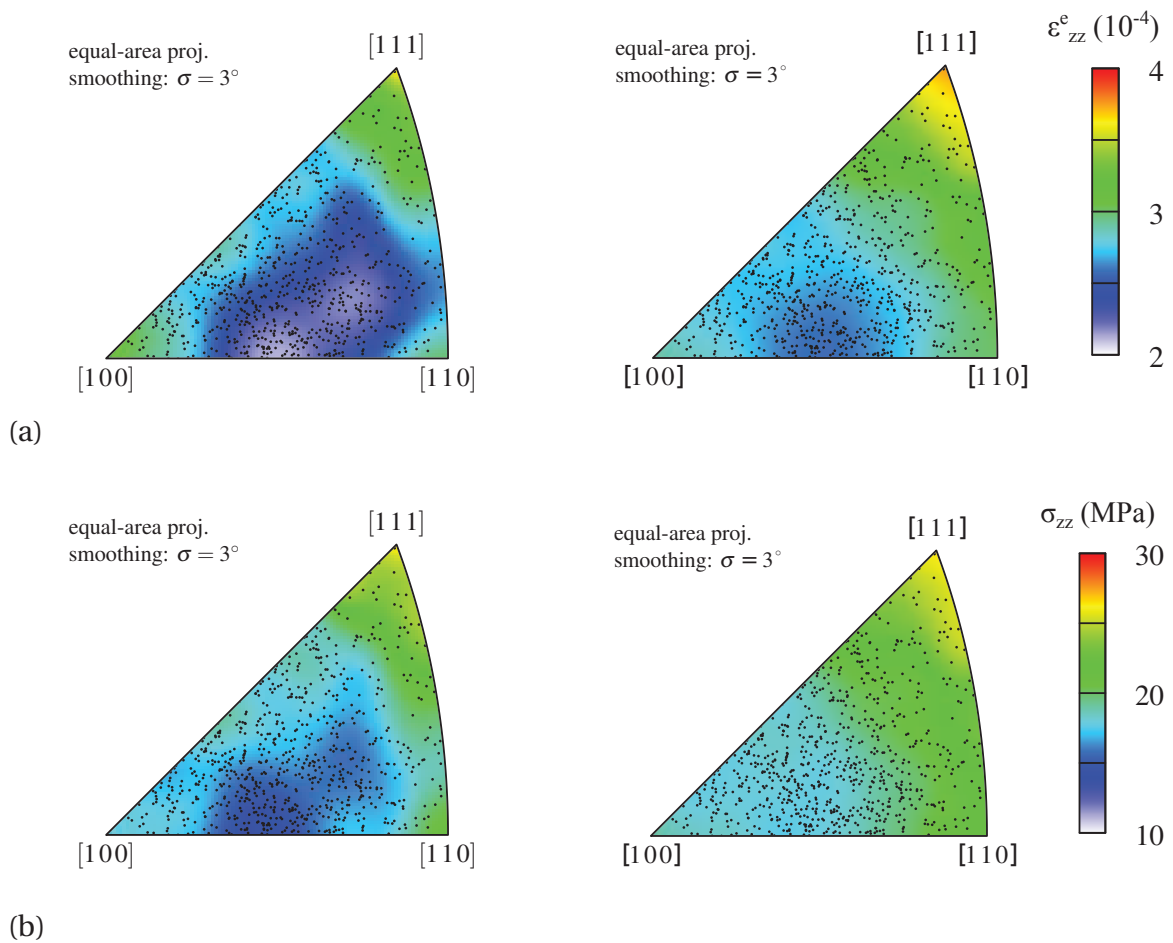


Figure VI.28 – Relation to orientation of the grain (a) axial elastic strains and (b) axial stresses at $\epsilon = 1.0\%$ (equal-area projections). Experiment on the left and simulation on the right.

VI.4.4 Grain-by-grain comparisons

The results are compared in Figure VI.29 for a selected grain, revealing a remarkable correspondance. Regarding first the representation against the applied stress, the onset of plasticity appears as inflections on the finite element curves at 10 MPa, well below the first experimental point at 20 MPa. The elastic strain and stress components evolve with near-linear trends up to 40 MPa ($\epsilon = 4.5\%$). The axial component increases according to the applied stress to reach about 5×10^{-4} and 40 MPa in the final state. In both experiment and simulation, the transverse component ϵ_{xx}^e is found to significantly decrease with the load and finally reaches about -4×10^{-4} . The same trend appears on σ_{xx} with a smaller amplitude. Similar responses can be observed between the experiment and the simulation for the other components, too, but within $\pm 2 \times 10^{-4}$ and ± 10 MPa, which makes the correlation less obvious. The largest discrepancy is found for the xx-transverse component at $\epsilon = 4.5\%$ and is comparable to the method accuracy (1×10^{-4} and 8 MPa). Regarding the representation against the applied deformation, the same comments can be made, although the experimental plastic strain levels are less precisely known. Lastly, the comparison can be directly drawn in the elastic strain-stress space of the grain, as illustrated in Figure VI.29-c and -d. Again, in the final state, we can observe a disagreement between experiment and simulation, which clearly affects both transverse components.

Overall, this example reveals that the differences between the corresponding curves lie within the experimental standard errors. To further investigate the differences between experiment and simulation, the absolute deviations are computed for all the 466 grains and represented as distributions. This is shown in Figure VI.30 for the xx-transverse, zz-axial and yz-shear components of strain and stress. The distributions are examined in Table VI.4 with regard to the measurement accuracies, 1×10^{-4} and 8 MPa. The best agreement is found for the shear components, shown in Figure VI.30-c, as the deviations are smaller than the accuracies at $\epsilon = 1.0\%$ and remains mostly smaller up to $\epsilon = 4.5\%$ (75% for strains and 90% for stresses). The agreement is good as well for the transverse component shown in Figure VI.30-a. Initially, at $\epsilon = 1.0\%$, the deviations are smaller than the corresponding accuracies for about 90% of the grains. This decreases to 62% and 56% at $\epsilon = 4.5\%$ for strains and stresses, respectively. The largest differences concern the axial component shown in Figure VI.30-b. However, the deviations remain smaller than the accuracies for more than 50% of the grains up to $\epsilon = 4.5\%$, which confirms a substantial agreement between the experiment and the finite element simulation.

Besides, the deviations between the full tensors, $\|\Delta \underline{\epsilon}^e\|$ and $\|\Delta \underline{\sigma}\|$, were also measured using the L^∞ distance, as:

$$\|\Delta \underline{\epsilon}^e\| = \left\| \underline{\epsilon}_{\text{Exp}}^e - \underline{\epsilon}_{\text{FEM}}^e \right\|_\infty \quad (\text{VI.20})$$

where

$$\|\mathbf{A}\|_\infty = \max\{|A_{ij}|\} \quad (\text{VI.21})$$

The same definition is used for $\|\Delta \underline{\sigma}\|$. The distributions are shown in Figure VI.31. On the average, the deviations are initially close to the measurement accuracies and gradually increase with plastic strain. The final values are 2 to 3 times larger, but remain reasonable.

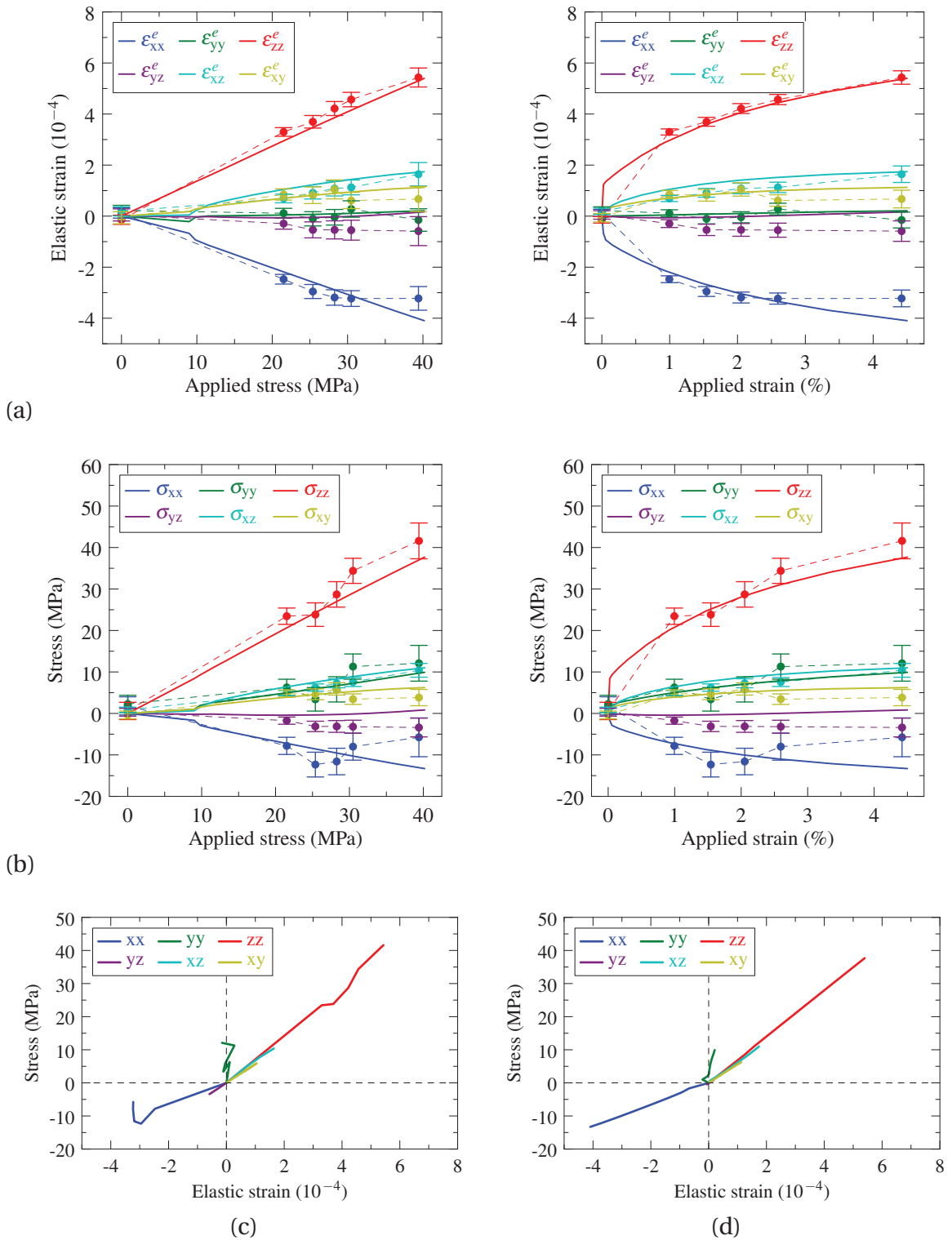


Figure VI.29 – Elastic strain and stress responses of a selected grain in the experiment and the finite element simulation. (a) Elastic strain components plotted against the applied stress and the applied strain. (b) Stress components plotted against the applied stress and the applied strain. (c) Experimental and (d) simulated elastic strain-stress curves. The errorbars in (a) and (b) represent the standard errors.

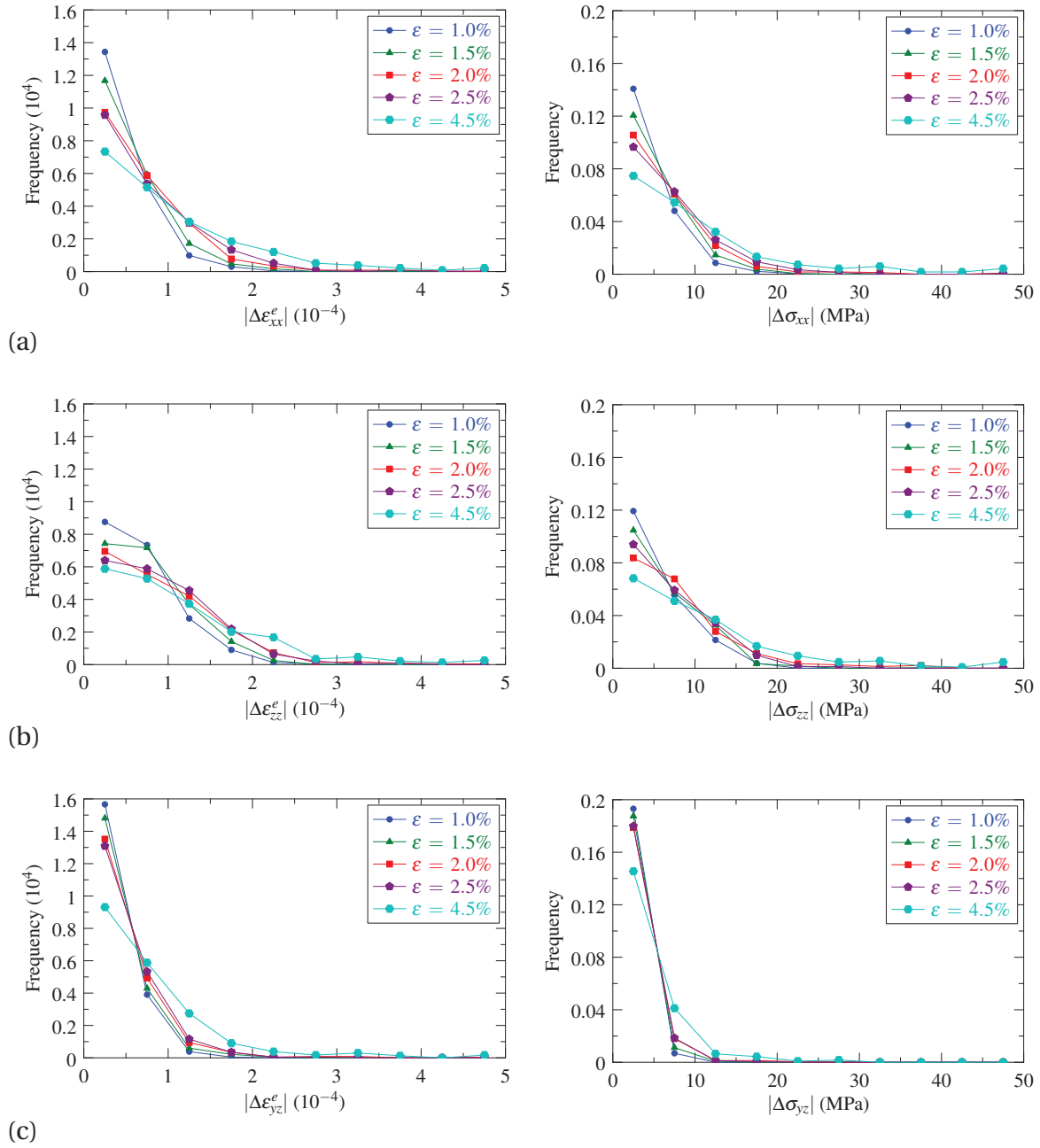
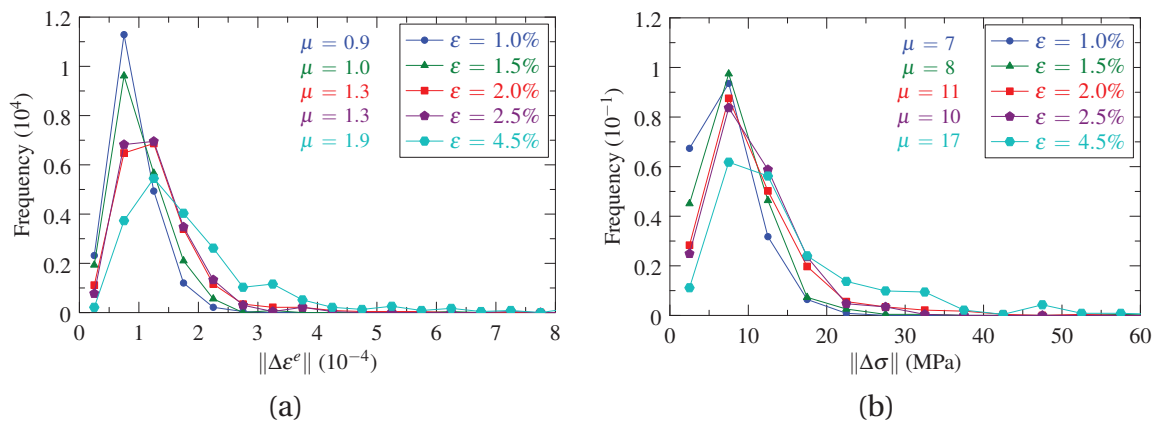


Figure VI.30 – Deviation between experimental and simulated elastic strains and stresses: absolute deviations of (a) xx-transverse components (b) zz-axial components and (c) yz-shear components.

Table VI.4 – Agreement between experimental and simulated elastic strains and stresses with regard to measurement accuracies (in percentage of the grains).

ϵ (%)	$ \Delta\epsilon < 10^{-4}$			$ \Delta\sigma < 8 \text{ MPa}$		
	xx	zz	yz	xx	zz	yz
1.0	93%	80%	98%	89%	78%	99%
1.5	88%	73%	95%	80%	72%	98%
2.0	78%	62%	92%	73%	65%	97%
2.5	74%	61%	92%	68%	68%	98%
4.5	62%	56%	75%	55%	50%	90%


 Figure VI.31 – Deviation between experimental and simulated elastic strains and stresses: L^∞ distance between full tensors. (a) Elastic strains and (b) stresses.

VI.5 Summary and discussion

In this chapter, the experimental results were mainly compared to simulation results from a finite element crystal plasticity model. The Taylor model was also applied on the experimental orientations to predict the grain rotations, and the attributes of the intra-grain orientation spreads were assessed through a simplified model, ISM, which assumes an isotropic stress variability about the grain nominal stress states. The finite element simulation was carried out based on the actual microstructure, which was fitted with a Laguerre tessellation and finely meshed. The comparisons are carried out in terms of distributions and grain by grain, considering the 466 grains that could be monitored from the initial state to the final strain level of 4.5%.

The *grain rotations* are examined in terms of angles and axes. The distributions at 4.5% indicate that the rotation angles are overestimated in both simulations. The difference is larger between the experiment and the finite element results; the average angles are 0.8° and 1.4° , respectively, and correspond to a relative deviation of about 50%. The experimental rotation axes are found to preferentially lie perpendicular to the tensile axis. This tendency is well quantitatively reproduced by the Taylor model, but not the finite element simulation.

The grain-by-grain comparisons of the rotation angles reveal moderate to low correlations between experiment and simulations, with coefficient value of 0.5 for the finite element and 0.1 for the Taylor model. The rotation axes are found to differ on average by 40° for the finite element simulation and 54° for the Taylor model (against 90° when uncorrelated). This indicates that both models provide a first-order agreement on the rotation axes, as was already concluded by Quey *et al.* [42] concerning a similar material deformed in hot plane-strain compression to a plastic strain of 1.2. The grain-by-grain differences are examined in relation to grain orientations. We observe that finite element predictions are statistically less accurate in the region close to the [1 0 0] corner of the stereographic triangle. The same tendency appears on the rotation axes of the Taylor model. These observations can be linked to the results of Winther *et al.* [8], who compared the lattice rotations of 95 Al grains to the predictions of the Taylor model and found large discrepancies close to the [1 0 0] corner. This can be attributed to a strong variability of the rotation axes in this region.

Contrary to the distributions, the grain-by-grain comparisons reveal a better statistical agreement with the finite element results. This can be explained from the viewpoint of the variability at constant orientation (VCO) of the rotations. In the experiment, the rotations of two grains of identical initial orientations differ on average by 45% (angles) and 49° (axes). These variabilities are attributed to local grain interactions. In the Taylor model, two grains of identical orientations have the same rotations. Hence, the model is by definition unable to provide a perfect match with the experiment. Instead, the average errors are close to the experimental VCOs. In the finite element simulation, grains interactions are included by ensuring the mechanical equilibrium over the polycrystal. This leads to VCOs of 44% and 53° , which are close to the experimental VCOs and allow for a better match than the Taylor model.

The *intra-grain orientation spreads* are examined in terms of average disorientation angles, anisotropy factors and preferential disorientation axes. The experimental and simulated orientation spreads grow up to 4.5% to produce comparable average disorientation angles of 0.6° in the experiment and 0.8° in the finite element simulation. A reasonable agreement is found as well on the anisotropy factors, ranging from 1.7 to 2.0 in

the experiment and constant at 1.75 in the finite element simulation. Regarding the preferential disorientation axes, the experiment indicates that the axes preferably lie perpendicular to the tensile axes, mainly aligned along X. A remarkable agreement is observed between the experimental and finite element distributions. The Taylor distribution shows clear differences, but exhibits the same tendency against the tensile axis.

These observations can be related to the deformation mechanisms through the finite element simulation results. The stress heterogeneities induce spatial variations of the local slip activities, which result in the development of intra-grain orientation distributions. The most variable systems also appear to be the most activated ones. Hence, the preferential disorientation axes are controlled by the slip vectors of the most active slip systems, which is confirmed by the agreement between both distributions. The same influence was observed by Oddershede *et al.* [50] in a Cu polycrystal, but based on three grains only. With 466 individual grains, our study is statistically sound. Besides, we have proposed an automated method to extract the intra-grain orientation spreads from 3DXRD measurements, without a priori assumption on the deformation mechanisms.

The grain-by-grain comparisons of the disorientation angles and anisotropy factors reveal low correlations between experiment and simulations, with correlation coefficient values lower than 0.4. The preferential disorientation axes are found to differ on average by 37° for the finite element simulation and 54° for the ISM (against 57° when uncorrelated). This indicates that the finite element method provides a first-order agreement on the disorientation axes. The agreement is not as good for the ISM, but the differences observed are clearly amplified by the sample texture. Away from $[1\ 0\ 0] \parallel Z$, the agreement between experiment and ISM is reasonable with regard to the plots in the Rodrigues orientation space. Near $[1\ 0\ 0] \parallel Z$, the simplified model is deficient.

The *grain elastic strains and stresses* are examined in the sample coordinate system. The experiment and simulation results are in good agreement at the macroscopic scale. The distributions of strain and stress components exhibit very similar evolutions, although the polycrystal appears to carry somewhat more axial strain and stress in the finite element simulation than in the experiment. In both, the sample is linearly stretched along the tensile axis up to a macroscopic load of about 40 MPa and contracts along the transverse directions. This is consistent with the conditions of uniaxial tension and leads to Poisson's ratios close to the theoretical value of 0.35.

The grain-by-grain comparisons reveal an appreciable agreement between the experiment and the finite element simulation. This was exemplified with a selected grain, which shows a remarkable agreement up to 4.5% on all the six elastic strain components and all the six stress components. When considering all the grains, the deviations indicate a good statistical agreement between experiment and simulation with regard to the measurement accuracies. The average deviations are initially of 0.9×10^{-4} and 7 MPa and progressively increase with plastic strain. This can be understood from the experimental viewpoint. The strain accuracy is assessed from the distribution of residual elastic strains in the initial, undeformed state. In fact, the estimated value of 1×10^{-4} is only valid for this state and may deteriorate with plastic straining, essentially because of diffraction spot broadening. We can thus observe in the experimental data a progressive increase of the standard errors up to $1\text{-}1.5 \times 10^{-4}$, which are two times as large as the initial standard errors.

Although the comparisons between experiment and finite element simulation is limited by the measurement accuracies, the observed differences can also be discussed from the viewpoint of modelling. First and foremost, we can question the selection of material

parameter values. These were obtained in the same manner as Wong *et al.* [113] by fitting the simulated macroscopic stress-strain curve to the experimental curve. Since the parameters are determined simultaneously, the uniqueness of the parameter set is not ensured. Therefore this approach does not necessarily allow to reproduce accurately the response of the material at the grain scale. This could be improved by using, for example, independent measurements and mechanical tests on single crystals. Another potential weak point of the simulation concerns the use of a Laguerre tessellation to approximate the experimental microstructure. The method produces convex grains only and is therefore unable to achieve a perfect, accurate match. In the literature, the influence of the polycrystal morphology was notably highlighted by Bunge *et al.* [114]. The authors tested the effects of different grain shapes and packing on the elastic properties of polycrystals, and found that their influence could reach up to 25% of the sole texture influence. Hence, in our comparison, although the differences between the experimental and modelled microstructures remain reasonable, we may ask whether or not this deviation had a significant influence on the results. In the absence of such an accurate representation of the microstructure, it seems therefore difficult to provide further explanations of the grain-by-grain discrepancies observed between the experiment and the finite element simulation.

As a conclusion, the experimental average behaviours of 466 grains in a polycrystal deformed to 4.5% have been quantitatively compared to the predictions of the Taylor model and a finite element simulation. The results reveal a first-order agreement between the experiment and the finite element simulation. This is notably true for the grain rotation axes, as they are better predicted with the finite element simulation than the Taylor model. This is largely due to the grain interactions, which result in the experiment and the finite element simulation to comparable (and high) variabilities at constant orientation. In contrast, the Taylor model exhibits zero variabilities and is therefore not adapted to grain-by-grain comparisons of polycrystal plasticity. The results also reveal that the finite element model provides good predictions of intra-grain orientation distributions for all grain orientations. The comparison with ISM indicates that the latter generally fails for orientations close to $[1\ 0\ 0] \parallel Z$. These data should, in the future, allow for improving the model and thus our understanding of the development of intra-grain orientation distributions. Lastly, the agreement between experimental and simulated elastic strains and stresses was found to be statistically substantial with regard to the experimental accuracies. Despite the observed discrepancies, we have shown that the combination of 3DXRD/DCT measurements and finite element simulations allow for valuable insights into the intra-grain deformation mechanisms.

Conclusion

Summary

The *literature review*, in Chapter I, explored the mechanisms and theories related to the plastic deformation of crystals and polycrystals. Two different models were considered for the transition from single to poly-crystalline scales: the Taylor model, which assumes that all the grains are subjected to the macroscopic strain, and the finite element method, which allows for directly solving the mechanical equilibrium on the 3D polycrystal. We discussed through literature results the potential of recent high-energy X-ray diffraction techniques to provide relevant experimental data for the study of polycrystal plasticity. The combination of 3DXRD and DCT, in particular, has the potential to draw detailed comparisons between experimental results and finite element simulations.

The *experiment*, described in Chapter II, was carried out at ESRF on the materials science beamline ID11. It involved three complementary high-energy X-ray diffraction techniques: DCT (imaging of undeformed polycrystals), HEDM (imaging of plastically deformed polycrystals) and 3DXRD (far-field measurement of grain average properties). Two tensile specimens of Al-0.3Mn were characterized. Sample A was plastically deformed to 1% of axial strain and measured in the same region by DCT and HEDM. Sample B was measured by DCT at the undeformed state and then *in situ* by 3DXRD during uniaxial tensile testing. A volume of $900 \times 900 \times 550 \text{ mm}^3$ could be monitored over six plastic strain levels: 0.0%, 1.0%, 1.5%, 2.0%, 2.5% and 4.5%.

The *3DXRD calibration and characterization* was detailed in Chapter III. It is based on a general description of the diffractometer geometry, using several coordinate systems and taking account of any potential misalignment with respect to the ideal configuration. A novel calibration procedure, reported in two publications in JAC [85, 86], was used to assess and reduce any source of error in the evaluation (tilts, distortions, etc.). The calibration was validated through simulations on the initial undeformed state of Sample B, revealing accuracies of about $3 \text{ }\mu\text{m}$, 0.03° , 1×10^{-4} and 8 MPa on the determination of grain centroids, orientations, elastic strains and stresses, respectively.

The *initial grain structure* of Sample B was validated in Chapter IV. First, the applicability of DCT on the Al-0.3Mn alloy was validated on Sample A. This led us to draw the first direct comparison of DCT and HEDM, reported in a publication in IUCrJ [100]. It revealed a 87% correspondence between the reconstructions and an average distance of $4 \text{ }\mu\text{m}$ between their respective grain boundaries. Second, the initial grain structures of Sample B, as given by DCT and 3DXRD, were compared. The comparison was based on 824 grains and revealed a close agreement between the datasets, with average discrepancies of $7 \text{ }\mu\text{m}$ and 0.03° on the grain centroids and orientations, respectively.

The *experimental results* of the in situ tensile test of Sample B, were presented and investigated in Chapter V. A representative set of 466 individual grains were monitored from the initial state up to 4.5% plastic strain. The grain rotations were analysed in terms of angles and axes. The rotation angles are relatively small, about 0.8° on average after 4.5%. The rotation axes exhibit a tendency to lie perpendicular to the tensile axis, which can be expected for uniaxial tension. The influence of grain interactions on the rotations was assessed by means of the variability at constant orientation (VCO). Hence, on average, two grains of the same orientation have rotation angles that differ by 44% and rotation axes that differ by 49° . The intra-grain orientation spreads were obtained from the diffraction spots by the development of a new method, assuming tri-Gaussian functions for the grain ODFs. The results were analysed in terms of average disorientation angles, anisotropy factors and preferential disorientation axes. The axes, in particular, exhibit a strong relation to the grain orientations and a tendency to align perpendicular to the tensile axis. The elastic strains and stresses were found to be valid at the macroscopic scale (Poisson's effect and macroscopic stress). Variabilities among the grain responses could be identified, as well as some dependency on the grain orientations.

The *simulation results* were detailed and quantitatively compared to the experimental results in Chapter VI. In the finite element simulation, a novel approach was developed to determine the Laguerre tessellation that approximates at the best the experimental microstructure. The polycrystal model was finely meshed and submitted to the experimental loading. The resulting mechanical and orientation fields were averaged over the individual grains for the comparison with the experiment, the Taylor model and the recently proposed Isotropic Stress Model (ISM). The grain average rotations were found to be better predicted by the finite element model than the Taylor model. This is to be attributed to the grain interaction, which is included in the finite element model and allows reproducing the experimental variabilities. The intra-grain orientation spreads appeared to be well predicted by the finite element model. Consistent with the experiment, the preferential disorientation axes align perpendicular to the tensile axis. Based on the simulation, this tendency can be related to the deformation mechanisms, that is, the slip rate variabilities of the most active systems. The comparison with the ISM results indicates that this model performs well for orientations away from $[1\ 0\ 0] \parallel Z$. Lastly, regarding the elastic strains and stresses, the macroscopic response was shown to be properly rendered, as well as the relative evolutions of the individual grain components. The grain-by-grain comparisons were carried out to the limit of measurement accuracies, revealing a reasonable agreement between experiment and finite element simulation, since the majority of the errors (50% to 90% depending of the strain level) were found to be smaller than the experimental accuracy.

As a conclusion, we have proposed a detailed and quantitative comparison between experimental and simulation results of individual grain plasticity in an aluminium polycrystal deformed in uniaxial tension. The average responses of 466 individual grains were investigated from 0.0 to 4.5% of plastic strain, in terms of rotations, orientation spreads, elastic strains and stresses. This is, to our knowledge, the first study of this kind. It can be emphasized from the results that the use of the finite element methods and the description of actual microstructures allow for better predictions than the classical orientation-based approaches. Although differences were found, it was shown that the combination between *in situ* 3DXRD/DCT experiments and finite element simulations already makes it possible to analyse the deformation mechanisms of the material. Hard points were identified, which should in time provide a direction toward further improvements of crystal plasticity models.

Outlook

Several routes of further works and improvements can be identified; we propose a non-exhaustive list.

ISAAC: a calibration software

There are several softwares dealing with tilt calibration of area detectors: *FIT2D* [87], *Fable* [58], *Datasqueeze* [115], *DIGIgrain* [106], *Nika* [116], *pyFAI* [117] and probably others. They generally consider though that images were corrected for spatial distortions using adequate grids and therefore overlook any additional or residual distortions. In that sense, our methodology is more general. We implemented it in a calibration software called ISAAC. Written in MATLAB[®], the program was developed with a graphical user interface and is intended to provide all the necessary tools to analyse powder diffraction images, calibrate detector tilts and assess radial distortions. The first release of the software is still at a preparatory stage and is expected for late 2016.

Multi-seed Laguerre tessellation

The Laguerre tessellation approximation is limited by the use of convex cells. A natural next step would be to extend the method to the description of non-convex grains, for example by describing each grain by a group of convex cells. This does not fundamentally change the approach, which can still be solved as an optimization problem. Such a method has already been implemented in Neper and provides remarkable fits of 2D microstructures. The 3D case appears to be more difficult, as small segments and faces in the tessellation lead to local over-refinements in the mesh.

Local orientation imaging

This study focused on the analysis of grain average responses, but could evidently benefit from the use of local orientation imaging techniques. As for Sample A, this could consist in measuring at each strain level several layers of the sample by HEDM. The comparison between experiment and finite element simulation would then require more advanced correlation procedures to achieve a finer characterization of the validity of the simulation results. Moreover, recent developments at ID11 aim at producing spatially-resolved orientation maps by means of DCT, using the so-called generalized algorithm of 6D-DCT [118].

Study of another material

This study could benefit from the use of a different and more adapted material, especially for the purpose of elastic strain and stress evaluations. The Al-0.3Mn exhibits a low elastic anisotropy and a very low yield strength of 7-10 MPa. This results in relatively large errors on the stress (>20%), with no relevant grain-to-grain variations to test out the predictions of the finite element simulation. The use of a harder material would allow to measure higher stress levels with better relative accuracies and, also, to analyse the elasto-plastic transition.

Description of the Isotropic Stress Model

Contents

A.1	Principles	165
A.2	Results for uniaxial tension	166

In the early stage of plastic deformation, the constitutive grains of a polycrystal generally exhibit narrow intra-grain orientation distributions. However, as a result of stress inhomogeneities at the intra-grain scale, spatial fluctuations of the plastic strain develop over the grain volume. This leads to different local lattice rotations and, therefore, to the fragmentation of intra-grain orientations. Recently, Quey *et al.* [15] proposed a new simplified approach to predict the attributes of intra-grain orientation distributions from the stress variability, using the Taylor model.

A.1 Principles

Let us consider a polycrystal deformed in uniaxial tension and an embedded grain of known orientation, for which we want to predict the attributes of the strain-induced orientation spreads.

Under the assumption of equal plastic strain, the lattice reorientation velocity, $\underline{\dot{\mathbf{R}}}$, is defined by Equation I.6, as:

$$\underline{\dot{\mathbf{R}}} = - \sum_s \dot{\gamma}^s \underline{\mathbf{Q}}^s \tag{A.1}$$

where $\underline{\mathbf{Q}}^s$ was defined as the skew-symmetrical Schmid tensor. It can also be written in terms of the reorientation velocity vector, $\dot{\mathbf{r}}$, yielding:

$$\dot{\mathbf{r}} = - \sum_s \dot{\gamma}^s \mathbf{t}^s \tag{A.2}$$

where \mathbf{t}^s stands for the spin direction corresponding to the slip system s and is obtained from the slip plane normal \mathbf{n}^s and the slip direction \mathbf{b}^s as $\mathbf{t}^s = \mathbf{n}^s \times \mathbf{b}^s$. The slip rate $\dot{\gamma}^s$ depends on the corresponding resolved shear stress τ_s through Equation VI.16. The resolved

shear stress τ_s is the projection of the stress on the system s , as:

$$\tau_s = \underline{\mathbf{M}}^s : \underline{\boldsymbol{\sigma}} \quad (\text{A.3})$$

where $\underline{\mathbf{M}}^s$ was defined as the symmetrical Schmid tensor.

Owing to the use of a viscoplastic material behaviour, it can be noticed from Equation A.2 that any variation of the stress may affect the slip rates of all the systems and result in a variation of the reorientation velocity. This can be evaluated from:

$$\frac{\partial \dot{\mathbf{r}}}{\partial \boldsymbol{\sigma}_v} = \frac{\partial}{\partial \boldsymbol{\sigma}_v} \left(- \sum_s \dot{\gamma}^s \mathbf{t}^s \right) \quad (\text{A.4})$$

where $\boldsymbol{\sigma}_v$ is the vectorial form of $\underline{\boldsymbol{\sigma}}$ in the Mandel-Voigt notation and $\frac{\partial \dot{\mathbf{r}}}{\partial \boldsymbol{\sigma}_v}$ is a second-rank, 3×6 tensor. Then, combining Equations A.3 and A.4, it is shown in Ref. [15] that the expression can be rewritten as:

$$\frac{\partial \dot{\mathbf{r}}}{\partial \boldsymbol{\sigma}_v} = - \sum_s \frac{\partial \dot{\gamma}^s}{\partial \tau^s} (\mathbf{t}^s \otimes \mathbf{m}_v^s) \quad (\text{A.5})$$

where \mathbf{m}_v^s is the vectorial form of the symmetrical Schmid tensor. The $(\mathbf{t}^s \otimes \mathbf{m}_v^s)$ factor depends only on the crystal orientation and the partial derivative is known from the viscoplastic behaviour law (Equation VI.16):

$$\frac{\partial \dot{\gamma}^s}{\partial \tau^s} = \frac{\dot{\gamma}_0}{m \tau_0^s} \left| \frac{\tau^s}{\tau_0^s} \right|^{\frac{1}{m}-1} \quad (\text{A.6})$$

Let us now consider the intra-grain stress heterogeneities as frequency distributions in the stress space, without taking into account the spatial variations. The reorientation distribution, resulting from an isotropic distribution in the stress space about the nominal stress state, can be assessed from the singular value decomposition,

$$\frac{\partial \dot{\mathbf{r}}}{\partial \boldsymbol{\sigma}_v} = \mathbf{U} \mathbf{S} \mathbf{V}^T \quad (\text{A.7})$$

where \mathbf{U} is a 3×3 orthogonal matrix, \mathbf{S} is a 3×6 diagonal matrix and \mathbf{V} is a 6×6 orthogonal matrix. Hence, the resulting reorientation distribution is described in terms of its principal directions and corresponding magnitudes, respectively given by the rows of \mathbf{U} and the diagonal components of \mathbf{S} ($S_{11} \leq S_{22} \leq S_{33}$). The preferential disorientation axis is given by the first row of \mathbf{U} . The distribution anisotropy factor is defined as $\lambda_a = S_{11} / \sqrt[3]{S_{11} S_{22} S_{33}}$.

A.2 Results for uniaxial tension

The method was applied to determine the preferential disorientation axes of 1000 random orientations. The results are shown in Figure A.1. The distribution of preferential disorientation axes resulting from uniaxial tension is projected onto the sample X-Y plane in Figure A.1-a and represented in the fundamental region of the Rodrigues orientation space in Figure A.1-b. The complete distribution over the Rodrigues fundamental region is shown in Figures A.1-c and d. We can observe that the axes are evenly distributed between X and Y, that is, perpendicular to the tensile axis Z.

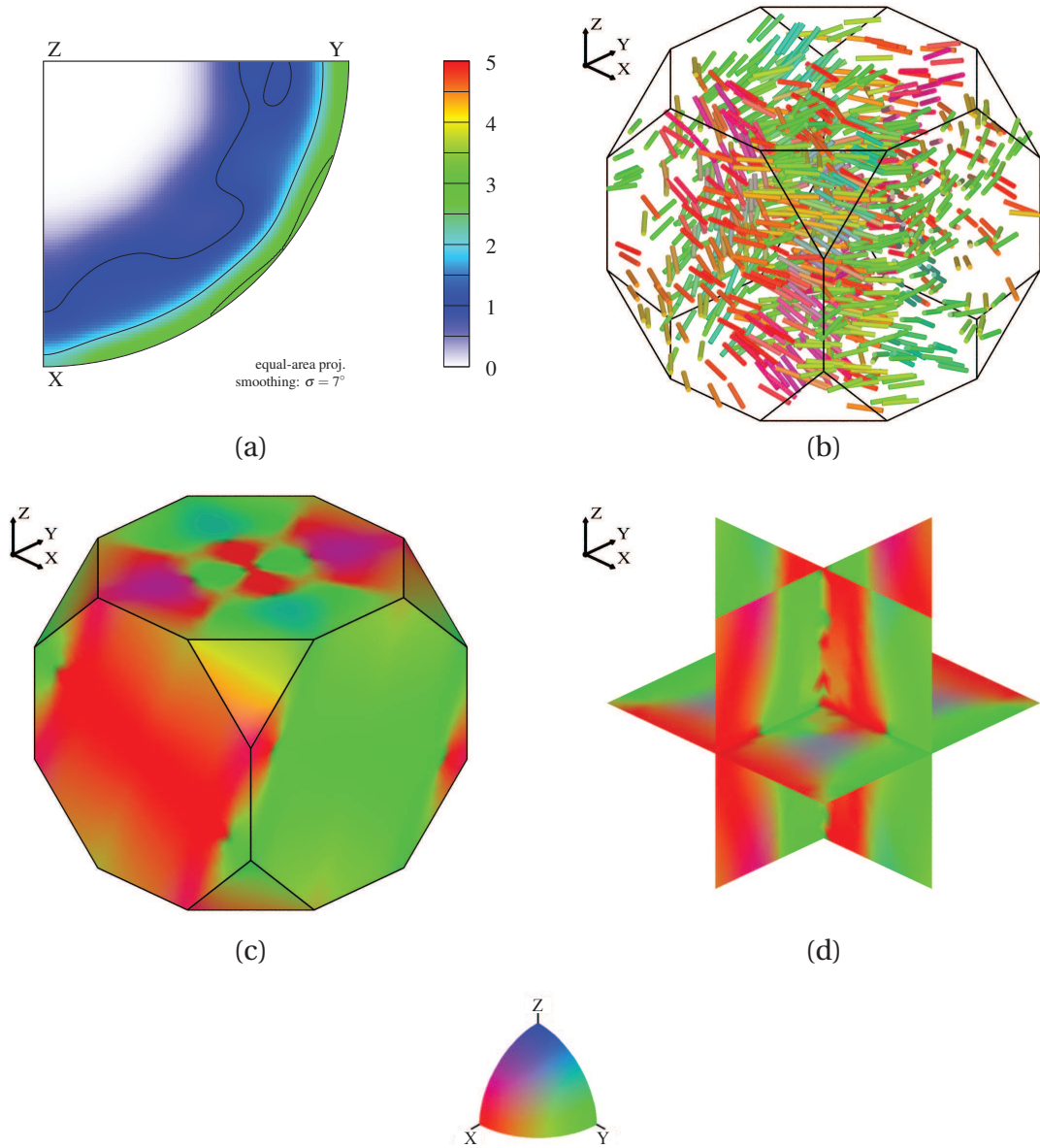


Figure A.1 – Preferential disorientation axes resulting from an isotropic stress variability in uniaxial tension, shown for 1000 random orientations as (a) distribution in the sample X-Y plane (equal-area projection) and (b) as a function of the orientation in the Rodrigues fundamental region. The complete distribution is shown over (c) the Rodrigues fundamental region and (d) slices along X, Y and Z planes. The colour RGB code is related to the preferential disorientation axis components.

APPENDIX -B-

Synthèse en français

Contents

Introduction	170
B.1 Chapitre I : revue bibliographique	172
B.1.1 Mécanique du cristal	172
B.1.2 Mécanique du polycristal	173
B.1.3 Approches expérimentales	174
B.1.4 Objectifs de la thèse	174
B.2 Chapitre II : moyens expérimentaux	176
B.2.1 Techniques de synchrotron	176
B.2.2 Matériau	178
B.2.3 Expériences à ESRF sur la ligne ID11	179
B.3 Chapitre III : mesure précise des propriétés moyennes par grain	181
B.3.1 Description de la géométrie	181
B.3.2 Calibration de la géométrie	182
B.3.3 Validation de la calibration	184
B.4 Chapitre IV : validation croisée de la microstructure initiale	186
B.4.1 Comparaison entre DCT, HEDM et EBSD	186
B.4.2 Comparaison entre DCT et 3DXRD	188
B.5 Chapitre V : suivi in-situ par 3DXRD du comportement des grains	190
B.5.1 Rotations moyennes	190
B.5.2 Dispersions d'orientations intra-granulaires	192
B.5.3 Déformations élastiques et contraintes	193
B.6 Chapitre VI : comparaison à la simulation par éléments finis	195
B.6.1 Modèle éléments finis	195
B.6.2 Rotations moyennes	196
B.6.3 Dispersions d'orientations intra-granulaires	198
B.6.4 Déformations élastiques et contraintes	200
Conclusion	202

Introduction

La plupart des matériaux employés dans l'ingénierie sont constitués de métaux ou alliages qui, soumis à un chargement, développent des champs mécaniques hétérogènes et complexes à l'échelle microscopique. Ces champs résultent de la nature polycristalline des matériaux : en effet, ceux-ci sont constitués de cristaux individuels, ou grains, qui tendent à se déformer différemment les uns des autres du fait de leur comportement anisotrope et des différences d'orientations. Ces phénomènes présentent un intérêt tout particulier pour de nombreuses applications industrielles : les pièces structurelles et composants métalliques sont généralement déformés plastiquement durant les étapes de préparation et de mise en forme, qui déterminent les propriétés mécaniques finales du matériau.

Depuis près d'un siècle, de nombreux chercheurs se sont efforcés d'expliquer le comportement des polycristaux et de leurs grains constitutifs lorsqu'ils sont soumis à une déformation plastique. Les premières recherches de Schmid et Boas, en 1935, ont permis d'identifier le glissement sur des systèmes cristallographiques spécifiques comme étant le mécanisme élémentaire de déformation du cristal [1]. Ces travaux initièrent le développement de la théorie actuelle de la plasticité cristalline et furent à l'origine de nombreuses avancées quant à la prédiction de la réponse d'un polycristal soumis à un chargement donné. Ainsi, à la suite des travaux précurseurs de Taylor, basés sur l'hypothèse d'un champ de déformation uniforme au sein du polycristal, de nombreux autres modèles furent proposés pour tenir compte de l'interaction intergranulaire avec un niveau de fidélité toujours croissant [2, 3]. De nos jours, la méthode des éléments finis est applicable au cas de structures polycristallines complexes soumises à des grandes déformations plastiques. De tels calculs peuvent inclure plusieurs millions de degrés de liberté et être exécutés sur un cluster de taille moyenne, pour fournir de formidables quantités de données [4]. De telles simulations permettent en outre de reproduire fidèlement l'interaction intergranulaire en résolvant directement et complètement l'équilibre mécanique du polycristal, donnant ainsi accès aux hétérogénéités des champs de contrainte et de déformation au sein de la microstructure [5]. Toutefois, malgré un niveau de raffinement des modèles toujours croissant, il existe encore assez peu de données expérimentales de référence avec lesquelles les comparer (et les valider), d'autant moins à l'échelle granulaire. C'est pourquoi, historiquement, les comparaisons entre expérience et simulation furent menées sur des propriétés macroscopiques, telles que les textures de déformation [6].

Au cours des quinze dernières années, des avancées importantes ont permis de mesurer le comportement de grains individuels, mais peu de résultats furent en fait confrontés à des simulations par éléments finis. Parmi les méthodes expérimentales développées, la microscopie 3D par diffraction des rayons X (3DXRD) a su démontrer son potentiel [7]. Cette technique est basée sur l'utilisation des rayonnements X à haute énergie de synchrotron et permet de caractériser de façon rapide et non-destructive les grains individuels au sein d'échantillons de taille millimétrique. Les positions, orientations et tenseurs de déformation élastiques de centaines de grains peuvent ainsi être obtenus et leurs évolutions respectives suivies tout au long de la déformation [8, 9].

Nous nous proposons dans cette thèse d'étudier par 3DXRD les réponses de grains individuels au sein d'un polycristal d'aluminium déformé en traction uniaxiale. Ce document est développé pas à pas et organisé en six chapitres. Le chapitre I présente les mécanismes et théories décrivant la déformation des mono- et poly-cristaux, avant d'examiner les précédents travaux disponibles dans la littérature. Le chapitre II décrit les techniques

expérimentales utilisées et les expériences menées à European Synchrotron Radiation Facility (ESRF) sur la ligne de lumière ID11. Les chapitres III et IV sont des chapitres de pré-résultats, détaillant le traitement et la validation des données expérimentales à partir des mesures de diffraction. Le chapitre V contient les résultats expérimentaux proprement dits, qui sont analysés en termes de rotations, de dispersions d'orientations intra-granulaires, de déformations élastiques et de contraintes. Pour finir, le chapitre VI présentent la comparaison entre les résultats expérimentaux et les données numériques obtenues à partir d'une simulation par éléments finis et du modèle de Taylor.

Ce travail s'inscrit dans une thématique forte au sein de l'École des Mines de Saint-Étienne et fait suite à de nombreuses thèses traitant de comparaisons entre expérience et simulation en plasticité polycristalline dans l'aluminium [10–13] ainsi que des travaux plus récents couplant la méthode des éléments finis et la description numérique de polycristaux [4, 14, 15].

B.1 Chapitre I : revue bibliographique

B.1.1 Mécanique du cristal

Un cristal idéal peut être représenté comme un arrangement périodique d'atomes. Lorsque celui-ci est soumis à un chargement, il se comporte tout d'abord de façon élastique : les atomes subissent un déplacement réversible par rapport à leur position d'équilibre, ce qui déforme la maille cristalline et donne naissance à des forces de réaction. Les contraintes résultantes sont décrites par la loi de Hooke, qui relie linéairement le tenseur des contraintes, $\underline{\sigma}$, de composantes σ_{ij} , au tenseur des déformations élastiques, $\underline{\epsilon}$, de composantes ϵ_{kl} . Dans le cas général d'un comportement anisotrope, la relation s'écrit :

$$\sigma_{ij} = C_{ijkl} \epsilon_{kl} \quad (\text{B.1})$$

où C_{ijkl} sont les coefficients du tenseur de raideur, $\underline{\underline{C}}$. Dans le cas d'un cristal cubique, ce tenseur d'ordre 4 peut en fait être complètement décrit à l'aide de trois constantes, C_{11} , C_{12} et C_{44} , dont les valeurs sont relativement bien connues pour l'Al pur [17, 18].

Lorsque le chargement augmente, le matériau finit par atteindre sa limite d'élasticité et se déforme plastiquement. Celle-ci s'opère le plus souvent par glissement de dislocations individuelles sur des systèmes cristallographiques spécifiques [1]. On se place ici dans le cadre de la modélisation continue de la plasticité cristalline, qui décrit ce phénomène en moyenne à l'échelle des systèmes de glissement. Dans le cas de l'Al, qui présente une structure cubique à faces centrées, il s'agit à température ambiante des douze systèmes octaédriques, $\{111\} \langle 110 \rangle$. D'un point de vue cinématique, la déformation plastique du cristal obéit à l'équation :

$$\underline{\dot{\mathbf{E}}} = \sum_{s=1}^N \underline{\mathbf{M}}^s \dot{\gamma}^s \quad (\text{B.2})$$

où $\underline{\dot{\mathbf{E}}}$ est la partie symétrique du gradient de vitesse imposé au cristal, $\underline{\mathbf{M}}^s$ est le tenseur de Schmid symétrisé et $\dot{\gamma}^s$ est la vitesse de glissement sur le système s . L'équation B.2 définit en fait un système de six équations (composantes de $\underline{\dot{\mathbf{E}}}$, connues) et N inconnues (les vitesses de glissement, $\dot{\gamma}^s$). Cinq de ces équations seulement sont indépendantes (condition d'incompressibilité). Ainsi, pour accommoder une déformation arbitraire, cinq systèmes de glissement au moins doivent être activés simultanément. Dans le cas de l'Al, les douze systèmes octaédriques sont activables indépendamment, d'où la nécessité de disposer de critères additionnels pour résoudre l'équation B.2. Dans ce travail, nous faisons appel à une loi de comportement visco-plastique, comme celle proposée par Hutchinson [22]. Cela se traduit par une loi puissance reliant la vitesse de glissement $\dot{\gamma}^s$ à la cission résolue τ^s :

$$\dot{\gamma}^s = \dot{\gamma}_0 \left| \frac{\tau^s}{\tau_0} \right|^{\frac{1}{m}} \text{sign}(\tau^s) \quad (\text{B.3})$$

où $\dot{\gamma}_0$ est une vitesse de référence, τ_0 est la cission résolue critique et m est la sensibilité de la contrainte à la vitesse. En combinant les équations B.2 et B.3, on obtient un système non-linéaire de cinq équations et cinq inconnues, qui peut être résolu de façon itérative.

B.1.2 Mécanique du polycristal

Un polycristal est, comme son nom l'indique, constitué de plusieurs cristaux, appelés grains, présentant des orientations cristallographiques, des formes et des tailles variées. Lorsque l'agrégat est déformé, les grains tendent à se comporter différemment les uns des autres du fait de leur comportement anisotrope et des différences d'orientations. Cependant, l'équilibre mécanique impose la compatibilité des contraintes et des déformations (notamment aux joints de grains), ce qui conduit à des hétérogénéités de déformation au sein du polycristal et des grains individuels. Ainsi, la réponse d'un grain ne dépend pas seulement de son propre comportement vis-à-vis de la déformation imposée, mais aussi de ceux de ses voisins. Différents modèles ont été proposés pour décrire la transition d'échelle du monocristal au polycristal, parmi lesquels figurent le modèle de Taylor, le modèle statique, les modèles auto-cohérents [23] et les modèles basés sur la méthode des éléments finis.

Proposé en 1938, le modèle de Taylor repose sur l'hypothèse que le gradient de vitesse est uniforme au sein du polycristal, ce qui implique que tous les grains soient soumis à la même déformation plastique (la composante élastique est négligée). Ainsi, la réponse de chaque grain dépend exclusivement de son orientation cristalline propre. Cette approche assure a fortiori la compatibilité des déformations, mais pas le respect de l'équilibre mécanique du polycristal. Ce modèle fournit une borne supérieure pour la puissance de déformation (contrainte d'écoulement).

Plus récemment, la méthode des éléments finis s'est imposée comme une alternative de choix pour simuler la déformation élastoplastique des matériaux polycristallins. En effet, couplée à la plasticité cristalline, elle permet de résoudre l'équilibre mécanique au sein d'une microstructure 3D pour rendre compte des hétérogénéités intragranulaires en contrainte, déformation et orientation, voir la Figure B.1. Un point essentiel est la représentation des morphologies microstructurales polycristallines. Les structures polycristallines réelles étant difficilement accessibles expérimentalement, diverses approches ont été proposées pour générer des modèles de microstructures réalistes, parmi lesquelles les partitions de Voronoi ou de Laguerre connaissent un certain succès [4]. Lorsque la structure réelle d'un polycristal est connue, il devient en principe possible de l'utiliser dans une simulation par éléments finis. Cela nécessite toutefois de produire un maillage de la structure en question, ce qui n'est pas trivial.

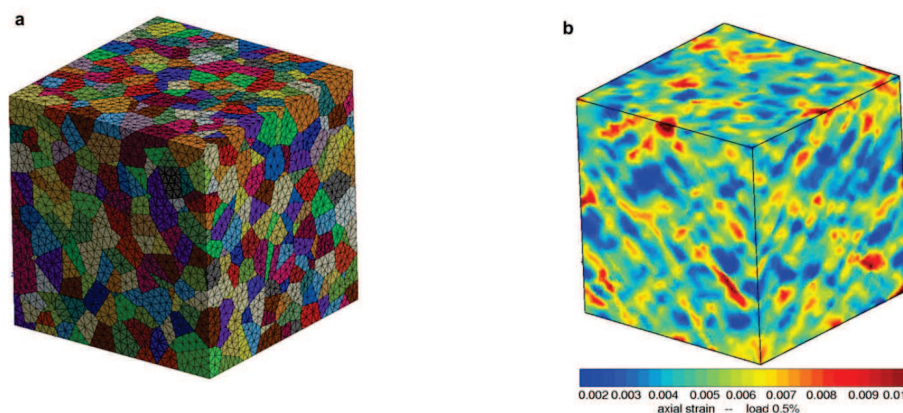


Figure B.1 – Hétérogénéités de déformation simulées par éléments finis au sein d'un polycristal déformé à 0.5% en traction uniaxiale, d'après Barbe *et al.* [30]: (a) polycristal maillé et (b) déformation axiale.

B.1.3 Approches expérimentales

Les prédictions des modèles de plasticité cristalline ont longtemps été testées par rapport aux textures de déformation mesurées, en particulier dans le domaine de la mise en forme. De telles comparaisons portent sur les distributions d'orientation cristalline développées par des grandes populations de grains, échelle à laquelle il devient difficile de réellement analyser et expliquer les différences observées pour proposer des pistes d'amélioration. C'est pourquoi de nombreux auteurs ont proposés de suivre l'évolution de grains individuels, ce que permettent quelques approches expérimentales seulement.

L'une d'elles consiste à combiner des analyses de surfaces, par exemple EBSD, avec un échantillon tranché constitué de deux parties accolées, ce qui permet d'observer les grains et la microstructure sur les faces internes jusqu'à des grandes déformations. Cette méthode a notamment été employée par Quey *et al.* pour étudier les rotations moyennes de grains à l'intérieur d'un polycristal d'Al déformé en compression plane à chaud [13–15, 41, 42], mettant en évidence une forte influence de l'interaction intergranulaire.

L'essor des techniques de synchrotron permet aujourd'hui de réaliser de telles études sur des polycristaux 3D. Le 3DXRD notamment exploite les rayons X de haute énergie et les détecteurs 2D pour caractériser de façon rapide et non-destructive des échantillons de taille millimétrique. Au regard de la littérature disponible, on peut tout d'abord mentionner les travaux de Poulsen, Winther, Oddershede et collaborateurs [8, 9, 47, 54] qui illustrent parfaitement le suivi des rotations cristallines et contraintes moyennes par grain avec des précisions de l'ordre de 0.05° et $1 - 2 \times 10^{-4}$. D'autres travaux plus récents par Oddershede *et al.* [50] montrent la possibilité de caractériser par ailleurs les dispersions d'orientations intra-granulaires à partir de la forme des taches de diffraction. Deux points sont toutefois à noter : nombre de ces études ne fournissent peu ou pas d'analyse réellement quantitative et aucun des résultats n'a jamais été comparé aux prédictions de simulations par éléments finis en plasticité cristalline.

B.1.4 Objectifs de la thèse

Depuis le modèle classique de Taylor jusqu'aux plus récents modèles exploitant la méthode des éléments finis, des efforts importants ont été engagés pour prédire le comportement plastique effectif d'agrégats polycristallins. En dépit de nombreux progrès, des questions essentielles demeurent sans réponse à ce jour, notamment en ce qui concerne l'influence relative de l'orientation initiale d'un grain et de son voisinage. Ce domaine de recherche a en effet manqué de données expérimentales de référence devant permettre de tester les différents choix de modélisation. Contrairement au modèle de Taylor, dont les prédictions peuvent être comparées à des mesures statistiques par diffraction des rayons X ou des neutrons, les simulations éléments finis nécessitent idéalement de mesurer la réponse individuelle des grains. L'essor des techniques de synchrotron et notamment du 3DXRD permet aujourd'hui d'envisager de telles études, comme le montre la littérature.

Dans cette thèse, nous nous proposons de combiner des expériences in-situ en synchrotron et des simulations par éléments finis pour étudier les réponses individuelles des grains formant un polycristal d'Al soumis à une déformation plastique. Pour cela, nous disposons de plusieurs techniques complémentaires : le DCT, qui donne accès à la structure 3D du polycristal non déformé, et le 3DXRD, qui permet de suivre les propriétés des grains individuels durant la déformation.

Nous disposons également de deux modèles de plasticité cristalline : celui de Taylor, basé exclusivement sur l'orientation initiale des grains, et un modèle elasto-viscoplastique, exploitant la méthode des éléments finis et permettant de prendre en compte la microstructure réelle. Cette dernière est fournie par la technique de DCT. Les résultats expérimentaux et numériques peuvent ensuite être confrontés qualitativement et quantitativement, en termes de distributions et surtout grain par grain. Une telle comparaison doit permettre d'évaluer la capacité du modèle de plasticité cristalline à reproduire les observations expérimentales.

B.2 Chapitre II : moyens expérimentaux

B.2.1 Techniques de synchrotron

Ce travail fait appel à trois techniques de synchrotron basées sur la diffraction des rayons X à haute énergie. Il s'agit de la microscopie 3D par diffraction des rayons X (3DXRD), la tomographie par contraste de diffraction (DCT) et la microscopie par diffraction à haute énergie (HEDM). Toutes trois reposent sur quelques principes communs représentés sur la Figure B.2 : l'utilisation d'un faisceau X monochromatique à haute énergie, l'utilisation de détecteurs 2D et l'acquisition de l'intensité diffractée durant une rotation de l'échantillon autour d'un axe vertical d'angle ω . Les taches de diffraction peuvent ensuite être extraites des clichés mesurés pour permettre la caractérisation des grains formant le volume illuminé de l'échantillon. Les trois techniques se différencient par leurs stratégies d'acquisition et d'analyse des mesures de diffraction.

La technique de 3DXRD [7] emploie un détecteur 2D de faible résolution (taille de pixel variant de 50 à 200 μm) placé loin de l'échantillon (distance variant de 200 mm à 1 m). Dans ces conditions, le diffractomètre présente une faible résolution spatiale (faible sensibilité à la position et à la forme des grains) et une forte résolution angulaire (forte sensibilité à l'orientation et à la déformation du réseau cristallin). Les taches de diffraction mesurées, repérées par la position de leur centre, donnent accès pour chaque grain présent dans le volume sondé, au centre de masse, à l'orientation cristalline moyenne et au tenseur moyen des déformations élastiques.

La technique de DCT [43] est dédiée à l'imagerie en orientation de structures cristallines recristallisées ou non-déformées. Elle emploie un détecteur 2D de haute résolution (taille de pixel de l'ordre du micron) placé proche de l'échantillon (distance de quelques millimètres). Ce dernier est illuminé par un faisceau large monochromatique, ce qui permet de mesurer simultanément l'intensité transmise (reconstruction tomographique de l'échantillon par contraste d'absorption) et l'intensité diffractée (imagerie en orientation), comme l'illustre la Figure B.3. L'indexation repose sur l'identification des paires de Friedel et fournit une orientation moyenne par grain. Dans l'hypothèse d'une structure recristallisée ou non-déformée, les taches de diffraction peuvent être considérées comme étant des projections parallèles de la forme des grains. L'enveloppe 3D de chaque grain est alors obtenue par rétroprojection des taches indexées et la microstructure complète est finalement reconstruite par assemblage des grains individuels.

La technique HEDM [44] est quant à elle dédiée à l'imagerie en orientation de structures cristallines déformées plastiquement. Elle emploie un faisceau plan monochromatique pour illuminer une couche micrométrique de l'échantillon. La mesure s'effectue à l'aide d'un détecteur 2D de haute résolution (taille de pixel de l'ordre du micron) pour plusieurs distances échantillon-détecteur, comme le montre la Figure B.4. La reconstruction fait appel à la simulation des clichés de diffraction et utilise pour cela un maillage fin de la couche matérielle mesurée, dans lequel chaque élément possède une orientation cristalline. Ces orientations locales sont ensuite déterminées par une procédure d'optimisation visant à maximiser le recouvrement entre les clichés de diffraction mesurés et simulés. La reconstruction s'effectue couche par couche et l'obtention d'un volume nécessite donc l'empilement de plusieurs couches.

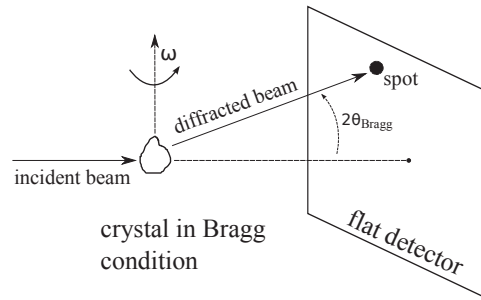


Figure B.2 – Méthode de rotation du cristal. Un cristal est illuminé par un faisceau X monochromatique parallèle et soumis à une rotation autour de l’axe vertical. Le faisceau incident est diffracté pour des angles ω satisfaisant la condition de Bragg. L’angle de diffraction, 2θ , est donné par la loi de Bragg $2d_{hkl} \sin\theta = \lambda$, où λ est la longueur d’onde du rayonnement and d_{hkl} est la distance interréticulaire pour la famille de plan (hkl) . Le faisceau diffracté est mesuré sous forme d’une tache sur le détecteur.

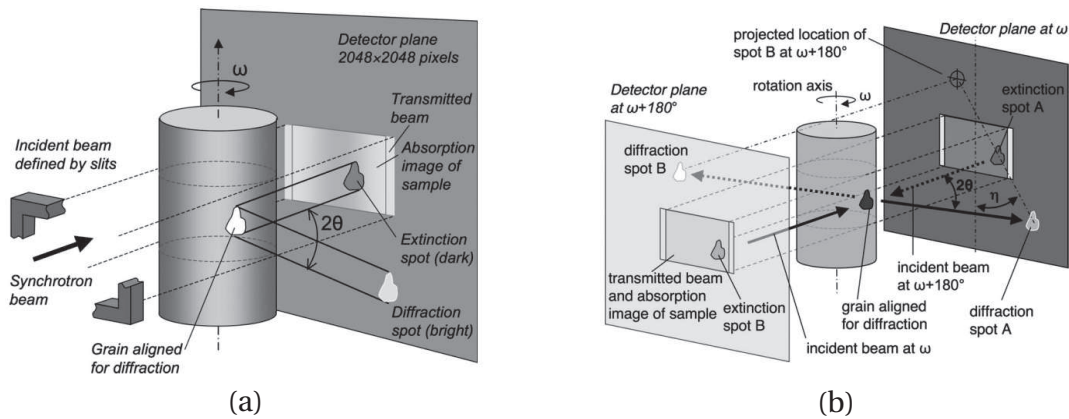


Figure B.3 – Principe du DCT, d’après Ref. [43]. (a) Configuration du DCT, montrant le faisceau large et le détecteur de haute résolution, placé près de l’échantillon et mesurant les intensités transmises et diffractés. (b) Représentation d’une paire de Friedel dans le référentiel de l’échantillon.

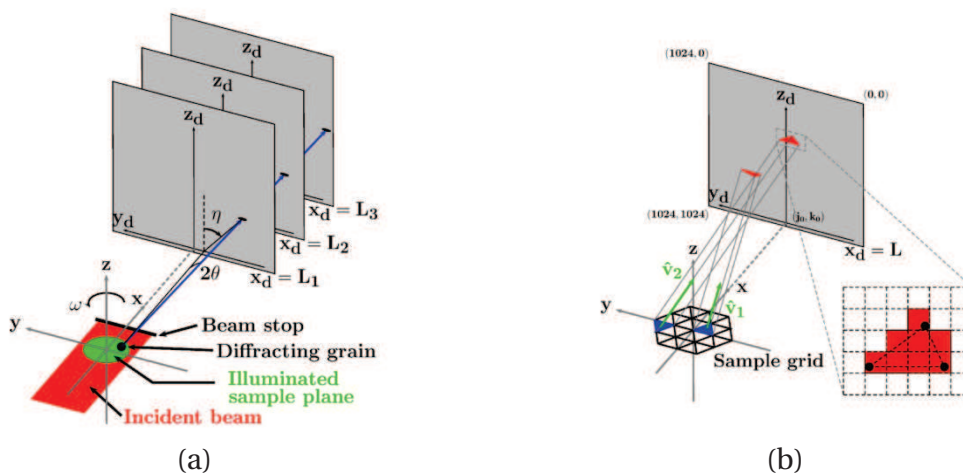


Figure B.4 – Principe du HEDM, d’après Ref. [44]. (a) Configuration du HEDM, montrant le faisceau plan et l’acquisition à plusieurs distances échantillon-détecteur. (b) Simulation des clichés mesurés, par projection de l’intensité diffractée à partir d’un maillage de la zone illuminée de l’échantillon (chaque élément correspondant à une orientation cristallographique locale).

B.2.2 Matériau

Le matériau étudié est un alliage binaire d'aluminium de haute pureté contenant 0.3% massique de manganèse (Al-0.3Mn). Précédemment utilisé dans plusieurs travaux de thèse au sein de notre laboratoire [13, 78, 79], ce matériau correspond à la matrice d'un alliage industriel de type AA3004. La présence de Mn en solution solide permet un meilleur contrôle de la recristallisation et tend à améliorer, légèrement, les faibles propriétés mécaniques de l'Al pure. Ce matériau présente d'autre part une haute énergie de faute d'empilement et se déforme donc exclusivement par glissement cristallographique.

Le matériau brut de coulée présentant des grains de taille millimétrique, le lingot de base fut d'abord laminé à froid en laboratoire, jusqu'à obtenir une réduction de la hauteur de 80%. Le matériau fut ensuite soumis à un traitement thermique de recristallisation : chauffe à 450°C pendant 25 min sous flux d'argon et refroidissement à l'air. La microstructure obtenue, observée par diffraction des électrons rétrodiffusés (EBSD) dans un microscope électronique à balayage (ZEISS Supra 55VP) après polissage mécanique et électrolytique, est illustrée sur la Figure B.5. La microstructure présente peu ou pas de texture cristallographique et des tailles de grain variant de 50 à 200 μm .

Le comportement mécanique du matériau a été caractérisé par une série de tests de traction uniaxiale. Pour cela, des éprouvettes de traction cylindriques (norme ASTM-E8M, diamètre de 4 mm et longueur utile de 20 mm) furent déformées jusqu'à rupture à une vitesse de 5.10^{-4} s^{-1} . La Figure B.6 fournit la courbe contrainte-déformation calculée entre 0 et 5% par rapport à la longueur utile initiale et la section nominale.

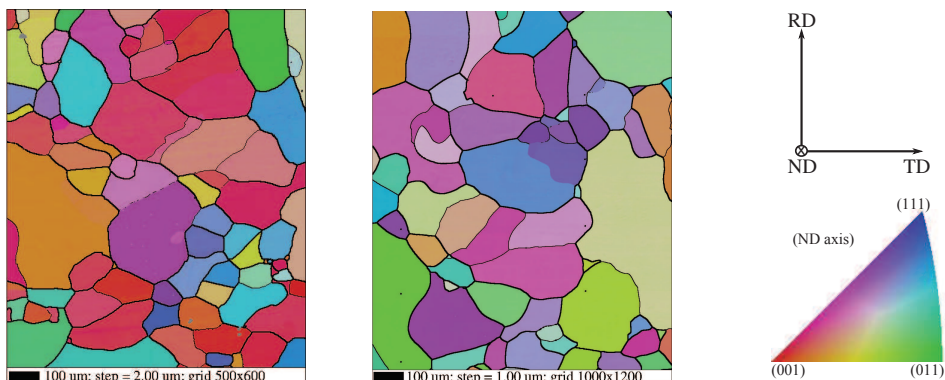


Figure B.5 – Microstructure recristallisée : deux cartographies EBSD montrant deux échantillons distincts. Coloration en figure de pole inverse et joints de grains.

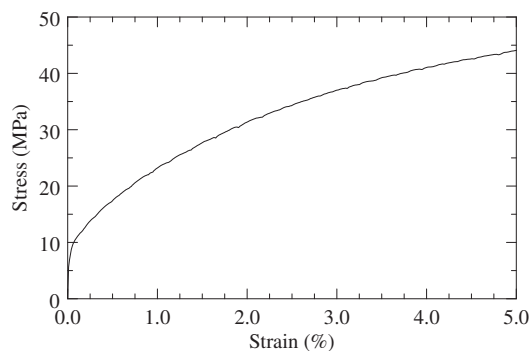


Figure B.6 – Courbe contrainte-déformation macroscopique mesurée en laboratoire pour l'alliage Al-0.3Mn.

B.2.3 Expériences à ESRF sur la ligne ID11

Pour les expériences in-situ, deux échantillons ont été découpés par électro-érosion dans le lingot laminé, polis mécaniquement pour retirer la couche de matériau affectée par l'usinage puis traités thermiquement pour obtenir la microstructure finale. Les dimensions sont détaillées dans la Figure B.7.

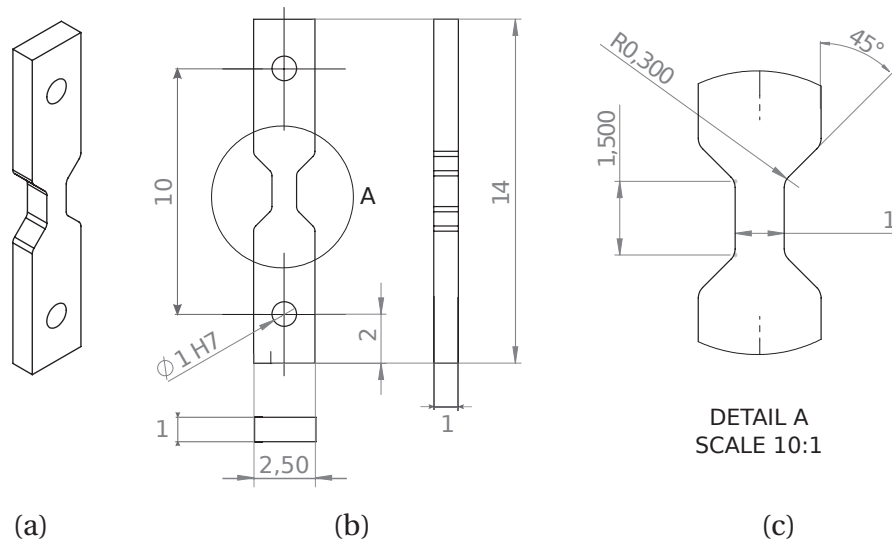


Figure B.7 – Forme et dimensions (mm) des échantillons destinés aux essais in-situ. (a) vue en perspective, (b) projections orthographiques et (c) agrandissement de la partie utile de l'éprouvette.

L'échantillon A a été déformé plastiquement en traction uniaxiale à 1% puis mesuré par DCT et HEDM à ESRF sur la ligne de lumière ID11. Par la suite, au laboratoire, la même région de l'échantillon a été caractérisée par EBSD pour comparaison. Les mesures de DCT ont été réalisées à une énergie de 41.7 keV, à l'aide d'un détecteur FReLoN de 2048×2048 pixels de $1.4 \mu\text{m}$, placé à une distance de 5 mm de l'échantillon. Les mesures de HEDM ont quant à elles été effectuées à une énergie de 60 keV à l'aide d'un faisceau plan focalisé de $2 \mu\text{m}$ d'épaisseur et d'un détecteur dit 3D : deux écrans semi-transparents de 2048×2048 pixels, présentant des tailles de pixel de $1.5 \mu\text{m}$ et $4.5 \mu\text{m}$ et placés respectivement à 5 mm et 15 mm de l'échantillon. Quatorze couches ont ainsi été mesurées. La disposition des différentes régions observées par DCT, HEDM et EBSD est représentée schématiquement sur la Figure B.8.

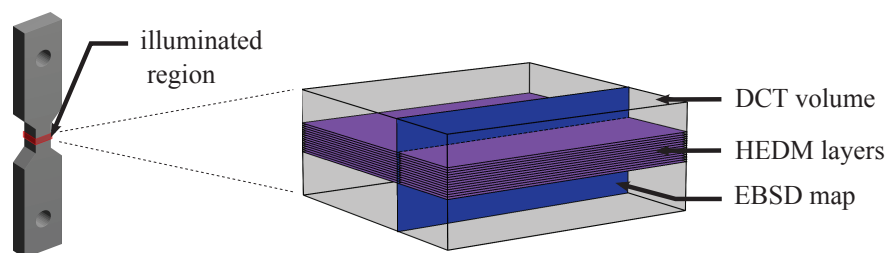


Figure B.8 – Vue schématique des régions mesurées par DCT, HEDM et EBSD.

L'échantillon B, monté dans une machine de traction adaptée aux essais in-situ, a été caractérisé à l'état non-déformé par DCT et 3DXRD puis à cinq niveaux successifs de déformation (1%, 1.5%, 2%, 2.5% et 4.5%) par 3DXRD. Les mesures de 3DXRD ont été réalisées à une énergie de 60 keV et à l'aide d'un détecteur FReLoN de 2048×2048 pixels de taille $48.5 \mu\text{m}$, placé à environ 200 mm de l'échantillon. La Figure B.9 illustre le dispositif. Initialement, des clichés de diffraction ont également été collectés à partir d'un échantillon de poudre standard de CeO_2 (certifié NIST) en vue de la calibration du détecteur. D'autre part, tout au long de l'essai, la longueur d'onde du faisceau a pu être suivie à l'aide d'un équipement dédié disponible sur la ligne.

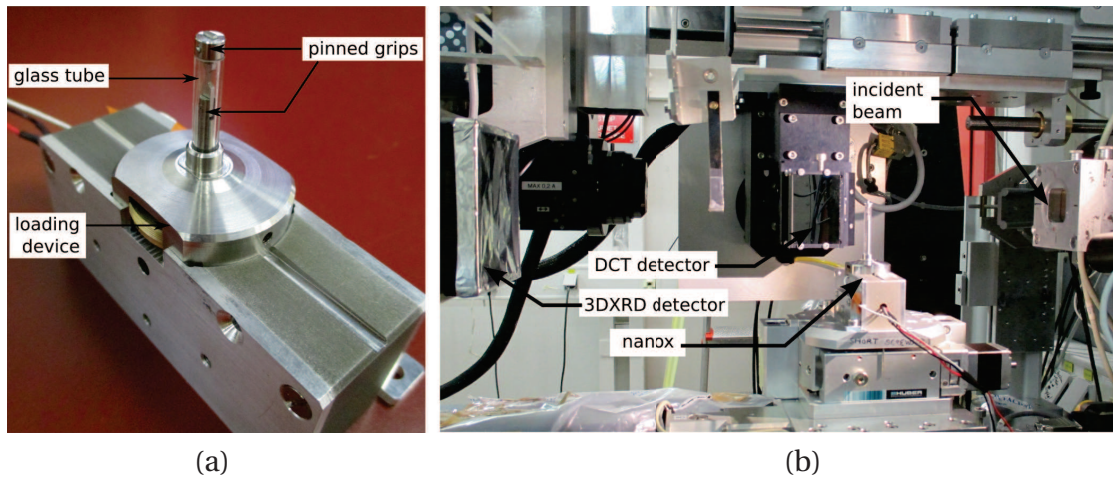


Figure B.9 – Dispositif expérimental in-situ à ID11. (a) Machine de traction Nanox. L'échantillon est fixé à chaque extrémité par des chevilles reposant sur un tube de verre, ce qui permet une rotation complète dans le diffractomètre. (b) Configuration du diffractomètre, incluant la machine du traction montée sur le goniomètre, le détecteur haute résolution utilisé pour le DCT et, plus loin, le détecteur employé pour le 3DXRD.

B.3 Chapitre III : mesure précise des propriétés moyennes par grain

B.3.1 Description de la géométrie

Un diffractomètre de 3DXRD est constitué de quelques éléments principaux : l'échantillon est placé sur une platine rotative d'axe verticale, illuminé par un faisceau X parallèle et monochromatique et l'intensité diffractée est mesurée par un détecteur 2D placé à distance de l'échantillon. L'usage a longtemps été dans la littérature de supposer une géométrie idéale présentant un détecteur et un axe de rotation parfaitement perpendiculaires à l'axe du faisceau, ce qui est très difficile à obtenir expérimentalement. Il apparaît toutefois qu'une caractérisation précise et valable doit pouvoir tenir compte de toutes les imperfections et sources d'erreurs affectant le dispositif de mesure.

Dans ce travail, nous avons développé une description de la géométrie du 3DXRD basée sur l'utilisation de différents repères et systèmes de coordonnées, permettant de relier les clichés de diffraction (images 16-bits de 2048×2048 pixels) à l'espace réciproque du ou des grains. La géométrie est décrite mathématiquement à l'aide d'un ensemble de paramètres bien choisis, détaillés dans le tableau B.1 : on distingue les neuf paramètres globaux, qui ne dépendent pas de l'échantillon caractérisé, et les douze paramètres définis pour chaque grain individuel.

Table B.1 – Paramètres globaux décrivant la géométrie du 3DXRD et paramètres des grains.

	Paramètre(s)	Description
Ensemble		
	n_1, n_2, n_3	tilt du détecteur
	v	tilt de l'image
Global	u_B, v_B	centre du faisceau
(9)	D	distance du détecteur
	w	tilt de l'axe
	λ	longueur d'onde
Grain		
	x_0, y_0, z_0	centroïde
	R_1, R_2, R_3	orientation
(12)	$a, b, c, \alpha, \beta, \gamma$	paramètres de maille

B.3.2 Calibration de la géométrie

La mise en oeuvre d'une expérience de 3DXRD passe par une étape préliminaire de calibration destinée à assurer la précision et la valabilité des résultats. Il s'agit en fait de la détermination des paramètres globaux, qui décrivent la géométrie et sont indépendants de l'échantillon mesuré. Au regard de la littérature disponible, on peut distinguer deux approches : celle d'Oddershede *et al.* [54] qui basent la calibration directement sur l'échantillon étudié et celle de Bernier *et al.* [66] qui exploitent des mesures indépendantes et sera donc de préférence utilisée dans ce travail.

Notre procédure de calibration repose dans un premier temps sur la caractérisation de l'inclinaison du détecteur à partir de clichés de diffraction obtenus sur un échantillon de poudre de référence (CeO_2 certifié NIST). L'intensité diffractée se présente sous la forme de cercles concentriques, appelés anneaux de Debye. Sous l'effet d'un défaut de perpendicularité, même faible, par rapport à l'axe du faisceau, ces anneaux deviennent des ellipses, dont la forme et l'excentricité donnent directement accès à l'inclinaison du détecteur. Cela passe par la résolution d'un problème simple d'optimisation non-linéaire pour déterminer les trois composantes du tilt, ainsi que pour estimer la position du centre du faisceau et la distance échantillon-détecteur. La méthode a été appliquée pour calibrer les mesures de 3DXRD réalisées sur l'échantillon B. L'examen des distorsions radiales résiduelles, illustré par la Figure B.10, montre que les erreurs sont majoritairement comprises entre $\pm 5 \times 10^{-5}$, ce qui est adapté à la mesure des contraintes.

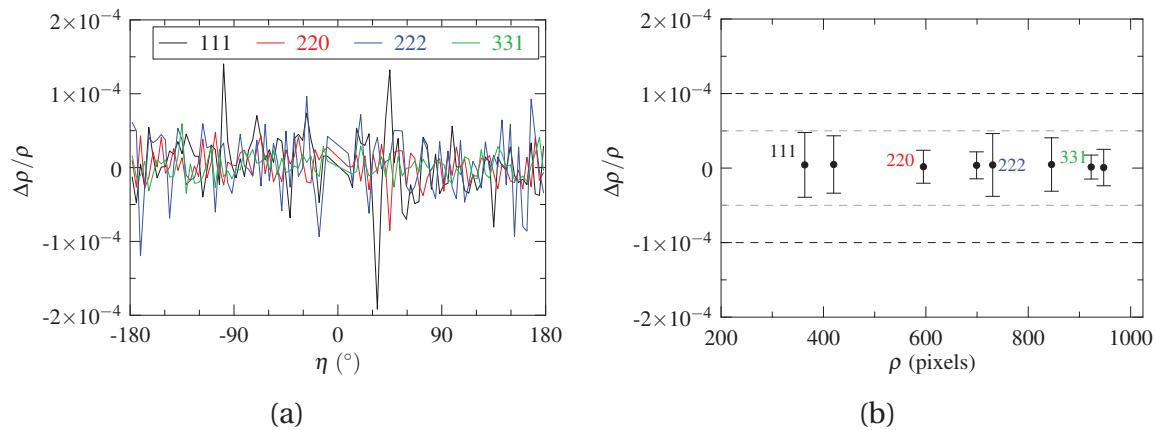


Figure B.10 – Distorsions radiales résiduelles du FReLoN-4M après correction et calibration : (a) Erreur radiale relative en fonction de η pour les anneaux 111, 220, 222 and 331. (b) Erreurs radiales moyennes en fonction de ρ , pour tous les anneaux disponibles (111, 200, 220, 311, 222, 400, 331 and 420).

Un autre paramètre important de la géométrie est la longueur d'onde du faisceau, qui doit être connue avec une précision au moins égale à la précision visée en termes de déformations élastiques. Comme nous l'avons mentionné précédemment, la longueur d'onde a pu être suivie tout au long de l'expérience à l'aide d'un équipement dédié, disponible sur la ligne ID11. Les résultats, présentés dans la Figure B.11, révèlent des variations significatives de l'ordre de 1×10^{-4} , prises en compte par la suite dans la caractérisation.

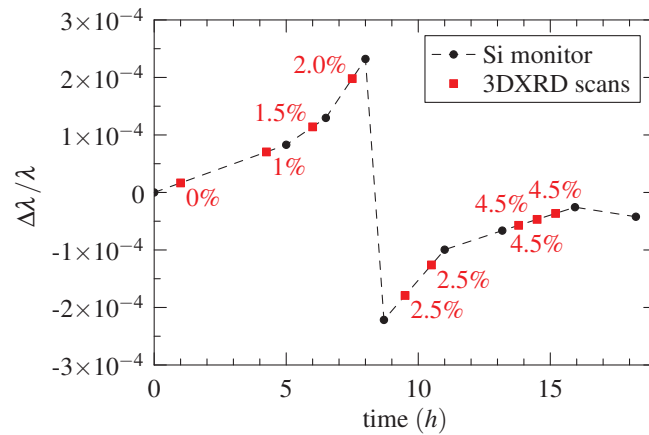


Figure B.11 – Variations de la longueur d’onde durant la mesure de l’échantillon B. La variation continue est à attribuer à une accumulation de chaleur par le monochromateur, après manipulation de l’onduleur.

La géométrie complète est obtenue directement à partir des mesures réalisées sur l’échantillon B. Une procédure itérative d’optimisation permet de déterminer les paramètres globaux restants, en utilisant l’équation de base du diffractomètre et une valeur de départ pour le paramètre de maille (structure cubique) déterminée en laboratoire. L’erreur résiduelle du diffractomètre est alors mesurée par les contraintes résiduelles déterminées dans l’échantillon. Une autre vérification concerne la distribution des paramètres de mailles, fournie dans la Figure B.12, qui est proche de la valeur obtenue pour un échantillon de poudre de Al-0.3Mn et donc caractéristique d’un polycristal relaxé. Les variations d’un grain à l’autre sont attribuables à des variations de la concentration de Mn.

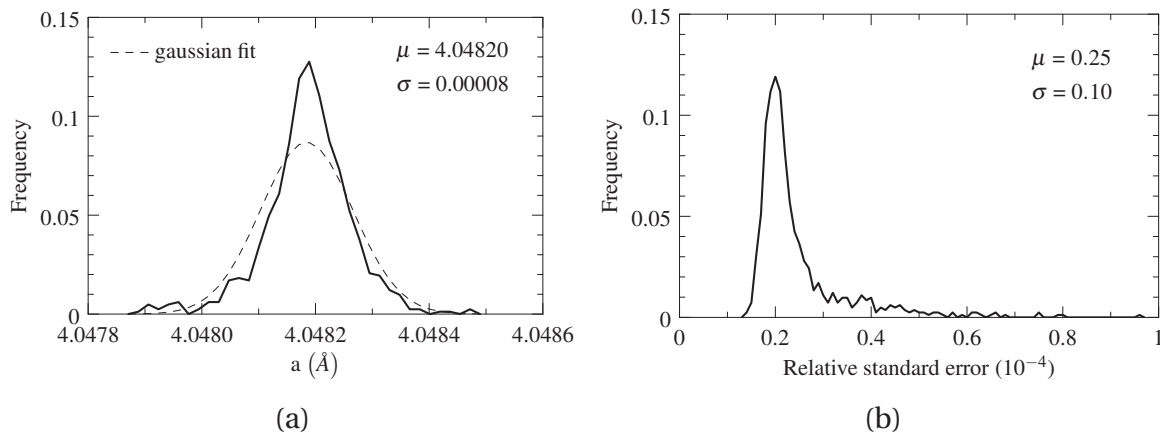


Figure B.12 – Distribution de paramètre de maille à l’état non-déformé de l’échantillon B : (a) paramètres de mailles and (b) erreurs standards relatives, pour 824 grains.

B.3.3 Validation de la calibration

Le lecteur aura sans doute noté dans la section précédente que la calibration est en fait étroitement liée à la détermination des propriétés moyennes des grains. La validation des résultats requiert d'examiner les déformations élastiques et contraintes résiduelles.

Les positions, orientations cristallines et volumes des grains sont calculées à partir de la position et de l'intensité des taches de diffraction. On représente les résultats pour les 824 grains de l'état non déformé de l'échantillon B sous la forme de sphères équivalentes (position, rayon) colorés selon l'orientation des grains, voir Figure B.13.

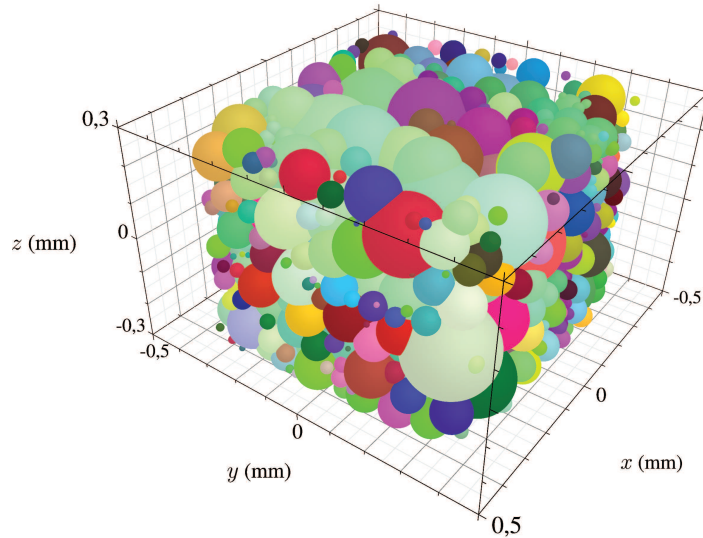


Figure B.13 – Microstructure initiale de l'échantillon B révélée par 3DXRD. Les 824 grains sont matérialisés par des sphères équivalentes colorées selon l'orientation des grains (composantes du vecteur de Rodrigues).

L'évaluation des déformations élastiques repose sur la définition du tenseur lagrangien des grandes déformations, qui s'écrit d'un point de vue cristallographique comme la variation du tenseur métrique par rapport à un état de référence :

$$\underline{\boldsymbol{\varepsilon}}^e = \frac{1}{2} \mathbf{B}_0 (\underline{\mathbf{G}} - \underline{\mathbf{G}}_0) \mathbf{B}_0^T \quad (\text{B.4})$$

où \mathbf{B}_0 est la matrice d'orthogonalisation. Le tenseur métrique $\underline{\mathbf{G}}$ est obtenu à partir de la norme des vecteurs de diffraction mesurés, par la relation :

$$\begin{pmatrix} h \\ k \\ l \end{pmatrix}^T \underline{\mathbf{G}}^* \begin{pmatrix} h \\ k \\ l \end{pmatrix} = \|\mathbf{g}\|^2 \quad (\text{B.5})$$

Enfin, les contraintes sont données par la loi de Hooke. Les résultats sont exprimés dans le repère du laboratoire et tracés dans les Figures B.14 et B.15 sous forme de distributions. Ces dernières sont centrées sur zéro et présentent des largeurs à mi-hauteur inférieures à 1×10^{-4} et 8 MPa, respectivement. L'étude nous permet de conclure sur des précisions expérimentales proches de 3 μm , 0,03°, 1×10^{-4} et 8 MPa en termes de position, orientation, déformation élastique et contrainte.

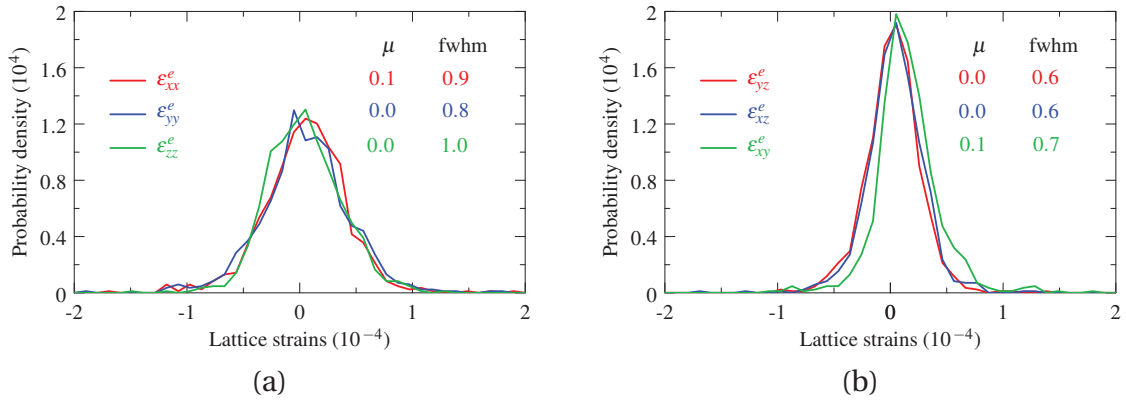


Figure B.14 – Déformations élastiques résiduelles dans l'échantillon B. Distributions (a) des composantes normales et (b) des composantes de cisaillement, calculées dans le repère du laboratoire.

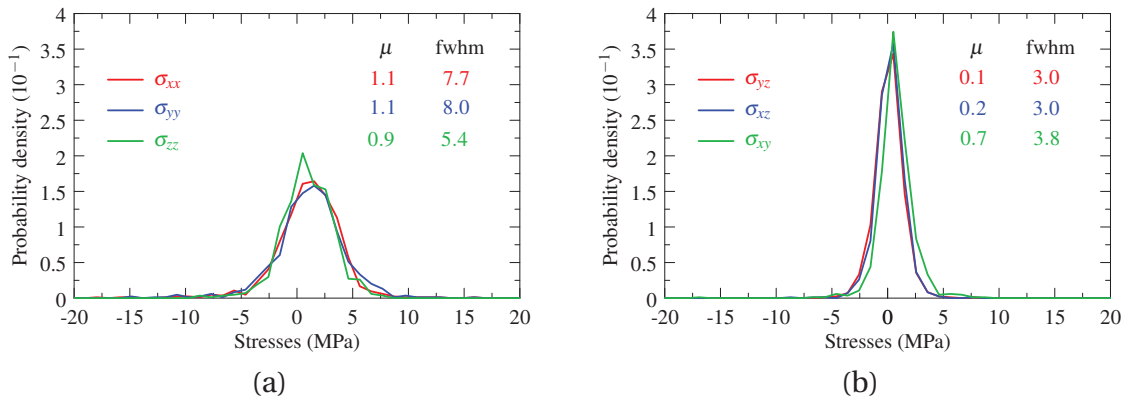


Figure B.15 – Contraintes résiduelles dans l'échantillon B. Distributions (a) des composantes normales et (b) des composantes de cisaillement, calculées dans le repère du laboratoire.

B.4 Chapitre IV : validation croisée de la microstructure initiale

B.4.1 Comparaison entre DCT, HEDM et EBSD

Le premier point de cette validation concerne l'applicabilité de la technique DCT à la reconstruction de la microstructure de l'alliage Al-0.3Mn étudié, qui contient en général des grains sous-structurés. Jusqu'à récemment les reconstructions de microstructures 3D comme celle obtenues par DCT étaient essentiellement validées par comparaison avec des observations EBSD [98, 99]. Toutefois, devant la multitude des techniques d'imagerie aujourd'hui disponibles en synchrotron, il devient tout à fait envisageable de réaliser une validation croisée directement à partir de deux techniques de diffraction, comme le DCT et le HEDM. Une telle comparaison peut être menée ici à partir des mesures réalisées sur l'échantillon A.

Pour cela, les mesures DCT ont été analysées à l'aide du logiciel *DCT* disponible sur la ligne ID11. Le volume reconstruit, fourni en Figure B.16-c, présente une taille de voxel de 1.4 μm , une épaisseur de 350 μm et contient 410 grains. Les mesures HEDM ont quant à elles été analysées à l'aide du logiciel *IceNine*, développé à Carnegie Mellon University. Les quatorze couches ainsi reconstruites, espacées verticalement les unes des autres de 6 μm , sont représentées sur la Figure B.16-b, tout comme la cartographie acquise en laboratoire par EBSD.

Une comparaison directe entre les différents jeux de données nécessite avant tout de déterminer la position de chaque couche HEDM dans le volume DCT. Si celle-ci peut être estimée visuellement, elle n'est pas connue précisément du fait notamment de l'utilisation de détecteurs différents. Pour remédier à cette difficulté, une nouvelle méthode de recalage de cartographies d'orientations a été proposée. Elle repose sur la résolution d'un problème simple d'optimisation non-linéaire, dont les paramètres décrivent toutes les sources possibles de décalage entre les cartographies (translation, rotation, grossissement et déformation) et la fonction objectif mesure la dissimilitude entre elles (angles de désorientation locale).

Les paramètres de recalage obtenus ont permis d'extraire du volume DCT des coupes 2D correspondantes aux couches HEDM, permettant ainsi d'établir une comparaison directe et quantitative. Après identification et appariement des grains individuels dans les deux microstructures, la proportion de pixels appartenant aux mêmes grains a fourni le taux de recouvrement entre DCT et HEDM : 87%. L'accord entre les deux techniques a également été mesuré par la distance entre leurs réseaux de joints de grains respectifs, comme le montre la Figure B.17 (méthode de la transformée de distances). La distance moyenne est de 4 μm , ce qui représente près de 4% de la taille de grain moyenne et indique un très bon accord entre les microstructures reconstruites. Une comparaison similaire a été menée avec la cartographie EBSD, comme l'illustre la Figure B.18, résultant en un recouvrement de 82% avec le DCT et une distance moyenne de 5.6 μm entre leurs réseaux de joints de grains. Si l'accord est légèrement plus faible, il vient tout de même soutenir les résultats de la première comparaison entre DCT et HEDM et permet de conclure sur la validité des reconstructions.

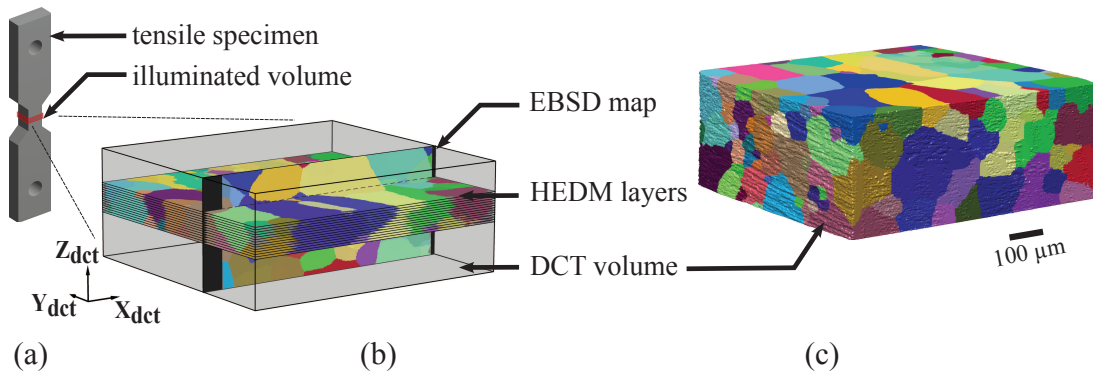


Figure B.16 – Microstructure de l'échantillon A révélée par DCT, HEDM et EBSD. (a) Échantillon A et région mesurée. (b) Disposition des coupes HEDM et EBSD dans le volume DCT. (c) Reconstruction DCT, de 350 μm d'épaisseur. Code couleur relié à l'orientation (composantes du vecteur de Rodrigues).

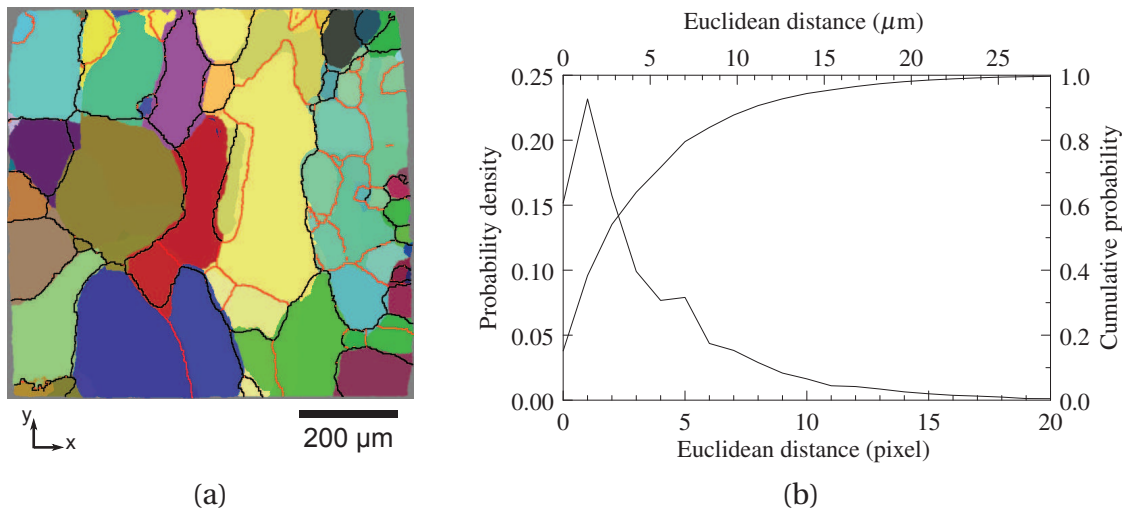


Figure B.17 – Comparaison de la position des joints de grains obtenus par DCT et HEDM. (a) Coupe de la microstructure reconstruite par DCT et réseau de joints de grains obtenu par HEDM. (b) Distribution de la distance entre les réseaux de joints de grains respectifs.

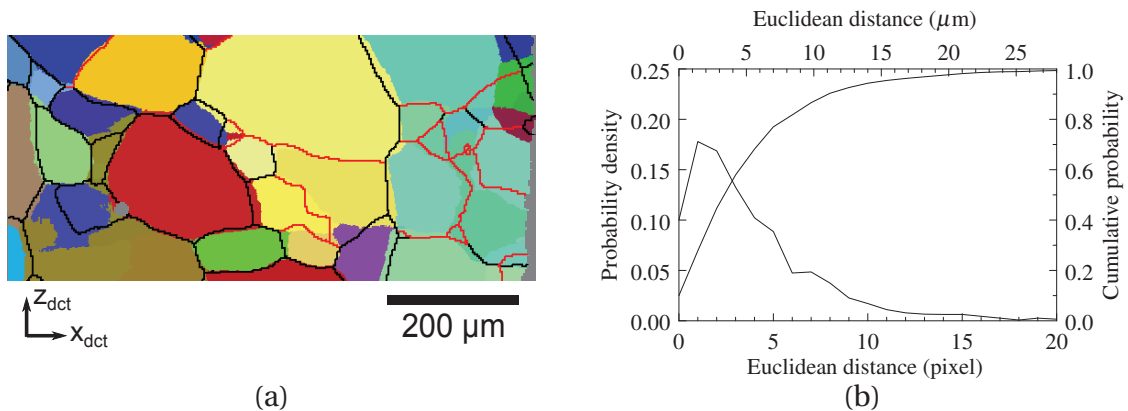


Figure B.18 – Comparaison de la position des joints de grains obtenus par DCT et EBSD. (a) Coupe de la microstructure reconstruite par DCT et réseau de joints de grains obtenu par EBSD. (b) Distribution de la distance entre les réseaux de joints de grains respectifs.

B.4.2 Comparaison entre DCT et 3DXRD

Le second point de la validation concerne l'état non-déformé de l'échantillon B et les microstructures révélées par DCT et 3DXRD, dont l'accord est un prérequis à la comparaison menée plus tard entre expérience (suivi des grains par 3DXRD) et simulation (modèle éléments finis basé sur la reconstruction DCT).

Comme précédemment, les mesures DCT ont été analysées à l'aide du logiciel *DCT* disponible sur la ligne de lumière ID11. Trois volumes distincts de 550 μm de haut ont ainsi été reconstruits, représentant les tiers inférieur, central et supérieur de la partie utile de l'éprouvette. Ceux-ci ont ensuite été fusionnés afin d'obtenir le volume complet, présentant une hauteur totale de 1 394 μm et contenant 1 885 grains, comme l'illustre la Figure B.19. La microstructure reconstruite a par la suite été utilisée pour faciliter l'analyse des mesures 3DXRD. En effet, considérant la partie centrale du volume complet, les propriétés moyennes obtenues pour les grains (ou parties de grains) présents ont permis l'indexation des taches de diffraction 3DXRD. Ainsi, sur les 860 grains initialement présents dans la microstructure DCT, 824 ont pu être retrouvés dans les données 3DXRD.

Encore une fois, une comparaison directe entre les différents jeux de données nécessite avant tout de déterminer la position précise de l'un par rapport à l'autre, du fait de l'utilisation de détecteurs et de logiciels d'analyse différents. Il en résulte une éventuelle (et faible) différence entre les repères de laboratoire utilisés, qui peut être modélisée par une simple transformation de corps rigide. Celle-ci peut être déterminée par la résolution d'un problème d'optimisation, dont les paramètres décrivent la transformation en question et la fonction objectif mesure l'écart entre DCT et 3DXRD (distance entre les centroïdes des grains).

La comparaison grain à grain des données DCT et 3DXRD obtenues pour l'état non-déformé de l'échantillon B est illustrée dans la Figure B.20. Les écarts de position montrent des distributions centrées en zéro et présentant des écarts-types inférieurs à 5 μm . La distribution des angles de désorientation, fournie en Figure B.20-b (ligne continue), présente une valeur moyenne de 0.03°. On observe également une nette amélioration entre la distribution avant (ligne discontinue) et après correction de la transformation de corps rigide, ce qui tend à valider l'approche. Ainsi, les différences observées sont inférieures à la taille de pixel utilisée en 3DXRD (47.5 μm) et au pas angulaire choisi pour les scans DCT (0.1°). Ces résultats sont tout à fait similaires à ceux obtenus par Nervo *et al.* [71]. On en conclut que l'accord obtenu entre DCT et 3DXRD, qui est très bon, représente une validation croisée de la structure granulaire initiale mesurée pour l'échantillon B.

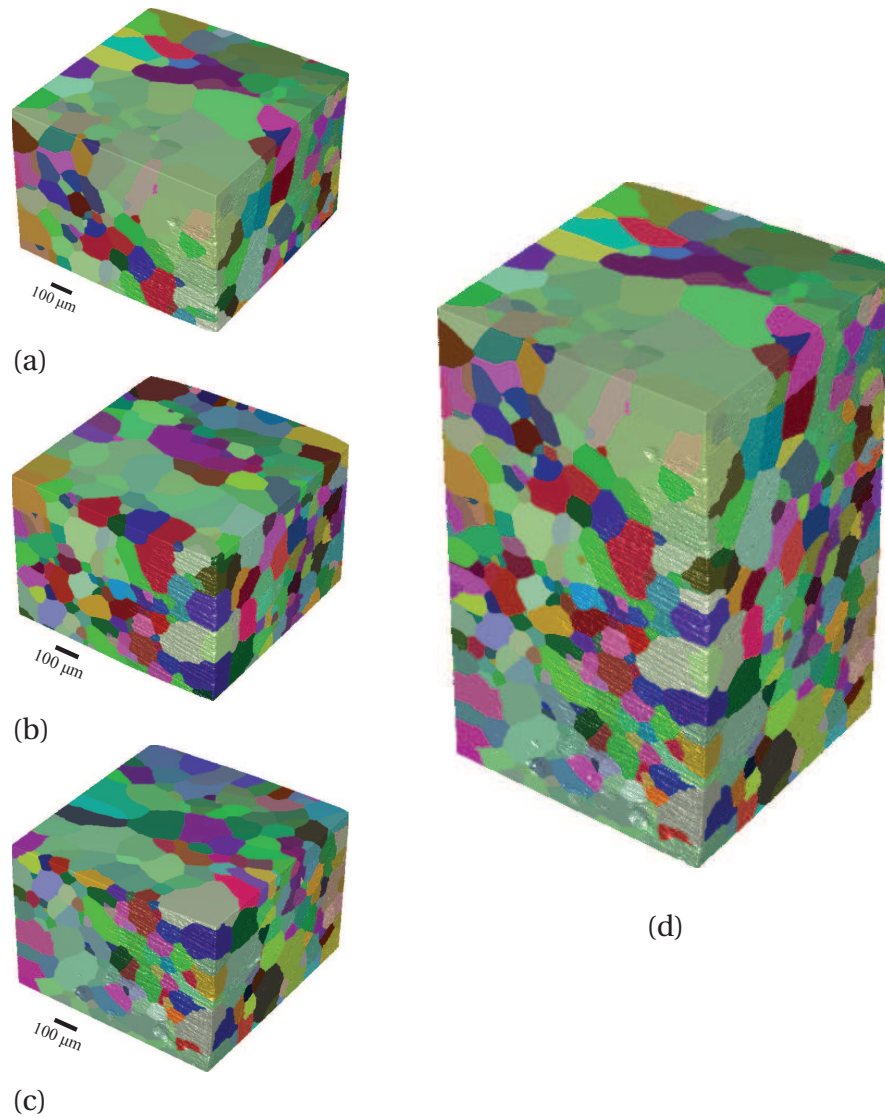


Figure B.19 – Microstructure de l'échantillon B révélée par DCT : (a) tier supérieur contenant 829 grains, (b) tier central contenant 857 grains, (c) tier inférieur contenant 794 grains et (d) volume complet de 1 384 μm de haut, contenant 1 885 grains.

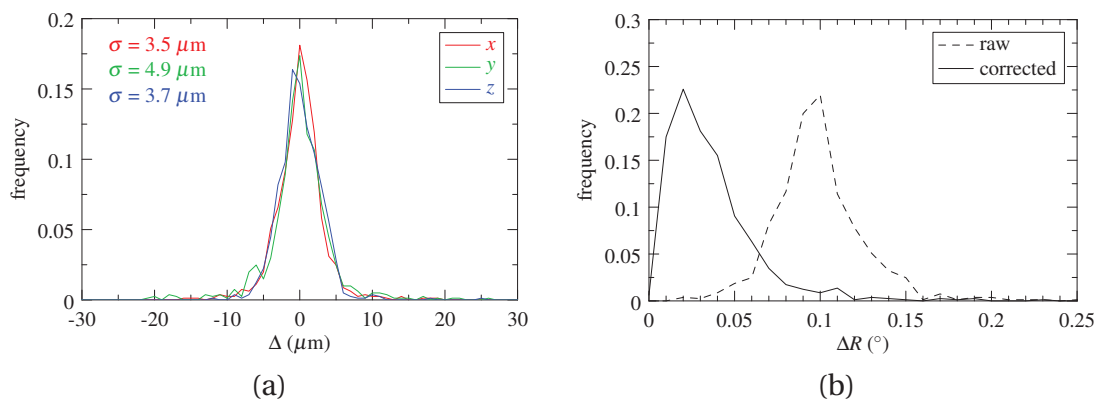


Figure B.20 – Écart de position et d'orientation entre les 824 grains DCT et 3DXRD. (a) Écart de position et (b) angles de désorientation entre les grains DCT et 3DXRD.

B.5 Chapitre V : suivi in-situ par 3DXRD du comportement des grains

Ce chapitre présente les résultats expérimentaux obtenus par 3DXRD pour 466 grains individuels, qui ont pu être suivis de 0% à 4.5%, c'est-à-dire tout au long de l'essai de traction in-situ réalisé sur l'échantillon B. Ils sont analysés en termes de rotations moyennes, dispersions d'orientations intragranulaires, déformations élastiques et contraintes.

B.5.1 Rotations moyennes

Les rotations moyennes peuvent tout d'abord être tracées sur une figure de pôle inverse afin d'identifier les effets d'orientation initiale et d'interaction intergranulaire. Cette représentation est utilisée dans la Figure B.21, montrant un certain accord avec les observations de Winther *et al.* [8] dans les régions 1 et 3 du triangle stéréographique (nette tendance à tourner en direction du segment $[1\ 0\ 0]$ - $[\bar{1}\ 1\ 1]$). On peut également constater que des grains présentant des orientations initiales proches peuvent se comporter de façons très différentes.

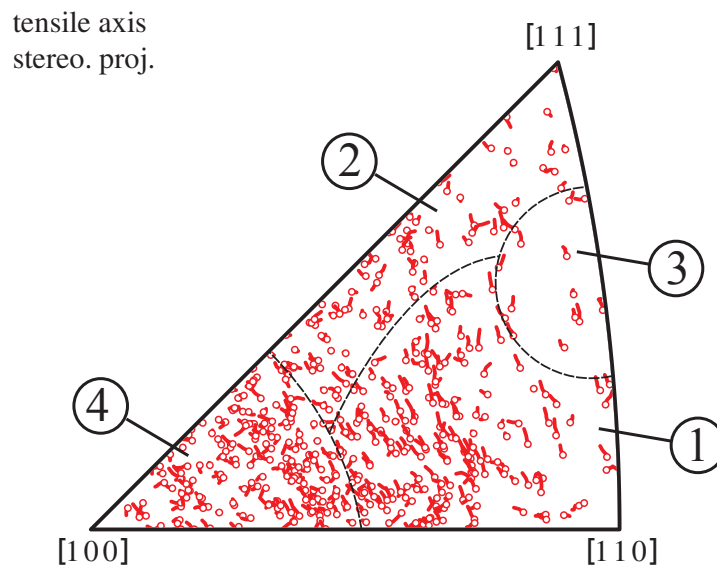
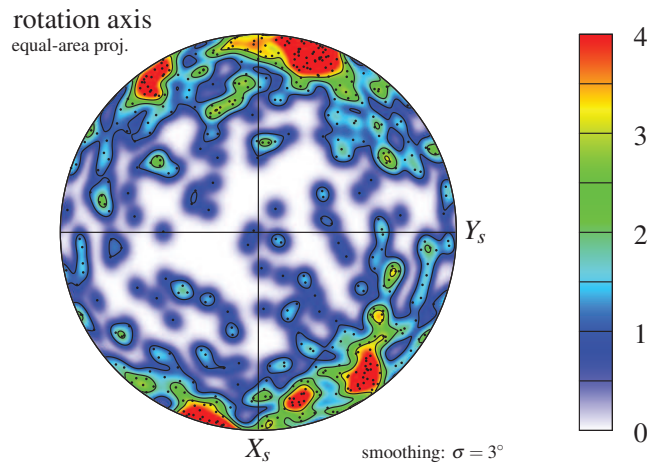
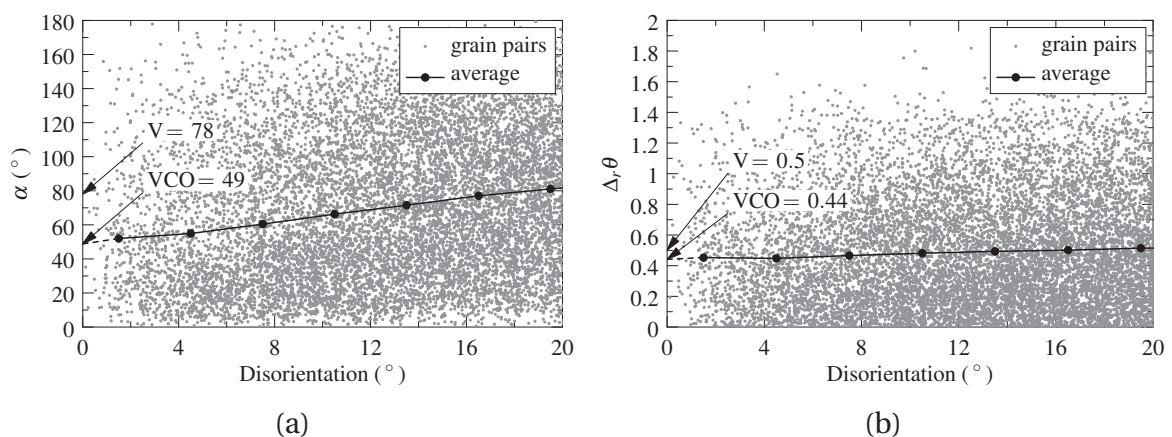


Figure B.21 – Rotations moyennes des 466 grains de 0 à 4.5%. Figure de pôle inverse (projection stéréographique) montrant les orientations initiales (point rouge) et chemins de rotation (ligne rouge). Le triangle est divisé en quatre régions, d'après Winther *et al.* [8].

En vue de mener des analyses plus quantitatives, nous décrivons chaque rotation par la combinaison d'un angle positif θ et d'un axe r . Cette approche a notamment été utilisée par Quey *et al.* [13, 41] pour l'étude de l'aluminium déformé en compression plane et est facilement adaptable au cas de la traction uniaxiale. Les angles de rotation après 4.5% sont en moyenne de 0.8° et distribués entre 0.1° et 1.6° , ce qui indique une forte variabilité des rotations moyennes parmi les grains. La distribution des axes de rotation, représenté dans la Figure B.22, montre un défaut d'axisymétrie attribuable à la texture de l'échantillon et indique une certaine tendance des axes de rotations à s'aligner perpendiculairement à l'axe de traction. Ce résultat peut être expliqué d'un point de vue cristallographique par l'activité du système de glissement le plus sollicité.


 Figure B.22 – Distribution des axes de rotations à $\epsilon = 4.5\%$.

La décomposition en angles et axes de rotation permet en outre de quantifier l'influence de l'orientation initiale sur les rotations moyennes, par le calcul de la variabilité à orientation constante (VCO). Alors que l'approche idéale serait de comparer les rotations de multiples grains pour une orientation donnée, l'approche proposée par Quey *et al.* [41], qui peut s'appliquer à un nombre limité de grains, est de déterminer la VCO en moyenne sur l'espace des orientations. Le principe général est de comparer les rotations des grains tout en prenant en compte la désorientation entre eux et de déterminer la variabilité à orientation constante des rotations par extrapolation à désorientation nulle. L'écart entre les rotations est mesuré par l'angle α entre les axes de rotation et l'écart relatif $\Delta_r\theta$ entre les angles de rotation. La Figure B.23 illustre la détermination de la VCO pour les 466 rotations moyennes de 0% à 4.5%. Les valeurs obtenues indiquent qu'en moyenne deux grains de même orientation initiale présentent des axes et des angles de rotation qui diffèrent de 49° et 44%, respectivement. Ces valeurs peuvent être comparées à celles de la variabilité globale, 78° et 50%, indiquant une remarquable influence de l'interaction intergranulaire sur les rotations.


 Figure B.23 – Variabilité à orientation constante (VCO) des rotations moyennes : (a) axes et (b) angles de rotation. V est la variabilité globale.

B.5.2 Dispersion d'orientations intra-granulaires

Nous proposons dans cette thèse une nouvelle méthode permettant la caractérisation des dispersions d'orientations intra-granulaires à partir de la forme de taches de diffraction mesurées par 3DXRD. On emploie pour cela un modèle simple gaussien pour décrire la fonction de distribution d'orientation de chaque grain, laquelle est utilisée pour simuler des taches de diffraction. Ces dernières sont comparées aux taches mesurées, ce qui permet par une approche d'optimisation de déterminer la distribution d'orientation approchant au plus près les données expérimentales. Les dispersions d'orientations intra-granulaires sont décrites à partir des modèles gaussiens en termes d'angles moyens de désorientation, de facteurs d'anisotropie et d'axes privilégiés de désorientation.

La méthode a été appliquée pour caractériser les dispersions d'orientations intragranulaires des 466 grains individuels après 4.5% de déformation plastique. Les résultats montrent que les angles moyens de désorientation sont de l'ordre des angles de rotation, de 0.6° et compris entre 0.1° et 1.6° . Les facteurs d'anisotropie sont en moyenne de 2.0 et distribués entre 1 et 4.5, ce qui indique des distributions plutôt anisotropes et ayant donc des directions privilégiées bien définies. Ces axes privilégiés de désorientation, tracés sur la Figure B.24, présentent une distribution similaire à celle des axes de rotation, avec un défaut d'axisymétrie et une tendance à s'aligner perpendiculairement à l'axe de traction. Toutefois, aucune dépendance entre les axes de rotation et de désorientation n'a pu être identifiée.

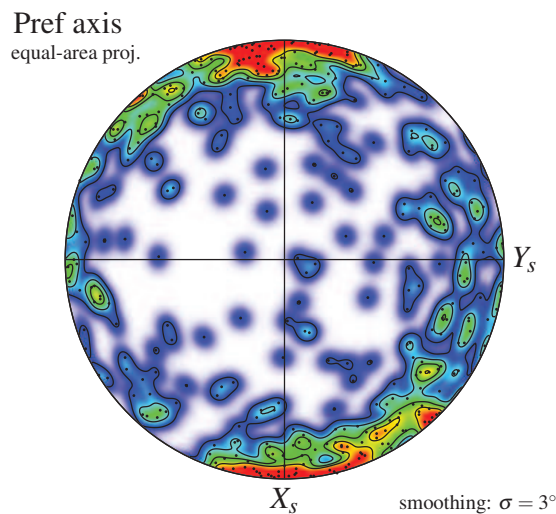


Figure B.24 – Distribution des axes privilégiés de désorientation à $\epsilon = 4.5\%$.

L'effet de l'orientation initiale sur les dispersions d'orientations intragranulaires peut être étudié dans l'espace de Rodrigues. Dans la Figure B.25-a, les dispersions sont représentées par des ellipsoïdes équivalents, centrés sur l'orientation initiale des grains et colorés selon la direction privilégiée de désorientation. Dans la Figure B.25-b, montrant une vue selon l'axe de traction, les dispersions sont représentées par des bâtonnets (dimensions constantes) alignés et colorés selon la direction privilégiée de désorientation. La seconde représentation met en avant une nette influence de l'orientation sur les axes privilégiés de désorientation, qui permet d'autre part d'expliquer le défaut d'axisymétrie observé dans la Figure B.24.

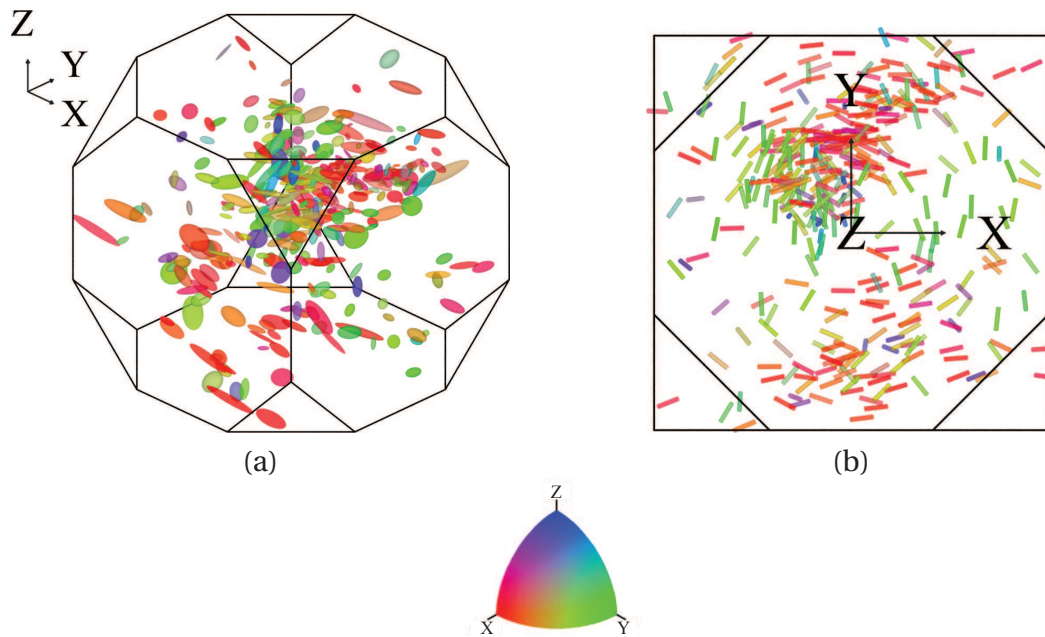


Figure B.25 – Effet de l'orientation initiale sur les dispersions d'orientations intragranulaires après 4.5%, illustré dans la zone fondamentale de l'espace de Rodrigues. Les dispersions sont représentées par des ellipsoïdes équivalents (facteur de grossissement de 10) ou comme des bâtonnets alignés selon la direction privilégiée de désorientation.

B.5.3 Déformations élastiques et contraintes

L'analyse des mesures 3DXRD fournit, pour chacun des 466 grains, l'évolution des six composantes du tenseur de déformation élastique et celle des six composantes du tenseur de contrainte, de 0% à 4.5%. La Figure B.26 présente les résultats obtenus pour un grain arbitraire. On observe une croissance quasi-linéaire des composantes axiales avec le chargement, jusqu'à des valeurs de déformation et de contrainte de 6×10^{-4} et 40 MPa.

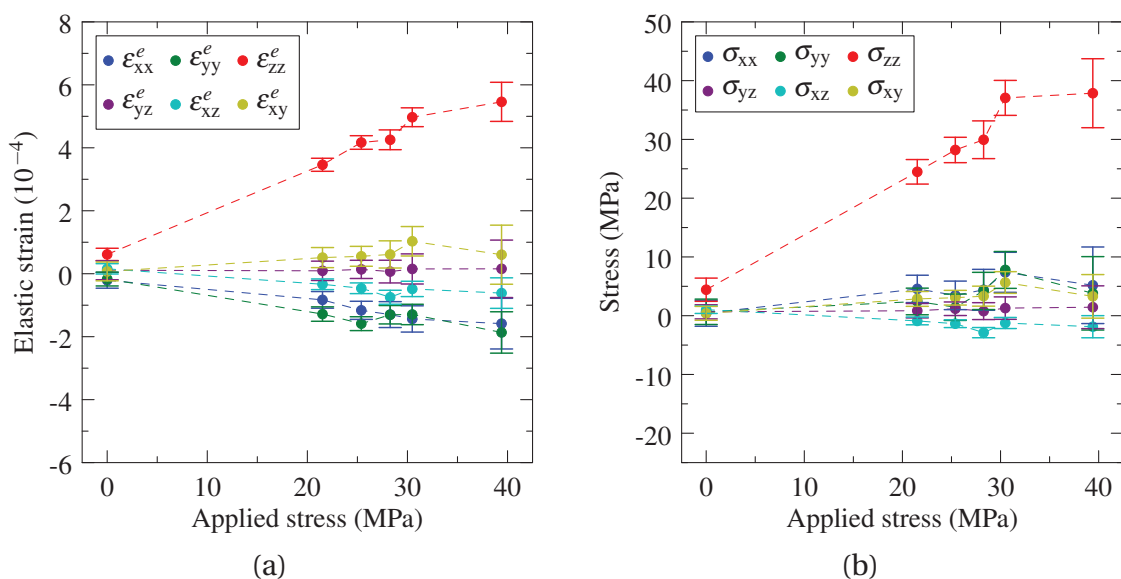


Figure B.26 – Exemple de la réponse mécanique d'un grain mesurée par 3DXRD. Évolution (a) du tenseur des déformations élastiques et (b) du tenseur des contraintes.

Une pré-validation des résultats est réalisée par examen du comportement macroscopique du polycristal. On calcule pour cela les déformations élastiques et contraintes moyennes, pondérées par les volumes des 466 grains. La Figure B.27 montre les valeurs de contrainte axiale ainsi obtenues, qui sont proches des valeurs nominales mesurées par la machine de traction, quoique légèrement plus faibles du fait sans doute d'un effet de relaxation durant l'essai. Les composantes macroscopiques de déformations élastiques sont quant à elle utilisées pour vérifier l'effet de Poisson, qui doit être observé en moyenne sur le polycristal. Des valeurs comprises entre 0.26 et 0.34 sont obtenues pour les coefficients de Poisson successifs, ce qui est plutôt en accord avec la valeur théorique de 0.35 pour l'Al pur.

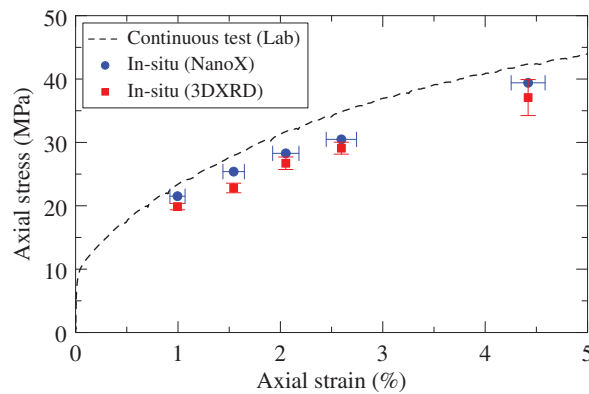


Figure B.27 – Réponse macroscopique du polycristal. Comparaison entre (a) traction de laboratoire et (b-c) expérience in-situ réalisée sur l'échantillon B.

L'effet de l'orientation cristalline sur la répartition des composantes axiales de déformation élastique et de contrainte est illustré par la Figure B.28. Les distributions à $\epsilon = 1.0\%$ sont tracées dans des figures de pôle inverse. Elles montrent notamment que les grains présentant des axes $[1\ 1\ 1]$ proches de l'axe de traction, sont en moyenne plus durs que les autres et subissent des déformations élastiques et des contraintes relativement plus élevées.

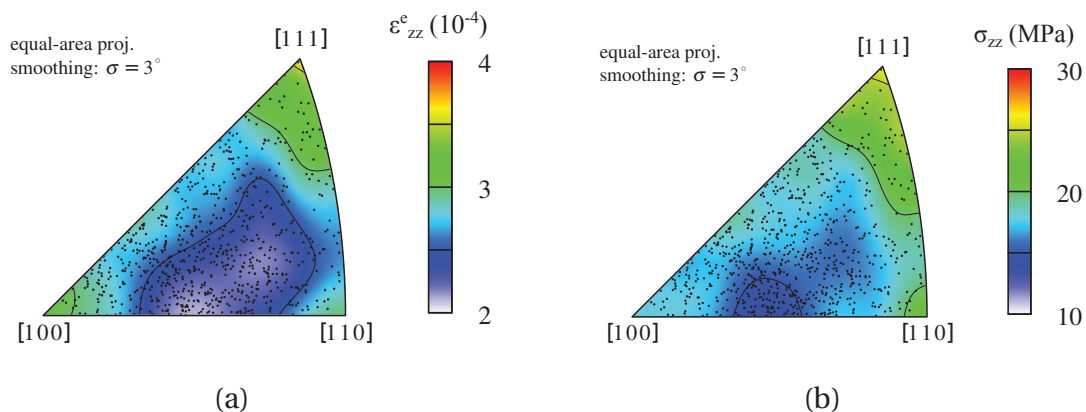


Figure B.28 – Effet de l'orientation sur les composantes axiales de déformation élastique et contrainte à $\epsilon = 1.0\%$.

B.6 Chapitre VI : comparaison à la simulation par éléments finis

B.6.1 Modèle éléments finis

Une simulation par éléments finis a été réalisée, reproduisant l'expérience en termes de microstructure et de chargement. Pour cela, une nouvelle méthode a été proposée et développée dans le logiciel Neper [102, 109] pour déterminer la partition de Laguerre approchant au mieux une microstructure expérimentale donnée, comme celle obtenue ici par DCT. Ainsi décrit de façon analytique par un ensemble de polyèdres convexes, le polycristal se prête alors très bien à la génération automatique de maillages de bonne qualité.

La méthode a été appliquée pour modéliser la microstructure de l'échantillon B reconstruite par DCT, comme le montre la Figure B.29. Du fait de la présence de grains non-convexes, la représentation par une partition de Laguerre ne peut être parfaite. Un très bon accord est toutefois obtenu, avec une erreur moyenne de 10 μm sur la position des joints de grains et un recouvrement volumique de 82%. La microstructure ainsi modélisée a ensuite pu être maillée à l'aide d'éléments tétraédriques à 10 noeuds, présentant une taille moyenne de 10 μm . Le maillage généré compte 1 256 000 éléments, pour une moyenne de 700 éléments par grain.

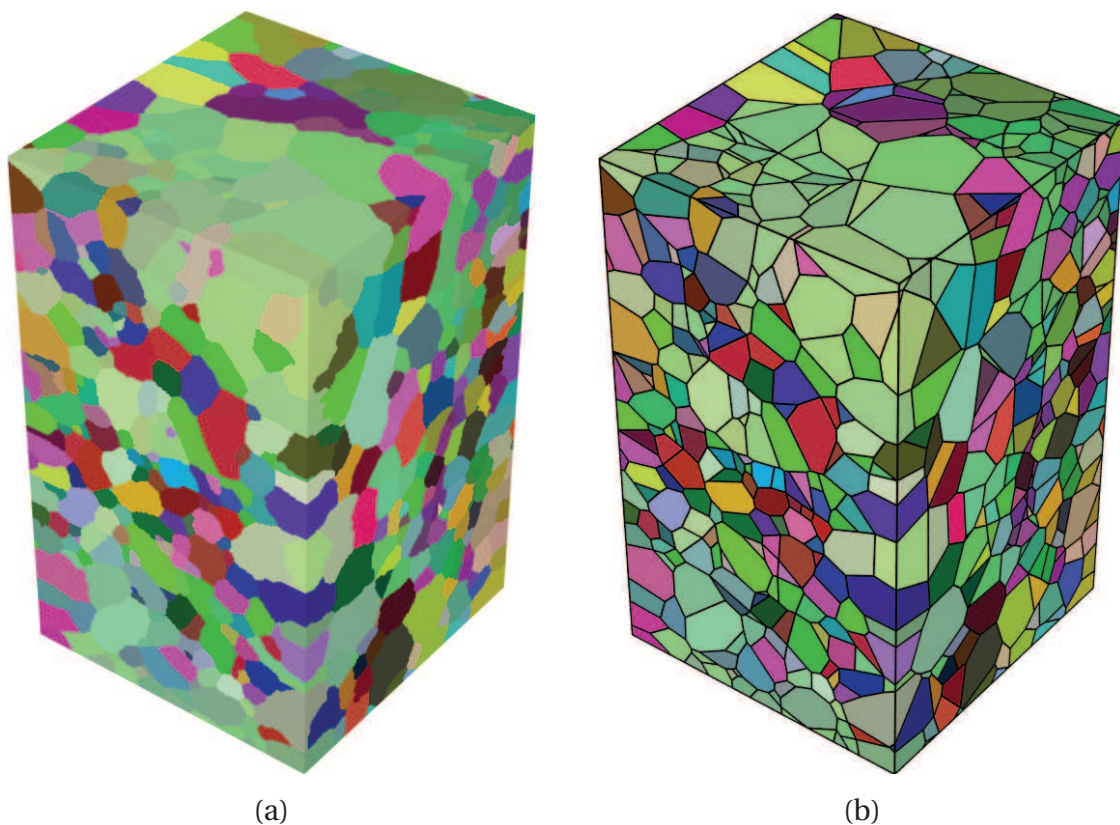


Figure B.29 – Approximation de la microstructure expérimentale de l'échantillon B. (a) Microstructure expérimentale et (b) partition de Laguerre optimisée. Coloration selon l'orientation cristalline.

La simulation a été réalisée à l'aide du logiciel FEpX [110]. La formulation élasto-visco-plastique utilisée est décrite en détail par Marin et Dawson [26] et repose notamment sur une loi de comportement visco-plastique pour les vitesses de glissement et une loi d'écrouissage saturante pour la cission résolue critique. Les paramètres de ces lois ont quant à eux été déterminés par identification à partir de la courbe de comportement macroscopique de l'alliage Al-0.3Mn. L'analyse des résultats de la simulation permet de déterminer, en moyenne par grain, les rotations, les dispersions d'orientations intragranulaires, les déformations élastiques et les contraintes. Ces données peuvent alors être comparées aux résultats expérimentaux du chapitre V.

B.6.2 Rotations moyennes

Comme précédemment, l'analyse des rotations moyennes est menée selon la décomposition en angles et axes de rotation. La comparaison des angles met en évidence une nette différence entre expérience et simulation, qui se traduit par une surestimation systématique des angles de rotation par le modèle éléments finis d'un facteur 2. L'accord grain par grain est mesuré par le coefficient de corrélation de Pearson. La valeur obtenue, de 0.54, indique une corrélation modérée, voire plutôt faible. La comparaison des axes de rotation met quant à elle en évidence un certain accord entre expérience et simulation. La Figure B.30 présentent les distributions tracées dans des figures de pôles. On observe à la fois des similitudes (défaut d'axisymétrie) et des différences (tendance moins prononcée de perpendicularité à l'axe de traction). L'accord grain à grain est quantifié par le calcul des angles α entre les axes expérimentaux et simulés. Les résultats, présentés dans la Figure B.31, indique une corrélation entre expérience et simulation par éléments finis, qui est d'autre part nettement supérieure à celle obtenue entre l'expérience et le modèle de Taylor.

Pour finir, la Figure B.32 présente les résultats de l'évaluation de la variabilité à orientation constante dans l'expérience et la simulation. On observe tout d'abord que pour le modèle de Taylor, dont les prédictions dépendent exclusivement de l'orientation initiale, les valeurs de VCO sont proches de zéro, ce qui permet de valider l'approche. Les variabilités obtenues pour la simulation éléments finis sont sensiblement proches des variabilités expérimentales, ce qui indique que le modèle éléments finis permet de très bien reproduire le niveau d'interaction intergranulaire expérimental.

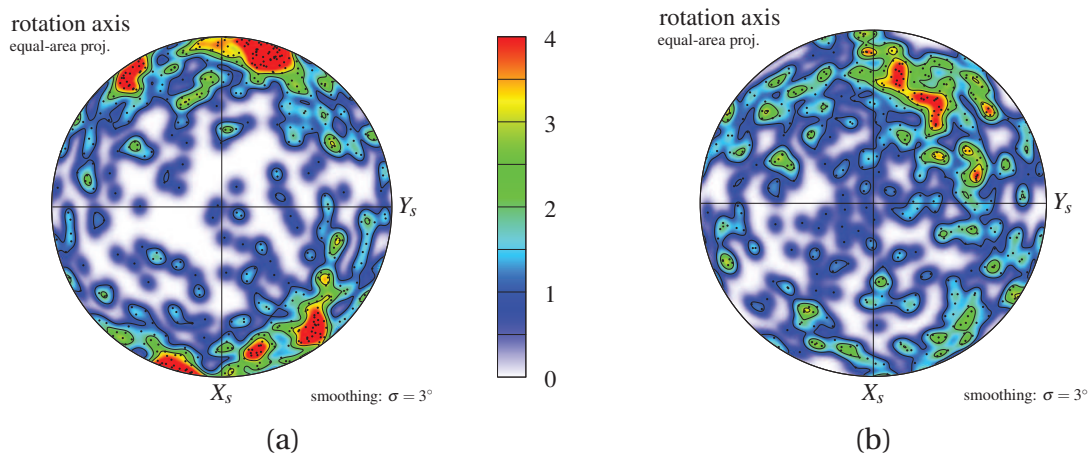


Figure B.30 – Axes de rotation expérimentaux et simulés : (a) expérience et (b) simulation par éléments finis, à $\varepsilon = 4.5\%$. Figures de pôle dans les axes de l'échantillon.

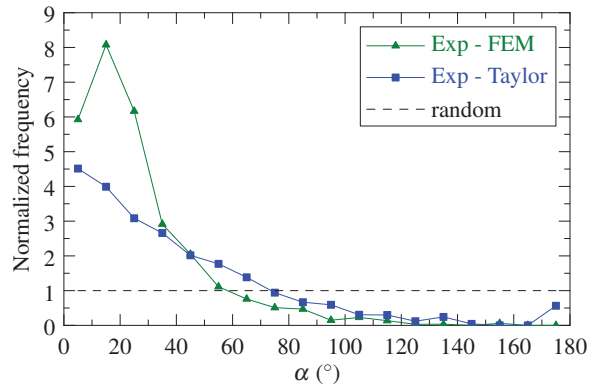


Figure B.31 – Écart angulaire entre les axes de rotation expérimentaux et simulés. Fréquences normalisées par la distribution aléatoire.

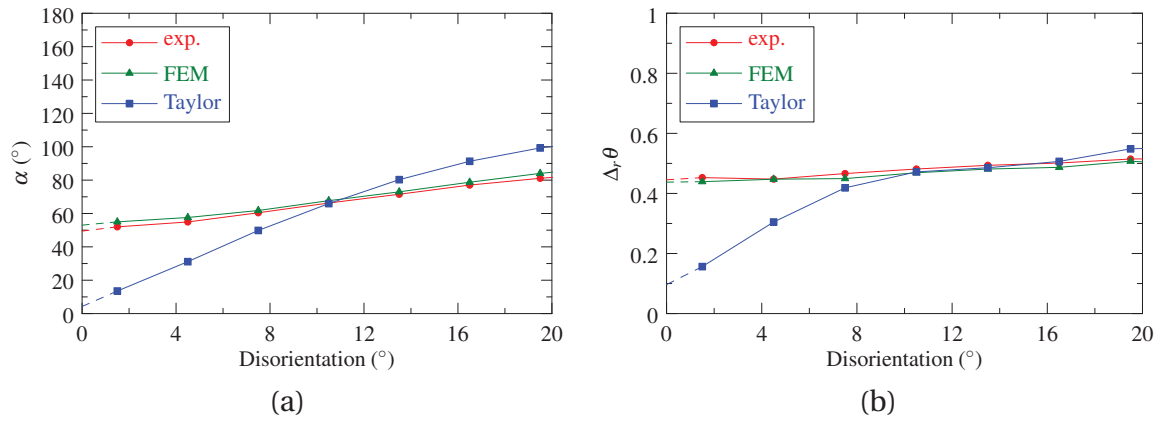


Figure B.32 – Variabilités à orientation constante des rotations expérimentales et simulées : (a) angles and (b) axes de rotation.

B.6.3 Dispersion d'orientations intra-granulaires

Comme dans le chapitre V, les dispersions d'orientations intra-granulaires sont analysées en termes d'angles moyens de désorientation, de facteurs d'anisotropie et d'axes privilégiés de désorientation. On se concentre ici sur l'étude des axes, tels qu'obtenus dans l'expérience, dans la simulation par éléments finis et prédits par le modèle ISM proposé par Quey *et al.* [15].

Les résultats montrent tout d'abord un accord entre expérience et simulation concernant la tendance des axes de désorientation à s'aligner perpendiculairement à l'axe de traction, comme l'illustre la Figure B.33. L'accord grain par grain est quantifié à partir des angles α entre les axes expérimentaux et simulés. Les distributions obtenues, présentées dans la Figure B.34, mettent en évidence un très bon accord avec la simulation par éléments finis, qui se traduit par un écart moyen de 37° (contre 57° dans le cas d'une absence de corrélation). L'accord entre l'expérience et le modèle ISM est quant à lui plutôt faible, avec un écart moyen de 54° .

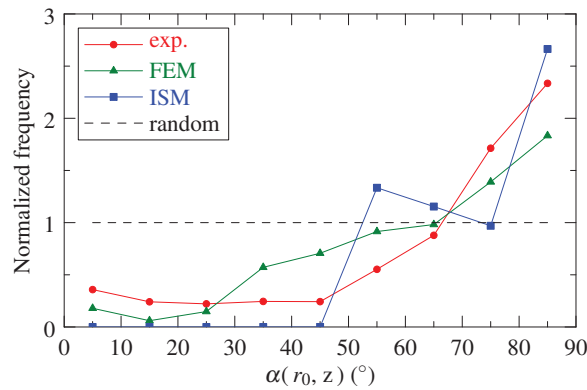


Figure B.33 – Axes privilégiés de désorientation : dépendance à l'axe de traction. Distributions normalisées des écarts entre les axes privilégiés de désorientation des 466 grains et l'axe de traction (expérience, simulation éléments finis et modèle ISM).

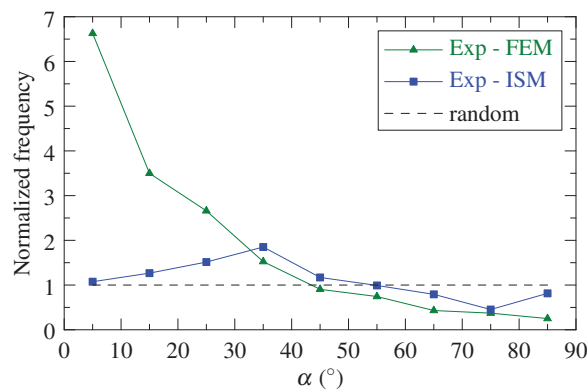


Figure B.34 – Écarts angulaires entre les axes de désorientation expérimentaux et simulés. Fréquences normalisées par la distribution aléatoire.

Comme pour les axes de désorientation expérimentaux, l'influence de l'orientation initiale peut être étudiée dans la zone fondamentale de l'espace de Rodrigues. On peut ainsi observer dans la Figure B.35 un très bon accord entre les distributions expérimentales et simulées par éléments, avec des axes majoritairement perpendiculaires à l'axe de traction et montrant la même dépendance à l'orientation. L'accord est moins bon avec le modèle ISM, qui est nettement mis en défaut pour les grains présentant des axes $[1\ 0\ 0]$ proches de l'axe de traction.

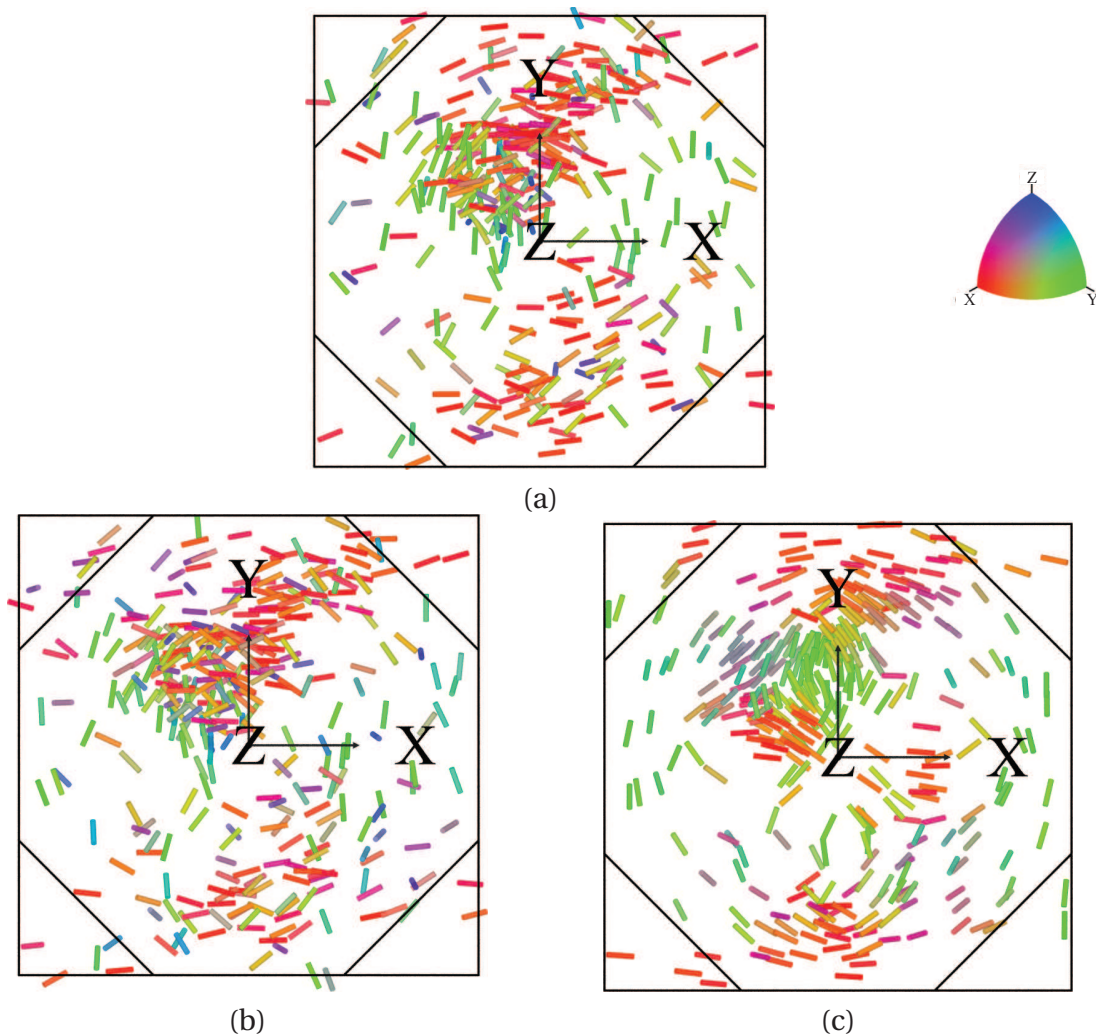


Figure B.35 – Effet de l'orientation initiale sur les dispersions d'orientations intragranulaires après 4.5%, illustré dans la zone fondamentale de l'espace de Rodrigues, pour (a) l'expérience, (b) la simulation éléments finis et (c) le modèle ISM. Les dispersions sont représentées par des bâtonnets alignés selon la direction privilégiée de désorientation.

B.6.4 Déformations élastiques et contraintes

Les résultats expérimentaux et simulés sont comparés dans la Figure B.36 pour un grain choisi arbitrairement. Concernant la représentation par rapport à la contrainte appliquée, on observe que les composantes de déformation élastique et de contrainte évoluent quasi-linéairement. Les composantes axiales augmentent pour atteindre des valeurs de 5×10^{-4} et 40 MPa, respectivement, à l'état final. On peut également remarquer une forte décroissance des composante transverse ε_{xx}^e jusqu'à une valeur de -4×10^{-4} . La même tendance est observée pour les contraintes, mais avec une amplitude moindre.

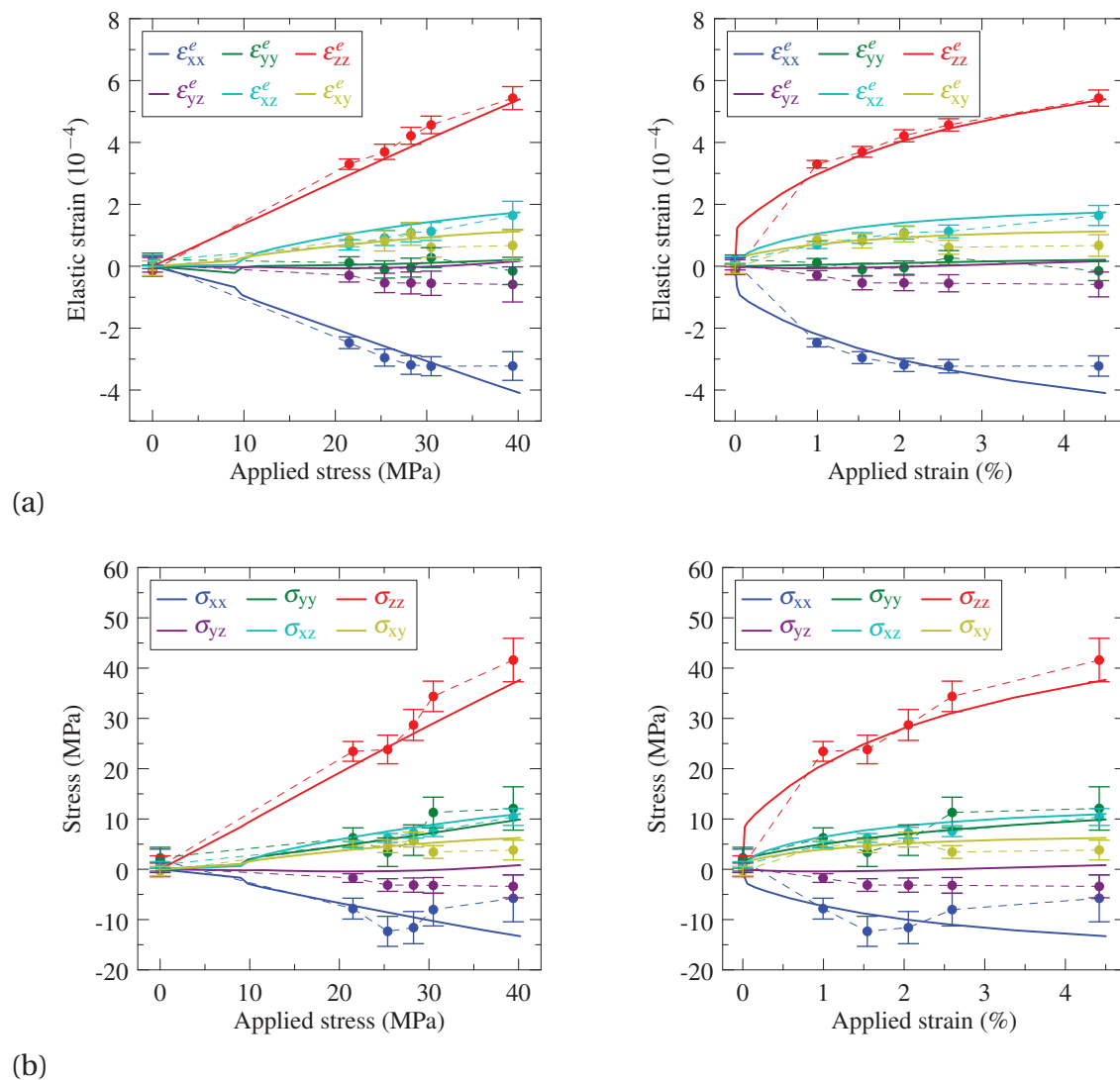


Figure B.36 – Comparaison avec la simulation de la réponse mécanique mesurée par 3DXRD pour un grain choisi arbitrairement. (a) Tenseur de déformation élastique et (b) tenseur de contrainte, en fonction de la contrainte nominale et de la déformation plastique appliquée.

Globalement, l'accord entre expérience et simulation semble plutôt satisfaisant et les erreurs observées sont de l'ordre des incertitudes de mesures. Afin de pousser plus loin l'analyse, on détermine la proportion de grains présentant des erreurs (entre expérience et simulation) supérieures aux précisions expérimentales de 1×10^{-4} et 8 MPa. Les résultats sont présentés dans le tableau B.2 et indiquent que l'accord entre expérience et simulation tend à diminuer tout au long de l'essai pour ne plus représenter qu'environ 50% des grains au final. Ce résultat suggère donc que la loi d'écrouissage utilisée dans le modèle éléments finis pourrait être améliorée.

Table B.2 – Accord grain par grain entre les déformations élastiques / contraintes mesurées par 3DXRD et simulées par éléments finis.

ϵ (%)	$ \Delta\epsilon < 10^{-4}$			$ \Delta\sigma < 8 \text{ MPa}$		
	xx	zz	yz	xx	zz	yz
1.0	93%	80%	98%	89%	78%	99%
1.5	88%	73%	95%	80%	72%	98%
2.0	78%	62%	92%	73%	65%	97%
2.5	74%	61%	92%	68%	68%	98%
4.5	62%	56%	75%	55%	50%	90%

Conclusion

La revue bibliographique du chapitre I aborde les théories permettant de décrire les mécanismes de déformation plastique des cristaux et polycristaux. Deux modèles sont considérés pour réaliser la transition de l'échelle mono- à l'échelle poly-cristalline : le modèle de Taylor, qui suppose que tous les grains sont soumis à la même déformation (la déformation macroscopique) et la méthode des éléments finis, qui permet de résoudre directement et complètement l'équilibre mécanique du polycristal. Le potentiel de récentes techniques de synchrotron pour l'étude de la plasticité cristalline, a pu être mis en évidence par le biais de différents résultats de la littérature. Il apparaît en particulier que la combinaison des techniques de 3DXRD et DCT permet en principe d'effectuer une comparaison détaillée entre des résultats expérimentaux et des simulations par éléments finis.

Les moyens expérimentaux sont décrits dans le chapitre II. Les expériences, réalisées à ESRF sur la ligne de lumière ID11, ont fait appel à trois techniques complémentaires de synchrotron basées sur la diffraction des rayons X à haute énergie : DCT (imagerie en orientation de polycristaux non-déformés), HEDM (imagerie en orientation de polycristaux déformés) et 3DXRD (propriétés moyennes des grains). Deux échantillons sont caractérisés : l'échantillon A, déformé à 1% en traction et mesuré par DCT et HEDM ; l'échantillon B mesuré initialement par DCT et 3DXRD, puis à cinq niveaux de traction par 3DXRD (1%, 1.5%, 2%, 2.5% et 4.5%). Un volume matériel de $900 \times 900 \times 550 \text{ mm}^3$ est ainsi suivi in-situ tout au long de l'essai.

L'analyse des mesures de 3DXRD est détaillée dans le chapitre III. L'approche repose sur une description très générale de la géométrie du diffractomètre, utilisant plusieurs systèmes de coordonnées et prenant en compte toutes les éventuelles imperfections du dispositif. Une méthode de calibration originale (deux publications dans JAC [85, 86]) permet de réduire l'influence des différentes sources d'erreurs sur l'évaluation (inclinaisons, distorsions, etc.). La calibration est validée par le biais de simulations menées sur l'état non-déformé de l'échantillon B, indiquant des précisions de $3 \text{ }\mu\text{m}$, 0.03° , 1×10^{-4} et 8 MPa en termes de position, orientation, déformations élastiques et contraintes, respectivement.

La structure granulaire initiale de l'échantillon B est validée dans le chapitre IV. Dans un premier temps, l'applicabilité de la technique de DCT sur l'alliage Al-0.3Mn est vérifiée à l'aide de l'échantillon A, par comparaison directe entre les reconstructions DCT et HEDM (publication dans IUCrJ [100]). Il est montré un recouvrement de 87% entre les deux microstructures reconstruites, ainsi qu'une distance moyenne de $4 \text{ }\mu\text{m}$ entre leurs joints de grains respectifs. Dans un second temps, la microstructure initiale de l'échantillon B, obtenue séparément par DCT et 3DXRD, est validée. La comparaison, basée sur 824 grains, indique un bon accord entre les deux techniques, avec des écarts moyens de $7 \text{ }\mu\text{m}$ et 0.03° en termes de position et orientation, respectivement.

Les résultats expérimentaux de l'essai in-situ mené sur l'échantillon B sont présentés et étudiés dans le chapitre V. Un ensemble représentatif de 466 grains individuels est suivi jusqu'à 4.5% de déformation plastique. Les rotations moyennes des grains sont examinées en termes d'angles et d'axes de rotations. Les angles de rotation sont relativement faibles, autour de 0.8° en moyenne après 4.5%. Les axes de rotation montrent une tendance à s'aligner perpendiculairement à l'axe de traction. L'influence de l'interaction intergranulaire est mise en évidence par le calcul de la variabilité à orientation constante

(VCO). En moyenne, on observe que deux grains de même orientation présentent des angles et des axes de rotation qui diffèrent de 44% et 49°, respectivement. Les dispersions d'orientations intragranulaires sont obtenues à l'aide d'une nouvelle méthode développée durant cette thèse et reposant sur un modèle simple gaussien de distribution d'orientations. Les résultats révèlent que les axes privilégiés de désorientation ont tendance à s'aligner perpendiculairement à l'axe de traction. Pour finir, les déformations élastiques et les contraintes sont validées à l'échelle macroscopique (effet de Poisson et contrainte macroscopique). Les résultats mettent en évidence une variabilité du comportement des grains individuels, ainsi qu'une certaine dépendance à l'orientation cristalline.

Les résultats de simulation sont détaillés et comparés quantitativement à l'expérience dans le chapitre VI. Pour construire le modèle éléments finis, une nouvelle approche permet de déterminer la partition de Laguerre approchant au plus près la microstructure expérimentale. Le polycristal ainsi obtenu est maillé finement et soumis au chargement expérimental. Les champs mécaniques et d'orientations calculés sont moyennés par grain et comparés aux résultats expérimentaux, ainsi qu'aux prédictions du modèle de Taylor et celles du modèle ISM récemment développé par Quey *et al.* [15]. Les rotations moyennes sont mieux prédites par la simulation par éléments finis, ce qui s'explique par la prise en compte de l'interaction intergranulaire. Les dispersions d'orientations expérimentales et simulées montrent un bon accord, avec la même tendance à s'aligner perpendiculairement à l'axe de traction. À l'aide de la simulation, cette tendance peut être reliée à la variabilité des vitesses de glissement sur les systèmes les plus actifs. Le modèle ISM, quant à lui, échoue à prédire les dispersions pour les grains d'orientations proches de $[1\ 0\ 0] \parallel Z$. Pour finir, concernant les déformations élastiques et les contraintes, la comparaison grain par grain est menée dans la limite de la précision de mesure. On observe un certain accord entre expérience et simulation, pour 90% des grains initialement, et diminuant progressivement tout au long de l'essai jusqu'à 50%.

En conclusion, nous avons proposé une comparaison détaillée et quantitative entre des résultats expérimentaux et simulés quant au comportement des grains individuels dans un polycristal d'Al déformé en traction uniaxial. Ainsi les comportements individuels de 466 grains ont été étudiés de 0 à 4.5% de déformation, en termes de rotations moyennes, de dispersions d'orientations intragranulaires, de déformations élastiques et de contraintes. Il s'agit, à notre connaissance, de la première étude de ce type. Malgré des différences notables, il est montré que l'utilisation de la méthode des éléments finis sur la microstructure réelle fournit de meilleurs résultats que le modèle de Taylor. Il est à noter également que la combinaison entre 3DXRD, DCT et simulation par éléments finis fournit de réels leviers dans l'analyse des mécanismes de déformation en plasticité cristalline. Des verrous ont été identifiés, dont la levée devrait permettre à terme de fournir des pistes d'amélioration pour les modèles actuels.

References

- [1] E. Schmid and W. Boas, "Plasticity of Crystals—a Translation from the German by FA Hughes & Co," *Limited of" KRISTALLPLASTIZITAET". London: FA Hughes & Co. Limited*, 1935. 1, 4, 170, 172
- [2] R. A. Lebensohn and C. N. Tomé, "A self-consistent anisotropic approach for the simulation of plastic deformation and texture development of polycrystals: application to zirconium alloys," *Acta metallurgica et materialia*, vol. 41, no. 9, pp. 2611–2624, 1993. 1, 170
- [3] G. B. Sarma and P. R. Dawson, "Texture predictions using a polycrystal plasticity model incorporating neighbor interactions," *International Journal of Plasticity*, vol. 12, no. 8, pp. 1023–1054, 1996. 1, 170
- [4] R. Quey, P. R. Dawson, and F. Barbe, "Large-scale 3D random polycrystals for the finite element method: Generation, meshing and remeshing," *Computer Methods in Applied Mechanics and Engineering*, vol. 200, pp. 1729–1745, apr 2011. 1, 2, 9, 124, 170, 171, 173
- [5] F. Barbe, L. Decker, D. Jeulin, and G. Cailletaud, "Intergranular and intragranular behavior of polycrystalline aggregates. Part 1: F.E. model," in *International Journal of Plasticity*, vol. 17, pp. 513–536, 2001. 1, 9, 170
- [6] P. Van Houtte, S. Li, M. Seefeldt, and L. Delannay, "Deformation texture prediction: from the Taylor model to the advanced Lamel model," *International Journal of Plasticity*, vol. 21, no. 3, pp. 589–624, 2005. 1, 170
- [7] H. F. Poulsen, *Three Dimensional X-Ray Diffraction Microscopy*, vol. 205. Berlin: Springer, 2004. 1, 13, 22, 23, 170, 176
- [8] G. Winther, L. Margulies, S. Schmidt, and H. F. Poulsen, "Lattice rotations of individual bulk grains Part II: Correlation with initial orientation and model comparison," *Acta Materialia*, vol. 52, no. 10, pp. 2863–2872, 2004. 1, 13, 14, 17, 18, 102, 103, 108, 109, 120, 139, 140, 158, 170, 174, 190
- [9] J. Oddershede, S. Schmidt, H. F. Poulsen, L. Margulies, J. Wright, M. Moscicki, W. Reimers, and G. Winther, "Grain-resolved elastic strains in deformed copper measured by three-dimensional X-ray diffraction," *Materials Characterization*, vol. 62, pp. 651–660, jul 2011. 1, 15, 16, 17, 170, 174
- [10] C. Maurice, *Textures de compression plane à chaud d'alliages d'aluminium: expériences et simulations*. PhD thesis, 1994. 2, 171

-
- [11] F. Perocheau, *Etude et simulation de textures de déformation à chaud d'alliages d'aluminium*. PhD thesis, 2000.
- [12] W. Robert, *Simulations et mesures de textures de laminage à chaud des tôles fortes d'alliage d'aluminium*. PhD thesis, Saint-Etienne, Ecole Nationale Supérieure des Mines, 2005.
- [13] R. Quey, *Suivi de microtextures dans l'aluminium en grande déformation à chaud*. PhD thesis, Ecole Nationale Supérieure des Mines, 2009. 2, 12, 17, 18, 29, 102, 171, 174, 178, 190
- [14] R. Quey, P. R. Dawson, and J. H. Driver, "Grain orientation fragmentation in hot-deformed aluminium: Experiment and simulation," *Journal of the Mechanics and Physics of Solids*, vol. 60, pp. 509–524, mar 2012. 2, 11, 12, 96, 171
- [15] R. Quey, J. Driver, and P. Dawson, "Intra-grain orientation distributions in hot-deformed aluminium: Orientation dependence and relation to deformation mechanisms," *Journal of the Mechanics and Physics of Solids*, vol. 84, pp. 506–527, 2015. 2, 12, 17, 18, 110, 141, 145, 165, 166, 171, 174, 198, 203
- [16] W. F. Hosford, "The mechanics of crystals and textured polycrystals," *Oxford University Press(USA)*, 1993,, p. 248, 1993. 4, 115, 118, 119, 149
- [17] G. Simmons and H. Wang, "Single crystal elastic constants and calculated aggregate properties," 1971. 5, 172
- [18] R. W. Hertzberg, "Deformation and fracture mechanics of engineering materials," *John Wiley & Sons*, p. 697, 1983. 5, 65, 172
- [19] P. Van Houtte, "A Comprehensive Mathematical Formulation of an Extended Taylor–Bishop–Hill Model Featuring Relaxed Constraints, the Renouard–Wintenberger Theory and a Strain Rate Sensitivity Model," *Textures and Microstructures*, vol. 8, no. C, pp. 313–350, 1988. 7
- [20] M. Renouard and M. Wintenberger, "Déformation homogène par glissements de dislocations de monocristaux de structure cubique faces centrées sous l'effet de contraintes et de déplacements imposés," *CR Acad. Sci., Paris B*, vol. 290, pp. 237–240, 1976. 7
- [21] R. J. Asaro and A. Needleman, "Overview Texture Development and Strain Hardening in Rate Dependent Polycrystals," no. 42, 1984. 7
- [22] J. W. Hutchinson, "Creep and plasticity of hexagonal polycrystals as related to single crystal slip," *Metallurgical Transactions A*, vol. 8, no. 9, pp. 1465–1469, 1977. 7, 172
- [23] A. Molinari, G. R. Canova, and S. Ahzi, "A self consistent approach of the large deformation polycrystal viscoplasticity," *Acta Metallurgica*, vol. 35, no. 12, pp. 2983–2994, 1987. 8, 173
- [24] U. F. Kocks, "The relation between polycrystal deformation and single-crystal deformation," *Metallurgical and Materials Transactions*, vol. 1, no. 5, pp. 1121–1143, 1970. 8

- [25] A. J. Beaudoin, P. R. Dawson, K. K. Mathur, and U. F. Kocks, "A hybrid finite element formulation for polycrystal plasticity with consideration of macrostructural and microstructural linking," *International Journal of Plasticity*, vol. 11, no. 5, pp. 501–521, 1995. 8
- [26] E. Marin and P. Dawson, "Elastoplastic finite element analyses of metal deformations using polycrystal constitutive models," *Computer Methods in Applied Mechanics and Engineering*, vol. 7825, no. 98, pp. 23–41, 1998. 8, 10, 124, 130, 196
- [27] D. P. Mika and P. R. Dawson, "Effects of grain interaction on deformation in polycrystals," *Materials Science and Engineering: A*, vol. 257, no. 1, pp. 62–76, 1998.
- [28] V. Bachu and S. R. Kalidindi, "On the accuracy of the predictions of texture evolution by the finite element technique for fcc polycrystals," *Materials Science and Engineering A*, vol. 5093, no. 98, pp. 108–117, 1998. 8
- [29] F. Barbe, L. Decker, D. Jeulin, G. Cailletaud, S. Forest, G. Cailletaud, L. Decker, D. Jeulin, and G. Cailletaud, "Intergranular and intragranular behavior of polycrystalline aggregates. Part 2: Results," in *International Journal of Plasticity*, vol. 17, pp. 537–563, jan 2001. 9
- [30] F. Barbe, R. Quey, A. Musienko, and G. Cailletaud, "Three-dimensional characterization of strain localization bands in high-resolution elastoplastic polycrystals," *Mechanics Research Communications*, vol. 36, pp. 762–768, oct 2009. 9, 10, 173
- [31] H. Proudhon, S. Forest, and W. Ludwig, "Large scale finite element simulations of polycrystalline aggregates: applications to X-ray diffraction and imaging for fatigue metal behaviour," *31st Risø International Symposium on Materials Science*, pp. 121–139, 2010. 9, 10
- [32] H. Proudhon, J. Li, P. Reischig, N. Guéninchault, S. Forest, and W. Ludwig, "Coupling Diffraction Contrast Tomography with the Finite Element Method," *Advanced Engineering Materials*, pp. 1–10, 2015. 9, 18
- [33] A. Lyckegaard, E. M. Lauridsen, W. Ludwig, R. W. Fonda, and H. F. Poulsen, "On the use of laguerre tessellations for representations of 3D grain structures," *Advanced Engineering Materials*, vol. 13, no. 3, pp. 165–170, 2011. 9, 124
- [34] A. Spettil, T. Brereton, Q. Duan, T. Werz, C. E. Krill, D. P. Kroese, and V. Schmidt, "Fitting Laguerre tessellation approximations to tomographic image data," *Philosophical Magazine*, vol. 96, pp. 166–189, jan 2016. 9
- [35] A. Skalli, "Crystal rotations during the rolling of large-grained aluminium sheet," vol. 33, no. 6, pp. 997–1007, 1985. 11
- [36] S. R. Kalidindi, A. Bhattacharyya, and R. D. Doherty, "Detailed analyses of grain-scale plastic deformation in columnar polycrystalline aluminium using orientation image mapping and crystal plasticity models," *Proceedings of the Royal Society of London A: Mathematical, Physical and Engineering Sciences*, vol. 460, no. 2047, pp. 1935–1956, 2004. 11, 18
- [37] C. S. Barrett and L. H. Levenson, "The structure of aluminum after compression," *Trans. Aime*, vol. 137, pp. 112–127, 1940. 11

- [38] S. Panchanadeeswaran and R. Doherty, "Direct observation of orientation change by channel die compression of polycrystalline aluminum—Use of a split sample," *Scripta metallurgica et materialia*, vol. 28, pp. 213–218, mar 1993. 12
- [39] R. Becker and S. Panchanadeeswaran, "Effects of grain interactions on deformation and local texture in polycrystals," *Acta Metallurgica Et Materialia*, vol. 43, no. 7, pp. 2701–2719, 1995.
- [40] S. Panchanadeeswaran, R. D. Doherty, and R. Becker, "Direct observation of orientation change by channel die compression of polycrystalline aluminum - Use of a split sample," *Acta Materialia*, vol. 44, no. 3, pp. 1233–1262, 1996. 12, 18
- [41] R. Quey, D. Piot, and J. Driver, "Microtexture tracking in hot-deformed polycrystalline aluminium: Experimental results," *Acta Materialia*, vol. 58, pp. 2271–2281, mar 2010. 12, 17, 18, 102, 108, 174, 190, 191
- [42] R. Quey, D. Piot, and J. H. Driver, "Microtexture tracking in hot-deformed polycrystalline aluminium: Comparison with simulations," *Acta Materialia*, vol. 58, pp. 2271–2281, apr 2010. 12, 17, 18, 120, 138, 158, 174
- [43] W. Ludwig, P. Reischig, A. King, M. Herbig, E. M. Lauridsen, G. Johnson, T. J. Marrow, and J. Y. Buffière, "Three-dimensional grain mapping by x-ray diffraction contrast tomography and the use of Friedel pairs in diffraction data analysis," *Review of Scientific Instruments*, vol. 80, no. 3, pp. –, 2009. 13, 25, 27, 70, 176, 177
- [44] R. Suter, D. Hennessy, C. Xiao, and U. Lienert, "Forward modeling method for microstructure reconstruction using x-ray diffraction microscopy: Single-crystal verification," *Review of scientific Instruments*, vol. 77, no. 123905, pp. 1–12, 2006. 13, 26, 27, 70, 176, 177
- [45] L. Margulies, G. Winther, and H. F. Poulsen, "In Situ Measurement of Grain Rotation During Deformation of Polycrystals," *Science*, vol. 291, pp. 2392–2394, mar 2001. 13
- [46] G. Winther, L. Margulies, H. F. Poulsen, S. Schmidt, A. Larsen, E. M. Lauridsen, S. Nielsen, and A. Terry, "Lattice Rotations of Individual Bulk Grains during Deformation," *Materials Science Forum*, vol. 408-412, pp. 287–292, 2002. 13
- [47] H. F. Poulsen, L. Margulies, S. Schmidt, and G. Winther, "Lattice rotations of individual bulk grains. Part I: 3D X-ray characterization," *Acta Materialia*, vol. 51, no. 13, pp. 3821–3830, 2003. 13, 14, 17, 174
- [48] R. Pokharel, J. Lind, S. F. Li, P. Kenesei, R. A. Lebensohn, R. M. Suter, and A. D. Rollett, "In-situ observation of bulk 3D grain evolution during plastic deformation in polycrystalline Cu," *International Journal of Plasticity*, vol. 67, pp. 217–234, 2015. 14, 26, 70, 110
- [49] H. F. Poulsen, U. Lienert, and W. Pantleon, "Characterisation of orientation distributions of individual grains within deformed metals," *Materials Science and Technology*, vol. 21, pp. 1397–1400, dec 2005. 14, 17, 94
- [50] J. Oddershede, J. P. Wright, A. Beaudoin, and G. Winther, "Deformation-induced orientation spread in individual bulk grains of an interstitial-free steel," *Acta Materialia*, vol. 85, pp. 301–313, 2015. 15, 17, 94, 159, 174

- [51] L. Margulies, T. Lorentzen, H. F. Poulsen, and T. Leffers, "Strain tensor development in a single grain in the bulk of a polycrystal under loading," *Acta Materialia*, vol. 50, pp. 1771–1779, apr 2002. 15, 16, 18
- [52] R. Martins, L. Margulies, S. Schmidt, H. F. Poulsen, and T. Leffers, "Simultaneous measurement of the strain tensor of 10 individual grains embedded in an Al tensile sample," *Materials Science and Engineering A*, vol. 387-389, pp. 84–88, dec 2004. 15, 18
- [53] C. C. Aydiner, J. V. Bernier, B. Clausen, U. Lienert, C. N. Tomé, D. W. Brown, C. Aydiner, J. V. Bernier, B. Clausen, U. Lienert, C. N. Tomé, and D. W. Brown, "Evolution of stress in individual grains and twins in a magnesium alloy aggregate," *Physical Review B*, vol. 80, pp. 1–6, jul 2009. 15
- [54] J. Oddershede, S. Schmidt, H. F. Poulsen, H. O. Sørensen, J. Wright, W. Reimers, H. O. Sørensen, J. Wright, W. Reimers, H. O. Sørensen, J. Wright, and W. Reimers, "Determining grain resolved stresses in polycrystalline materials using three-dimensional X-ray diffraction," *Journal of Applied Crystallography*, vol. 43, pp. 539–549, apr 2010. 15, 17, 18, 45, 54, 55, 67, 174, 182
- [55] J. L. Schlenker, G. V. G. Gibbs, and M. B. Boisen, "Strain-tensor components expressed in terms of lattice parameters," *Acta Crystallographica Section ...*, vol. 34, no. 1, pp. 52–54, 1978. 15
- [56] H. Abdolvand, M. Majkut, J. Oddershede, J. P. Wright, and M. R. Daymond, "Study of 3-D stress development in parent and twin pairs of a hexagonal close-packed polycrystal: Part I – in-situ three-dimensional synchrotron X-ray diffraction measurement," *Acta Materialia*, vol. 93, pp. 246–255, 2015. 16, 18
- [57] H. Abdolvand, M. Majkut, J. Oddershede, J. P. Wright, and M. R. Daymond, "Study of 3-D stress development in parent and twin pairs of a hexagonal close-packed polycrystal: Part II – crystal plasticity finite element modeling," *Acta Materialia*, vol. 93, pp. 235–245, 2015. 16, 18
- [58] J. Wright et al., "Fable, a scientific workbench based on Eclipse/RCP and a framework for 3D xray diffraction.," 2003. Accessed: 2016-01-21. 16, 163
- [59] P. C. Hansen, H. O. Sørensen, Z. Sükösd, and H. F. Poulsen, "Reconstruction of Single-Grain Orientation Distribution Functions for Crystalline Materials," *SIAM Journal on Imaging Sciences*, vol. 2, pp. 593–613, jan 2009. 17, 94
- [60] R. Pokharel, J. Lind, A. K. Kanjarla, R. A. Lebensohn, S. F. Li, P. Kenesei, R. M. Suter, and A. D. Rollett, "Polycrystal Plasticity: Comparison Between Grain - Scale Observations of Deformation and Simulations," *Annual Review of Condensed Matter Physics*, vol. 5, no. 1, pp. 317–346, 2014. 18
- [61] R. Pokharel, "3D bulk grain evolution in polycrystalline Cu: comparison between HEDM observation and FFT based crystal plasticity simulations," in *Society of Engineering Science 51st Annual Technical Meeting*, no. October, 2014. 18
- [62] M. P. Miller and P. R. Dawson, "Understanding local deformation in metallic polycrystals using high energy X-rays and finite elements," *Current Opinion in Solid State and Materials Science*, vol. 18, no. 5, pp. 286–299, 2014. 22

- [63] C. Giacobazzo, H. L. Monaco, D. Viterbo, F. Scordari, G. Gilli, G. Zanotti, M. Catti, C. Giacobazzo, and P. Paufler, *Fundamentals of Crystallography*, vol. 28. Oxford Science Publications, 1993. 22, 58
- [64] E. Lauridsen and S. Schmidt, “Tracking: a method for structural characterization of grains in powders or polycrystals,” *Journal of applied crystallography*, vol. 34, pp. 744–750, 2001. 23
- [65] M. Moscicki, *In situ diffraction analysis of single grain behaviour during tensile straining of polycrystals*. PhD thesis, Ruhr-Universität Bochum, 2010. 23
- [66] J. V. Bernier, N. R. Barton, U. Lienert, and M. P. Miller, “Far-field high-energy diffraction microscopy: a tool for intergranular orientation and strain analysis,” *The Journal of Strain Analysis for Engineering Design*, vol. 46, pp. 527–547, jul 2011. 23, 45, 182
- [67] H. Sharma, R. M. Huizenga, and S. E. Offerman, “A fast methodology to determine the characteristics of thousands of grains using three-dimensional X-ray diffraction. I. Overlapping diffraction peaks and parameters of,” *Journal of applied crystallography*, vol. 45, pp. 693–704, jul 2012. 23, 51
- [68] S. Schmidt, “GrainSpotter : a fast and robust polycrystalline indexing algorithm,” *Journal of Applied Crystallography*, vol. 47, pp. 276–284, jan 2014. 23
- [69] F. C. Frank, “Orientation mapping,” *Metallurgical Transactions A*, vol. 19, no. March, pp. 403–408, 1988. 23, 72, 98
- [70] A. King, W. Ludwig, M. Herbig, J.-Y. Buffière, A. Khan, N. Stevens, and T. Marrow, “Three-dimensional in situ observations of short fatigue crack growth in magnesium,” *Acta Materialia*, vol. 59, pp. 6761–6771, oct 2011. 25
- [71] L. Nervo, A. King, J. P. Wright, W. Ludwig, P. Reischig, J. Quinta Da Fonseca, and M. Preuss, “Comparison between a near-field and a far-field indexing approach for characterization of a polycrystalline sample volume containing more than 1500 grains,” *Journal of Applied Crystallography*, vol. 47, pp. 1402–1416, aug 2014. 25, 86, 188
- [72] W. Ludwig, A. King, M. Herbig, and P. Reischig, “Characterization of polycrystalline materials using synchrotron X-ray imaging and diffraction techniques,” *Journal of Microscopy*, vol. 62, pp. 22–28, dec 2010. 25
- [73] M. Herbig, A. King, P. Reischig, H. Proudhon, E. M. Lauridsen, J. Marrow, J. Y. Buffière, and W. Ludwig, “3-D growth of a short fatigue crack within a polycrystalline microstructure studied using combined diffraction and phase-contrast X-ray tomography,” *Acta Materialia*, vol. 59, no. 2, pp. 590–601, 2011. 25, 70
- [74] F. Li, *Imaging of Orientation and Geometry in Microstructures : Development and Applications of High Energy X-ray Diffraction Microscopy*. PhD thesis, Carnegie Mellon University, 2011. 26
- [75] C. M. Hefferan, J. Lind, S. F. Li, U. Lienert, A. D. Rollett, and R. M. Suter, “Observation of recovery and recrystallization in high-purity aluminum measured with forward modeling analysis of high-energy diffraction microscopy,” *Acta Materialia*, vol. 60, pp. 4311–4318, jun 2012. 70

- [76] S. F. Li, J. Lind, C. M. Hefferan, R. Pokharel, U. Lienert, A. D. Rollett, and R. M. Suter, "Three-dimensional plastic response in polycrystalline copper via near-field high-energy X-ray diffraction microscopy," *Journal of Applied Crystallography*, vol. 45, no. 6, pp. 1098–1108, 2012. 26, 70
- [77] H. Sharma, R. R. M. Huizenga, and S. E. Offerman, "A fast methodology to determine the characteristics of thousands of grains using three-dimensional X-ray diffraction. II. Volume, centre-of-mass position, crystallographic orientation and strain state of grains," *Journal of Applied Crystallography*, vol. 45, pp. 705–718, jul 2012. 28
- [78] F. Barou, *Étude de la croissance des sous-grains dans des alliages binaires aluminium – manganèse*. PhD thesis, École Nationale Supérieure des Mines de Saint-Étienne, 2009. 29, 178
- [79] A. Albou, *Influence de l'orientation cristalline sur les microstructure de déformation et l'adoucissement d'alliages Al-Mn*. PhD thesis, École Nationale Supérieure des Mines de Saint-Étienne, 2010. 29, 178
- [80] J.-C. Labiche, O. Mathon, S. Pascarelli, M. A. Newton, G. G. Ferre, C. Curfs, G. B. M. Vaughan, A. Homs, and D. F. Carreiras, "The fast readout low noise camera as a versatile x-ray detector for time resolved dispersive extended x-ray absorption fine structure and diffraction studies of dynamic problems in materials science, chemistry, and catalysis," *Review of Scientific Instruments*, vol. 78, no. 9, p. 91301, 2007. 32, 34
- [81] H. F. Poulsen, W. Ludwig, E. M. Lauridsen, S. Schmidt, W. Pantleon, U. Olsen, J. Oddershede, P. Reischig, A. Lyckegaard, J. Wright, and G. Vaughan, "4D characterization of metals by 3DXRD," in *31st Risø International Symposium on Materials Science*, pp. 101–119, 2011. 32
- [82] J. Wright, "Crystal wafer as a wavelength monitor," *Acta Crystallographica Section A*, vol. 70, no. a1, p. C1760, 2014. 33, 52
- [83] H. Proudhon and W. Ludwig, "Deformation and fatigue behaviour of polycrystalline nickel based superalloy," *ESRF experimental report ma1921*, 2014. 33
- [84] W. R. Busing and H. A. H. Levy, "Angle calculations for 3-and 4-circle X-ray and neutron diffractometers," *Acta Crystallographica*, vol. 22, pp. 457–464, apr 1967. 42
- [85] A. Borbély, L. Renversade, P. Kenesei, and J. Wright, "On the calibration of high-energy X-ray diffraction setups. I. Assessing tilt and spatial distortion of the area detector," *Journal of Applied Crystallography*, vol. 47, pp. 1042–1053, may 2014. 45, 46, 47, 48, 161, 202
- [86] A. Borbély, L. Renversade, and P. Kenesei, "On the calibration of high-energy X-ray diffraction setups. II. Assessing the rotation axis and residual strains," *Journal of Applied Crystallography*, vol. 47, no. 5, pp. 1585–1595, 2014. 45, 52, 53, 55, 161, 202
- [87] A. P. Hammersley, S. O. Svensson, M. Hanfland, a. N. Fitch, and D. Hausermann, "Two-dimensional detector software: From real detector to idealised image or two-theta scan," *High Pressure Research*, vol. 14, pp. 235–248, jan 1996. 45, 163

- [88] M. L. Hart, M. Drakopoulos, C. Reinhard, and T. Connolley, "Complete elliptical ring geometry provides energy and instrument calibration for synchrotron-based two-dimensional X-ray diffraction.," *Journal of applied crystallography*, vol. 46, pp. 1249–1260, oct 2013. 46
- [89] J. H. Lee, C. C. Aydiner, J. D. Almer, J. V. Bernier, K. W. Chapman, P. J. Chupas, D. R. Haeffner, K. Kump, P. L. Lee, U. Lienert, A. Miceli, and G. Vera, "Synchrotron applications of an amorphous silicon flat-panel detector.," *Journal of Synchrotron Radiation*, vol. 15, no. Ccd, pp. 477–88, 2008. 47
- [90] B. B. He, *Two-Dimensional X-ray Diffraction*. John Wiley & Sons, 2009. 47
- [91] J. C. Glez and J. Driver, "Orientation distribution analysis in deformed grains," *Journal of Applied Crystallography*, vol. 34, no. 3, pp. 280–288, 2001. 53, 96, 110, 132
- [92] J. K. Edmiston, N. R. Barton, J. V. Bernier, G. C. Johnson, and D. J. Steigmann, "Precision of lattice strain and orientation measurements using high-energy monochromatic X-ray diffraction," *Journal of Applied Crystallography*, vol. 44, no. 2, pp. 299–312, 2011. 55
- [93] V. A. Lubarda, "On the effective lattice parameter of binary alloys," *Mechanics of Materials*, vol. 35, no. 1-2, pp. 53–68, 2003. 57
- [94] D. E. Sands, *Vectors and Tensors in Crystallography*. Dover Publications, 1982. 58
- [95] A. King, G. Johnson, D. Engelberg, W. Ludwig, and J. Marrow, "Observations of Intergranular Stress Corrosion Cracking in a Grain-Mapped Polycrystal," *Science*, vol. 321, no. 5887, pp. 382–385, 2008. 70
- [96] S. F. Li and R. M. Suter, "Adaptive reconstruction method for three-dimensional orientation imaging," *Journal of Applied Crystallography*, vol. 46, no. 2, pp. 512–524, 2013. 70
- [97] A. D. Spear, S. F. Li, J. F. Lind, R. M. Suter, and A. R. Ingraffea, "Three-dimensional characterization of microstructurally small fatigue-crack evolution using quantitative fractography combined with post-mortem X-ray tomography and high-energy X-ray diffraction microscopy," *Acta Materialia*, vol. 76, pp. 413–424, 2014. 70
- [98] G. Johnson, A. King, M. G. Honnicke, J. Marrow, and W. Ludwig, "X-ray diffraction contrast tomography: A novel technique for three-dimensional grain mapping of polycrystals. II. The combined case," *Journal of Applied Crystallography*, vol. 41, no. 2, pp. 310–318, 2008. 70, 72, 99, 128, 186
- [99] M. Syha, A. Trenkle, B. Lödermann, A. Graff, W. Ludwig, D. Weygand, and P. Gumbsch, "Validation of three-dimensional diffraction contrast tomography reconstructions by means of electron backscatter diffraction characterization.," *Journal of applied crystallography*, vol. 46, pp. 1145–1150, aug 2013. 70, 186
- [100] L. Renversade, R. Quey, W. Ludwig, D. Menasche, S. Maddali, R. M. Suter, and A. Borbély, "Comparison between diffraction contrast tomography and high-energy diffraction microscopy on a slightly deformed aluminium alloy," *IUCrJ*, vol. 3, no. 1, pp. 1–11, 2016. 70, 161, 202

- [101] W. Ludwig et al., “Diffraction contrast tomography analysis code,” 2008. Accessed: 2015-12-18. 70
- [102] R. Quey, H. Suhonen, J. Laurencin, P. Cloetens, and P. Bleuet, “Direct comparison between X-ray nanotomography and scanning electron microscopy for the microstructure characterization of a solid oxide fuel cell anode,” *Materials Characterization*, vol. 78, pp. 87–95, apr 2013. 71, 72, 124, 195
- [103] T. Rowan, *Functional Stability Analysis of Numerical Algorithms*. PhD thesis, University of Texas at Austin, 1990. 72, 99, 128
- [104] R. Quey, “Orilib: a collection of routines for orientation manipulation,” 2012. 72, 99, 132
- [105] P. E. Danielsson, “Euclidean distance mapping,” *Computer Graphics and Image Processing*, vol. 14, no. 3, pp. 227–248, 1980. 73
- [106] P. Kenesei, “DIGIgrain Manual,” 2010. 90, 163
- [107] A. Kumar and P. R. Dawson, “Dynamics of texture evolution in face-centered cubic polycrystals,” *Journal of the Mechanics and Physics of Solids*, vol. 57, no. 3, pp. 422–445, 2009. 96
- [108] P. S. Bate, R. D. Knutsen, I. Brough, and F. J. Humphreys, “The characterization of low-angle boundaries by EBSD,” *Journal of Microscopy*, vol. 220, no. 1, pp. 36–46, 2005. 104
- [109] R. Quey, “Neper, a software package for polycrystal generation and meshing,” 2007. 124, 128, 195
- [110] P. R. Dawson and D. E. Boyce, “FEpX – Finite Element Polycrystals Theory, Finite Element Formulation, Numerical Implementation and Illustrative Examples,” 2015. 124, 130, 131, 196
- [111] C. Lautensack, *Random Laguerre tessellations*. PhD thesis, Universitat Karlsruhe, 2007. 124
- [112] E. Gabriel, G. E. Fagg, G. Bosilca, T. Angskun, J. J. Dongarra, J. M. Squyres, V. Sahay, P. Kambadur, B. Barrett, A. Lumsdaine, R. H. Castain, D. J. Daniel, R. L. Graham, and T. S. Woodall, *Open MPI: Goals, Concept, and Design of a Next Generation MPI Implementation*, pp. 97–104. Berlin, Heidelberg: Springer Berlin Heidelberg, 2004. 128
- [113] S. L. Wong, J. S. Park, M. P. Miller, and P. R. Dawson, “A framework for generating synthetic diffraction images from deforming polycrystals using crystal-based finite element formulations,” *Computational Materials Science*, vol. 77, pp. 456–466, 2013. 160
- [114] H. J. Bunge, R. Kiewel, T. Reinert, and L. Fritsche, “Elastic properties of polycrystals - influence of texture and stereology,” *Journal Of The Mechanics And Physics Of Solids*, vol. 48, no. 1, pp. 29–66, 2000. 160
- [115] P. Heiney, “Datasqueeze software, graphical tools for X-ray data analysis.,” 2002. Accessed: 2016-01-21. 163

- [116] J. Ilavsky, “Nika: software for two-dimensional data reduction,” *Journal of Applied Crystallography*, vol. 45, no. 2, pp. 324–328, 2012. 163
- [117] J. Kieffer and D. Karkoulis, “PyFAI, a versatile library for azimuthal regrouping,” *Journal of Physics: Conference Series*, vol. 425, p. 202012, 2013. 163
- [118] N. Viganò, W. Ludwig, and K. J. Batenburg, “Reconstruction of local orientation in grains using a discrete representation of orientation space,” in *Journal of Applied Crystallography*, vol. 47, pp. 1826–1840, International Union of Crystallography, 2014. 163

List of figures

I.1	Finite element model of an Al polycrystal containing 512 elements (or crystals).	10
I.2	Strain field in a high-resolution polycrystal deformed to 0.5% uniaxial tension.	10
I.3	Generation of a 3D mesh from an experimental polycrystal.	10
I.4	Split sample deformed by plane strain compression in a channel die.	12
I.5	Sketch of the 3DXRD experimental setup.	14
I.6	Lattice rotations of individual bulk grains in an Al polycrystal.	14
I.7	Elastic strains of a single bulk grain in a Cu polycrystal under loading.	16
I.8	Axial strains of 1118 grains in a cylindrical Cu polycrystal.	16
II.1	Rotating crystal method.	24
II.2	Effects of deformation on the far-field diffraction spots.	24
II.3	Principle of DCT.	27
II.4	Principle of HEDM.	27
II.5	Recrystallized microstructures.	30
II.6	Distribution of intra-granular disorientations in the recrystallized material.	30
II.7	Tensile strain-stress curve of the material.	30
II.8	Shape and dimensions of the dog bone, tensile test specimens.	31
II.9	Schematic view of the regions characterized by DCT, HEDM and EBSD.	32
II.10	In situ deformation setup.	33
II.11	Spot broadening with strain (1%, 2% and 4.5%).	35
III.1	Example of a far-field spot, chopped over six successive images.	38
III.2	Laboratory and detector coordinate systems of the 3DXRD geometry.	40
III.3	Schematic of a spot projection in the 3DXRD geometry.	44
III.4	Principle of radial distortion assessment.	47
III.5	Distortion field of the FReLoN-4M.	49
III.6	Polar transformation of a powder diffraction image.	49
III.7	Residual distortions of the FReLoN-4M after correction and calibration.	50
III.8	Numerical simulations of the fit errors and accuracies as a function of the integration step $\delta\omega$	53
III.9	Variations of the wavelength during the 3DXRD measurements of Sample B.	53
III.10	Distribution of grain lattice parameters in the initial state of Sample B.	57
III.11	Effect of calibration errors on orientation accuracy.	60
III.12	Residual lattice strains due to calibration errors.	60
III.13	Effect of peak-coordinate errors on the accuracy of grain quantities.	61
III.14	Cumulative effect of calibration and peak-coordinate errors on the accuracy of grain quantities.	62
III.15	Initial microstructure of Sample B given by 3DXRD.	64
III.16	Standard errors for grain positions and orientations.	64

III.17 Residual lattice strains in Sample B.	65
III.18 Residual stresses in Sample B.	65
IV.1 Sample A and grain structure imaged with DCT, HEDM and EBSD.	71
IV.2 Vertical distribution of the 14 HEDM layers, as given by the registration.	73
IV.3 Disorientation angle distribution of DCT and HEDM grain boundary pixels.	74
IV.4 Comparison between the DCT and HEDM microstructures on a single layer.	75
IV.5 Comparison between the positions of the grain boundaries of the DCT and HEDM microstructures.	76
IV.6 Local disorientation between the DCT and HEDM microstructures.	76
IV.7 Comparison between the DCT and EBSD microstructures.	77
IV.8 Comparison between the positions of the grain boundaries of the DCT and EBSD microstructures.	77
IV.9 Grain boundaries as uncertainty regions in DCT and HEDM reconstructions.	78
IV.10 Grain structure of Sample B as imaged by DCT.	80
IV.11 Comparison between the middle-part and bottom-part absorption tomograms.	81
IV.12 Distribution of orientation changes caused by merging.	81
IV.13 Completeness ratios resulting from the indexing of 3DXRD spots.	82
IV.14 Average representation of the microstructure of Sample B given by DCT and 3DXRD.	83
IV.15 Difference in grain position between the DCT and 3DXRD data.	84
IV.16 Distribution of disorientation angles between DCT and 3DXRD data.	84
IV.17 Comparison of DCT and 3DXRD grain sizes.	85
IV.18 Distribution of grain size in Sample B.	85
V.1 Example of three overlapping spots at $\epsilon = 2.0\%$	90
V.2 Evolution of grain completenesses with strain.	91
V.3 Representation of the grains indexed in the successive deformed states.	93
V.4 Illustration of azimuthal projection of an experimental spot.	95
V.5 Representation of tri-Gaussian ODFs by ellipsoids.	96
V.6 Truncation and discretization of a grain ODF.	97
V.7 Comparison between experimental and simulated spots for a selected grain.	101
V.8 Macrotecture of Sample B.	103
V.9 Orientation and rotation of the tensile axis of individual grains.	103
V.10 Rotation angles of the successive deformation increments.	104
V.11 Correlation between the rotation angles of the successive strain increments.	105
V.12 Rotation angles with respect to the initial orientations for the successive deformed states.	106
V.13 Rotation axes with respect to the initial orientations for $\epsilon = 4.5\%$	107
V.14 Orientation dependency of the angle between the tensile axis and the spin vector of the most stressed slip system.	107
V.15 Distribution of angles between the tensile axis and the spin vector of the most stressed slip system.	107
V.16 Influence of axial symmetry on the disorientation of grain pairs.	109
V.17 Variability at constant orientation of the grain rotations.	109
V.18 Variability at constant orientation of the grain rotations in the four IPF regions.	109
V.19 Estimation of the average disorientation angle of a tri-Gaussian ODF.	111

V.20	Evolution with strain of the average disorientation of the intra-grain orientation spreads with strain.	111
V.21	Evolution with strain of the anisotropy of the intra-grain orientation spreads.	111
V.22	Evolution of the preferential disorientation axes with strain.	113
V.23	Correlation between the orientation spreads and the orientation of the grains, illustrated in the Rodrigues fundamental region.	114
V.24	Mechanical responses against the applied stress of two selected grains.	116
V.25	Evolution of the distribution of axial elastic strains and stresses.	116
V.26	Macroscopic stress-strain curve.	117
V.27	Average mechanical response of Sample B during in situ tensile test.	117
V.28	Poisson effect in Sample B during in situ tensile test.	117
V.29	Relation to orientation of the grain axial elastic strains and axial stresses at $\epsilon = 1.0\%$	119
V.30	Axial mechanical response in orientation fibres.	119
V.31	Influence of the Taylor factor on the axial stress.	119
VI.1	Example of a polycrystal generated by Laguerre tessellation.	125
VI.2	Optimization procedure exemplified for a 2D microstructure.	127
VI.3	Approximation of the experimental microstructure of Sample B.	128
VI.4	Finite element mesh of Sample B.	129
VI.5	Macroscopic stress-strain curves.	132
VI.6	Disorientation, axial elastic strain and axial stress fields in the finite element simulation after $\epsilon = 4.5\%$	133
VI.7	Analysis of the orientation distribution in a finite element grain.	134
VI.8	Experimental and simulated rotation angles: distributions of $\hat{\theta}_i$	136
VI.9	Experimental and simulated rotation angles: distributions of θ_0	136
VI.10	Experimental and simulated rotation axes.	137
VI.11	Experimental and simulated rotation axes: correlation with the tensile direction Z.	137
VI.12	Variability at constant orientation of the experimental and simulated rotations.	138
VI.13	Correlation between the experimental and simulated rotation angles.	139
VI.14	Deviation between the experimental and simulated rotation axes.	140
VI.15	Comparison of experimental and simulated rotations in the four IPF regions.	140
VI.16	Experimental and simulated average disorientation angles.	142
VI.17	Experimental and simulated anisotropy factors.	142
VI.18	Experimental and simulated preferential disorientation axes at 4.5%.	144
VI.19	Experimental and simulated preferential disorientation axes after 4.5%: correlation with the tensile direction Z.	144
VI.20	Distribution of active spin vectors in the finite element simulation at $\epsilon = 1.0\%$	145
VI.21	Relation between slip rate variability and slip activity.	146
VI.22	Correlation between the experimental and simulated (FEM) average disorientation angles.	147
VI.23	Deviation between experimental and simulated preferential disorientation axes.	147
VI.24	Experimental and simulated disorientation axes: relation to the grain orientations.	148
VI.25	Evolution of the experimental and simulated elastic strain distributions with plastic strain.	150

VI.26 Evolution of the experimental and simulated stress distributions with plastic strain.	151
VI.27 Average axial elastic strain and stress: correlation between experiment and finite element simulation.	152
VI.28 Relation to orientation of the grain axial elastic strains and axial stresses at $\epsilon = 1.0\%$	153
VI.29 Elastic strain and stress responses of a selected grain in the experiment and the finite element simulation.	155
VI.30 Deviation between experimental and simulated elastic strains and stresses.	156
VI.31 Deviation between experimental and simulated elastic strains and stresses.	157
A.1 Preferential disorientation axes resulting from an isotropic stress variability in uni-axial tension.	167
B.1 Hétérogénéités de déformation simulées par éléments finis au sein d'un polycristal déformé à 0.5% en traction uniaxiale.	173
B.2 Méthode de rotation du cristal.	177
B.3 Principe du DCT	177
B.4 Principe du HEDM.	177
B.5 Microstructure recristallisée.	178
B.6 Courbe contrainte-déformation macroscopique mesurée en laboratoire pour l'alliage Al-0.3Mn.	178
B.7 Forme et dimensions des échantillons destinés aux essais in-situ.	179
B.8 Vue schématique des régions mesurées par DCT, HEDM et EBSD.	179
B.9 Dispositif expérimental in-situ.	180
B.10 Distorsions radiales résiduelles du FReLoN-4M après correction et calibration.	182
B.11 Variations de la longueur d'onde durant la mesure de l'échantillon B.	183
B.12 Distribution de paramètre de maille à l'état non-déformé de l'échantillon B.	183
B.13 Microstructure initiale de l'échantillon B révélée par 3DXRD.	184
B.14 Déformations élastiques résiduelles dans l'échantillon B.	185
B.15 Contraintes résiduelles dans l'échantillon B.	185
B.16 Microstructure de l'échantillon A révélée par DCT, HEDM et EBSD.	187
B.17 Comparaison de la position des joints de grains DCT et HEDM.	187
B.18 Comparaison de la position des joints de grains DCT et EBSD.	187
B.19 Microstructure de l'échantillon B révélée par DCT.	189
B.20 Écarts de position et d'orientation entre les grains DCT et 3DXRD.	189
B.21 Rotations moyennes des 466 grains de 0 à 4.5%.	190
B.22 Distribution des axes de rotations à $\epsilon = 4.5\%$	191
B.23 Variabilité à orientation constante des rotations moyennes.	191
B.24 Distribution des axes privilégiés de désorientation à $\epsilon = 4.5\%$	192
B.25 Effet de l'orientation initiale sur les dispersions d'orientations intragranulaires.	193
B.26 Exemple de la réponse mécanique d'un grain mesurée par 3DXRD.	193
B.27 Réponse macroscopique du polycristal.	194
B.28 Effet de l'orientation sur les composantes axiales de déformation élastique et contrainte à $\epsilon = 1.0\%$	194
B.29 Approximation de la microstructure expérimentale de l'échantillon B.	195
B.30 Axes de rotation expérimentaux et simulés.	196
B.31 Écarts angulaires entre les axes de rotation expérimentaux et simulés.	197

B.32	Variabilités à orientation constante des rotations expérimentales et simulées.	197
B.33	Axes privilégiés de désorientation : dépendance à l'axe de traction.	198
B.34	Écarts angulaires entre les axes de désorientation expérimentaux et simulés.	198
B.35	Effet de l'orientation initiale sur les dispersions d'orientations intragranulaires dans l'expérience et la simulation	199
B.36	Comparaison avec la simulation de la réponse mécanique mesurée par 3DXRD pour un grain arbitraire.	200

List of tables

I.1	Elastic constants for Al crystals	5
II.1	Scan parameters used for 3DXRD during in situ tensile test.	34
III.1	Global and grain parameters describing the 3DXRD geometry.	42
III.2	The detector tilt components (n_1, n_2, n_3), the detector distance D and the beam centre (u_B, v_B) obtained from the calibration of the FReLoN-4M.	50
III.3	Calibration parameters: values of the global parameters after each calibration step. The numbers in parenthesis indicate the standard errors in the unit of the last decimal.	57
V.1	Evolution of grain indexing and tracking with strain.	92
V.2	Assessment of intra-grain orientation spreads: results of the fitting procedure for a selected grain. The principal axis is the longest axis (corresponding to λ_1).	100
VI.1	Material parameters determined from the laboratory test and used in the finite element simulation.	131
VI.2	Variabilities at constant orientation and overall variabilities of the experimental and simulated rotations.	138
VI.3	Evolution of the average disorientation angles and anisotropy factors with strain in the experiment and the simulations.	143
VI.4	Agreement between experimental and simulated elastic strains and stresses with regard to measurement accuracies (in percentage of the grains).	157
B.1	Paramètres globaux décrivant la géométrie du 3DXRD et paramètres des grains.	181
B.2	Accord grain par grain entre les déformations élastiques / contraintes mesurées par 3DXRD et simulées par éléments finis.	201

NNT : 2016LYSEM019

Loïc RENVERSADE

EXPERIMENTAL AND NUMERICAL ANALYSIS OF SINGLE GRAIN PLASTICITY IN AN ALUMINIUM POLYCRYSTAL DEFORMED IN UNIAXIAL TENSION

Speciality: Materials Science

Keywords: polycrystal, crystal plasticity, 3DXRD, DCT, finite elements, lattice rotations, stress, aluminium

Abstract:

This work aims to improve our understanding of the local deformation of polycrystalline materials. To this end, in situ synchrotron experiments and finite element simulations are coupled to study the individual grain responses in an aluminium polycrystal during plastic deformation.

In the experiment, the initial microstructure is mapped by Diffraction Contrast Tomography (DCT). The specimen is deformed in uniaxial tension and 466 grains are followed by 3D X-Ray Diffraction (3DXRD) up to 4.5% plastic strain. New original analysis methods provide the grain average orientations, elastic strains and stresses, and allow determining the intra-grain orientation distributions from the 3DXRD measurements.

In the simulation, the real microstructure (DCT) is modeled by a Laguerre tessellation, finely meshed and submitted to the experimental loading. The resulting mechanical and orientation fields can be compared to the experimental data.

The comparison reveals a first-order agreement between experiment and simulation. The experimental rotations exhibit a high variability, associated to grain interaction and well reproduced in the simulation. The orientation distributions exhibit preferential spread directions perpendicular to the tensile direction, which can be related to the deformation mechanisms. Lastly, the stresses are found to be in agreement within the measurement accuracies. Such a rich dataset provides routes to improve crystal plasticity models.

NNT : 2016LYSEM019

Loïc RENVERSADE

ANALYSE EXPÉRIMENTALE ET NUMÉRIQUE DE LA PLASTICITÉ À L'ÉCHELLE DES GRAINS INDIVIDUELS DANS UN POLYCRISTAL D'ALUMINIUM DÉFORMÉ EN TRACTION UNIAXIALE

Spécialité : Science et Génie des Matériaux

Mots clés : polycrystal, plasticité cristalline, 3DXRD, DCT, éléments finis, rotations cristallines, contraintes, aluminium

Résumé :

Ce travail vise à améliorer la compréhension de la déformation locale des matériaux polycristallins. Pour cela, les comportements des grains individuels d'un polycrystal d'aluminium déformé plastiquement sont étudiés par une approche couplant expériences in situ en synchrotron et simulation par élément finis.

Dans l'expérience, la microstructure initiale est cartographiée par tomographie en contraste de diffraction (DCT). L'éprouvette est déformée en traction uniaxiale et 466 grains sont suivis par microscopie 3D par diffraction des rayons X (3DXRD) jusqu'à une déformation de 4.5%. De nouvelles méthodes d'analyse originales donnent accès aux orientations, déformations élastiques et contraintes, en moyenne par grain, et permettent de déterminer les distributions d'orientations intragranulaires à partir des données 3DXRD. Dans la simulation, la microstructure réelle (DCT) est modélisée par une partition de Laguerre, maillée finement et soumise au chargement expérimental. Les champs mécaniques et les champs d'orientations résultants peuvent être comparés aux données expérimentales.

La comparaison entre expérience et simulation révèle un accord au premier ordre. Les rotations expérimentales montrent une forte variabilité associée à l'interaction intergranulaire et bien reproduite dans la simulation. Les distributions d'orientations ont des directions d'étalement privilégiées perpendiculaires à la direction de traction, ce qui est relié aux mécanismes de déformation du matériau. Les contraintes montrent un bon accord, dans la limite de la précision de mesure. Ces données, très riches, fournissent des pistes d'amélioration pour les modèles de plasticité cristalline.